İSTANBUL TECHNICAL UNIVERSITY ★ INSTITUTE OF SCIENCE AND TECHNOLOGY

EXTREMUM SEEKING METHOD AND ITS APPLICATIONS IN AUTOMOTIVE CONTROL

Ph.D. Thesis by
Erkin DİNÇMEN

Department : Mechanical Engineering

Programme : Mechanical Engineering

MAY 2011

İSTANBUL TECHNICAL UNIVERSITY ★ INSTITUTE OF SCIENCE AND TECHNOLOGY

EXTREMUM SEEKING METHOD AND ITS APPLICATIONS IN AUTOMOTIVE CONTROL

Ph.D. Thesis by
Erkin DİNÇMEN
(503042017)

Date of submission : **04 February 2011**
Date of defence examination : **03 May 2011**

Supervisor (Chairman): **Assoc. Prof. Dr. Bilin AKSUN GÜVENÇ (OKAN)**
Co-Supervisor : **Assoc. Prof. Dr. Tankut ACARMAN (GSU)**
Examining Committee : **Assoc. Prof. Dr. Şeniz ERTUĞRUL (ITU)**
Prof. Dr. Emre KÖSE (BU)
Assoc. Prof. Dr. Gökhan İNALHAN (ITU)
Prof. Dr. Levent GÜVENÇ (OKAN)
Assist. Prof. Dr. Erdinç ALTUĞ (ITU)

MAY 2011

İSTANBUL TEKNİK ÜNİVERSİTESİ ★ FEN BİLİMLERİ ENSTİTÜSÜ

EKSTREMUM ARAMA METODU VE OTOMOTİV KONTROLU ALANINDA UYGULAMALARI

DOKTORA TEZİ

Erkin DİNÇMEN
(503042017)

Tezin Enstitüye Verildiği Tarih : 04 Şubat 2011
Tezin Savunulduğu Tarih : 03 Mayıs 2011

Tez Danışmanı : Doç. Dr. Bilin AKSUN GÜVENÇ (OKAN)
Eş Danışman : Doç.Dr. Tankut ACARMAN (GSÜ)
Diğer Jüri Üyeleri : Doç. Dr. Şeniz ERTUĞRUL (İTÜ)
Prof. Dr. Emre KÖSE (BÜ)
Doç. Dr. Gökhan İNALHAN (İTÜ)
Prof. Dr. Levent GÜVENÇ (OKAN)
Yrd. Doç. Dr. Erdinç ALTUĞ (İTÜ)

MAYIS 2011

To my family,

FOREWORD

I would like to express my deep appreciation to my advisor Assoc. Prof. Dr. Bilin Aksun Güvenç for her instructions, guidance, encouragement and constant support throughout my PhD study.

I would like to extend my gratitude to my co-advisor Assoc. Prof. Dr. Tankut Acarman for introducing me with the extremum seeking control and for suggesting me to work on this area.

I wish to thank Prof. Dr. Levent Güvenç, Prof. Dr. Emre Köse, Assoc. Prof. Dr. Şeniz Ertuğrul and Assoc. Prof. Dr. Gökhan İnalhan for their valuable suggestions during the stages of my work. I would like to express my gratitude to all my friends for their helps and encouragements.

I would like to acknowledge support of European Commission Framework Program 6 AUTOCOM Project, DPT Drive Safe Project and TÜBİTAK.

This long journey would have never occurred without the loving support of my family. The dissertation is dedicated to them.

February 2011

Erkin Dinçmen

Mechanical Engineer, M.Sc.

TABLE OF CONTENTS

Page

FOREWORD .... **vii**
TABLE OF CONTENTS .... **ix**
ABBREVIATIONS .... **xi**
LIST OF TABLES .... **xiii**
LIST OF FIGURES .... **xv**
LIST OF SYMBOLS .... **xix**
SUMMARY .... **xxiii**
ÖZET .... **xxv**
1. INTRODUCTION **1**
1.1 Introduction and Scope of the Dissertation 1
1.2 Contributions of the Dissertation 2
1.3 Outline of the Dissertation 5
2. LITERATURE REVIEW **7**
2.1 Extremum Seeking Algorithm 7
2.1.1 Sliding mode based extremum-seeking algorithm 7
2.1.2 Perturbation based extremum seeking algorithm 16
2.1.3 Numerical optimization based extremum seeking algorithm 21
2.1.4 Gradient-based extremum seeking algorithm 23
2.2 ABS Control Problem 27
2.3 Hybrid Electric Vehicle Control Problem 32
2.4 Chapter Summary 42
3. ABS CONTROL VIA EXTREMUM SEEKING WITH PARAMETER TUNING **43**
3.1 Introduction 43
3.2 Problem Description 44
3.3 Control Algorithm 46
3.4 Simulation Study 52
3.5 Real Time Simulations 58
3.6 Chapter Summary 60
4. ABS CONTROL ALGORITHM VIA EXTREMUM SEEKING METHOD WITH ENHANCED LATERAL STABILITY **63**
4.1 Introduction 63
4.2 Algorithm Development 64
4.3 Simulations 72
4.3.1 Simulation model 72
4.3.2 Validation of the vehicle model with actual vehicle measurements 83
4.3.3 Simulation scenario 1 85
4.3.4 Simulation scenario 2 88
4.4 Modified ESA with Lateral Force Improvement 89
4.5 Simulations 92

4.5.1 Simulations with scenario 2 92
4.5.2 Simulation scenario 3 97
4.5.3 Simulation scenario 4 100
4.6 Chapter Summary 102
5. EXTREMUM SEEKING BASED ENERGY MANAGEMENT STRATEGY FOR HYBRID ELECTRIC VEHICLES 103
5.1 Introduction 103
5.2 Hybrid Electric Vehicle Model 104
5.3 Control Algorithm 111
5.3.1 Upper level controller 111
5.3.2 Extremum seeking algorithm 114
5.4 Dynamic Programming 120
5.4.1 Introduction 120
5.4.2 Application of DP for calculation of minimum fuel consumption 122
5.5 Simulation Study 125
5.5.1 Simulation study 1 125
5.5.2 Simulation study 2 127
5.5.3 Real Time Simulations 136
5.6 Chapter Summary 141
6. CONCLUSIONS 143
REFERENCES 147
APPENDICES 155
CURRICULUM VITAE 165

ABBREVIATIONS

ABS	: Anti-lock Braking System
AMT	: Automated Mechanical Transmission
c.g	: Center of Gravity
CIDI	: Compression-Ignition Direct-Injection
DP	: Dynamic Programming
dof	: Degree of Freedom
ECMS	: Equivalent Consumption Minimization Strategy
EM	: Electric Motor
EMS	: Energy Management Strategy
ESA	: Extremum Seeking Algorithm
HEV	: Hybrid Electric Vehicle
ICE	: Internal Combustion Engine
LTI	: Linear Time Invariant
NEDC	: New European Driving Cycle
PHEV	: Parallel Hybrid Electric Vehicle
SI	: Spark Ignition
SOC	: State of Charge

LIST OF TABLES

Page

Table 3.1: Burckhardt tire model parameters for different road conditions [84]...... 45
Table 4.1: Vehicle parameter values.. 73
Table 5.1: NEDC fuel consumption results. 132
Table 5.2: ECE_R15 fuel consumption results. 133
Table 5.3:USA CITY_I fuel consumption results.. 135

LIST OF FIGURES

Page

Figure 2.1 : Sliding mode based extremum seeking scheme [6]. 8
Figure 2.2 : Change of s and $\dot{s}$ according to **(2.11)** when $dJ(\sigma)/d\sigma$ >0. 10
Figure 2.3 : Change of s and $\dot{s}$ according to **(2.11)** when $dJ(\sigma)/d\sigma$ <0. 11
Figure 2.4 : Longitudinal tire force characteristics. 12
Figure 2.5 : Change of s and $\dot{s}$ according to **(2.21)**. 14
Figure 2.6 : Perturbation based extremum seeking scheme [13]. 18
Figure 2.7 : Numerical optimization based extremum seeking scheme [35]. 21
Figure 2.8 : Deceleration threshold based ABS algorithm [45]. 27
Figure 2.9 : Tire model. 28
Figure 2.10 : Longitudinal tire force characteristics. 29
Figure 2.11 : Series hybrid electric vehicle configuration [60]. 33
Figure 2.12 : Parallel hybrid electric vehicle configuration [60]. 33
Figure 2.13 : Combined hybrid electric vehicle configuration [60]. 33
Figure 2.14 : Generic ICE efficiency map [63]. 35
Figure 2.15 : Engine efficiency map in [68]. 38
Figure 3.1 : Change of the friction coefficient μ_x with respect to the tire slip κ for different road conditions. 46
Figure 3.2 : Phase plane of s and $\dot{s}$ subject to the sliding motion dynamics. 50
Figure 3.3 : Operating region. 51
Figure 3.4 : The overall controller structure. 52
Figure 3.5 : Hydraulic brake actuator system. 53
Figure 3.6 : Responses of the vehicle speed u and ωR on the road with μ_{max} = 0.8. 54
Figure 3.7 : Responses of the braking forces on the road with μ_{max} = 0.8. 55
Figure 3.8 : Change of the tire-road friction function on the road with μ_{max} = 0.8. 55
Figure 3.9 : Change of the longitudinal tire slip κ on the road with μ_{max} = 0.8. 56
Figure 3.10 : Change of the braking moment input T_b on the road with μ_{max} = 0.8. . 56
Figure 3.11 : Change of the tire road friction function on the road with μ_{max}=0.4. ... 56
Figure 3.12 : Change of the longitudinal tire slip κ on the road with μ_{max} = 0.4. 57
Figure 3.13 : Change of the tire road friction function when the road condition changes from μ_{max} =0.6 to μ_{max} = 1.2. 57
Figure 3.14 : Change of the longitudinal tire slip κ when the road condition changes from μ_{max} =0.6 to μ_{max} = 1.2. 58
Figure 3.15 : Change of the braking moment input T_b when the road condition changes from μ_{max} =0.6 to μ_{max} = 1.2. 58
Figure 3.16 : Setup for real time simulations. 59
Figure 3.17 : Power supply and MicroAutoBox. 59
Figure 3.18 : Change of the tire road friction function in various road conditions with μ_{max} =0.4, μ_{max} =0.6, μ_{max} =0.8, and μ_{max} = 1. 60
Figure 3.19 : Change of the tire road friction function when the road condition changes from μ_{max} =0.8 to μ_{max} = 0.4. 60

Figure 4.1 : Change of the longitudinal tire forces on different road conditions. ... 64
Figure 4.2 : Vehicle axis system. ... 72
Figure 4.3 :Top view of the vehicle. ... 73
Figure 4.4 : Vehicle suspension model. ... 75
Figure 4.5 : Roll motion of the sprung mass. ... 76
Figure 4.6 : Forces and moments acting on the front axle. ... 77
Figure 4.7 : Forces and moments acting on the wheel. ... 78
Figure 4.8 : Change of the longitudinal tire forces with respect to the tire slip ratio under pure longitudinal slip condition. ... 80
Figure 4.9 : Change of the lateral tire forces with respect to the tire side slip angle under pure lateral slip condition. ... 80
Figure 4.10 : Change of the longitudinal tire forces in combined slip case. ... 81
Figure 4.11 : Change of the lateral tire forces in combined slip case. ... 81
Figure 4.12 : Hydraulic brake actuator system. ... 82
Figure 4.13 : Inertial measurement unit installed in the vehicle. ... 83
Figure 4.14 : Instrumented vehicle. ... 83
Figure 4.15 : Driver steering input. ... 84
Figure 4.16 : Validation results: Lateral acceleration. ... 84
Figure 4.17 : Validation results: Roll rate. ... 84
Figure 4.18 : Validation results: Yaw rate. ... 85
Figure 4.19 : Change of the normalized longitudinal tire forces in dry road. ... 85
Figure 4.20 : Change of the tire slip ratios in dry road. ... 86
Figure 4.21 : Change of the braking moments in dry road. ... 86
Figure 4.22 : Change of the normalized longitudinal tire forces in snowy road. ... 87
Figure 4.23 : Change of the tire slip ratios in snowy road. ... 87
Figure 4.24 : Change of the braking moments in snowy road. ... 88
Figure 4.25 : Driver steering input for the simulation scenario 2 ... 89
Figure 4.26 : Change of the tire slip ratios in simulation scenario 2. ... 89
Figure 4.27 : Change of the slip ratios in simulation scenario 2, dry road. (red: first version, blue: modified version). ... 92
Figure 4.28 : Change of lateral tire forces in simulation scenario 2, dry road. ... 93
Figure 4.29 : Change of longitudinal tire forces in simulation scenario 2, dry road. 93
Figure 4.30 : Change of longitudinal speed in simulation scenario 2, dry road. ... 94
Figure 4.31 : Change of lateral accelerations in simulation scenario 2, dry road ... 94
Figure 4.32 : Vehicle trajectories in simulation scenario 2, dry road. ... 94
Figure 4.33 : Change of the slip ratios in simulation scenario 2, snowy road. ... 95
Figure 4.34 : Change of lateral tire forces in simulation scenario 2, snowy road. ... 95
Figure 4.35 : Longitudinal tire forces in simulation scenario 2, snowy road. ... 96
Figure 4.36 : Longitudinal speed in simulation scenario 2, snowy road. ... 96
Figure 4.37 : Lateral accelerations in simulation scenario 2, snowy road. ... 97
Figure 4.38 : Vehicle trajectories in simulation scenario 2, snowy road. ... 97
Figure 4.39 : Normalized longitudinal tire forces in simulation scenario 3. ... 98
Figure 4.40 : Lateral tire forces in simulation scenario 3. ... 98
Figure 4.41 : Longitudinal tire slip ratios in simulation scenario 3. ... 99
Figure 4.42 : Longitudinal speeds in simulation scenario 3. ... 99
Figure 4.43 : Lateral accelerations in simulation scenario 3. ... 100
Figure 4.44 : Vehicle trajectories in simulation scenario 3. ... 100
Figure 4.45 : Longitudinal tire slip ratios in simulation scenario 4. ... 101
Figure 4.46 : Lateral tire forces in simulation scenario 4. ... 101
Figure 4.47 : Lateral accelerations in simulation scenario 4. ... 102

Figure 5.1 : Parallel hybrid electric vehicle powertrain model. 105
Figure 5.2 : Representative ICE efficiency map. 105
Figure 5.3 : Representative EM efficiency map in [85]. 106
Figure 5.4 : Equivalent circuit of the battery [60]. 108
Figure 5.5 : Function of open circuit voltage U_{oc}. 109
Figure 5.6 : Function of battery discharge resistance R_{dis}. 109
Figure 5.7 : Function of battery charge resistance R_{chg}. 110
Figure 5.8 : Longitudinal vehicle and tire dynamic models. 110
Figure 5.9 : Flowchart of the control algorithm. 112
Figure 5.10 : Matlab/Stateflow diagram of the upper level controller. 112
Figure 5.11 : Power flow during battery charging. 114
Figure 5.12 : The ESA scheme for efficiency maximization. 120
Figure 5.13 : Paths resulting from all allowable decisions at *b* [88]. 121
Figure 5.14 : State space of the DP algorithm. 123
Figure 5.15 : Torque distribution area between ICE and EM. 126
Figure 5.16 : Powertrain efficiency η_T with change of EM torque 126
Figure 5.17 : Torque distribution result of the ESA. 127
Figure 5.18 : Powertrain efficiency result of the ESA. 127
Figure 5.19 : Speed profile for the NEDC in [85]. 128
Figure 5.20 : Gear profile for the NEDC in [85]. 128
Figure 5.21 : ICE operating points in the conventional vehicle for NEDC. 129
Figure 5.22 : ICE operating points in HEV for NEDC. 129
Figure 5.23 : EM operating points in HEV for NEDC. 129
Figure 5.24 : Change of SOC for NEDC. 130
Figure 5.25 : DP solution of ICE operating points for NEDC. 130
Figure 5.26 : DP solution of EM operating points for NEDC. 131
Figure 5.27 : DP solution of normalized battery energy level for NEDC. 131
Figure 5.28 : Fuel consumption results for NEDC. 131
Figure 5.29 : ECE_R15 speed profile [85]. 132
Figure 5.30 : ECE_R15 fuel consumption results 132
Figure 5.31 : Change of *SOC* for ECE_R15. 133
Figure 5.32 : DP solution of normalized battery energy level for ECE_R15. 133
Figure 5.33 : USA CITY_I speed profile [85]. 134
Figure 5.34 : USA CITY_I fuel consumption results. 134
Figure 5.35 : Change of *SOC* for USA CITY_I. 134
Figure 5.36 : DP solution of normalized battery energy level for USA CITY_I. ... 135
Figure 5.37 : CarMaker simulation screen shot. 136
Figure 5.38 : CarMaker interface. 137
Figure 5.39 : CarMaker model represented as Simulink S-function blocks. 137
Figure 5.40 : DS1005 hardware and CarMaker screenshot. 138
Figure 5.41 : Real time simulation result of the vehicle speed for NEDC. 138
Figure 5.42 : Real time simulation results of fuel consumptions for NEDC. 139
Figure 5.43 : Real time simulation result of *SOC* for NEDC. 139
Figure 5.44 : Real time simulation result of the vehicle speed for USA CITY_I. .. 139
Figure 5.45 : Real time simulation results of fuel consumption for USA CITY_I. 140
Figure 5.46 : Real time simulation result of *SOC* for USA CITY_I. 140
Figure A.1 : Position vectors of a point *P* relative to a fixed system and a moving system. 157

Figure A.2 : Vehicle axis system... 158
Figure A.3 : Roll motion of the sprung mass. 158

LIST OF SYMBOLS

a_{xs}	: Sprung Mass Longitudinal Acceleration
a_{xu}	: Unsprung Mass Longitudinal Acceleration
a_{ys}	: Sprung Mass Lateral Acceleration
a_{yu}	: Unsprung Mass Lateral Acceleration
a_{zs}	: Sprung Mass Vertical Acceleration
A	: Orifice Area
A_f	: Vehicle Frontal Area
$A_{\omega c}$	: Wheel Cylinder Area
B	: Stiffness Factor in Magic Formula
B_F	: Brake Factor
c_1, c_2, c_3	: Burckhardt Tire Model Parameters
c_{d1i} , c_{d2i}	: Valve Control Inputs in Hydraulic Brake System
C	: Shape Factor in Magic Formula
C_d	: Aerodynamic Drag Coefficient
C_{dv}	: Orifice Discharge Coefficient
C_f	: Front Suspension Damping Ratio
C_r	: Rear Suspension Damping Ratio
C_{roll}	: Rolling Resistance Coefficient
d	: Pneumatic Trail
D	: Peak Factor in Magic Formula
e	: Distance From Roll Center to the Sprung Mass c.g.
E	: Curvature Factor in Magic Formula
E_{bat}	: Battery Energy Level
E_{cap}	: Total Energy Capacity of the Battery
F_a	: Aerodynamic Drag Force
F_x	: Total Longitudinal Tire Force
F_{xf}	: Front Tire Longitudinal Force
F_{xr}	: Rear Tire Longitudinal Force
F_{si}	: i'th Suspension Force
F_{xi}	: i'th Tire Longitudinal Force
F_y	: Total Lateral Tire Force
F_{yi}	: i'th Tire Lateral Force
F_z	: Tire Load
F_{zi}	: i'th Tire Load
g	: Acceleration due to Gravity
h_f	: Height of the Front Unsprung Mass c.g
h_r	: Height of the Rear Unsprung Mass c.g
H_u	: Lower Heating Value of the Fuel
I	: Battery Current
I_{chg}	: Battery Charge Current
I_{dis}	: Battery Discharge Current
I_ω	: Wheel Inertia

I_X	: Total Moment of Inertia on the Roll Axis
I_{XS}	: Sprung Mass Moment of Inertia on the Roll Axis
I_Y	: Total Moment of Inertia on the Pitch Axis
I_{YS}	: Sprung Mass Moment of Inertia on the Pitch Axis
I_Z	: Total Moment of Inertia on the Yaw Axis
I_{ZS}	: Sprung Mass Moment of Inertia on the Yaw Axis
J	: Performance Function
k_t	: Tire Stiffness
K	: A Positive Constant
K_f	: Front Suspension Spring Stiffness
K_r	: Rear Suspension Spring Stiffness
K_{rbf}	: Front Antiroll Bar Stiffness
K_{rbr}	: Rear Antiroll Bar Stiffness
l_f	: Distances from Vehicle c. g. to the Front Axle
l_r	: Distances from Vehicle c.g. to the Rear Axle
l_ω	: Front and Rear Track Widths
L	: Distance between the Front and Rear Axles
m	: Vehicle Mass
m_f	: Fuel Consumption
m_s	: Vehicle Sprung Mass
m_u	: Vehicle Unsprung Mass
M	: Positive Adaptation Gain in ESA
n	: Time Increasing Function
o	: Time Increasing Positive Function in ESA
p	: Roll Rate
p_f	: Height of the Front Roll Center
p_r	: Height of the Rear Roll Center
P_i	: i-th Wheel Cylinder Pressure
P_{low}	: Reservoir Pressure
P_p	: Pump Pressure
P_{out}	: Push Out Pressure
P_{bat}	: Battery Internal Power
P_{req}	: Required Power on ICE and EM Shafts
P_{fuel}	: Fuel Power
P_{wh}	: Wheel Power
P_t	: EM Power Discharging or Charging the Battery
q	: Pitch Rate
Q	: Electric Charge
Q_0	: Constant Battery Nominal Charge Capacity
r	: Yaw Rate
r_r	: Effective Rotor Radius
R	: Tire Effective Radius
R_{chg}	: Battery Internal Resistance while Charging
R_{dis}	: Battery Internal Resistance while Discharging
R_i	: Battery Internal Resistance
s	: Sliding Surface Variable
s_i	: i’th Tire Sliding Surface Variable
S	: Road Slope
S_i	: Road Input for the i’th Tire
SOC	: Variable Indicating the Charge Level of the Battery

t	: Time Index
T_b	: Braking Moment
T_{bi}	: i'th Tire Braking Moment
T_d	: Traction Moment
T_{di}	: i'th Tire Traction Moment
T_{bat}	: Battery Temperature
T_{em}	: EM Torque
$T_{em,cmd}$	: EM Torque Command
T_{ice}	: ICE Torque
$T_{ice,cmd}$	: ICE Torque Command
T_{req}	: Required Torque on ICE and EM Shafts
T_s	: Distance between the Left and Right Suspensions
u	: Vehicle Model Longitudinal Speed
u_{ti}	: Velocity on the Rolling Direction for the i'th Individual Tire
U_{oc}	: Battery Open-Circuit Voltage
U	: Battery Terminal Voltage
v	: Vehicle Model Lateral Speed
V	: Lyapunov Function
V_ω	: Wheel Cylinder Volume
W	: Positive Constant in Tire Force Observer
x	: Roll Axis
y	: Pitch Axis
z	: Yaw Axis
z_s	: Vertical Motion of the Sprung Mass c.g.
z_u	: Vertical Motion of the Unsprung Mass c.g.
z_{ui}	: Vertical Motion of the i'th Unsprung Mass
α_i	: i'th Tire Side Slip Angle
β_f	: Brake Fluid Bulk Modulus
δ_f	: Driver Steering Input
ε	: Positive Constant in ESA
Φ	: Roll Angle
γ	: Positive Constant in ESA
η	: Hydraulic Brake System Mechanical Efficiency
η_{bat}	: Battery Efficiency
η_{em}	: EM Efficiency
η_{ice}	: ICE Efficiency
η_T	: Overall Powertrain Efficiency
κ	: Tire Slip Ratio
κ_i	: i'th Tire Slip Ratio
μ_x	: Tire-Road Friction Function
μ_{max}	: Maximum Value of the Tire-Road Friction Function
θ	: Pitch Angle
ρ	: Positive Constant in ESA
ρ_a	: Air Density
ρ_f	: Brake Fluid Density
ρ_0	: Positive Constant in ESA
σ	: Scalar Parameter
τ_{em}	: Time Constant of EM
τ_{ice}	: Time Constant of ICE
ω	: Wheel Angular Velocity

ω_i : i’th Wheel Angular Velocity
ω_{em} : EM Angular Speed
ω_{ice} : ICE Angular Speed
ω_f : Front Wheel Angular Velocity
ω_r : Rear Wheel Angular Velocity

EXTREMUM SEEKING METHOD AND ITS APPLICATIONS IN AUTOMOTIVE CONTROL

SUMMARY

The mainstream methodology in control applications is to regulate the considered system to known set points or reference trajectories. However, in some control problems, the relation between the system setpoint and a desired system performance is unknown a priori. One situation is that, the reference-to-output map has an extremum and the objective is to select the set point to keep the output at that extremum value. The uncertainty in the reference-to-output map makes it necessary to use an adaptation method to find the set point which maximizes (or minimizes) the output. This problem can be solved via the Extremum Seeking Algorithm (ESA). The algorithm fits problems that possess completely or partially unknown performance functions that may also change in time or that have nonlinear systems with structured or unstructured uncertainties and disturbances.

For example, as needed in an emergency braking case, the maximization of the tire force between the tire contact patch and the road in the presence of unknown road conditions is a challenging task. The road friction coefficient is mostly unknown a priori and it is difficult to estimate it on-line. The ABS control algorithm should find the optimal set point of brake hydraulic pressure, which maximizes the wheel braking force subject to unknown and possibly changing road conditions. A misjudgment about the optimal set point choice may cause lower performance of braking via either less friction force generation or via blocking the tire rotation. The minimum stopping distance is ensured when the tires operate at the peak point of the braking force versus slip characteristic curve subject to unknown road conditions. In addition, lateral stability and steerability are also improved as locking of the wheels is prevented.

In this thesis, firstly, an Extremum Seeking Algorithm (ESA) integrated with the adaptation of the tire model parameters is proposed for maximizing braking force without utilizing optimum slip value information. A quarter car vehicle model is considered in this section of the thesis. Most of the commonly used extremum seeking algorithms in the literature search for the optimal operating point in order to maximize or minimize a given cost function which is measured on a real-time basis. The control algorithm introduced in this dissertation removes the on-line cost function measurement requirement and instead, an analytic approach with adaptive parameter tuning is developed along the ESA. Stability and reaching the global maximum operating point of the unknown cost function are proved using Lyapunov stability analysis. Simulation study for ABS control under different road pavement conditions is presented to illustrate the effectiveness of the proposed approach.

Secondly, an ABS control algorithm based on ESA is presented for considering lateral motion in addition to the longitudinal emergency braking, such as the obstacle avoidance maneuvers, also. The optimum slip ratio between the tire contact patch

and the road is searched online without having to estimate the road friction conditions. This is achieved by adapting the ESA as a self-optimization routine that seeks the peak point of the force-slip curve. As a novel addition to the literature, the proposed algorithm incorporates driver steering input information into the ABS braking procedure to determine the operating region of the tires on the “tire force”-“slip ratio” characteristic curve. The algorithm operates the tires near the peak point of the force-slip curve during straight line braking. When the driver demands lateral motion in addition to braking, the operating regions of the tires are modified automatically, for improving the lateral stability of the vehicle by increasing the tire lateral forces. Simulations with a full vehicle model validated with actual vehicle measurements show the effectiveness of the algorithm.

Thirdly, an energy management strategy for a parallel type hybrid electric vehicle (HEV) is proposed. HEVs are developed in the need of more efficient, less polluting vehicles. Electric vehicles seem as a promising solution but for now, their short driving distance combined with the long recharging period for batteries postpones their widespread use to the future. HEVs offer an acceptable, intermediate solution. In a hybrid electric vehicle, an electric motor (EM) powered by an electrochemical battery is used along with the internal combustion engine (ICE) powered by fossil fuel. They appear to be one of the most viable technologies with significant potential to reduce fuel consumption and pollutant emissions. The main objective of the HEV energy management strategy given in the thesis is maximizing the powertrain efficiency and hence improving the fuel consumption while meeting the driver’s power demand, sustaining the battery state of charge and considering constraints such as engine and electric motor power limits.

In the proposed energy management strategy, extremum seeking algorithm searches constantly optimum torque distribution between the internal combustion engine and electric motor for maximizing the powertrain efficiency. The control strategy has two levels of operation: the upper and lower levels. The upper level decision making controller chooses the vehicle operation mode such as the simultaneous use of the internal combustion engine and electric motor, use of only the electric motor, use of only the internal combustion engine, or regenerative braking. In the simultaneous use of the internal combustion engine and electric motor, the optimum energy distribution between these two sources of energy is determined via the extremum seeking algorithm that searches for maximum powertrain efficiency. In the literature, this is the first time an extremum seeking algorithm is applied to the HEV control problem. A dynamic programming (DP) solution is also obtained and used to form a benchmark for performance evaluation of the proposed method. DP solution gives the minimum obtainable fuel consumption in a considered driving cycle and driving conditions. In order to apply DP procedure, the whole driving cycle and driving conditions should be known in advance. Since future driving conditions are unknown in a real vehicle, DP cannot be utilized in a real time controller. The dynamic programming solution is used offline for performance evaluation of the real time control algorithm. Detailed simulations with various driving cycles and using a realistic vehicle model are presented to illustrate the effectiveness of the methodology.

EKSTREMUM ARAMA METODU VE OTOMOTİV KONTROLU ALANINDA UYGULAMALARI

ÖZET

Kontrol uygulamalarındaki ana yöntem, ele alınan bir sistemi belli bir çalışma noktasına veya referans yörüngesine oturtmaktır. Fakat bazı kontrol problemlerinde, arzu edilen sistem performansı ile o performansı sağlayacak sistem çalışma noktası arasındaki ilişki önceden bilinmemektedir. Örneğin sistemin çalışma noktası ile çıkışı arasında o şekilde bir ilişki olabilir ki, bu fonksiyonun bir ekstremumu olabilir ve amaç, sistem çıkışını bu ekstremum değere getirecek çalışma noktasının aranması olabilir. Sistemin çalışma noktası ile çıkışı arasındaki fonksiyonun belirsizliği, çıkışı maksimize (veya minimize) edecek çalışma noktasının bulunması için bir uyarlama algoritmasının kullanımını gerekli kılmaktadır. Bu problem Ekstremum Arama Algoritması (EAA) ile çözülebilmektedir. Bu algoritma, sistemin performans fonksiyonunun tamamen veya kısmen bilinmediği, zamanla değişebildiği, sistemin eğrisel olduğu, belirsizlik ve bozucular içerdiği durumlar için uygundur.

Örneğin acil durum frenlemesinde ihtiyaç duyulduğu gibi, bilinmeyen yol koşullarında tekerlek ile yol arasındaki teker kuvvetlerinin maksimize edilmesi başa çıkılması gereken zor bir iştir. Yol sürtünme katsayısı genellikle önceden bilinmemektedir ve anlık olarak kestirimi zordur. ABS kontrol algoritması, bilinmeyen yol koşullarında teker frenleme kuvvetini maksimize edecek hidrolik fren basıncının optimum çalışma noktasını bulmalıdır. Optimum çalışma noktası seçimindeki bir yanlış karar, ya olabilecekten daha az frenleme kuvvetinin üretilmesine ya da tekerleklerin kilitlenmesine, böylece aracın kontrol edilebilirliğinin ortadan kalkmasına sebep olacaktır. Minimum durma mesafesi ancak tekerleklerin, tekerlek kuvveti-tekerlek kayma oranı eğrisinde en tepe noktasında çalışmaları durumunda gerçekleşir. Bu durumda tekerleklerin kilitlenmesi engellendiği için aracın yanal kararlılığı ve direksiyon ile yönlendirilebilirliği de iyileşecektir.

Tezde önce, optimum tekerlek kayma değeri bilinmeden tekerlek kuvvetinin maksimize edilmesi için, tekerlek modeli parametrelerinin uyarlanması yöntemi ile entegre edilmiş bir Ekstremum Arama Algoritması (EAA) önerilmiştir. Bunun için bir çeyrek araç modeli ele alınmıştır. Literatürdeki çoğu ekstremum arama algoritmaları, optimum çalışma noktasını ararken amaç fonksiyonunun gerçek zamanlı olarak ölçümüne dayanmaktadır. Bu çalışmada önerilen kontrol algoritması, amaç fonksiyonunun anlık ölçümü gereksinimini ortadan kaldırarak onun yerine parametre uyarlamalı analitik bir yöntem geliştirmiştir. Kararlılık ve global maksimum noktasına yakınsama durumları, Lyapunov kararlılık analizi ile gösterilmiştir. Önerilen yaklaşımın etkinliğini göstermek için farklı yol koşullarında simulasyon çalışmaları yapılmıştır.

İkinci olarak, boyuna frenleme yanında engelden kaçınma manevrasında olduğu gibi yanal hareketi de gözönüne alan EAA temelli bir ABS kontrol algoritması sunulmuştur. Bu algoritmada, yol sürtünme katsayısını kestirmeye gerek kalmadan,

tekerlek ve yol arasındaki optimum kayma oranı anlık olarak aranmaktadır. Literatüre getirilen bir yenilik olarak, “tekerlek kuvveti”-“kayma oranı” karakteristik eğrisi üzerinde tekerleklerin çalışma bölgesini belirlemek için sürücü direksiyon girişi ABS frenleme prosedürüne eklenmiştir. Sadece boyuna frenleme durumunda algoritma, tekerleklerin çalışma bölgesini, kuvvet-kayma eğrisinin tepe noktası yakınında tutmaktadır. Eğer sürücü frenlemeye ek olarak yanal hareket de talep ederse, tekerleklerin çalışma bölgesi otomatik olarak değiştirilmekte ve böylece yanal tekerlek kuvvetleri arttırılarak aracın yanal kararlılığı iyileştirilmektedir. Gerçek bir araçtan alınan ölçümlerle doğrulanmış bir tam araç modeli kullanılarak yapılan simülasyonlar algoritmanın etkinliğini göstermektedir.

Üçüncü olarak, bir paralel tip hibrid elektrikli araç (HEA) için enerji yönetimi stratejisi önerilmiştir. HEA’lar, daha verimli, daha az çevreyi kirleten araçlara gereksinim sonucunda geliştirilmiştir. Elektrikli araçlar parlak bir çözüm olsa da şu andaki kısa menzilleri ve uzun batarya şarj süreleri, yaygın kullanımlarını geleceğe ötelemektedir. HEA’lar bu doğrultuda kabul edilebilir bir ara çözüm sunmaktadırlar. Hibrid bir elektrikli araçta, elektrokimyasal bir batarya ile güç verilen bir elektrikli motor (EM), fosil yakıt tarafından güç verilen içten yanmalı motor (İYM) ile birlikte kullanılmaktadır. Bunlar, yakıt tüketimi ve emisyonları azaltmadaki önemli potansiyelleri ile günümüzde en uygulanabilir teknoloji olarak görülmektedirler. Tezde verilen HEA enerji yönetim stratejisinin ana amacı, toplam verimi maksimize ederek yakıt tüketimini iyileştirmek ve bunu yaparken de sürücünün güç isteğini karşılamak, batarya şarj durumunu korumak ve İYM, EM güç kısıtları gibi çeşitli kısıtları göz önüne almaktır.

Önerilen enerji yönetimi stratejisinde, ekstremum arama algoritması, toplam verimi maksimize edecek şekilde içten yanmalı motor ve elektrik motoru arasında optimum tork dağılımını belirlemektedir. Kontrol stratejisi üst seviye ve alt seviye olmak üzere iki seviyelidir: Üst seviyedeki karar verme kontrolcüsü aracın hangi modda çalışacağını tespit eder. Bu modlar: İçten yanmalı motor ve elektrik motorunun eşzamanlı çalışması, yalnızca elektrik motoru, yalnızca içten yanmalı motor, veya rejeneratif frenleme modlarıdır. İçten yanmalı motor ve elektrik motorunun eşzamanlı çalışması sırasında, bu iki enerji kaynağı arasındaki optimum enerji dağılımını ekstremum arama algoritması, toplam verimi maksimize edecek şekilde belirlemektedir. Böylece literatürde ilk defa bir ekstremum arama algoritması HEA kontrol problemine uyarlanmıştır. Önerilen kontrol algoritmasının performans değerlendirmesi için ayrıca bir dinamik programlama (DP) çözümü de elde edilmiştir. DP çözümü, ele alınan sürüş çevrimi ve sürüş koşulları için elde edilebilecek minimum yakıt tüketimini hesaplamaktadır. DP prosedürünü uygulamak için, bütün bir sürüş çevrimi ve sürüş koşulları önceden bilinmelidir. Gerçek bir araçta gelecekteki sürüş koşulları bilinmediği için DP gerçek zamanlı bir kontrolcü olarak kullanılamaz. Dinamik programlama çözümü gerçek zamanlı kontrol algoritmasının performansının değerlendirilmesi için kullanılmaktadır. Tezde önerilen kontrol algoritmasının etkinliğini göstermek için gerçekçi bir araç modeli kullanılarak çeşitli sürüş çevrimleri ile simülasyonlar yapılmıştır.

1. INTRODUCTION

1.1 Introduction and Scope of the Dissertation

Traditional control system design deals with the problem of stabilization of a known reference trajectory or set point that are called “tracking” and “regulation” problems. However, in some occasions it can be very difficult to find a suitable reference value. For example in ABS control problems, the maximization of the tire force between the tire contact patch and the road during an emergency braking maneuver in the presence of unknown road conditions is a challenging task. The road friction coefficient is mostly unknown a priori and it is difficult to estimate it on-line. The ABS control algorithm should find the optimal set point of brake hydraulic pressure, which maximizes the wheel braking moment subject to unknown and possibly changing road conditions. A misjudgment about the optimal set point choice may cause lower performance of braking via either less friction force generation or via blocking the tire rotation. The minimum stopping distance is ensured when the tires operate at the peak point of the braking force versus slip characteristics subject to unknown road conditions. In addition, headway stability and steerability are also improved as locking of the wheels is prevented.

Unlike the classical regulative control schemes, extremum seeking covers control problems where the reference trajectory or reference set point is not known but is searched in real time in order to maximize or minimize a performance function of a nonlinear, possibly time varying, uncertain system. In this scheme, the relationship between the outputs and the inputs or states of the system does not have to be known in advance. Besides, there is no a priori knowledge of the optimum operating point of the considered system. It is called as Extremum Seeking Control, Extremum Control, Extremal Control or Self-Optimizing Control. In the framework of automotive control applications, some application area examples are: ABS/Traction control problem where the aim is to maximize the longitudinal tire forces with respect to the different road conditions, air/fuel ratio control where the optimal fuel amount is to be decided online for a given air flow according to an optimality criterion, optimization of intake, exhaust, and spark timings to improve fuel consumption. In this thesis, extremum seeking control is applied to ABS and Hybrid Electric Vehicle Control Problems.

Anti-lock brake systems (ABS) are originally developed to prevent wheels from locking up during hard braking. Modern ABS systems not only try to prevent wheels from locking but also try to maximize the braking forces generated by the tires by preventing the longitudinal slip ratio from exceeding an optimum value. Locking of the wheels reduces the braking forces generated by the tires and results in the vehicle taking a longer time to come to a stop. Further, locking of the front wheels prevents the driver from being able to steer the vehicle while it is coming to a stop. Common commercial ABS algorithms use the deceleration threshold based algorithm where the wheel deceleration signal is used to predict if the wheel is about to lock. Threshold based ABS algorithms are simple and prevent wheel lockup but they may not provide full braking potential of the tires. More advanced solutions are studied in the literature based on maximization of the tire forces by regulating the current slip ratio of the tires to some optimum slip ratio value.

The concept of Hybrid Electric Vehicle (HEV) originated from the fact that by using an extra energy source and properly managing the energy conversions between the existing energy source (Internal Combustion Engine - ICE) and the added energy source (Battery), more efficient, less polluting and less energy consuming vehicles can be developed. In HEV, the propulsion energy is transmitted to the wheels by two different energy conversion devices. One is the internal combustion engine (gasoline or diesel engine) and the other is the electric motor (EM). The electric motor converts the chemical energy from batteries into kinetic energy in the wheels. The path of energy flow from the batteries into the wheels is reversible which means that while braking, the electric motor operates as a generator and recharges the batteries. They appear to be one of the most viable technologies with significant potential to reduce fuel consumption and pollutant emissions.

1.2 Contributions of the Dissertation

The contributions of this dissertation to the literature are presented in this section as given below:

- The first contribution is that the extremum seeking algorithm is developed for maximizing braking force of a quarter-car vehicle model without having to know or utilize optimum slip value information. The novelty is that the search algorithm is integrated with the adaptation of the tire model parameters for maximizing braking force. Most common extremum seeking algorithms in the literature are searching for an optimal operating point in order to maximize or minimize a given cost function which is measured on a real-time basis. The control algorithm introduced in this dissertation removes the on-line cost function measurement requirement and instead, an analytic approach with adaptive parameter tuning is developed along the extremum seeking algorithm. Stability and reaching to the global maximum operating point of the unknown cost function are proved on a Lyapunov stability basis. Simulation study for ABS control under different road pavement conditions is presented to illustrate the effectiveness of the proposed approach. In order to show the real-time applicability of the algorithm, simulations are repeated in a real time hardware, the dSPACE Microautobox.
- Extremum seeking based ABS control algorithm is further developed for emergency braking cases combined with lateral motion such as those necessary in obstacle avoidance maneuvers. The optimum slip ratio between the tire contact patch and the road is searched online without having to estimate the road friction conditions. As a novel contribution to the existing literature, the proposed algorithm incorporates driver steering input into the ABS algorithm to determine the operating region of the tires on the "tire force"-"slip ratio" characteristic curve. The algorithm operates the tires near the peak point of the force-slip curve during straight line braking. When the driver demands lateral motion in addition to braking, the operating regions of the tires are modified automatically, for improving the lateral stability of the vehicle by increasing the tire lateral forces. For the simulations, a 15 degree of freedom (6 dof from longitudinal, lateral, vertical, yaw, roll, pitch motions, 4 dof from suspension units, 4 dof from tire rotations and 1 dof from front wheel steering) vehicle model is developed. Measurements from a real vehicle are used for validation of the developed vehicle model. Magic Formula Tire Model is integrated into the vehicle model for realistic

calculation of the forces that occur between the road and the tires. A hydraulic brake actuator model is used to generate required brake pressure on the wheel cylinders. It is shown that the braking algorithm can be improved for better steerability in the presence of driver steering input.

- An extremum seeking based energy management strategy for a parallel type hybrid electric vehicle (HEV) model is proposed as a further contribution to the existing literature. An upper level controller chooses vehicle operation mode such as regenerative braking, EM only, ICE only, or ICE plus EM-charge modes. In the ICE plus EM-charge mode, optimum torque distribution between the internal combustion engine and the electric motor is determined via the extremum seeking algorithm that searches for maximum powertrain efficiency. In the literature, this is the first time an extremum seeking algorithm is applied to the hybrid electric vehicle control problem.
- A parallel type hybrid electric vehicle model including internal combustion engine (ICE), electric motor (EM), battery model and vehicle dynamics is developed for the study. ICE and EM efficiency maps are used to calculate powertrain efficiency and fuel consumption values.
- A dynamic programming (DP) solution is obtained and used to form a benchmark for performance evaluation of the proposed method based on extremum seeking. DP solution gives the minimum obtainable fuel consumption in a considered driving cycle and driving conditions. In order to apply DP procedure, the whole driving cycle and driving conditions should be known in advance. Since future driving conditions are unknown in a real vehicle, DP cannot be utilized in a real time controller. The dynamic programming solution is used offline for performance evaluation of the real time control algorithm.
- In order to show the real-time applicability of the algorithm in HEV control problem, simulations are repeated with CarMaker software and dSPACE DS1005 real time hardware.

1.3 Outline of the Dissertation

In Chapter 2, the literature review for the extremum seeking algorithm (ESA), ABS and hybrid electric vehicle (HEV) control problems are given. In Chapter 3, extremum seeking algorithm is developed for a quarter car vehicle model ABS control problem. Sliding mode based extremum seeking algorithm is combined with the adaptation of the tire model parameters. In Chapter 4, ABS control algorithm is improved by considering driver steering input. The algorithm operates the tires near the peak point of the force-slip curve during straight line braking. When the driver demands lateral motion in addition to braking, the operating regions of the tires are modified automatically, for improving the lateral stability of the vehicle. A validated full vehicle model is presented and used in the simulation study. In Chapter 5, the energy management strategy using extremum seeking algorithm is proposed for a parallel type hybrid electric vehicle model. Hybrid vehicle model including internal combustion engine, electric motor and battery model is developed for the study In order to evaluate performance of the proposed algorithm; the DP procedure is applied to calculate minimum attainable fuel consumption value. Real-time simulation study with CarMaker software and dSPACE DS1005 hardware is given to show the real-time applicability of the control algorithm. Chapter 6 presents conclusions.

In Appendix A, derivation of the full vehicle model acceleration vector is presented. Appendix B presents formulation of the Magic Formula Tire Model. Matlab M File for calculation of the tire forces according to the Magic Formula Tire Model is presented in Appendix C. Appendix C introduces also the computer program, which calculates minimum attainable fuel consumption of the hybrid electric vehicle via the dynamic programming method.

2. LITERATURE REVIEW

A survey of the related literature on the different methods of achieving extremum seeking control and the existing control methods for ABS braking and HEV power distribution are presented in this chapter.

2.1 Extremum Seeking Algorithm

Extremum Seeking Control is a class of control algorithm that searches maximum (or minimum) point of the performance function of a system. The system to be regulated may be nonlinear, time varying, possess structured or unstructured uncertainties and the performance function of the system is completely or partially unknown. It covers control problems where the reference trajectory or reference set point is not known but it is searched on-line. In the literature, it is also called Extremum Control, Peak-Seeking Control or Self-Optimizing Control. Some application areas are maximization of braking and traction forces in vehicles [3,5,7,20,32,37], source seeking control of autonomous vehicles and mobile robots [24-26], maximum power point tracking control of fuel cell power plants [21], matching problem in a charged particle accelerator [23], control of electromechanical valve actuator [27], operation of air-side economizer [29], internal combustion engine operation [11,30,31], optimization of batch systems in industrial chemical processes [44].

In the literature, mainly four different types of extremum seeking schemes are studied. These are sliding mode based extremum seeking [1-11], perturbation based extremum seeking [12-30], numerical optimization based extremum seeking [31-37] and gradient based extremum seeking control algorithms [38-43].

2.1.1 Sliding mode based extremum-seeking algorithm

In the sliding mode based extremum-seeking approach, the shape of the performance function is considered unknown but its output can be measured. A sliding surface is defined where on that surface the performance function is forced to follow an increasing (or decreasing) function. Since the shape of the performance function is unknown, this is a control problem with uncertain direction of control vector. Hence, the search signal is selected as discontinuous periodic switching. The basic scheme of the sliding mode based extremum seeking algorithm is shown in Figure 2.1.

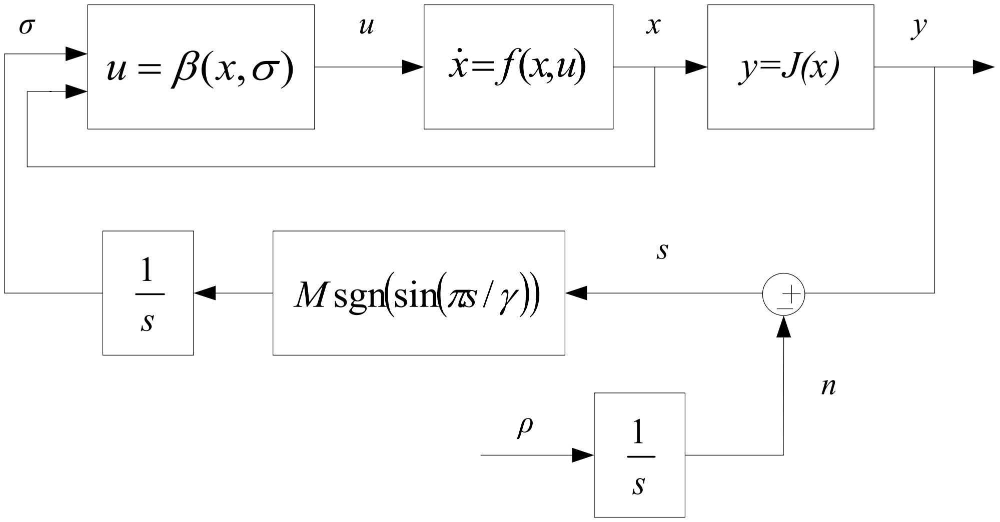

Figure 2.1 : Sliding mode based extremum seeking scheme [6].

The control objective is considered as the optimization of a closed loop system via the adaptation of a scalar control parameter while a preselected stabilizing controller is already in the loop. The adopted scheme assumes a regulative controller, which produces equilibrium for the closed-loop system, parameterized by a free control parameter, and employs a sliding mode optimization method to adapt this parameter to increase the performance of the overall system. A nonlinear system of the form

$$\dot{x} = f(x,u) \tag{2.1}$$

is considered. The control objective is determined by a control structure, which enables the system to operate robustly at the peak of a performance surface defined by

$$y = J(x) \tag{2.2}$$

where y is the performance variable. The proposed design has two consecutive phases. First, a control law is determined to create a unique equilibrium point as a smooth function of a free scalar parameter inserted into the closed loop through the control law and in order to stabilize the closed-loop system about this equilibrium point. Second, this control parameter is adapted to move the resulting equilibrium to increase the performance of the overall system. As an example, the following scalar system is taken into consideration

$$\frac{dx}{dt} = u \tag{2.3}$$

with the performance variable in **(2.2)**. Here x is the state and u is the control. Since the relative degree from the control input to the performance variable is one, the sliding mode optimization technique could easily be used to determine a discontinuous control law to keep x in the vicinity of its optimum value at which the performance variable y is maximized without requiring any derivative information on y. A two-phase design approach is used. First, a control law which regulates x to a given parameter σ is found and then an optimization logic is employed to adapt this parameter σ. Selecting the control input as

$$u = -\lambda(x - \sigma) \tag{2.4}$$

where λ is a positive constant. The following dynamics

$$\dot{x} = -\lambda(x - \sigma) \tag{2.5}$$

is obtained which has the equilibrium point of

$$x = \sigma \tag{2.6}$$

Then the problem becomes calculating σ where **(2.2)** can be written as

$$y = J(\sigma) \tag{2.7}$$

and selecting the sliding variable as

$$s = y - n(t) \tag{2.8}$$

where $n(t)$ is a time increasing function with $\dot{n} = \rho$. Here, ρ is a positive constant. Then, the derivative of the sliding variable is

$$\dot{s} = \frac{dJ(\sigma)}{d\sigma}\dot{\sigma} - \rho \tag{2.9}$$

Here, the sign of $\frac{dJ(\sigma)}{d\sigma}$ is unknown, because the shape of the performance function is considered to be unknown. Hence, this is a control problem with uncertain direction of control vector. A periodic switching function is selected for the time derivative of the parameter σ as

$$\dot{\sigma} = M \operatorname{sgn}\left(\sin(\frac{\pi s}{\gamma}) \right) \tag{2.10}$$

where M and γ are positive Then the sliding surface dynamics becomes

$$\dot{s} = \frac{dJ(\sigma)}{d\sigma} M \operatorname{sgn} \sin(\pi s / \gamma) - \rho \tag{2.11}$$

In this dynamics, as long as the following condition holds

$$\left| \frac{dJ(\sigma)}{d\sigma} \right| > \frac{\rho}{M} \tag{2.12}$$

the change of s and $\dot{s}$ will be similar as shown in Figure 2.2 and Figure 2.3 where the first one is the case for $dJ(\sigma)/d\sigma$ >0 while the second one is for $dJ(\sigma)/d\sigma$ <0.

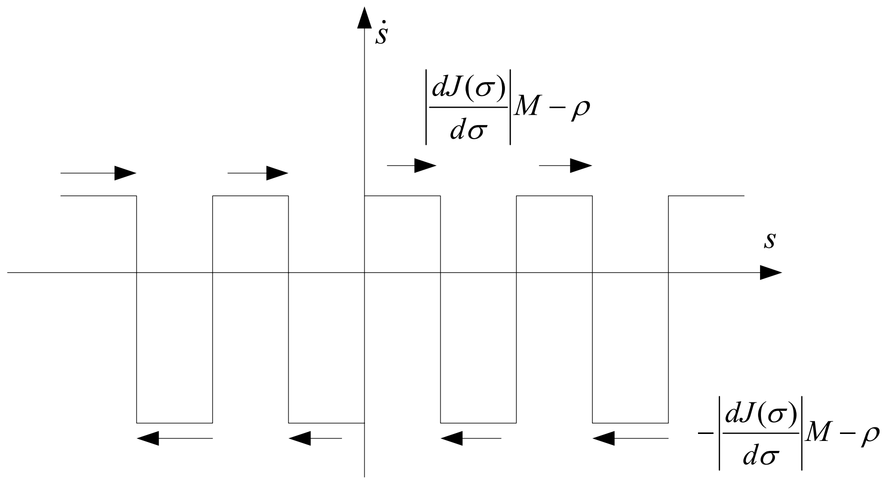

Figure 2.2 : Change of s and $\dot{s}$ according to **(2.11)** when $dJ(\sigma)/d\sigma$ >0.

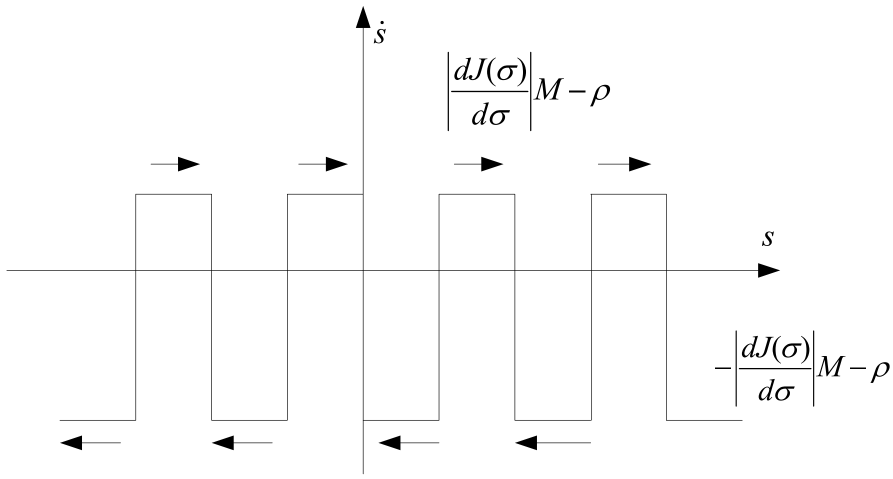

Figure 2.3 : Change of s and $\dot{s}$ according to **(2.11)** when $dJ(\sigma)/d\sigma$<0.

The arrows in Figure 2.2 and Figure 2.3 show the direction of the variable s. It is realized that s converges to a constant value after a finite time interval (finite time due to the discontinuous sign function). Then, by denoting this constant value as w

$$s = w \tag{2.13}$$

Since the sliding surface is selected as **(2.8)**, then

$$y = n(t) + w \tag{2.14}$$

Henceforth, the performance variable y will increase with the slope of ρ converging to the maximum operating point as long as the condition **(2.12)** holds. By choosing ρ and M, one defines the location of the operating point. Choosing a bigger value for the right hand side of **(2.12)**, the condition holds shorter, i.e. the increment of y lasts shorter. In other words, the operating region will be further away from the maximum value. On the contrary, choosing a smaller right hand side of **(2.12)**, the condition will hold longer, eventually, the operating region will be closer to the maximum value.

In [1], sliding mode approach for the optimization problem without any information about the gradient of the performance function is introduced. The discontinuous search signal is obtained through a hysteresis loop.

In [2] the periodic search signal is generated with a more simple approach than in [1] using sine and signum functions.

In [3] extremum seeking control is applied to the Antilock Braking System Problem. The optimal slip value is searched for maximizing the tire braking forces. The algorithm does not need any prior information of the optimal slip value with respect to the different road conditions. The longitudinal tire force characteristic is shown in Figure 2.4.

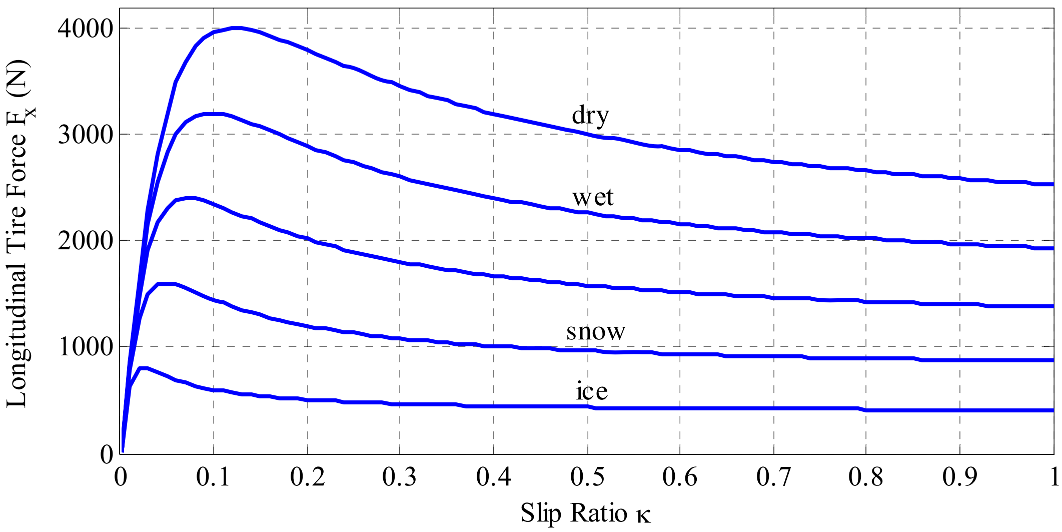

Figure 2.4 : Longitudinal tire force characteristics.

As it is shown in Figure 2.4, until some value of the tire slip ratio, the longitudinal tire force keeps increasing. After some value of the slip ratio value, the tire force starts to decrease. The optimum tire slip ratio, where the tire force has its maximum, depends on the road conditions. In order to get the maximum tire force during emergency braking, the optimum tire slip ratio has to be known a priori. The algorithm in [3] is based on the sliding mode self-optimization method using a periodic switching function. The methodology is given as follows: The longitudinal tire force is written as a function of the slip ratio and time as follows

$$y_i = F_{xi}(t, \kappa_i) \tag{2.15}$$

where κ_i and F_{xi} are tire slip ratio and longitudinal tire force for the i'th tire. Taking the derivative of **(2.15)** one can get

$$\dot{F}_{xi} = \frac{\partial F_{xi}}{\partial \kappa_i}\dot{\kappa}_i + \frac{\partial F_{xi}}{\partial t} \tag{2.16}$$

Here, the sign of the product term for $\dot{\kappa}_i$, which is $\frac{\partial F_{xi}}{\partial \kappa_i}$, is unknown. As it is shown in Figure 2.4, if the tire operating region is on the left side of the maximum tire force, then the sign is positive. On the contrary, if the tire operating region is on the right side of the maximum tire force, then the sign is negative. Since the road condition is considered unknown, the current operating region can be either in the left or right side of the maximum point. Hence, this is a control problem with uncertain direction of control vector. A periodic switching function is selected for the time derivative of the slip ratio ($\dot{\kappa}_i$).

$$\dot{\kappa}_i = -M \sin\left(n(t) + bF_{xi}\right) \quad \textbf{(2.17)}$$

Here "sin" is the sinusoidal function and

$$s_i = n(t) + bF_{xi} \quad \textbf{(2.18)}$$

is the sliding surface for the *i*'th tire. $n(t)$ is simply an increasing function with time as $\dot{n} > 0$. *M* and *b* are positive constants. Putting **(2.17)** into **(2.16)** one can get

$$\dot{F}_{xi} = -M \frac{\partial \dot{F}_{xi}}{\partial \kappa_i} \sin\left(n(t) + by_i\right) + \frac{\partial \dot{F}_{xi}}{\partial t} \quad \textbf{(2.19)}$$

Time derivative of the sliding surface is

$$\dot{s}_i = \dot{n} + b\dot{F}_{xi} \quad \textbf{(2.20)}$$

By putting **(2.19)** into **(2.20)**

$$\dot{s}_i = \dot{n} + bA_i(t) + bB_i(t)\sin(s_i) \quad \textbf{(2.21)}$$

where

$$A_i(t) = \frac{\partial F_{xi}}{\partial t}, \quad B_i(t) = -M \frac{\partial F_{xi}}{\partial \kappa_i} \quad \textbf{(2.22)}$$

If the condition

$$\left|bB_i\right| > \left|\dot{n} + bA_i\right| \quad \textbf{(2.23)}$$

holds, then the change of s_i and $\dot{s}_i$ according to **(2.21)** will be similar as given in Figure 2.5.

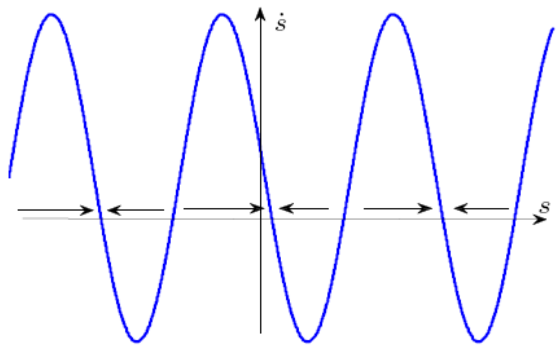

Figure 2.5 : Change of s and $\dot{s}$ according to **(2.21)**.

Starting in a point in s axis, the value of s will converge to a some constant value. There are multiple stable equilibrium points. In the classical sliding mode theory, the aim is to make s=0. Rather than that, here

$$s_i = l\pi \tag{2.24}$$

occurs where $(l \in R)$. Since the sliding surface is

$$s_i = n(t) + bF_{xi} \tag{2.25}$$

then

$$bF_{xi} = -n(t) + l\pi \tag{2.26}$$

is obtained. Since $n(t)$ is a time increasing function with $\dot{n} > 0$, braking force, which is negative, will continue to increase in magnitude and approach its maximum point as long as the condition given in **(2.23)** holds. The condition in **(2.23)** is equivalent to the following condition

$$\left|\frac{\partial F_{xi}}{\partial \kappa_i}\right| > \frac{|\dot{n}| + |bA_i|}{|Mb|} \tag{2.27}$$

In **(2.27)**, the left hand side is the slope value in Figure 2.4. As long as the slope value is greater than the right hand side, the tire force will continue to increase. After some time, since the slope starts to decrease while approaching the maximum point, the condition **(2.27)** does not hold anymore. It means that the tires are forced to operate in an operating region around the extremum point. After the tire forces get into the region, they cannot leave the region. By proper selection of the coefficients in the right hand side of **(2.27)**, the size of the operating region can be increased or decreased. If the size of the operating region is decreased, then the tire will operate near its maximum point but in this case, there will be high control activity to keep operating the tire in that region. On the contrary, if the size of the operating region is increased, then the tire will operate further away from its maximum point but in this case there will be less control activity. The optimum size should be selected between these criteria.

In [4], a two-time scale sliding mode optimization method is introduced. The basic ingredient of their approach is to introduce a free parameter to the closed loop through the control law and to adapt this parameter in a slower time scale to optimize the performance of the overall system.

In [5], a traction control algorithm to prevent wheel spin is given. The sliding mode based extremum seeking algorithm calculates spark timing value to adjust the engine torque and hence obtain maximum traction force.

In [6], a rigorous analysis of the sliding mode based extremum seeking scheme is introduced. The mechanism of the scheme is discussed in detail and the criteria for optimally choosing the control parameters are defined. As a result of the trade-off between convergence speed and control accuracy, a sliding mode extremum seeking control with variable parameters will be proposed to obtain fast convergence and high control accuracy with the consideration of system dynamics.

In [7], extremum seeking control is developed via sliding mode to apply to systems with time delay and to avoid the problem of excessive oscillation. The proposed method is applied to a pneumatic Anti-lock brake system (ABS) example to achieve better braking performance and to avoid the lock-up phenomenon.

In [8], extremum-seeking control scheme enforced by a second order sliding mode control strategy is proposed. It is characterized by the advantage of "second order" sliding mode design with smooth control input and null derivative of sliding manifold.

In [9], the extremum seeking control with sliding mode is extended to solve the Nash equilibrium solution for an *n*-person linear quadratic dynamic game. For each player, a sliding mode extremum seeking controller is designed to let the player's linear quadratic performance index track a decreasing signal so that the Nash equilibrium point is reached.

[10] proposes an algorithm to solve the Nash equilibrium solution for an *n*-person noncooperative dynamic game by the extremum seeking with sliding mode. For each player, a switching function is defined as the difference between the player’s cost function and a reference signal. The extremum seeking controller for each player is designed so that the system converges to a sliding boundary layer defined in the vicinity of a sliding mode corresponding to the switching function and inside the boundary layer, the cost function tracks the reference signal and converges to the Nash equilibrium solution.

[11] proposes a closed loop multivariable Exhaust Gas Recirculation (EGR)/Spark Timing management system for maximum dilution control while maintaining a desired level of combustion stability. A combustion stability measure derived from in-cylinder ionization signals is used as feedback. An extremum seeking algorithm is employed to modulate spark timing in a slow-time scale in order to maximize the steady-state EGR amount.

2.1.2 Perturbation based extremum seeking algorithm

In the perturbation based extremum seeking algorithm, a perturbation is added to the search signal. By observing the effect of the perturbation on the performance function measurement, it is determined whether to increase or decrease the search signal to reach its optimum value and hence maximize (or minimize) the performance function. It is assumed that the shape of the performance function is unknown and only the value of the function can be measured.

In [12] and [13] the proof of stability of an extremum seeking feedback scheme by employing the tools of averaging and singular perturbation analysis is given. In this method, slope information is obtained from a continuous small perturbation signal, such as a sinusoidal signal. The general problem is studied where the nonlinearity with an extremum is a reference-to-output equilibrium map for a general nonlinear (non-affine in control) system, stabilizable around each of these equilibria by a local feedback controller. It is shown that solutions of the closed-loop system converge to a small neighborhood of the extremum of the equilibrium map. The size of the neighborhood is inversely proportional to the adaptation gain and the amplitude and the frequency of a periodic signal used to achieve extremum seeking. In [13], the general SISO nonlinear model

$$\dot{x} = f(x,u) \tag{2.28}$$

$$y = h(x) \tag{2.29}$$

where x, u and y are the state, input and output of the system, respectively, is considered. A smooth control law is taken as

$$u = \beta(x,\sigma) \tag{2.30}$$

parameterized by a scalar parameter σ. The closed loop system

$$\dot{x} = f(x,\beta(x,\sigma)) \tag{2.31}$$

then has an equilibrium point parameterized by σ. It is assumed that there exist a smooth function $l: R \rightarrow R^n$ such that

$$\dot{x} = f(x,\beta(x,\sigma)) = 0 \text{ if and only if } x = l(\sigma) \tag{2.32}$$

and for each $\sigma \in R$, the equilibrium $x = l(\sigma)$ of the system **(2.31)** is locally exponentially stable. Hence it is assumed that the control law **(2.30)** which is robust with respect to its own parameter σ in the sense that it exponentially stabilizes any of the equilibrium that σ may produce.

Next it is assumed that the output equilibrium map $y = h(l(\sigma))$ has a maximum at $\sigma = \sigma*$. The objective is to develop a feedback mechanism which maximizes the steady state value of y but without requiring the knowledge of either σ^* or the functions h and l. The perturbation scheme proposed in [13] has the structure shown in Figure 2.6.

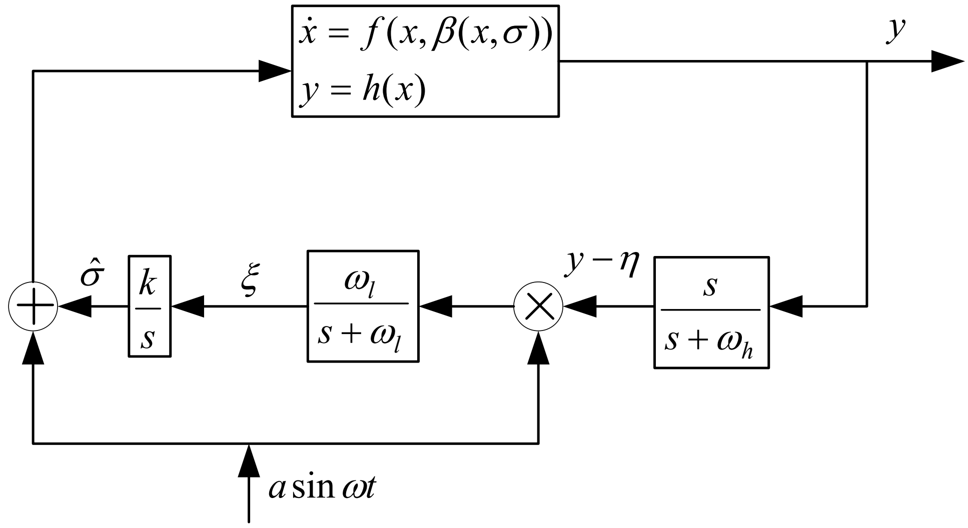

Figure 2.6 : Perturbation based extremum seeking scheme [13].

The starting point of the idea is as follows: It is impossible to conclude that a certain point is a maximum without visiting the neighborhood on both sides of it. For this reason, the slow periodic perturbation $a\sin\omega t$ which is added to the signal $\hat{\sigma}$, the best estimate of σ^*, is used. If the perturbation is slow, the plant can be viewed, as a static map $y = h(l(\sigma))$ and its dynamics do not interfere with the peak-seeking scheme. If $\hat{\sigma}$ is on either side of σ^*, the perturbation $a\sin\omega t$ will create a periodic response of y which is either in phase or out of phase with $a\sin\omega t$. The high pass filter $\frac{s}{s+\omega_h}$ eliminates the DC component of y. Thus, $a\sin\omega t$ and $\frac{s}{s+\omega_h}y$ will be (approximately) two sinusoids which are in phase for $\hat{\sigma}<\sigma^*$ and out of phase for $\hat{\sigma}>\sigma^*$. In either case, the product of the two sinusoids will have a DC component which is extracted by the low-pass filter $\frac{\omega_l}{s+\omega_l}$. The DC component ξ is the update law for $\hat{\sigma}$ which tunes $\hat{\sigma}$ to σ^*. The analysis using the method of averaging and singular perturbation methods is given in [13], where it is shown that the above system given in Figure 2.6 will converge to a neighborhood of the extremum point.

In [14], the inclusion of a dynamic compensator in the extremum seeking algorithm is proposed which improves the stability and performance properties of the method. The compensator is added to the integrator used for adaptation to improve the overall degree and phase response of the extremum seeking loop.

In [15], non-local stability properties of perturbation based extremum seeking controllers are proven. This non-local stability result is proved by showing semi-global practical stability of the closed-loop system with respect to the design parameters. It is shown that reducing the size of the parameters typically slows down the convergence rate of the extremum seeking controllers and enlarges the domain of the attraction. The paper provides guidelines on how to tune the controller parameters in order to achieve extremum seeking.

In [16], modification of a standard extremum seeking controller is introduced. It is equipped with an accelerator to the original one aimed at achieving the maximum operating point more rapidly. This accelerator is designed by making use of a polynomial identification of an uncertain output map, the Butterworth filter to smoothen the control, and analog-digital converters.

[17] presents first extension of the extremum-seeking method to the case in which equilibrium operation is impossible (unstable) and the system is always in a limit cycle. The objective of the scheme is to reduce the size of the limit cycle to a minimum. The algorithm is a slight variation on the standard extremum-seeking algorithm with an excitation signal.

[18] presents an extremum seeking control algorithm for discrete-time systems. By using the two-time scale averaging theory, a very mild sufficient condition is derived under which the system output exponentially converges to an $O(\alpha^2)$ neighborhood of the extremum value, where α is the magnitude of the modulation signal.

[19] provides a multivariable extremum seeking scheme, the first for systems with general time-varying parameters. A stability test is derived in a simple SISO format. A systematic design algorithm based on standard LTI (Linear Time Invariant) control techniques to satisfy the stability test is developed. An analytical quantification of the level of design difficulty in terms of the number of parameters and in terms of the shape of the unknown equilibrium map is also presented.

In [20], perturbation based extremum seeking algorithm is applied to the ABS control problem. The design objective is to regulate the wheel slip as close as possible to the peak of the friction curve under any road condition.

[21] proposes a maximum power point tracking controller that can keep the fuel cell working at maximum power point (MPP) in real time. A two-loop cascade controller

with an intermediate converter is designed to operate fuel cell power plants at their MPPs. The outer loop uses an adaptive extremum seeking algorithm to estimate the real-time MPP, and then gives the estimated value to the inner loop as the set-point, at which the inner loop forces the fuel cell to operate.

In [22] slope seeking is introduced. It involves driving the output of a plant to a value corresponding to a commanded slope of its reference-to-output map. The results obtained therein constitute a generalization of perturbation-based extremum seeking, which seeks a point of zero slope, to the problem of seeking a general slope. To achieve this objective, a slope reference input is introduced into a sinusoidal perturbation-based extremum seeking scheme.

In [23], extremum seeking is introduced as an effective optimization technique to find an optimal matching solution both on-line (real-time experiment) and off-line (simulated environment) for a four-quadrupole or six-quadrupole matching channel. By optimal matching solution it is understood a set of lens focusing strengths which minimizes a cost function that measures the ‘‘error’’ between the actual beam envelope trajectory and the target or desired beam envelope trajectory, i.e., that measures the degree of matching.

In [24] the algorithm is enhanced to be applicable to a plant with moderately unstable poles and the autonomous vehicle target-tracking problem is studied.

[25] considers the problem of seeking the source of a scalar signal using an autonomous vehicle modeled as the non-holonomic unicycle and equipped with a sensor of that scalar signal but not possessing the capability to sense either the position of the source nor its own position. It is assumed that the signal field is the strongest at the source and decays away from it. The functional form of the field is not available to the vehicle. Extremum seeking is employed to estimate the gradient of the field in real time and steer the vehicle towards the point where the gradient is zero (the maximum of the field, i.e., the location of the source).

In [26] the use of extremum seeking is explored for the navigation of vehicles operating in three dimensions. It presents the solution to the problem of localization and pursuit of signal sources using only local signal measurement and without position measurement in three dimensions.

In [27], extremum-seeking control is applied in an experimental setup for smooth operation of an electromechanical valve actuator. By measuring the sound intensity, the impact velocity of the valve is reduced.

[28] proposes a global extremum seeking scheme which can seek the global optimal value in the presence of local extrema. It is shown that the proposed global extremum-seeking scheme can converge to an arbitrarily small neighborhood of the global extremum starting from an arbitrarily large set of initial conditions if sufficient conditions are satisfied.

In [29], an extremum-seeking control based self-optimizing strategy is proposed to minimize the energy consumption of an airside economizer, with the feedback of chilled water supply command rather than the temperature and humidity measurements. The mechanical cooling load is minimized by seeking the optimal outdoor air damper opening in real time.

In [30], it is demonstrated how extremum seeking can be used for the determination of an optimal combustion-timing setpoint on an experimental Homogenous-Charge-Compression-Ignition (HCCI) engine.

2.1.3 Numerical optimization based extremum seeking algorithm

As the third group of algorithms, the numerical optimization based extremum seeking scheme uses iterative methods such as line search, steepest descent, trust region. Numerical optimization algorithm chooses the next state and a state regulator forces the system to follow the new state. A block diagram of numerical optimization-based extremum seeking control can be found in Figure 2.7.

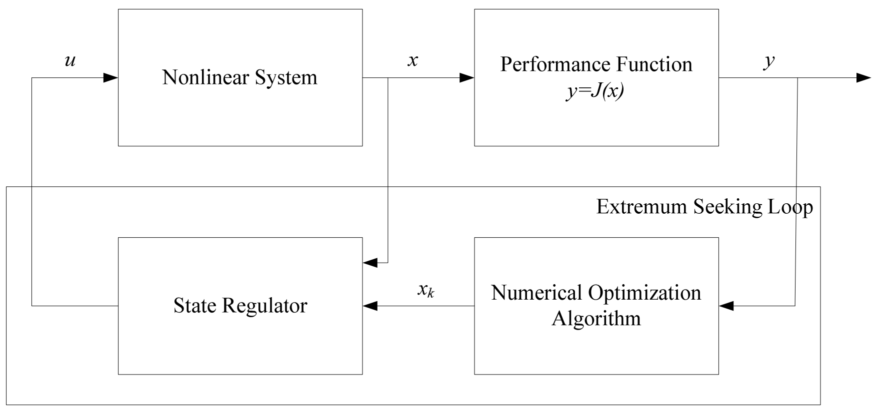

Figure 2.7 : Numerical optimization based extremum seeking scheme [35].

Based on the measurements of the state, function values $J(x)$, or gradient $\nabla J(x)$, the extremum seeking loop is expected to regulate the state as guided by the search sequence $\{x_k\}$, and eventually minimizes the performance output. Gradient information is required only at step times, not a continuously feedback of the gradient measurements. A basic framework for such extremum seeking control is given in [35] as follows:

Step 0 Given t_0=0, let x_0=$x(t_0)$ and k=0.

Step 1 Use an optimization algorithm to produce x_{k+1} based on current state x_k=$x(t_k)$ and, the computations of $J(x(t_k)), \nabla J(x(t_k))$ or $\nabla^2 J(x(t_k))$. Denote

$$x_{k+1}=\text{OPTIMIZER}(x(t_k))$$

Step 2 Design a state regulator u that regulates the state $x(t_k)$ to x_{k+1} in a finite time δ_k, let t_{k+1}=t_k+ δ_k.

Step 3 Set $k \leftarrow k+1$. Go to step 1.

In [31], the specific problem under consideration is optimization of intake, exhaust, and spark timings to improve the brake specific fuel consumption of a dual-independent variable cam-timing engine. Extremum seeking is explored as a method to find the optimal setting of the parameters. During extremum seeking, the engine is running at fixed speed and torque in a dynamometer test cell, while an optimization algorithm is iteratively adjusting the three parameters. The optimization of intake, exhaust, and spark timings is accomplished via an experimental setup to improve the brake specific fuel consumption.

In [32], numerical optimization algorithms are incorporated into the set up of an extremum seeking control scheme. The convergence of the proposed extremum seeking control scheme is guaranteed if the optimization algorithm is globally convergent and with appropriate state regulation. The robustness of line search methods and trust region methods, which relax the design requirement for the state regulator and provides further flexibility in designing robust extremum seeking control scheme, are also analyzed. Furthermore, an application of ABS design via extremum seeking control is used to illustrate the feasibility of the proposed scheme.

[33] and [34] consider the employment of numerical optimization and state regulation to solve the extremum seeking control problem, which does not separate

the dynamics from the extremum seeking loop. Extremum seeking is realized via a state regulator that drives the state traveling along a convergent set point sequence generated by a numerical optimization algorithm.

In [35], a new design of state regulator is proposed via output tracking, which trades off finite time state regulation to obtain flexibility in designing a robust asymptotic state regulator to deal with input disturbances and unknown plant dynamics. At the same time, the robustness of the optimization algorithm guarantees that the asymptotic state regulator can be used and the convergence of the numerical optimization based extremum-seeking algorithm is still ensured.

[36] contains an analysis of the dynamics associated with the interconnection of a dynamical system with a discrete-time approximate nonlinear programming algorithm designed to locate an extremum on the steady-state output map (readout map) of the dynamical system

In [37], the extremum seeking control problem is treated as a real time optimization problem with dynamic system constraints. A non-gradient trust region based extremum seeking control scheme is proposed firstly for state feedback linearizable systems, and then for input-output feedback linearizable systems. Simulation study of antilock braking system (ABS) design is addressed to illustrate the feasibility of the proposed scheme.

2.1.4 Gradient-based extremum seeking algorithm

As the fourth group of algorithms, gradient-based extremum seeking algorithms differ from the algorithms discussed above. In the above algorithms, the objective function is unknown but measurable. In gradient-based scheme, in contrast to the above schemes, an explicit structure of the objective function is required. It assumes that the objective function is explicitly known as a convex function of the system states and uncertain parameters from the system dynamic equations. Unlike conventional extremum seeking schemes, the objective function to be maximized is not directly measurable. Parametric uncertainty makes it impossible to construct the true cost online, so only an estimated value based on parameter estimates is available. The control objective is to simultaneously identify, and regulate the system to the operating point of lowest cost, which depends on the uncertain parameters.

Considering the maximization of a performance function $y = J(\sigma)$, if the derivative $dJ / d\sigma$ is known, the optimizing law for σ can be chosen as

$$\dot{\sigma} = M \frac{dJ}{d\sigma}, M > 0 \tag{2.33}$$

By letting σ^* be an isolated local maximizer of $J(\sigma)$, a Lyapunov candidate $V = J(\sigma^*) - J(\sigma)$ can be chosen, then

$$\dot{V} = -\frac{dJ}{d\sigma}\dot{\sigma} = -M\left(\frac{dJ}{d\sigma}\right)^2 \leq 0 \tag{2.34}$$

Thus, σ converges to $\dot{V} = 0$ that is $dJ / d\sigma = 0$, which occurs at $\sigma = \sigma^*$. Thus the optimizing law **(2.33)** can succesfully maximize $J(\sigma)$. It can be changed into a minimizing law by changing the sign of *M*. Optimum point σ^* can be also obtained by solving the equation $dJ / d\sigma = 0$ by considering the knowledge of the derrivative at hand. When precise gradient information is not at hand then it should be estimated. When only the sign of the gradient is known, then one can chose

$$\dot{\sigma} = M \,\mathrm{sgn}\left(\frac{dJ}{d\sigma}\right), M > 0 \tag{2.35}$$

where sgn is the signum function. Then taking the derivative of the same Lyapunov function candidate,

$$\dot{V} = -M \frac{dJ}{d\sigma}\mathrm{sgn}\left(\frac{dJ}{d\sigma}\right) = -M\left|\frac{dJ}{d\sigma}\right|^2 \leq 0 \tag{2.36}$$

σ converges again to $\sigma = \sigma^*$ where $dJ / d\sigma = 0$. Considering a general *n* dimensional gradient system

$$\dot{x} = M\nabla J(x),\ M > 0 \tag{2.37}$$

it is known that the maximal points of *J* are stable equilibria of the gradient system **(2.37)**. The trajectory of *x* will converge asymptotically to the set of stationary points of *J*. If the gradient $\nabla J(x)$ is known, a control law *u* can be designed to force the nonlinear system $\dot{x} = f(x,u)$ with performance function $y = J(x)$ to behave as the gradient system **(2.37)**. Considering a linear time invariant (LTI) system

$$\dot{x} = Ax + Bu \tag{2.38}$$

where $x \in \Re^n$ and x^* is a local maximum of the performance function *J(x)*. Considering a Lyapunov function candidate $V = J(x^*) - J(x)$, then

$$\dot{V} = -\nabla J(x)^T \dot{x} = -\nabla J(x)^T (Ax + Bu) \tag{2.39}$$

A control law should be designed for $\dot{V} \le 0$. Given the LTI system is square, that is $u \in \Re^n$ and *B* is nonsingular, then

$$u = MB^{-1}(\nabla J(x) - Ax), \quad M > 0 \tag{2.40}$$

can be used. Then, $\dot{V} = -M\|\nabla J(x)\|^2 \le 0$ and it is concluded that the state will converge to the stationary points of *J*.

In [38], the inverse optimal design technique is used to develop the controller. It is assumed that unknown parameters exist in both the plant model and the performance function. The proposed adaptive extremum seeking controller is “inverse optimal” in the sense that it minimizes a meaningful cost function that incorporates penalty on both the performance error and control action.

In [39], an extremum-seeking control problem is proposed for a class of nonlinear systems with unknown dynamical parameters, whose states are subject to convex, pointwise inequality constraints. Using a barrier function approach, an adaptive method is proposed for generating setpoints online, which converge to the feasible minimizer of a convex objective function containing the unknown dynamic parameters. A tracking controller regulates system states to the generated setpoint via state feedback, while maintaining feasibility of the state constraints.

In [40] a control algorithm is presented that incorporates real-time optimization and receding horizon control technique to solve an output feedback extremum seeking control problem for a linear unknown system. The development of the controller consists of two steps. First, the optimum setpoint that minimizes a given performance function is obtained via an update law and secondly, the control input that drives the system to the optimum is computed. State estimation filters and a parameter update law are used at each iteration step, to update the unknown states and parameters in the optimization scheme. The resulting controller is able to drive the system states to the desired unknown optimum by requiring a Lyapunov restriction and a satisfaction of a persistency of excitation condition.

In [41], a real-time optimizing controller is developed to steer a differentially flat nonlinear control system to closed-loop trajectories that optimize a cost functional of interest. An interior-point optimization method with penalty function is used to formulate a real-time optimization scheme. The problem is posed as a real-time optimal trajectory generation problem in which the optimal trajectories are computed using an adaptive extremum-seeking approach.

In [42], an extremum-seeking controller is developed to steer a periodic system to orbits that maximize a functional of interest for a class of differentially flat nonlinear systems. The problem is posed as a real-time optimal trajectory generation problem in which the optimal orbit is computed using an extremum-seeking approach. Using the flatness property of the dynamics, the original dynamic optimization problem is transformed to a parameterized optimization problem, which can be solved in real-time to approximate the optimal orbit. The control algorithm provides tracking of the optimal orbit.

[43] addresses the problem of parameter convergence in adaptive extremum-seeking control design. An alternate version of the popular persistence of excitation condition is proposed for a class of nonlinear systems with parametric uncertainties. The condition is translated to an asymptotic sufficient richness condition on the reference set-point. Since the desired optimal setpoint is not known a priori in this type of problem, the proposed method includes a technique for generating a perturbation signal that satisfies this condition in closed-loop.

In [44], a methodology for designing and implementing a real-time optimizing controller for batch processes is proposed. The controller is used to optimize a user-defined cost function subject to a parameterization of the input trajectories, a nominal model of the process and general state and input constraints. An interior point method with penalty function is used to incorporate constraints into a modified cost functional, and a Lyapunov based extremum seeking approach is used to compute the trajectory parameters.

2.2 ABS Control Problem

Anti-lock brake systems (ABS) are originally developed to prevent wheels from locking up during hard braking. Modern ABS systems not only try to prevent wheels from locking but also try to maximize the braking forces generated by the tires by preventing the longitudinal slip ratio from exceeding an optimum value. Locking of the wheels reduces the braking forces generated by the tires and results in the vehicle taking a longer time to come to a stop. Further, locking of the front wheels prevents the driver from being able to steer the vehicle while it is coming to a stop.

Most common commercial ABS algorithms are of the deceleration threshold based algorithm category. The wheel deceleration signal is used to predict if the wheel is about to lock. A common version of the deceleration threshold algorithm is summarized in [45] and shown in Figure 2.8, where a_1, a_2 are wheel deceleration threshold values.

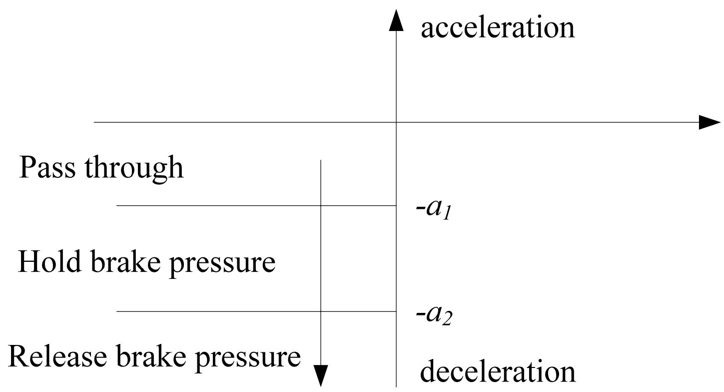

Figure 2.8 : Deceleration threshold based ABS algorithm [45].

When the driver presses on the brake pedal, if the wheel deceleration is less than a_l, then the driver's braking action is directly passed through to the brakes. When the deceleration exceeds a_l for the first time, the driver's braking action is no longer directly passed through to the brakes. Instead, the braking pressure is held constant at the pressure value achieved when the deceleration first exceeds a_l. If the wheel deceleration continues to increase further and exceeds the value a_2, then the braking pressure at the wheel is decreased. This will prevent the wheel from decelerating any further and could eventually result in the wheel gaining speed or accelerating. If the wheel deceleration reduces to the value a_2, then the pressure drop is stopped. If the wheel deceleration drops below the value a_l, then the driver's braking action is once again directly passed through to the brakes.

Threshold based ABS algorithms are simple and prevent wheel lockup but they may not provide full braking potential of the tires. More advanced solutions are studied in the literature based on maximization of the tire forces by regulating the current slip ratio of the tires to some optimum slip ratio value. Tire slip ratio is defined by referring to Figure 2.9 as follows:

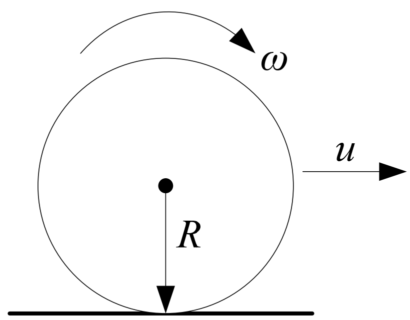

Figure 2.9 : Tire model.

Considering a tire rolling with angular velocity of ω and longitudinal velocity of u, then the tire slip ratio κ is defined as

$$\kappa = \frac{u - \omega R}{u} \tag{2.41}$$

where R is the effective tire radius. When tire longitudinal velocity u is equal to its equivalent rotational velocity ωR, then slip ratio is equal to zero, i.e. there is no slip between the tire and the road. However, when there is a slip between the tire and road then $u > \omega R$ or $u < \omega R$, where first case occurs at deceleration and the second case at acceleration. When the tires are locked during braking i.e. $\omega = 0$ then $\kappa=1$. In Figure 2.10, the longitudinal tire force characteristic for braking case is shown for different road conditions. As shown in Figure 2.10, until some optimum slip ratio value κ, braking force F_x increases with increasing longitudinal slip κ. After the peak point is exceeded, F_x decreases and therefore the tire's braking capability is not fully utilized. In order to maximize the longitudinal tire force, the tire's current slip ratio should be regulated to the optimum slip ratio value. As shown in Figure 2.10, optimum slip ratio for maximum braking force changes with respect to the road conditions.

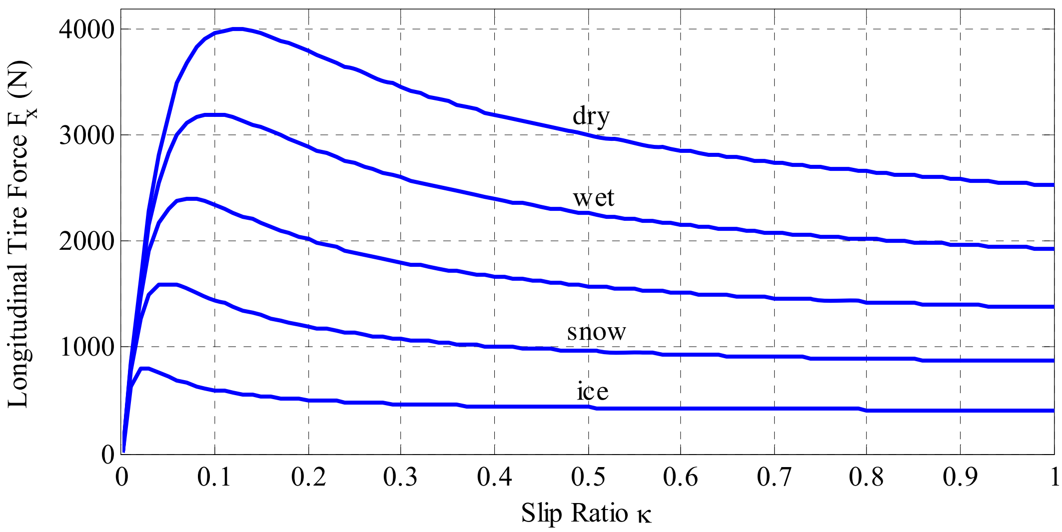

Figure 2.10 : Longitudinal tire force characteristics.

During emergency braking maneuver, maximization of the tire force between the tire patch and the road is a challenging task of autonomous control of the friction brake system subject to unknown road conditions. The road friction coefficient is mostly unknown *a priori* and it may be very complicated to estimate it on-line. The control algorithm should find the optimal set point of the brake system, which maximizes the wheel braking moment input subject to unknown and mostly changing road condition. A misjudgment about the optimal set point choice may cause lower performance of braking via either less friction force generation or blocking the tire rotation and its steer ability. When the tires operate at the peak point of braking force versus slip characteristics subject to unknown road condition, the minimum stopping distance is ensured while headway stability and steer ability are also guaranteed by preventing locking of the wheels.

In the literature, there are mainly three different approaches for ABS control problems. In the first group of algorithms as given in [46-52], a desired slip ratio value for maximizing the braking force is considered to be known a priori and the control problem is to regulate current slip ratio to this desired slip ratio value.

In [46], through iterative learning process, the electric motor torque of an electrical vehicle or a hybrid electric vehicle is optimized to keep the tire slip ratio corresponding to the peak traction coefficient during braking. The algorithm uses desired slip ratio value information.

In [47], an optimized fuzzy controller is proposed. The objective function is defined to maintain the wheel slip to a desired level so that maximum wheel traction force and maximum vehicle deceleration are obtained.

[48] uses desired slip ratio information and regulation problem is solved via sliding mode control.

[49] proposes a sliding mode controller coupled with a gray predictor to track the target value of the wheel slip. Target wheel slip is taken to be a velocity-dependent variable. As the velocity of the vehicle changes, the optimum value of the wheel slip alters.

In [50], the control law is developed by minimizing the difference between the predicted and desired responses of the wheel slip and its integral. A predictive approach is applied to design a non-linear model-based controller for the wheel slip. The integral feedback technique is also employed to increase the robustness of the designed controller.

[51] uses fuzzy model reference learning control that changes the rule base to maintain the desired fixed wheel slip in the presence of disturbances resulting from adverse road conditions.

In [52], a self-learning fuzzy sliding-mode control design method for ABS is proposed where the control objective is to find a control law so that the slip can track the desired trajectory. The controller has the advantages that it can automatically adjust and reduce the fuzzy rules.

In the second group of control algorithms as given in [53-57], the road friction is estimated first, and then the slip ratio is regulated to the slip value, which is appropriate for the estimated road condition.

In [53], a number of the road surface models are stored in the controller's memory. Then, a decision logic component uses the wheel slip and the torque to select the road surface that best matches the given wheel slip and torque. Using the selected road surface model, the fuzzy-logic controller produces the appropriate brake torque.

In [54], a sliding mode observer is constructed to estimate tire friction and a sliding mode controller calculates required braking moment input utilizing this estimated friction information.

[55] proposes an ABS controller that employs a non-derivative neural optimizer and fuzzy logic control. The role of the non-derivative optimizer is to identify the road surface and then search for the optimal wheel slip that corresponds to the maximal road adhesion coefficient. The desired braking torque is obtained by using fuzzy logic controller that uses the optimal slips from the non-derivative optimizer.

In [56], Takagi-Sugeno fuzzy identification model of road conditions is introduced to detect the current road condition and generate corresponding optimal slip.

In [57], the use of adaptive anti-lock braking system comprising of a road surface identification system and road surface information modules is presented. The proposed ABS system is capable of identifying and differentiating different types of road surfaces, and applying an amount of brake force appropriate to the road surface type being encountered in order to prevent wheel lockup as well as to minimize the braking distance.

In the third group of control algorithms as given in [32,58,59] both the value of the desired slip ratio and the road conditions are considered to be unknown. Optimum slip ratio for maximum tire force is searched online during braking.

In [32], numerical optimization and state regulator is combined to form an extremum seeking control scheme, where a numerical optimization algorithm provides search candidates of the unknown extremum and a state regulator is designed to regulate the state to where the search sequence leads. Then, the proposed numerical optimization based extremum seeking algorithm is applied to the ABS control problem.

In [58], sliding mode based extremum seeking algorithm is employed to achieve the maximum value of the friction force without a priori knowledge of the optimum slip value.

[59] proposes a nonlinear output feedback control law for active braking control systems. The control algorithm allows to detect—without the need of a friction estimator—if the closed-loop system is operating in the unstable region of the friction curve, thereby allowing to enhance both braking performance and safety. The algorithm uses slip set-point values but while operating in this set value, it can also detect instability by monitoring the wheel slip value when operating point is located in the unstable region of the friction curve.

2.3 Hybrid Electric Vehicle Control Problem

Continuously increasing demands on lower emission levels and better fuel economy have led researchers to develop more efficient, less polluting vehicles. Electric vehicles seem as a promising solution but for now, their short driving distance combined with the long recharging period for batteries postpones their widespread use to the future. Hybrid electric vehicles (HEV) offer an acceptable, intermediate solution. In a hybrid electric vehicle, an electric motor (EM) powered by an electrochemical battery is used along with the internal combustion engine (ICE) powered by fossil fuel. They appear to be one of the most viable technologies with significant potential to reduce fuel consumption and pollutant emissions.

HEVs are classified mainly as parallel hybrid, series hybrid and series-parallel hybrid as shown in Figure 2.11, Figure 2.12, and Figure 2.13. In series hybrid electric vehicles shown in Figure 2.11, only the electric motor drives the wheels while the internal combustion engine is used to provide power to the generator to charge the battery. Regenerative braking is possible using the traction motor as a generator. In parallel hybrid electric vehicles shown in Figure 2.12, both the ICE and electric motor deliver power in parallel to drive the wheels. The propulsion power may be supplied by the ICE alone, by the electric motor, or by both. The electric motor can be used as a generator to charge the battery by regenerative braking or by absorbing power from the ICE. Combined hybrid electric vehicle configuration shown in Figure 2.13 has the ability to operate as series or as parallel hybrids. A power flow from the engine to the planetary gear set always implies a power flow to the generator. Consequently, a pure ICE operation is not possible with such a configuration but it is always associated with a power flow through the generator and the motor. In series hybrid electric vehicle, the thermal path is uncoupled from the wheels allowing controlling the internal combustion engine easily in more efficient regions. However, the number of energy conversions is more than the parallel hybrid electric vehicle, which makes it less efficient at the end. Henceforth, in this thesis, parallel type is chosen as the hybrid electric vehicle configuration.

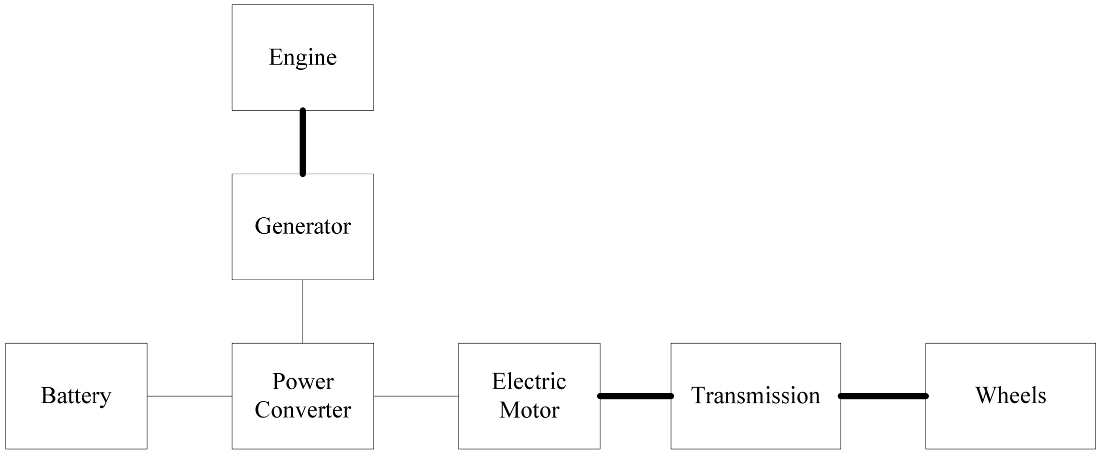

Figure 2.11 : Series hybrid electric vehicle configuration [60].

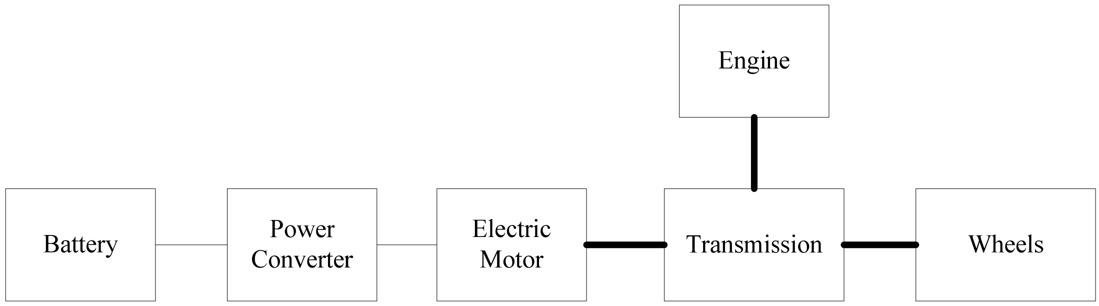

Figure 2.12 : Parallel hybrid electric vehicle configuration [60].

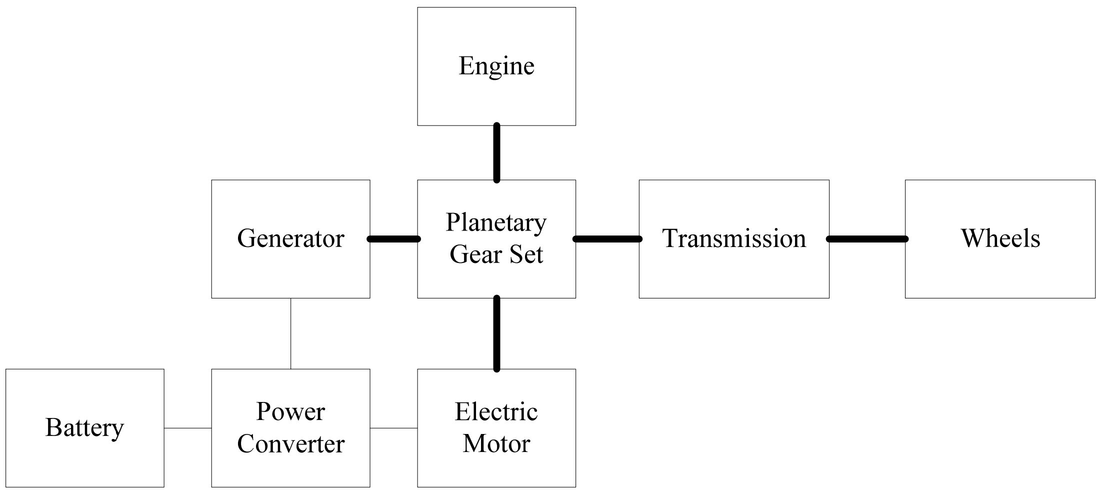

Figure 2.13 : Combined hybrid electric vehicle configuration [60].

The main objectives of the hybrid electric vehicle energy management strategies are minimizing fuel consumption and pollutant emissions while meeting driver's power demand, sustaining the battery state of charge and considering constraints such as engine and electric motor power limits.

During urban driving, the internal combustion engine operates inefficiently because of the idling and frequent stop-and-go operations. In these cases, turning off the internal combustion engine and operating the vehicle through the electric motor will minimize the fuel consumption. On the contrary, in highway driving, since internal combustion engine operates efficiently, it will drive the vehicle and at the same time drive the electric motor in the generator mode to charge the batteries if needed. When the driver torque demand is beyond the internal combustion engine limits, the electric motor may assist the engine to accelerate the vehicle properly. During braking, the braking energy may be used through the electric motor to charge the batteries. This is called regenerative braking.

Before using the electric motor, the charge level of the batteries should be taken into consideration. The charge level is called *SOC* (State of Charge). As long as the *SOC* level permits, the electric motor can be used to drive the vehicle or charge the batteries as a generator. If the *SOC* level is too low, the electric motor should not be operated to drive the vehicle since it will cause full depletion of the battery. If the *SOC* level is too high, then charging the battery for example through the regenerative braking will cause overcharge of the battery. Use of the battery at improper *SOC* level will decrease the battery life. The *SOC* level should be maintained between lower and upper limits for a long life battery operation.

Various solutions have been proposed in the literature to control a hybrid electric vehicle. Since in this thesis the control algorithm is developed for a parallel type hybrid electric vehicle model, the literature review here focuses mainly on the parallel hybrid electric vehicles.

In [61,62], the state of the art control strategies for HEVs are classified and overviewed. In [63-70], rule based control strategies are developed for hybrid electric vehicle energy management problem.

In [63], the internal combustion engine operation points are forced into the vicinity of the best point of efficiency using an efficiency map. The operation strategy is explained by examining the efficiency map in Figure 2.14.

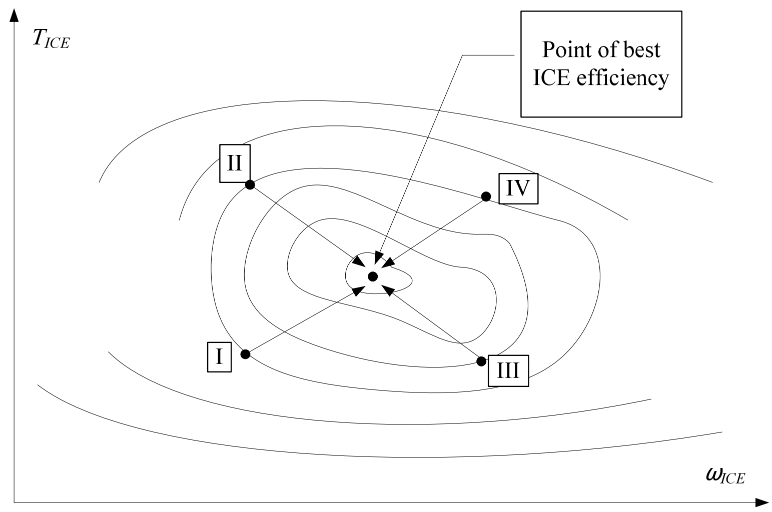

Figure 2.14 : Generic ICE efficiency map [63].

In Figure 2.14, point I is where the engine speed and torque level are too low according to the best efficiency point. To remedy this situation, the gear ratio must be increased (which means downshifting in a manual transmission), the accelerator command must be increased, and to maintain a constant overall power-train power output, the electric motor must be operated as a generator. This operation as a generator keeps the excess torque that is generated by the internal combustion engine from being delivered to the powertrain.

Supposing that the torque and speed needed to overcome the road load is given by operation point II in Figure 2.14. In this case, the engine speed is too low and the torque is too high for the best efficiency of the internal combustion engine. To remedy this situation, the gear ratio to the engine must be increased (which means downshifting in a manual transmission) and the accelerator command must be decreased. It becomes immediately apparent that once this control move is exercised on the engine, there will not be enough torque to overcome the road load. The electric motor must therefore be adjusted to meet the deficit. In order to overcome the road load and maintain a constant overall power-train power output, the electric motor must be operated as a motor.

The *SOC* of the battery pack has to be considered in order to decide whether the required torque contribution of the electric motor is possible or not. If the batteries are completely charged, the electric motor cannot be allowed to operate as a generator. If they are totally discharged, a positive torque contribution will not be possible.

Since point IV in Figure 2.14 is not very efficient, one would like to shift it as close to the peak efficiency point as possible. This will be done by decreasing the engine speed (up shifting) and decreasing the accelerator command (which decreases torque).

In [63], a fuzzy logic rule based controller is used with three inputs (γ_a, $T_{EM,D}$ and SOC), two outputs ($\Delta\alpha$ and T_{EM}), and a total of 847 rules where γ_a is the accelerator command input, $T_{EM,\ D}$ is the desired electric motor torque, SOC is Battery State of Charge, $\Delta\alpha$ is change in accelerator command to the internal combustion engine, T_{EM} is actual electric motor torque.

The fuzzy controller works by using the values of the three inputs (γ, $T_{EM,D}$, and SOC) and incorporating the expert's knowledge of the system to calculate the change in accelerator command to the internal combustion engine, $\Delta\alpha$, and the actual electric motor torque, T_{EM}. A subset of typical rules for the fuzzy logic controller is given by the following list.

1)If γ_a is positive large and $T_{EM,\ D}$ is positive large and the SOC is positive medium large, then $\Delta\alpha$ is zero and T_{EM} is positive large.

2)If γ_a is positive medium and $T_{EM,\ D}$ is negative low and the SOC is positive large, then $\Delta\alpha$ is zero and T_{EM} is zero.

3)If γ_a is positive medium and SOC is positive large and $T_{EM,\ D}$ is negative low, then $\Delta\alpha$ is zero and T_{EM} is zero.

4)If γ_a is negative large and SOC is positive large and $T_{EM,\ D}$ is negative low, then $\Delta\alpha$ is zero and T_{EM} is zero.

5)If γ_a is positive low and SOC is positive medium and $T_{EM,\ D}$ is positive low, then $\Delta\alpha$ is positive low and T_{EM} is negative low.

In rule 1, the driver wants full acceleration and there is sufficient SOC in the battery, thus the EM will operate as a motor. $\Delta\alpha$ that is requested is zero. This is because the driver is already putting the pedal to the floor in his/her request for full acceleration. There is no need to change his/her request. The torque needed from the ICE (T_{ICE}) may be more or less than what the vehicle needs to overcome the load torque. The EM torque T_{EM} compensates the difference between the T_{LOAD} and T_{ICE}. Rule 2 is explained by the following: If the driver wants moderate acceleration, the desired EM torque is slightly negative, and the SOC of the battery pack is at its highest allowable, then do not increase the accelerator command and do not apply a negative torque with the EM. Rule 3 is explained by the following: If the driver is braking heavily and the SOC is below its highest allowable limit, then apply as much negative torque as the EM can supply and do not adjust the accelerator command. This is the regenerative braking scenario in which the application of the brake is used in charging the batteries. Rule 4 is explained by the following. If the driver is braking heavily and the *SOC* is at its highest allowable limit, then apply no negative torque with the EM and do not adjust the accelerator command. This keeps one from overcharging the batteries. Rule 5 is explained by the following. If slight acceleration is being requested and the desired EM torque is negative and the battery *SOC* is below its maximum limit, then add a positive change to the accelerator and supply negative torque with the EM. In this final case, extra torque is added to the ICE and that extra torque is used to charge the EM's batteries.

In [64-66], fuzzy logic based controllers are developed for the HEV energy management problem as given in [63] above.

In [67] the control strategy is implemented on a proof-of-concept vehicle where the algorithm switches between states according to battery charge level and requested power values.

In [68] firstly preliminary rule-based control strategy is introduced. Then a dynamic optimization method is applied. The design procedure starts by defining a cost function, such as minimizing a combination of fuel consumption and selected emission species over a driving cycle. Dynamic programming (DP) is then utilized to find the optimal control actions including the gear-shifting sequence and the power split between the engine and motor while subject to a battery *SOC*-sustaining constraint. Through analysis of the behavior of DP control actions, rule based control is improved. The design process starts by interpreting the driver pedal motion as a power request P_{req}. According to the power request and the vehicle status, the operation of the controller is determined by one of the three control modes: Braking Control, Power Split Control, and Recharging Control. If P_{req} is negative, the Braking Control is applied to decelerate the vehicle. If P_{req} is positive, either the Power Split or the Recharging Control will be applied, depending on the battery state of charge (*SOC*). A high-level charge-sustaining strategy tries to maintain the battery *SOC* within defined lower and upper bounds. Under normal propulsive driving conditions, the Power Split Control determines the power flow in the hybrid powertrain. When *SOC* drops below the lower limit, the controller will switch to the

Recharging Control until the *SOC* reaches the upper limit, and then the Power Split Control will take over. The basic logic of each control rule is described below.

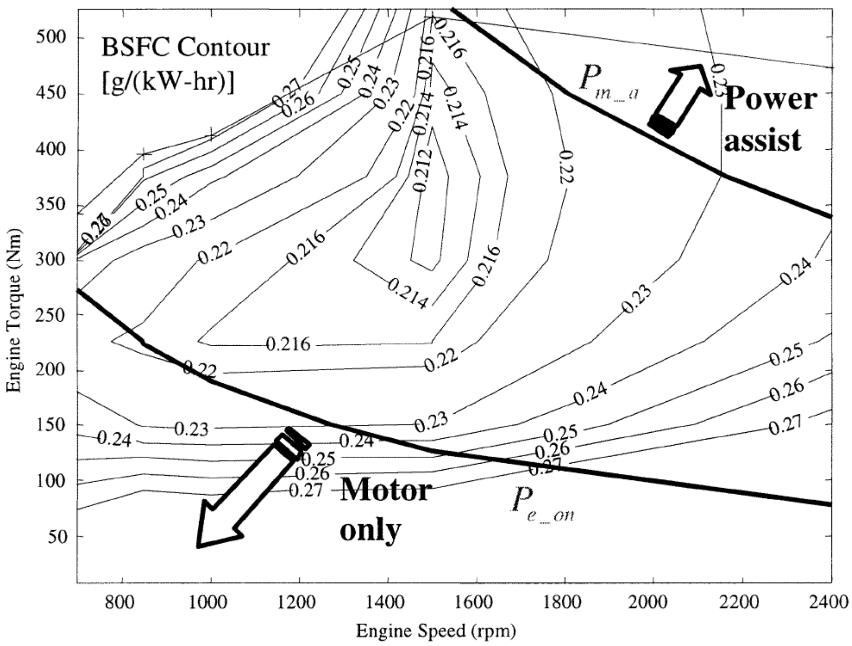

Figure 2.15 : Engine efficiency map in [68].

Power Split Control: Based on the engine efficiency map shown in Figure 2.15, an "engine on" power line P_{e_on}, and "motor assist" power line P_{m_a}, are chosen to avoid engine operation in inefficient areas. If P_{req} is less than P_{e_on}, the electric motor will supply the requested power alone. Beyond P_{e_on}, the engine becomes the sole power source. Once P_{req} exceeds P_{m_a}, engine power is set at P_{m_a} and the motor is activated to make up the difference (P_{req} -P_{m_a}).

Recharging Control: In the recharging control mode, the engine needs to provide additional power to charge the battery in addition to powering the vehicle. Commonly, a preselected recharge power level, P_{ch}, is added to the driver's power request, which becomes the total requested engine power ($P_e = P_{req} + P_{ch}$). The motor power command becomes negative ($P_m = - P_{ch}$) in order to recharge the battery. One exception is that when the total requested engine power is less than P_{e_on}, the motor alone will propel the vehicle to prevent the engine from operating in the inefficient operation. In addition, when P_{req} is greater than the maximum engine power, the motor power will become positive to assist the engine.

Braking Control: A simple regenerative braking strategy is used to capture as much regenerative braking energy as possible. If P_{req} exceeds the regenerative braking capacity P_{m_min}, friction brakes will assist the deceleration ($P_b = P_{req} - P_{m\_min}$).

After preliminary rule-based control strategy is introduced, dynamic programming method is applied to improve rule-based control strategy in [68].

Dynamic programming (DP) solutions in HEV energy management strategies give global optimum values for the considered performance functions but the algorithm requires the information of the whole driving cycle (Acceleration, vehicle speed, braking information) in advance. Since future driving conditions are unknown, it cannot be utilized in a real time controller. Rather than that, DP techniques are used for performance evaluation of real time control algorithms or to improve them as introduced in [68]. In [68], the objective in DP is minimizing the fuel consumption and pollutant emissions. The optimization goal is to find the control input $u(k)$ to minimize a cost function, which consists of the weighted sum of fuel consumption and emissions for a given driving cycle.

In [69], a genetic-fuzzy control strategy for parallel HEVs is proposed. The genetic-fuzzy control strategy is a fuzzy control strategy, which is tuned offline using GA. First, a fuzzy logic controller is designed, whose rule base is extracted based on expert knowledge. The parameters defining the membership functions are then tuned via GA. The main objective is to minimize fuel consumption and emissions.

In [70], energy optimization control for a parallel hybrid electric system with automated mechanical transmission (AMT) is proposed. The optimal torque distribution strategy is proposed to minimize the powertrain equivalent specific fuel consumption by considering the power conversion efficiency, which distributes the vehicle single torque request into separate torque requests for the internal combustion engine and the electric motor. The distribution results are expressed in a table format and can be found from the simple process of looking up in the table using the vehicle torque request, the ICE speed, and the battery state of charge (*SOC*). The AMT shift control is suggested to maximize the powertrain system efficiency and optimizes the speed as the basis for the above-mentioned torque distribution, in which the ICE efficiency, the EM efficiency, and the battery efficiency are all explicitly taken into account. The AMT optimal shift control law and the EM optimal torque are essentially look-up-table-based control according to the ICE power, the EM power, the vehicle velocity, and the battery *SOC* after offline calculations.

[71] proposes an online power-balancing strategy (PBS) for near-optimal fuel efficiency in fully hybridized PHEVs. Its underlying concept is to use the electrical system to control the ICE within its peak-efficiency region. Results show that a newly proposed parallel hybrid electric vehicle assisted by the integrated starter generator (ISG-assisted PHEV) enables the PBS controller to operate the ICE very close to the point of the highest efficiency, similar to the function of continuously variable drivers.

[72] introduces a power distribution strategy to minimize the loss in power flow and to operate the engine at an efficient point. The strategy employs control maps to reduce the calculation load in deriving the most efficient operating point. Furthermore, an energy strategy to decide the optimal charging/discharging power of a battery is established using the results of the power distribution strategy.

In [73], the control strategies for the energy management between the two power sources are optimized with respect to fuel consumption with a classical dynamic programming (DP) method. A method based on the Pontryagin Minimum Principle is proposed which furnishes results very close to the DP results for a significantly reduced calculation time. These optimization results furnish the optimal control laws from which the control laws to be implemented on the vehicle could be derived.

In [74-78] the methodology, which is called Equivalent Consumption Minimization Strategy (ECMS), is developed and studied. The algorithm includes minimizing a cost function which is the sum of the real fuel consumption of the internal combustion engine and the equivalent fuel consumption of the electric motor as shown in **(2.42)**, where $\varsigma(P_{em}(t))$ is the fuel equivalent of the electric energy and $\dot{m}_{ice}$ is the fuel consumption. This is a unified representation of both the energy used from the battery and fuel consumption.

$$J = \dot{m}_{ice}(P_{ice}(t) + \varsigma(P_{em}(t)) \tag{2.42}$$

Equivalent fuel consumption of the electric motor is calculated according to the following concept. Considering the situation that at a sample time *t*, some energy is drawn from the battery to provide some motive power for the vehicle. At the same time, the fuel provides the rest of the energy used to propel the vehicle. To ensure that the state of charge remains constant, the same amount of energy will have to be used for the battery charge in the future. This energy will be provided by the ICE, which will imply extra fuel consumption. The equivalent fuel consumption is defined as the extra fuel consumption that will be required for the battery charge. This charge will be done in the future. Considering another situation, this time the battery is recharged at the current sample time. To maintain a constant state of charge, a future discharge of the battery is required. This discharge will be done by using the electric motor, which will produce some mechanical power used to propel the vehicle. The fuel consumption reduction due to the electric motor is the equivalent fuel consumption with the negative sign. The equivalent fuel consumption of the electric motor cannot be calculated exactly due to unknown efficiencies. To calculate the equivalent fuel consumption, mean efficiencies should be used.

In [79] a new rule-based energy management strategy is introduced, based on the combination of Rule-Based and Equivalent Consumption Minimization Strategies (RB-ECMS). The RB-ECMS uses only one decision variable and requires no tuning of many threshold control values and parameters. [80] considers three different energy management approaches which are: a rule-based control, an adaptive equivalent fuel consumption minimization strategy (A-ECMS), and H_∞ control. Results, compared with the optimal solution given by dynamic programming, show that the A-ECMS strategy is the best performing strategy.

[81] implements as a real-time strategy the Equivalent Consumption Minimization Strategy. The control law is inferred from Pontryagin's Minimum Principle, where the Lagrange multiplier is deduced from optimization results of Dynamic Programming on given driving cycles.

In [82], to accomplish real time energy distribution management system in a plug-in hybrid electric vehicle, firstly, a specific model is established which contains most of the powertrain properties and partly vehicle dynamics. Secondly, an optimal control problem with inequality constraints is analyzed and formulated mathematically. Thirdly, the particle swarm optimization (PSO) is applied to search for global near-optimum at each time interval. However, PSO is time-consuming so it can be used only as an off-line controller. To overcome this drawback neural network is designed to get sub-optimal real-time controller by employing the near-optimal results obtained from aforementioned PSO.

In [83] a parallel hybrid electric vehicle (PHEV) configuration consisting of an extra one-way clutch and an automatic mechanical transmission (AMT) is taken as the study subject. An energy management strategy (EMS) combining a logic threshold approach and an instantaneous optimization algorithm is developed for the investigated PHEV. The objective of this EMS is to achieve acceptable vehicle performance and drivability requirements while simultaneously maximizing engine fuel economy and maintaining the battery state of charge (SOC) in its rational operation range at all times.

Rule based solutions as given in [63-70] are simple and easy to implement. However, these kind of energy management strategies requires correct tuning of all the controller parameters in order to assure the correct behavior of the algorithm. The approach is not easily exportable to other vehicle configurations.

Instantaneous optimization methods based on equivalent consumption minimization strategy as given in [74-78] provide a real time near optimal solution. Since the electrical energy and the fuel energy are not directly comparable, an equivalence factor is needed to calculate equivalent fuel consumption value. The performance of the control algorithm depends heavily on the calculation of the equivalence factor. An error in calculating the equivalence factor will affect the performance of the controller considerably.

2.4 Chapter Summary

This chapter presented a review of the literature related to the dissertation. The different approaches to extremum seeking control were presented in Section 2.1. The automotive applications that were chosen for application of the extremum seeking control method in this dissertation were treated in Sections 2.2 and 2.3. The existing literature on ABS control was reviewed in Section 2.2. The existing literature on hybrid electric vehicle power management control was reviewed in Section 2.3. The application of sliding mode based extremum seeking control to ABS braking, ABS braking with improved lateral control and HEV power distribution will be presented in Chapters 3, 4 and 5, respectively.

3. ABS CONTROL VIA EXTREMUM SEEKING WITH PARAMETER TUNING

3.1 Introduction

The maximization of the tire force between the tire patch and the road during an emergency braking maneuver in the presence of unknown road conditions, as needed in an ABS brake system, is a challenging task. The road friction coefficient is mostly unknown a priori and it is difficult to estimate it on-line. The ABS brake control algorithm should find the optimal set point of brake hydraulic pressure, which maximizes the wheel braking moment subject to unknown and possibly changing road conditions. A misjudgment about the optimal set point choice may cause lower performance of braking via either less friction force generation or via blocking the tire rotation and hence the vehicle steer ability. The minimum stopping distance is ensured when the tires operate at the peak point of the braking force versus slip characteristics subject to unknown road conditions. In addition, headway stability and steer ability are also improved as locking of the wheels is prevented.

Three main approaches exist in the literature for maximization of the tire forces during emergency ABS braking. In the first group of algorithms given in [46-52], a desired slip ratio is considered to be known a priori and the control problem is to regulate the current slip ratio about this desired slip ratio value. In the second group of ABS control algorithms given in [53-57], the road friction is first estimated and the slip ratio is controlled to the slip value which is appropriate for the estimated road condition. In the third group of ABS control algorithms given in [32,58,59], optimum slip ratio value for maximum tire forces is searched online during braking. The first group of algorithms, where the desired slip ratio is considered to be known, do not possess optimality since the optimum slip ratio for maximum braking force is not constant and changes with respect to different road conditions. The performance of the second group of algorithms depends on the accuracy of the estimation procedure, which is difficult in a short period of time such as emergency braking.

In this chapter, without knowing optimum value of the slip ratio a priori, and without trying to estimate road conditions, optimum slip for maximum tire force is searched online. The proposed algorithm belongs to the third group of ABS algorithms as given in [32,58,59]. The self-optimization routine seeks the peak point of the force-slip curve without utilizing optimum slip information. A sliding mode based extremum seeking algorithm is combined with the adaptation of the tire model parameters. Thus, unlike common extremum seeking algorithms in the literature, where on-line measurement of the objective function is a necessity, the control design considered here does not require objective function measurements. Consequently, the control algorithm accomplishes its task with minimum measurement requirements. The chapter is organized as follows. Section 3.2 presents the problem description. The control algorithm is introduced in Section 3.3. A simulation study is presented in Section 3.4. In order to show real time applicability of the considered algorithm, simulations are repeated with a real time hardware, the Microautobox general purpose electronic control unit. Real time simulation results are shown in Section 3.5. The chapter concludes with conclusions being made in Section 3.6.

3.2 Problem Description

The quarter car model is taken into consideration where the dynamic equations are written as follows

$$m\dot{u} = -F_x \tag{3.1}$$

$$I_\omega \dot{\omega} = RF_x - T_b \tag{3.2}$$

Here m (kg) is the mass of the quarter car, u (m/s) is the longitudinal speed, F_x (N) is the longitudinal tire force, I_ω (kgm^2) is the wheel inertia, ω (rad/s) is the wheel angular speed, R (m) is the tire effective radius and T_b (Nm) is the braking moment. Aerodynamic drag and rolling resistance effects are neglected due to simplicity. The calculation of the longitudinal tire force is carried out as

$$F_x = F_z \mu_x \tag{3.3}$$

where F_z (N) is the vertical tire force and μ_x is the longitudinal tire-road friction function. Various analytic and empirical tire models have been developed in the literature for calculating the tire forces. Some of them are the Magic Formula, Dugoff, LuGre, Burckhardt tire models. In this study, the Burckhardt approach is considered for controller development. Longitudinal tire-road friction function is calculated as given in [84]

$$\mu_x(\kappa, c) = c_1\left(1 - e^{-c_2\kappa}\right) - c_3\kappa \tag{3.4}$$

where c_1, c_2, and c_3 are the tire model parameters. By choosing different sets of c's as given in Table 3.1 [84], an accurate tire-road friction function may be modeled for different road conditions. In **(3.4)**, κ is the longitudinal tire slip value, which is defined for the braking case as

$$\kappa = \frac{u - \omega R}{u} \tag{3.5}$$

It can be seen from **(3.5)** that by increasing braking action, slip value κ increases from 0 to 1. κ = 1 denotes that wheels are locked (ω = 0).

Table 3.1 : Burckhardt tire model parameters for different road conditions [84].

	c_1	c_2	c_3
Asphalt dry	1.2801	23.99	0.52
Asphalt wet	0.857	33.822	0.347
Concrete dry	1.1973	25.168	0.5373
Cobblestones dry	1.3713	6.4565	0.6691
Cobblestones wet	0.4004	33.7080	0.1204
Snow	0.1946	94.129	0.0646
Ice	0.05	306.39	0

Using the parameter sets given in Table 3.1, the change of the tire-road friction function μ_x with respect to the slip κ is plotted in Figure 3.1 for different road conditions. In Figure 3.1, the common characteristics of the curves are shown: Until some optimum slip value, μ_x increases with respect to increasing κ. After the peak point is exceeded, μ_x is decreasing and therefore the tire's braking capability is not fully utilized. In addition to the degraded braking performance, the lateral force generation capability of the tire is also decreased due to excessive braking which results in a loss of the vehicle steer ability. Hence, during emergency braking, regulating braking systems operation in the vicinity of the peak point of the $\mu_x - \kappa$ curve is a vital control problem.

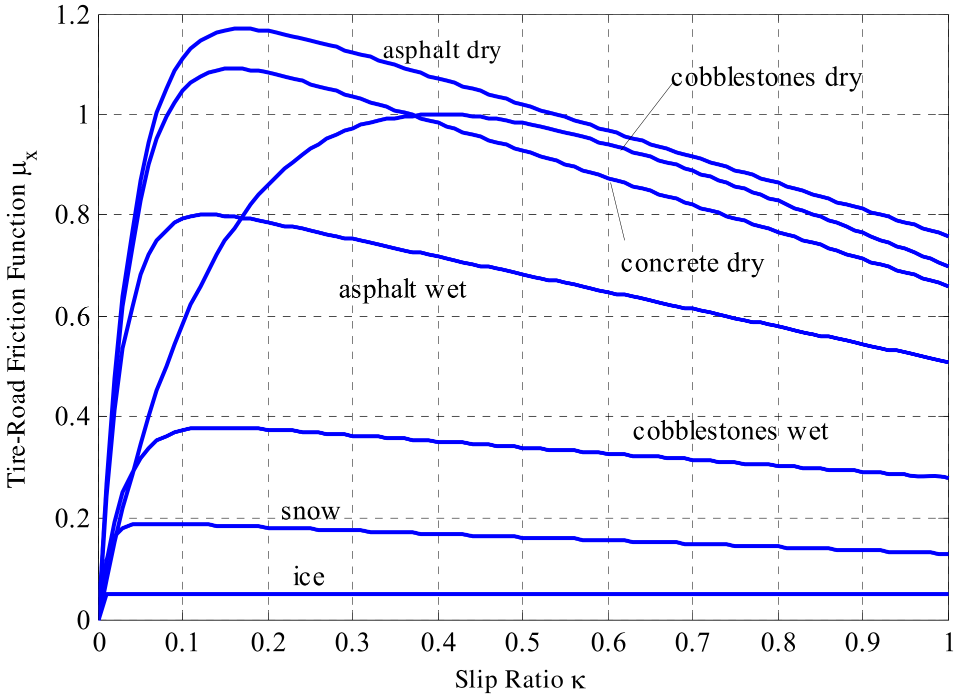

Figure 3.1 : Change of the friction coefficient μ_x with respect to the tire slip κ for different road conditions.

As it is shown in Figure 3.1, the optimum slip value for maximizing the braking force depends on the road conditions. In order to find optimum slip value, the road condition should be known. However, estimation of the road conditions in a short period of time such as during emergency braking is a very difficult and unreliable approach. In this chapter, rather than estimation of the road condition, a self-optimization routine is proposed to seek the optimum slip set point.

3.3 Control Algorithm

Taking the time-derivative of **(3.5)** and by integrating with **(3.1)**, **(3.2)**, **(3.3)**, and **(3.4)**, the slip dynamics may be given as

$$\dot{\kappa} = -\frac{F_z}{u}\left(\frac{1-\kappa}{m} + \frac{R^2}{I_\omega}\right)\left(c_1 - c_1 e^{-c_2\kappa} - c_3\kappa\right) + \frac{R}{uI_\omega}T_b \qquad \textbf{(3.6)}$$

To simplify the notation, the following expression is defined

$$c_4 = c_1 e^{-c_2 \kappa} \tag{3.7}$$

Then **(3.6)** is rewritten as

$$\dot{\kappa} = -\frac{F_z}{u}\left(\frac{1-\kappa}{m} + \frac{R^2}{I_\omega}\right)(c_1 - c_4 - c_3\kappa) + \frac{R}{uI_\omega}T_b \tag{3.8}$$

Let $\hat{\kappa}$ be a prediction of the slip denoted by κ where the slip, κ, and the wheel braking moment, T_b are assumed to be measured,

$$\dot{\hat{\kappa}} = -\frac{F_z}{u}\left(\frac{1-\kappa}{m} + \frac{R^2}{I_\omega}\right)(\hat{c}_1 - \hat{c}_4 - \hat{c}_3\kappa) + \frac{R}{uI_\omega}T_b + K(\kappa - \hat{\kappa}) \tag{3.9}$$

where K >0 is a constant. Here, $\hat{c}_1$, $\hat{c}_3$, $\hat{c}_4$ are the parameter estimates that are changing with time. Note that c_1, c_2, c_3 are the unknown constant tire parameters. The prediction error is defined as,

$$e = \kappa - \hat{\kappa} \tag{3.10}$$

Subtracting **(3.9)** from **(3.8)**, the error dynamics is written as,

$$\begin{aligned}\dot{e} = &-\frac{F_z}{u}\left(\frac{1-\kappa}{m} + \frac{R^2}{I_\omega}\right)(c_1 - \hat{c}_1) + \frac{F_z}{u}\left(\frac{1-\kappa}{m} + \frac{R^2}{I_\omega}\right)(c_4 - \hat{c}_4) \\ &+ \frac{F_z}{u}\left(\frac{1-\kappa}{m} + \frac{R^2}{I_\omega}\right)(c_3 - \hat{c}_3)\kappa - Ke\end{aligned} \tag{3.11}$$

For stability analysis, a Lyapunov function candidate is chosen as

$$V = \frac{1}{2}e^2 + \frac{a_1}{2}(c_1 - \hat{c}_1)^2 + \frac{a_3}{2}(c_3 - \hat{c}_3)^2 + \frac{a_4}{2}(c_4 - \hat{c}_4)^2 \tag{3.12}$$

where a_1, a_3, a_4 are positive constants. Taking the time derivative of **(3.12)**

$$\dot{V} = e\dot{e} - (c_1 - \hat{c}_1)a_1\dot{\hat{c}}_1 - (c_3 - \hat{c}_3)a_3\dot{\hat{c}}_3 + (c_4 - \hat{c}_4)a_4\left(\dot{c}_4 - \dot{\hat{c}}_4\right) \tag{3.13}$$

By taking the time derivative of **(3.7)** and inserting into **(3.13)**

$$\dot{V} = e\dot{e} - (c_1 - \hat{c}_1)a_1\dot{\hat{c}}_1 - (c_3 - \hat{c}_3)a_3\dot{\hat{c}}_3 + (c_4 - \hat{c}_4)a_4\left(-c_1c_2e^{-c_2\kappa}\dot{\kappa} - \dot{\hat{c}}_4\right) \tag{3.14}$$

is obtained. From **(3.11)** and **(3.14)**

$$\dot{V} = -e\frac{F_z}{u}\left(\frac{1-\kappa}{m}+\frac{R^2}{I_\omega}\right)(c_1-\hat{c}_1)+e\frac{F_z}{u}\left(\frac{1-\kappa}{m}+\frac{R^2}{I_\omega}\right)(c_4-\hat{c}_4)$$
$$+e\frac{F_z}{u}\left(\frac{1-\kappa}{m}+\frac{R^2}{I_\omega}\right)(c_3-\hat{c}_3)\kappa - Ke^2 \qquad \textbf{(3.15)}$$
$$-(c_1-\hat{c}_1)a_1\dot{\hat{c}}_1-(c_3-\hat{c}_3)a_3\dot{\hat{c}}_3+(c_4-\hat{c}_4)a_4\left(-c_1c_2e^{-c_2\kappa}\dot{\kappa}-\dot{\hat{c}}_4\right)$$

The update law for estimation of the parameters is chosen as follows:

$$\dot{\hat{c}}_1 = -\frac{e}{a_1}\frac{F_z}{u}\left(\frac{1-\kappa}{m}+\frac{R^2}{I_\omega}\right)$$
$$\dot{\hat{c}}_4 = \frac{e}{a_4}\frac{F_z}{u}\left(\frac{1-\kappa}{m}+\frac{R^2}{I_\omega}\right)-c_{1av}c_{2av}e^{-c_{2av}\kappa}\dot{\kappa} \qquad \textbf{(3.16)}$$
$$\dot{\hat{c}}_3 = \kappa\frac{e}{a_3}\frac{F_z}{u}\left(\frac{1-\kappa}{m}+\frac{R^2}{I_\omega}\right)$$

where c_{1av} and c_{2av} are average values of c_1 and c_2 in Table 3.1. When **(3.16)** is inserted into **(3.15)**

$$\dot{V} = -Ke^2+(c_4-\hat{c}_4)a_4\left(c_{1av}c_{2av}e^{-c_{2av}\kappa}\dot{\kappa}-c_1c_2e^{-c_2\kappa}\dot{\kappa}\right) \qquad \textbf{(3.17)}$$

is obtained. From **(3.17)** one can write

$$\frac{dV}{dt} \le |c_4-\hat{c}_4|a_4\left|c_{1av}c_{2av}e^{-c_{2av}\kappa}\dot{\kappa}-c_1c_2e^{-c_2\kappa}\dot{\kappa}\right|-Ke^2 \qquad \textbf{(3.18)}$$

In **(3.18)**, when the following inequality holds

$$|e| > \left(\frac{|c_4-\hat{c}_4|a_4\left|c_{1av}c_{2av}e^{-c_{2av}\kappa}\dot{\kappa}-c_1c_2e^{-c_2\kappa}\dot{\kappa}\right|}{K}\right)^{1/2} \qquad \textbf{(3.19)}$$

one gets

$$\frac{dV}{dt} < 0 \qquad \textbf{(3.20)}$$

Hence, e is uniformly bounded and converges to the vicinity of zero. Reformulating **(3.11)** as

$$\dot{e} = -\frac{1}{u}\left(\frac{1-\kappa}{m}+\frac{R^2}{I_\omega}\right)\left(F_x(\kappa,c)-F_x(\kappa,\hat{c})\right)-Ke \qquad \textbf{(3.21)}$$

It is realized that the convergence of $F_x(\kappa,\hat{c}) \rightarrow F_x(\kappa,c)$ is assured. Next, the extremum seeking algorithm for maximizing the tire braking force is presented. The algorithm will not require a priori the optimum value of the slip ratio or the information of the road friction coefficient. For the extremum seeking algorithm via sliding modes, [4] formulates a sliding surface where the objective function is enforced to follow a time increasing function and a discontinuous switching function is selected for the optimization parameter. This methodology is adapted here where the aim is to maximize $F_x(\kappa,\hat{c})$. Since $F_x(\kappa,\hat{c}) \rightarrow F_x(\kappa,c)$ will be maintained, reaching to the peak point of the characteristics $F_x(\kappa,\hat{c})$ versus κ will maximize the friction tire force $F_x(\kappa,c)$. The sliding surface is selected as

$$s = F_x(\kappa,\hat{c}) - \rho t \tag{3.22}$$

where ρ is a positive constant and t is the time variable. Selection of ρ will be clarified later. Taking the time derivative of s,

$$\dot{s} = \frac{\partial F_x(\kappa,\hat{c})}{\partial \kappa}\dot{\kappa} + \frac{\partial F_x(\kappa,\hat{c})}{\partial \hat{c}}\dot{\hat{c}} - \rho \tag{3.23}$$

The update law for the optimization parameter κ is chosen as,

$$\dot{\kappa} = M \operatorname{sgn} \sin \frac{\pi s}{\gamma} - \left(\frac{\partial F_x(\kappa,\hat{c})}{\partial \kappa}\right)^{-1} \left[\frac{\partial F_x(\kappa,\hat{c})}{\partial \hat{c}}\dot{\hat{c}}\right] \tag{3.24}$$

which is

$$\dot{\kappa} = M \operatorname{sgn} \sin \frac{\pi s}{\gamma} - \left(\frac{\partial F_x(\kappa,\hat{c})}{\partial \kappa}\right)^{-1} \left[\frac{\partial F_x(\kappa,\hat{c})}{\partial \hat{c}_1}\dot{\hat{c}}_1 + \frac{\partial F_x(\kappa,\hat{c})}{\partial \hat{c}_3}\dot{\hat{c}}_3 + \frac{\partial F_x(\kappa,\hat{c})}{\partial \hat{c}_4}\dot{\hat{c}}_4\right] \tag{3.25}$$

where M and γ are positive constants. Note that when $\partial F_x(\kappa,\hat{c})/\partial\kappa = 0$, which is the peak point of the ($F_x(\kappa,\hat{c}) - \kappa$) curve, there occurs a singularity in **(3.25)**. This is not a concern here since it will be shown that via the selected algorithm; not exactly the peak point but a small neighborhood of the peak point will be approached. From the analytical expression of the tire force,

$$F_x(\kappa,\hat{c}) = F_z\left(\hat{c}_1 - \hat{c}_1 e^{-\hat{c}_2\kappa} - \hat{c}_3\kappa\right) = F_z\left(\hat{c}_1 - \hat{c}_4 - \hat{c}_3\kappa\right) \tag{3.26}$$

the partial derivatives for **(3.25)** are arranged as

$$\frac{\partial F_x(\kappa,\hat{c})}{\partial \kappa} = F_z\left(\hat{c}_1\hat{c}_2 e^{-\hat{c}_2\kappa} - \hat{c}_3\right) \tag{3.27}$$

$$\frac{\partial F_x(\kappa,\hat{c})}{\partial \hat{c}_1} = F_z\left(1 - e^{-\hat{c}_2\kappa}\right) \tag{3.28}$$

$$\frac{\partial F_x(\kappa,\hat{c})}{\partial \hat{c}_3} = -F_z\kappa \tag{3.29}$$

$$\frac{\partial F_x(\kappa,\hat{c})}{\partial \hat{c}_4} = -F_z \tag{3.30}$$

Inserting **(3.25)** into **(3.23)** one can get

$$\dot{s} = \frac{\partial F_x(\kappa,\hat{c})}{\partial \kappa} M \operatorname{sgn}\left[\sin\left(\frac{\pi s}{\gamma}\right)\right] - \rho \tag{3.31}$$

In **(3.31)** when the condition

$$\left|\frac{\partial F_x(\kappa,\hat{c})}{\partial \kappa}\right| M > \rho \tag{3.32}$$

holds, the change of s and $\dot{s}$ according to **(3.31)** will be similar to Figure 3.2.

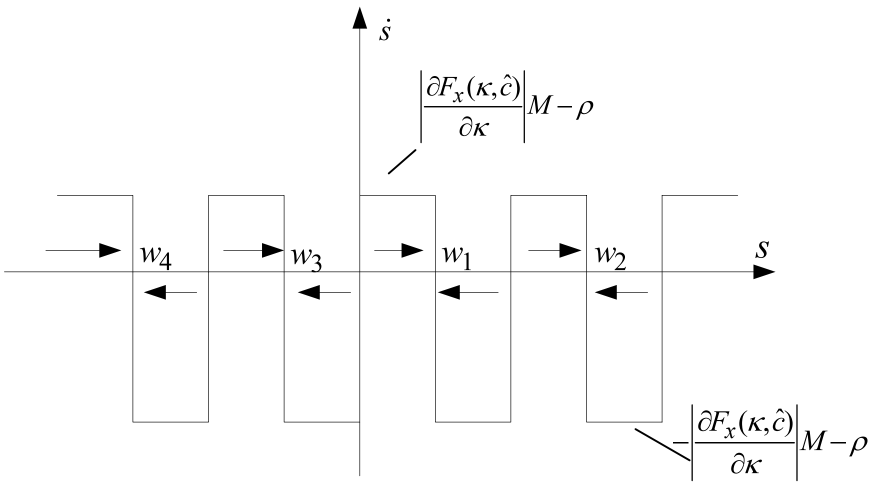

Figure 3.2 : Phase plane of s and $\dot{s}$ subject to the sliding motion dynamics.

In Figure 3.2, the arrows show the change of the variable s according to **(3.31)**. As long as the condition **(3.32)** holds, the dynamics of **(3.31)** provide that the s value will increase or decrease and after a finite time interval, s will approach one of the constant values $w_i = \gamma k$ depending on its initial value $s(0)$ where k is an integer number (0,±1,±2, ...). Unlike the classical sliding mode control theory, the sliding surface variable s will not tend to zero but to a constant value w_i (i = 1, 2, . . .). In Figure 3.2, the distance between the two grids is γ. Choosing a small γ will shorten the time interval for s to reach the constant value. From the definition of the sliding surface in **(3.22)**, after a finite time interval, when $s = w_i$ and $\dot{s} = 0$,

$$s = w_i = F_x(\kappa, \hat{c}) - \rho t \tag{3.33}$$

$$\dot{F}_x(\kappa, \hat{c}) = \rho \tag{3.34}$$

Hence, the objective function $F_x(\kappa, \hat{c})$ will increase with the slope of ρ. Note that this is accomplished when the condition **(3.22)** is satisfied. Rewriting the condition

$$\left|\frac{\partial F_x(\kappa, \hat{c})}{\partial \kappa}\right| M > \rho \tag{3.35}$$

The condition **(3.35)** can be interpreted as the gradient value $\left|\partial F_x(\kappa, \hat{c}) / \partial \kappa\right|$ being larger than a defined constant value ρ/M. As long as the gradient is higher than ρ/M, the extremum seeking algorithm will force the objective function to increase. Since $F_x(\kappa, \hat{c}) \rightarrow F_x(\kappa, c)$ is assured, $F_x(\kappa, c)$ approaches a small neighborhood of its peak point as is shown in Figure 3.3. Note that by choosing a bigger ρ, the tire force increases faster as shown in **(3.34)**. But in that case, the tire operating region will be bigger according to condition **(3.35)**, which means that the tire will operate farther than the optimum point. The braking moment is written from **(3.6)**,

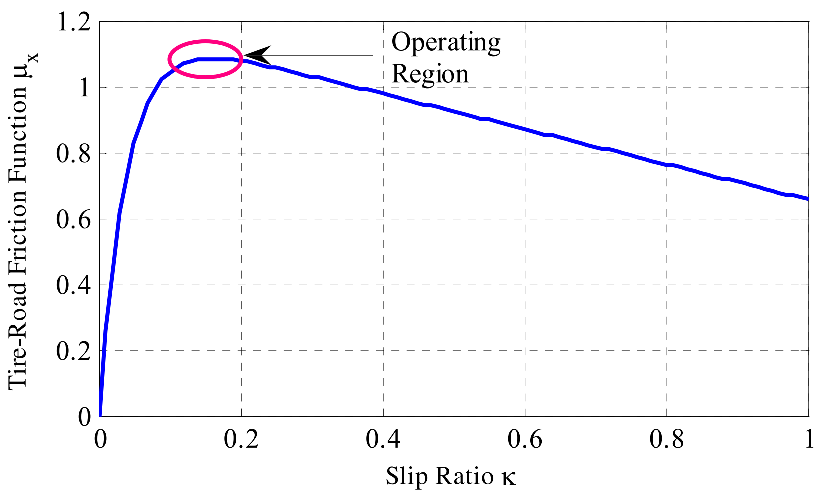

Figure 3.3 : Operating region.

$$T_b = \frac{I_\omega}{R}\left(\frac{1-\kappa}{m} + \frac{R^2}{I_\omega}\right)F_z\left(c_1 - c_1 e^{-c_2\kappa} - c_3\kappa\right) + \frac{uI_\omega}{R}\dot{\kappa} \tag{3.36}$$

Putting **(3.25)** into **(3.36)** and replacing c_1, c_2, c_3 with $\hat{c}_1, \hat{c}_2\ \hat{c}_3$ one gets the braking moment input as

$$T_b = \frac{I_\omega}{R}\left(\frac{1-\kappa}{m} + \frac{R^2}{I_\omega}\right)F_z\left(\hat{c}_1 - \hat{c}_1 e^{-\hat{c}_2\kappa} - \hat{c}_3\kappa\right) + \frac{uI_\omega}{R} M \operatorname{sgn} \sin\frac{\pi s}{\gamma}$$
$$-\frac{uI_\omega}{R}\left(\frac{\partial F_x(\kappa,\hat{c})}{\partial\kappa}\right)^{-1}\left[\frac{\partial F_x(\kappa,\hat{c})}{\partial\hat{c}_1}\dot{\hat{c}}_1 + \frac{\partial F_x(\kappa,\hat{c})}{\partial\hat{c}_3}\dot{\hat{c}}_3 + \frac{\partial F_x(\kappa,\hat{c})}{\partial\hat{c}_4}\dot{\hat{c}}_4\right] \tag{3.37}$$

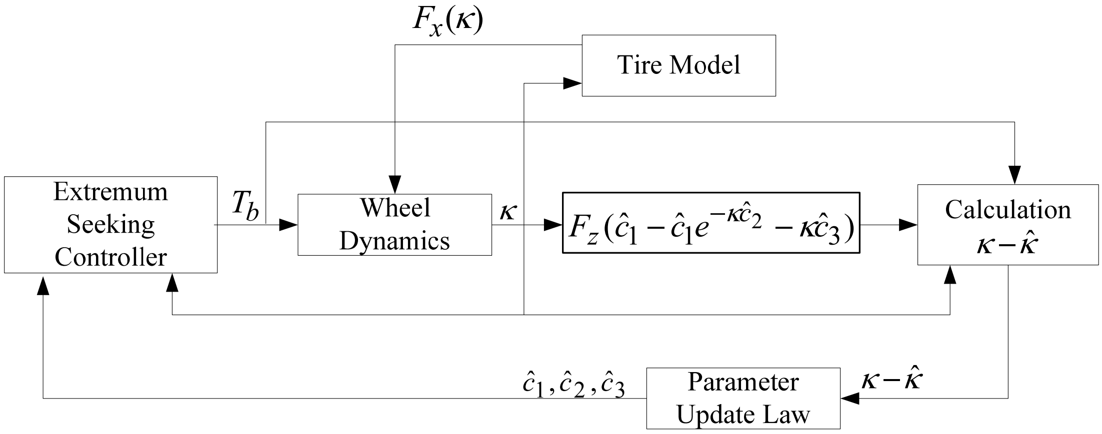

Figure 3.4 : The overall controller structure.

The overall controller structure is shown in Figure 3.4. The control algorithm is developed by using the Burckhardt tire model. In the simulations, a more complicated and detailed tire model (Magic Formula Tire Model) is used in the vehicle model, which is denoted as "Tire Model" in Figure 3.4.

3.4 Simulation Study

To be able to analyze precisely the performance of the controller, a hydraulic brake actuator model proposed in [3] composed of a master cylinder, pump, reservoir, build-dump valve pair and wheel cylinder as illustrated in Figure 3.5, is taken into account for the simulation study. To increase brake pressure and consequently brake force between the tire patch and the road, the build valve opens and the dump valve closes as the brake pad presses on the brake disc. To decrease brake pressure and the braking force, the build valve closes and the dump valve opens as the fluid flows from the wheel cylinder to the reservoir. This operation is controlled by two inputs and is governed by the following differential equation,

$$\dot{P} = \frac{\beta_f}{V_\omega} C_{dv} A c_{d1} \sqrt{\frac{2}{\rho_f}(P_p - P)} - \frac{\beta_f}{V_\omega} C_{dv} A c_{d2} \sqrt{\frac{2}{\rho_f}(P - P_{low})} \tag{3.38}$$

where β_f is brake fluid bulk modulus, V_w wheel cylinder volume, C_{dv} orifice discharge coefficient, A orifice area, ρ_f fluid density, P_p pump pressure, P wheel cylinder pressure, P_{low} reservoir pressure. c_{d1} and c_{d2} are valve control inputs, which can take the values of 1 or 0 to open or close the valves and they are not allowed to be ”1” at the same time, i.e., $c_{d1}c_{d2} \neq 1$.

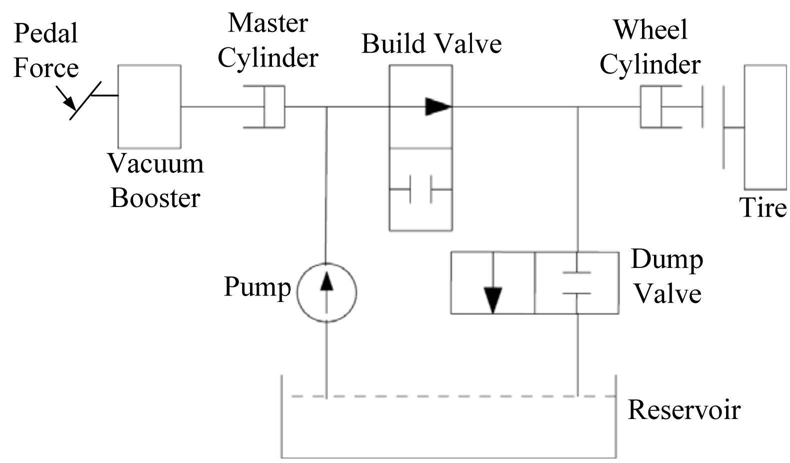

Figure 3.5 : Hydraulic brake actuator system.

For the hydraulic brake actuator, the relationship between the wheel cylinder pressure and braking moment is given as follows

$$T_b = \left(P - P_{out}\right) A_{\omega c} \eta B_F r_r \tag{3.39}$$

where P_{out} is push out pressure, A_{wc} wheel cylinder area, η mechanical efficiency, B_F brake factor, r_r effective brake disc radius. The control algorithm calculates the necessary braking moment from **(3.37)** in order to optimize braking action. Using **(3.39)**, the desired braking pressure is deduced as

$$P_{des} = P_{out} + \left(A_{\omega c} \eta B_F r_r\right)^{-1} T_b^{des} \tag{3.40}$$

Dump and build valves in the hydraulic brake system given in Figure 3.5 will be opened and closed appropriately to obtain the desired brake pressure in the wheel cylinder using pressure measurement from the pressure sensor. In the simulations, the nonlinear Magic Formula (Also known as Pacejka model) has been used as the tire model in the vehicle dynamics. The general form of the formulae given in [86] is as follows

$$\mu_x(\kappa) = D\sin[C\arctan\{B\kappa - E(B\kappa - \arctan B\kappa)\}]/F_z \tag{3.41}$$

$$F_x(\kappa) = \mu_x(\kappa)F_z \tag{3.42}$$

where B is the tire stiffness factor, C the shape factor, D the peak value, E the curvature factor In this chapter, lateral vehicle dynamics is ignored and hence only the longitudinal tire force is calculated. The tire model parameters are taken from [86] page 614 where the considered tire is 205/60R15. Simulation study has been conducted to show the performance of the proposed control algorithm. The parameters for the quarter car model are chosen as m = 200(kg), R = 0.3(m), I_ω=1(kgm^2). In the first simulation, a road where the maximum value of the tire-road friction function is μ_{max} = 0.8 is selected. During braking, the change of the tire-road friction function approaches 0.8 and this means that the maximum friction potential between the tire and the road is utilized. In Figure 3.6, change of the vehicle speed versus tire equivalent speed is plotted. The initial vehicle speed is $u(0)$ = 20(m/s).

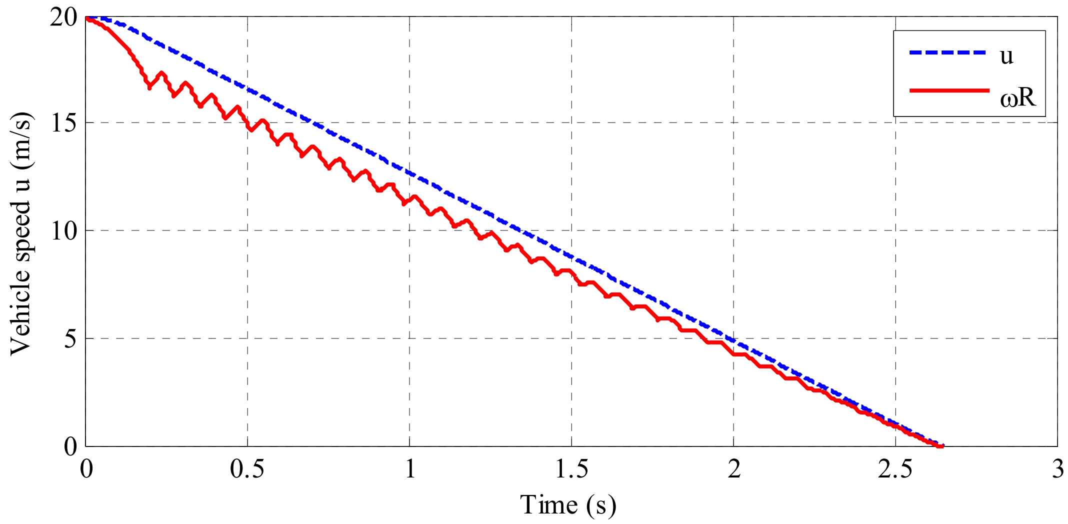

Figure 3.6 : Responses of the vehicle speed u and ωR on the road with μ_{max} = 0.8.

The tire forces are plotted in Figure 3.7 where it is shown that the tire force, used by the control algorithm, is close to the actual tire force.

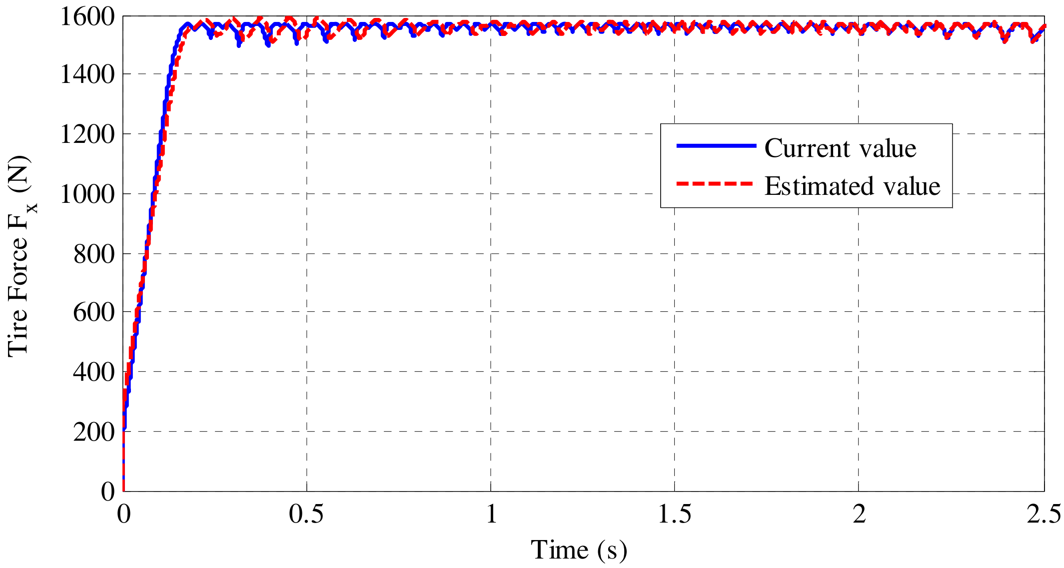

Figure 3.7 : Responses of the braking forces on the road with $\mu_{max} = 0.8$.

The response of the friction coefficient $\mu_x(\kappa)$ is plotted in Figure 3.8. It is shown that the controller manages to utilize the friction potential of the road such that the maximum attainable friction coefficient $\mu_{max} = 0.8$ is obtained.

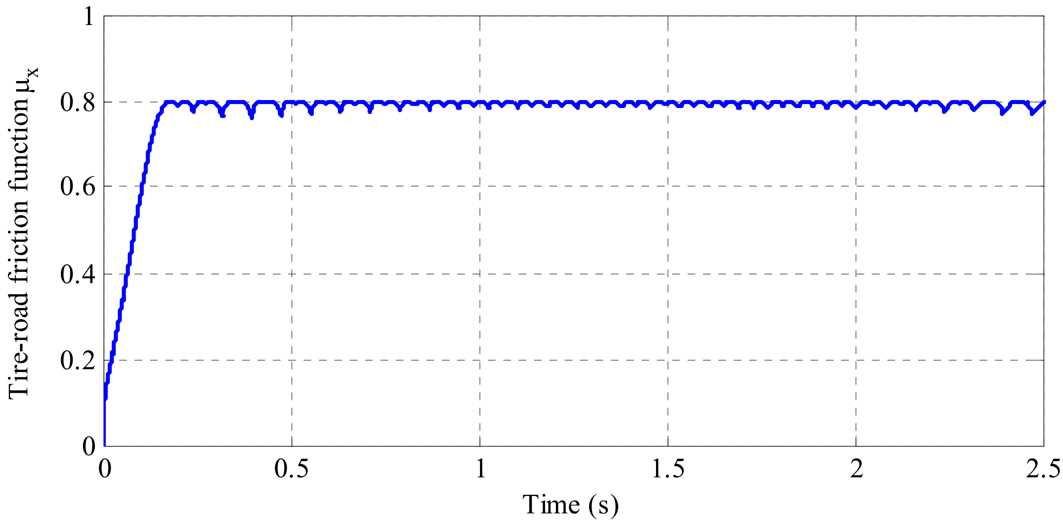

Figure 3.8 : Change of the tire-road friction function on the road with $\mu_{max} = 0.8$.

From Figure 3.9 it is shown that, slip ratio increases and then oscillates around the optimum slip value. The braking moment input calculated from the control algorithm is plotted in Figure 3.10. Due to the sign function in **(3.37)**, oscillations do take place. The factor of the sign function has the velocity value u. Since the velocity decreases during braking, the oscillations decrease with respect to the decreasing velocity.

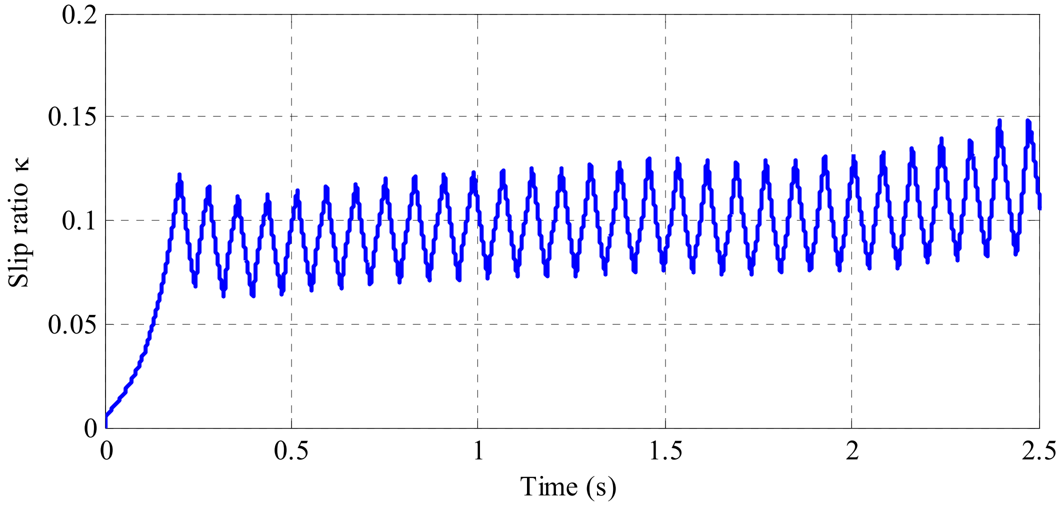

Figure 3.9 : Change of the longitudinal tire slip κ on the road with μ_{max} = 0.8.

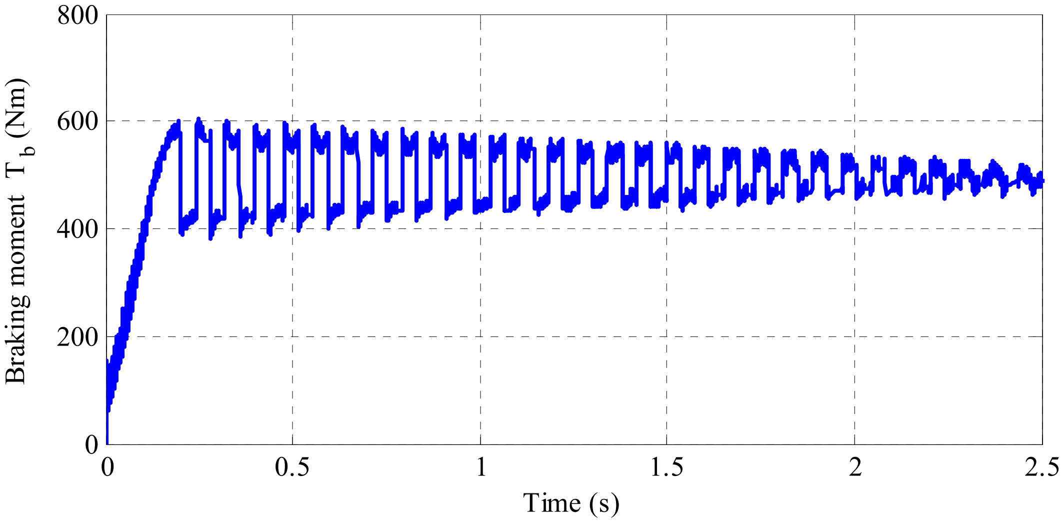

Figure 3.10 : Change of the braking moment input T_b on the road with μ_{max} = 0.8.

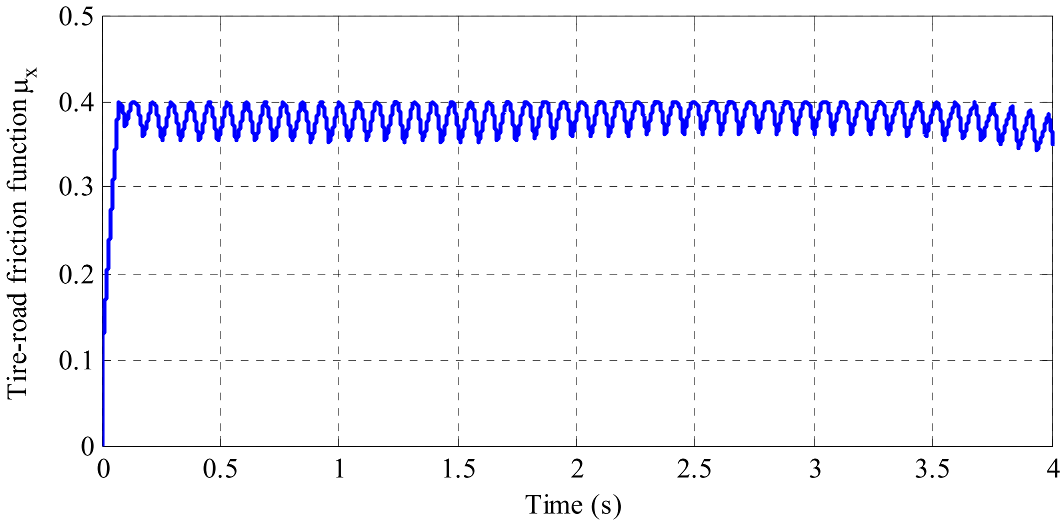

Figure 3.11 : Change of the tire road friction function on the road with μ_{max}=0.4.

To illustrate the robustness of the proposed control algorithm, different road conditions are used in simulations. The simulation scenario is conducted for a road with friction coefficient value μ_{max} = 0.4. Simulation results are shown in Figure 3.11 and Figure 3.12.

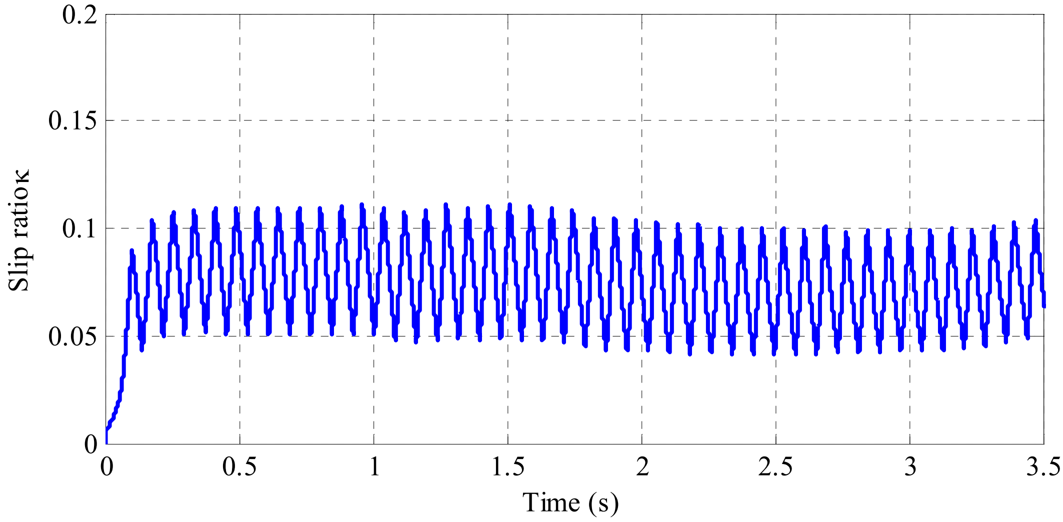

Figure 3.12 : Change of the longitudinal tire slip κ on the road with μ_{max} = 0.4.

To show that the algorithm can track the maximum tire force value when the road condition changes during braking, the simulation is conducted where the road friction changes from μ_{max} = 0.6 to μ_{max} = 1.2. From Figure 3.13 and Figure 3.14 it is realized that the control algorithm manages to utilize maximum friction potential of the road when its condition changes during braking. Braking moment input is shown in Figure 3.15.

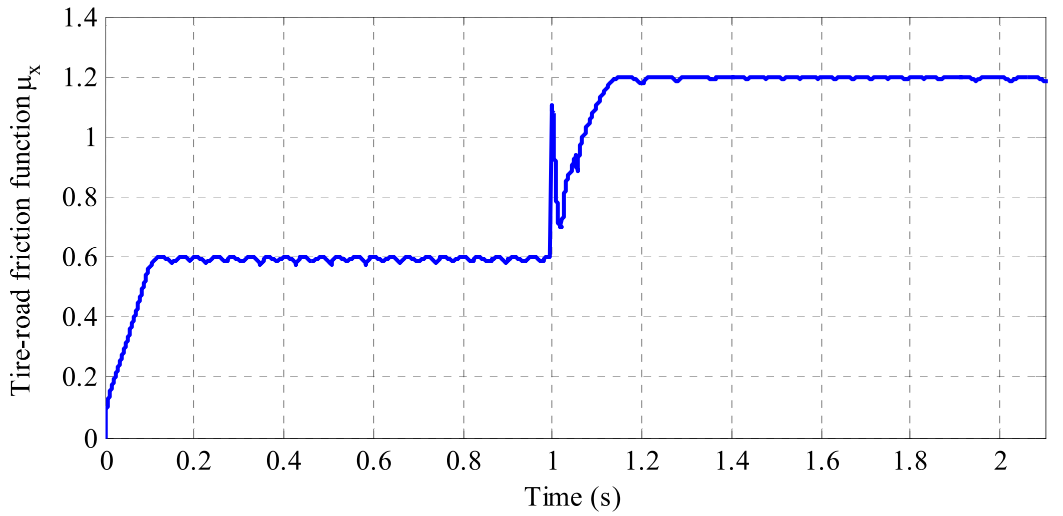

Figure 3.13 : Change of the tire road friction function when the road condition changes from μ_{max} =0.6 to μ_{max} = 1.2.

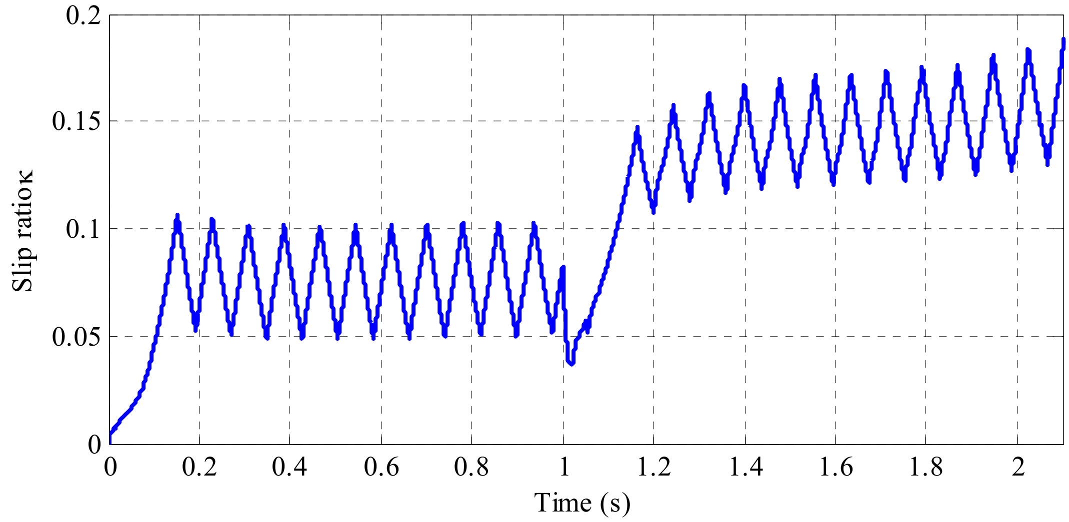

Figure 3.14 : Change of the longitudinal tire slip κ when the road condition changes from μ_{max} =0.6 to μ_{max} = 1.2.

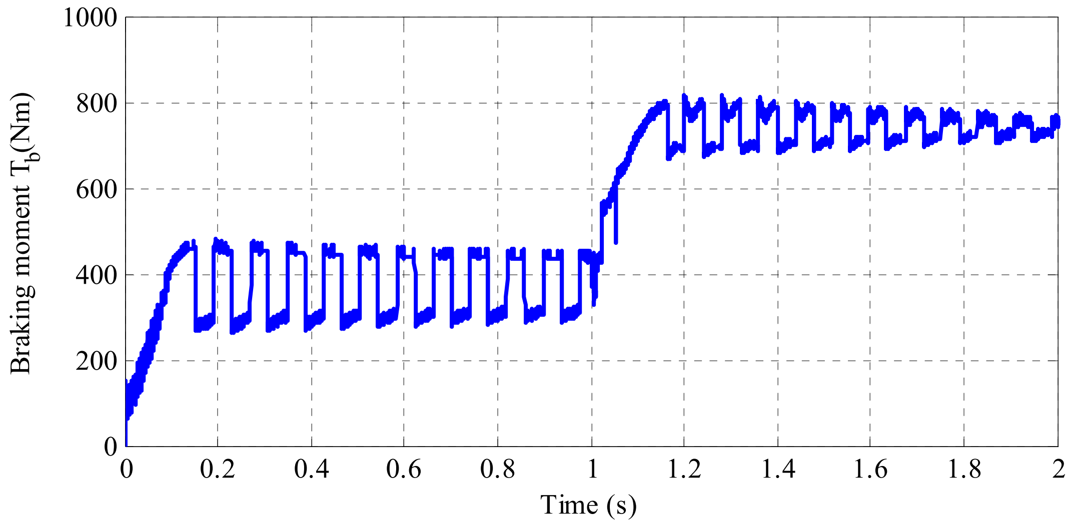

Figure 3.15 : Change of the braking moment input T_b when the road condition changes from μ_{max} =0.6 to μ_{max} = 1.2.

3.5 Real Time Simulations

Real time simulations were conducted to show the real time applicability of the proposed control algorithm. For real time simulations, dSPACE-MicroAutoBox is used. dSPACE-MicroAutoBox is a platform that can operate independently from a computer or user and can perform real time simulations. The setup is shown in Figure 3.16 and Figure 3.17.

The simulation model created with Matlab/Simulink is converted into C code by Matlab/Real-Time Workshop and then loaded into MicroAutoBox hardware. Once loaded into the platform, a real time application is created which can work independently from a computer or a user. Real time simulation results are shown in Figure 3.18 and Figure 3.19. In Figure 3.18, simulation results are shown for braking in different road conditions such as μ_{max} =0.4, μ_{max} =0.6, μ_{max} =0.8, and μ_{max} = 1. It is shown that maximum friction potential of the road is utilized in different road conditions. Figure 3.19 show that the algorithm can track maximum friction potential in changing road conditions. The sampling time used in the real time simulations was one msec.

Figure 3.16 : Setup for real time simulations.

Figure 3.17 : Power supply and MicroAutoBox.

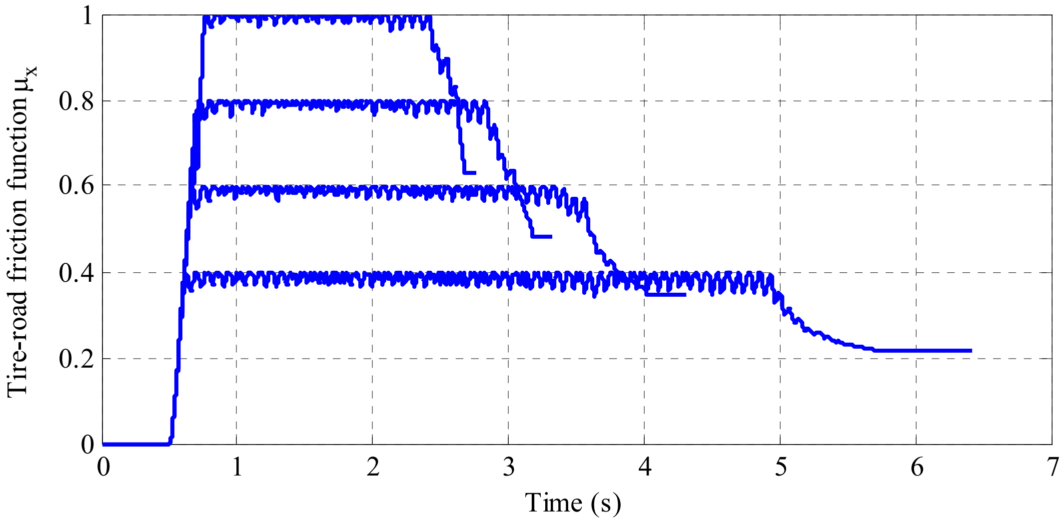

Figure 3.18 : Change of the tire road friction function in various road conditions with μ_{max} =0.4, μ_{max} =0.6, μ_{max} =0.8, and μ_{max} = 1.

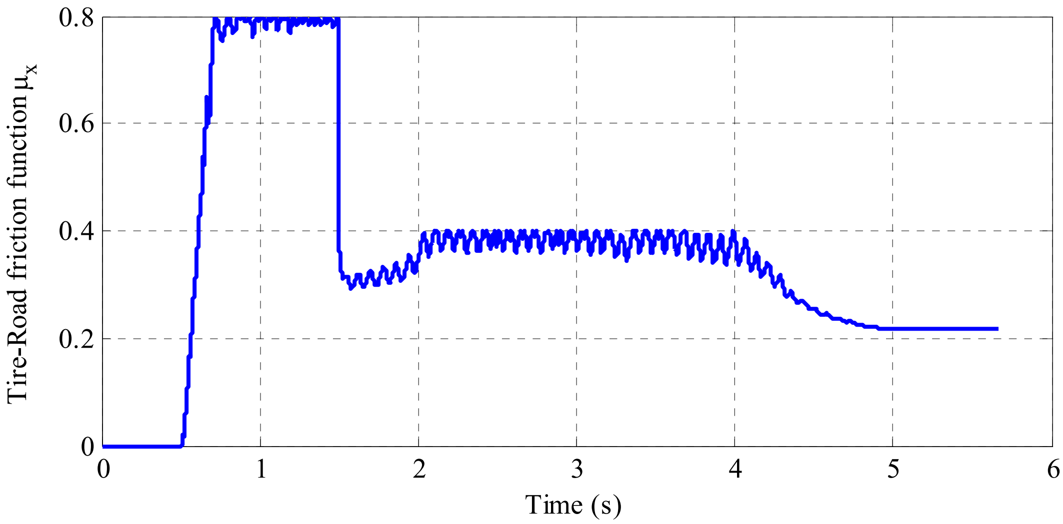

Figure 3.19 : Change of the tire road friction function when the road condition changes from μ_{max} =0.8 to μ_{max} = 0.4.

3.6 Chapter Summary

In this chapter, a control algorithm for maximizing tire braking force by combining sliding mode based extremum seeking algorithm with the adaptation of the tire model parameters was introduced. Unlike the common extremum seeking algorithms in the literature, where the black box approach is conducted by considering a completely unknown objective function, an analytic approach is performed by utilizing adaptation of the tire model parameters integrated with the self-optimization routine and hence the necessity of the online objective function measurement is removed. Simulation studies show that the proposed controller manages to maximize friction potential of the road without estimating the road conditions. The robustness of the proposed control algorithm is shown with simulations of different road conditions. Real time simulations were conducted with Microautobox hardware to show real time applicability of the proposed control algorithm.

4. ABS CONTROL ALGORITHM VIA EXTREMUM SEEKING METHOD WITH ENHANCED LATERAL STABILITY

4.1 Introduction

An ABS control algorithm based on extremum seeking is presented in this chapter. The optimum slip ratio between the tire patch and the road is searched online without having to estimate the road friction conditions. This is achieved by adapting the extremum seeking algorithm (ESA) as a self-optimization routine that seeks the peak point of the force-slip curve. As an additional novelty, the proposed algorithm incorporates driver steering input into the optimization procedure to determine the operating region of the tires on the “tire force”-“slip ratio” characteristic curve. The algorithm operates the tires near the peak point of the force-slip curve during straight line braking. When the driver demands lateral motion in addition to braking, the operating regions of the tires are modified automatically, for improving the lateral stability of the vehicle by increasing the tire lateral forces. A validated full vehicle model is presented and used in a simulation study to demonstrate the effectiveness of the proposed approach. Simulation results show the benefits of the proposed ABS controller.

When lateral and longitudinal tire forces occur simultaneously, for example during steering, achieving the maximum longitudinal tire force will result in unacceptably low lateral tire force due to the inherent coupling between tire forces in the longitudinal and lateral directions. Low lateral tire forces reduce the handling ability of a road vehicle. Therefore, longitudinal tire force should be reduced below its maximum possible value during combined braking and steering situations in order to keep lateral tire force at acceptable levels. The proposed ESA based ABS control algorithm incorporates driver steering input information into the optimization procedure to determine the operating region of the tires on the tire force-slip ratio characteristics curve. The algorithm operates the tires near the peak point of the force-slip curve during straight line braking. When the driver demands lateral motion in addition to emergency braking, the operating regions of the tires are modified for improving lateral stability of the vehicle also. It is shown that during cornering, while achieving large braking forces, lateral tire forces can be improved considerably. Hence, the cornering capability of the vehicle can be enhanced significantly. This is the main contribution of this chapter to the existing literature.

The chapter is organized as follows. In Section 4.2, the sliding mode based extremum seeking scheme is adapted for the ABS problem. Section 4.3 shows the performance of the algorithm in various road conditions during straight line braking. The simulation study is repeated for simultaneous braking and steering. It is shown that the braking algorithm can be improved for better steer ability in the presence of driver steering input. Section 4.4 presents the modification of the algorithm for improving steer ability. Simulations with the modified and unmodified algorithms are compared in Section 4.5. The chapter ends with conclusions given in Section 4.6.

4.2 Algorithm Development

Most of the available vehicle dynamics control methods assume knowledge of the road friction coefficient and ignore the braking problem complexities. Actually, for short-term emergency maneuvering tasks, or in the driver assistance proposals, braking model, road conditions, tire model and other dynamics such as hydraulics need to be taken into account.

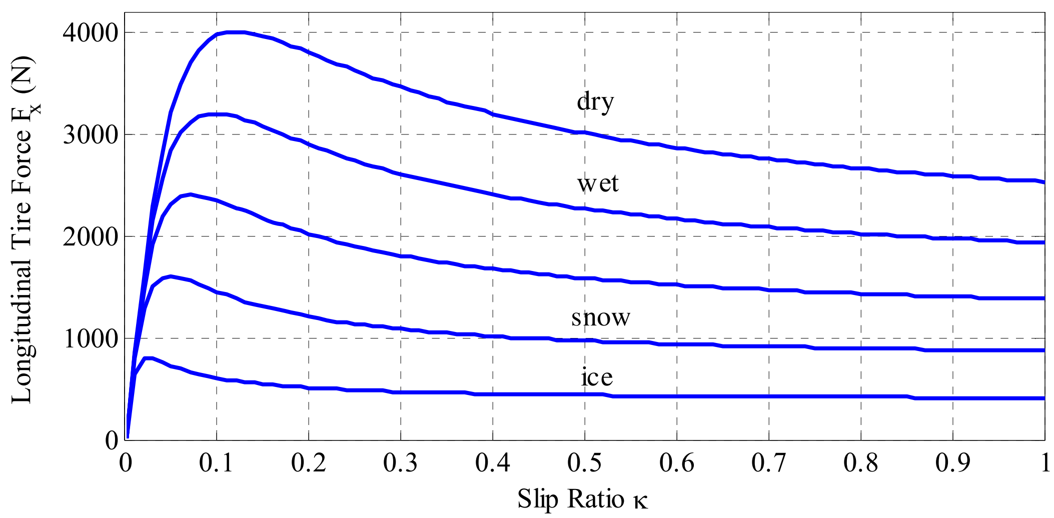

Figure 4.1 : Change of the longitudinal tire forces on different road conditions.

In ABS controller design, the aim is to find an optimal slip ratio, which makes longitudinal tire forces maximum. But since tire longitudinal forces depend on the tire/road friction coefficient, in order to find an optimum slip ratio, the friction coefficient needs to be known a priori. Maximum braking force in the longitudinal direction occurs at different slip ratios as given in Figure 4.1. Using the extremum seeking algorithm, without a priori knowledge of the friction coefficient, tire forces are maximized at the optimum slip ratio operation point and they are maintained at these desired operating points by the proper switching of the individual brake actuator control inputs.

For the extremum seeking algorithm via sliding modes, [4] formulates a sliding surface where the objective function is forced to follow a time increasing function and a discontinuous switching function is selected for the optimization parameter. This methodology is adapted here with the aim of maximizing F_{xi} for i=1,2,3,4 where *i* designates the different tires. The sliding surface variable s_i for the *i*'th tire is selected as

$$s_i = F_{xi}(\kappa_i, \alpha_i) + \rho t \tag{4.1}$$

where t is the time index, ρ is a constant value, F_{xi}, κ_i and α_i are *i*'th tire longitudinal tire force, longitudinal slip ratio and lateral side slip angle, respectively. By selecting the sliding surface as in **(4.1)**, one aims to force F_{xi} into following the time increasing function ρt. Taking the time derivative of s_i

$$\dot{s}_i = \frac{\partial F_{xi}(\kappa_i, \alpha_i)}{\partial \kappa_i}\dot{\kappa}_i + \frac{\partial F_{xi}(\kappa_i, \alpha_i)}{\partial \alpha_i}\dot{\alpha}_i + \rho \tag{4.2}$$

The update law for the slip ratio κ_i is chosen as,

$$\dot{\kappa}_i = M \operatorname{sgn}\left[\sin\left(\frac{\pi s_i}{\gamma}\right)\right] \tag{4.3}$$

where M and γ are positive constants. The function sgn is defined as

$$\operatorname{sgn}(x) = \begin{cases} 1 & \text{if } x > 0 \\ 0 & \text{if } x = 0 \\ -1 & \text{if } x < 0 \end{cases} \tag{4.4}$$

Inserting **(4.3)** into **(4.2)** one can get

$$\dot{s}_i = \frac{\partial F_{xi}(\kappa_i, \alpha_i)}{\partial \kappa_i} M \operatorname{sgn}\left[\sin\left(\frac{\pi s_i}{\gamma}\right)\right] + \frac{\partial F_{xi}(\kappa_i, \alpha_i)}{\partial \alpha_i} \dot{\alpha}_i + \rho \tag{4.5}$$

Theorem: In **(4.5)** when the condition

$$\left| \frac{\partial F_{xi}(\kappa_i, \alpha_i)}{\partial \kappa_i} \right| > \frac{\left| \frac{\partial F_{xi}(\kappa_i, \alpha_i)}{\partial \alpha_i} \dot{\alpha}_i \right|}{M} + \frac{\rho}{M} \tag{4.6}$$

holds, after a finite time interval, s_i approaches to a constant value $w = k\gamma$ depending on its initial value $s_i(0)$ where k is an integer number with $k = (0, \pm 1, \pm 2, \ldots)$. Then from **(4.1)**

$$s_i = w = F_{xi}(\kappa_i, \alpha_i) + \rho t \tag{4.7}$$

$$F_{xi}(\kappa_i, \alpha_i) = -\rho t + w \tag{4.8}$$

$$\dot{F}_{xi} = -\rho \tag{4.9}$$

Hence, braking force $F_{xi}(\kappa_i, \alpha_i)$, which is negative, will increase with the slope of ρ, i.e. tires' operating point approaches to the peak point of the force-slip curve, as long as the condition **(4.6)** holds.

Proof: Assume that at the start of optimization the value of s_i in **(4.1)** is between the values of γ and 2γ

$$\gamma < s_i(0) < 2\gamma \tag{4.10}$$

Then, on that interval, the following mathematical expression is true

$$\operatorname{sgn}\left[\sin\left(\frac{\pi s_i}{\gamma}\right)\right] = -\operatorname{sgn}(s_i - \gamma) = \operatorname{sgn}(s_i - 2\gamma) \tag{4.11}$$

Assuming that the current operating region satisfies

$$\frac{\partial F_{xi}(\kappa_i, \alpha_i)}{\partial \kappa_i} > \frac{\left| \frac{\partial F_{xi}(\kappa_i, \alpha_i)}{\partial \alpha_i} \dot{\alpha}_i \right|}{M} + \frac{\rho}{M} \tag{4.12}$$

By combining **(4.5)** and **(4.11)** one gets

$$\dot{s}_i = -\frac{\partial F_{xi}(\kappa_i,\alpha_i)}{\partial \kappa_i} M\,\mathrm{sgn}(s_i-\gamma) + \frac{\partial F_{xi}(\kappa_i,\alpha_i)}{\partial \alpha_i}\dot{\alpha}_i + \rho \tag{4.13}$$

Defining a variable λ_1 as

$$\lambda_1 = s_i - \gamma \tag{4.14}$$

$$\dot{\lambda}_1 = \dot{s}_i \tag{4.15}$$

Then from **(4.13)**

$$\dot{\lambda}_1 = -\frac{\partial F_{xi}(\kappa_i,\alpha_i)}{\partial \kappa_i} M\,\mathrm{sgn}(\lambda_1) + \frac{\partial F_{xi}(\kappa_i,\alpha_i)}{\partial \alpha_i}\dot{\alpha}_i + \rho \tag{4.16}$$

$$\lambda_1\dot{\lambda}_1 = -\frac{\partial F_{xi}(\kappa_i,\alpha_i)}{\partial \kappa_i} M|\lambda_1| + \frac{\partial F_{xi}(\kappa_i,\alpha_i)}{\partial \alpha_i}\dot{\alpha}_i\lambda_1 + \rho\lambda_1 \tag{4.17}$$

The following inequality can be written using **(4.17)**

$$\lambda_1\dot{\lambda}_1 \le -\frac{\partial F_{xi}(\kappa_i,\alpha_i)}{\partial \kappa_i} M|\lambda_1| + \left|\frac{\partial F_{xi}(\kappa_i,\alpha_i)}{\partial \alpha_i}\dot{\alpha}_i\right||\lambda_1| + \rho|\lambda_1| \tag{4.18}$$

$$\lambda_1\dot{\lambda}_1 \le -|\lambda_1|\left[\frac{\partial F_{xi}(\kappa_i,\alpha_i)}{\partial \kappa_i} M - \left|\frac{\partial F_{xi}(\kappa_i,\alpha_i)}{\partial \alpha_i}\dot{\alpha}_i\right| - \rho\right] \tag{4.19}$$

Since **(4.12)** is hypothesized, **(4.19)** can be expressed that

$$\lambda_1\dot{\lambda}_1 < 0\,;\,\lambda_1 \to 0\,;\,s_i \to \gamma \tag{4.20}$$

Hence, after a finite time interval, (Finite time; because of the discontinuous sign function)

$$s_i = \gamma \tag{4.21}$$

Contrary to **(4.12)**, if the current operating region satisfies

$$\frac{\partial F_{xi}(\kappa_i,\alpha_i)}{\partial \kappa_i} < -\frac{\left|\frac{\partial F_{xi}(\kappa_i,\alpha_i)}{\partial \alpha_i}\dot{\alpha}_i\right|}{M} - \frac{\rho}{M} \qquad \textbf{(4.22)}$$

then from **(4.5)** and **(4.11)**

$$\dot{s}_i = \frac{\partial F_{xi}(\kappa_i,\alpha_i)}{\partial \kappa_i} M\,\mathrm{sgn}(s_i - 2\gamma) + \frac{\partial F_{xi}(\kappa_i,\alpha_i)}{\partial \alpha_i}\dot{\alpha}_i + \rho \qquad \textbf{(4.23)}$$

Defining λ_2 as

$$\lambda_2 = s_i - 2\gamma \qquad \textbf{(4.24)}$$

$$\dot{\lambda}_2 = \dot{s}_i \qquad \textbf{(4.25)}$$

From **(4.23)**

$$\dot{\lambda}_2 = \frac{\partial F_{xi}(\kappa_i,\alpha_i)}{\partial \kappa_i} M\,\mathrm{sgn}(\lambda_2) + \frac{\partial F_{xi}(\kappa_i,\alpha_i)}{\partial \alpha_i}\dot{\alpha}_i + \rho \qquad \textbf{(4.26)}$$

$$\lambda_2\dot{\lambda}_2 = \frac{\partial F_{xi}(\kappa_i,\alpha_i)}{\partial \kappa_i} M|\lambda_2| + \frac{\partial F_{xi}(\kappa_i,\alpha_i)}{\partial \alpha_i}\dot{\alpha}_i\lambda_2 + \rho\lambda_2 \qquad \textbf{(4.27)}$$

$$\lambda_2\dot{\lambda}_2 \le \frac{\partial F_{xi}(\kappa_i,\alpha_i)}{\partial \kappa_i} M|\lambda_2| + \left|\frac{\partial F_{xi}(\kappa_i,\alpha_i)}{\partial \alpha_i}\dot{\alpha}_i\right||\lambda_2| + \rho|\lambda_2| \qquad \textbf{(4.28)}$$

$$\lambda_2\dot{\lambda}_2 \le |\lambda_2|\left[\frac{\partial F_{xi}(\kappa_i,\alpha_i)}{\partial \kappa_i} M + \left|\frac{\partial F_{xi}(\kappa_i,\alpha_i)}{\partial \alpha_i}\dot{\alpha}_i\right| + \rho\right] \qquad \textbf{(4.29)}$$

Since **(4.22)** is hypothesized,

$$\lambda_2\dot{\lambda}_2 < 0\,;\lambda_2 \to 0\,; s_i \to 2\gamma \qquad \textbf{(4.30)}$$

Hence after a finite time interval

$$s_i = 2\gamma \qquad \textbf{(4.31)}$$

It has been shown that when the value of s_i starts between $\gamma < s_i(0) < 2\gamma$, then it converges to either γ or 2γ depending on whether **(4.12)** or **(4.22)** holds. This analysis can be generalized not only for the interval of $\gamma < s_i(0) < 2\gamma$ but for any starting point $s_i(0)$. By combining the conditions **(4.12)** and **(4.22)**, it is concluded that as long as the condition

$$\left|\frac{\partial F_{xi}(\kappa_i,\alpha_i)}{\partial \kappa_i}\right| > \frac{\left|\frac{\partial F_{xi}(\kappa_i,\alpha_i)}{\partial \alpha_i}\dot{\alpha}_i\right|}{M} + \frac{\rho}{M} \qquad \textbf{(4.32)}$$

holds s_i will converge to one of the following points

$$s_i = k\gamma \qquad (k = 0, \pm 1, \pm 2, \ldots) \qquad \textbf{(4.33)}$$

After s_i converges to $k\gamma$, equation **(4.1)** becomes

$$s_i = k\gamma = F_{xi}(\kappa_i,\alpha_i) + \rho t \qquad \textbf{(4.34)}$$

$$F_{xi}(\kappa_i,\alpha_i) = -\rho t + k\gamma \qquad \textbf{(4.35)}$$

$$\dot{F}_{xi}(\kappa_i,\alpha_i) = -\rho \qquad \textbf{(4.36)}$$

Hence, braking force $F_{xi}(\kappa_i,\alpha_i)$ will increase with the slope of ρ converging to the maximum operating point. Choosing a bigger ρ will ensure approaching to the optimum point faster. **(End of proof)**

When both **(4.12)** and **(4.22)** do not hold, increasing of the performance function is not guaranteed. By selecting the values of control parameters ρ and M, one defines the operating region of the ESA. By decreasing the size of the region where **(4.12)** and **(4.22)** do not hold, the success of the optimization algorithm is increased.

Considering the straight line braking case where $\alpha_i = 0$ for i=1, 2, 3, 4, then the condition **(4.32)** turns into

$$\left|\frac{dF_{xi}(\kappa_i)}{d\kappa_i}\right| > \frac{\rho}{M} \qquad \textbf{(4.37)}$$

The condition **(4.37)** can be interpreted as the gradient value $\left|dF_{xi}(\kappa_i)/d\kappa_i\right|$ being larger than a constant value ρ/M. As long as the gradient is larger than ρ/M, extremum seeking algorithm will force the objective function to increase. Finally, F_{xi} will approach to a small neighborhood of its peak point where the gradient is not large enough, i.e. the condition **(4.37)** does not hold anymore. By selecting proper values for ρ and M, the size of the operating region can be adjusted.

When there is a lateral motion, then the condition **(4.32)** includes an additional term of $\left|(\partial F_{xi}(\kappa_i,\alpha_i)/\partial\alpha_i)\dot{\alpha}_i\right|/M$ in the right hand side of the inequality. The effect of this additional term on the search algorithm is explained in the following. When there is a lateral motion, i.e. $\dfrac{\partial F_{xi}(\kappa_i,\alpha_i)}{\partial\alpha_i}\dot{\alpha}_i \neq 0$, then the right hand side of **(4.32)** increases. This results in condition **(4.32)** holding for a shorter time than the case without lateral motion. This is because by approaching to the peak point of the force-slip curve, the gradient $\left|\partial F_{xi}(\kappa_i,\alpha_i)/\partial\kappa_i\right|$ is getting smaller and smaller, and the region, where the condition **(4.32)** does not hold, is approached more quickly. When the condition holds shorter, the increment of F_{xi} lasts shorter. In other words, the tire will operate further than its maximum force value. This is advantageous since as far as the tires operate further than the maximum point, i.e. when the slip ratio is kept small, lateral tire forces will be large, which increases cornering capability of the vehicle.

Braking moment values T_{bi} are calculated as follows. The simplified tire rotational equation of motion can be written as

$$\dot{\omega}_i = \frac{-T_{bi} - RF_{xi}}{I_\omega} \tag{4.38}$$

where the rolling resistance effect is neglected. In **(4.38)**, I_ω is the wheel inertia, R is the effective tire radius, ω_i is the i'th tire angular velocity. Similarly, the simplified longitudinal vehicle dynamics is written as

$$m\dot{u} = F_{xsum} = F_{x1} + F_{x2} + F_{x3} + F_{x4} \tag{4.39}$$

where aerodynamic effects and lateral dynamics are ignored. In **(4.39)**, m is the vehicle mass and u is the longitudinal speed. The simplified equation of the wheel slip ratio is given as

$$\kappa_i = -\frac{u - \omega_i R}{u} \tag{4.40}$$

where it is assumed that the tire velocities on rolling directions are equal to the vehicle longitudinal velocity u. Taking the time-derivative of **(4.40)** and integrating with **(4.38)** and **(4.39)** the slip dynamics can be written as

$$\dot{\kappa}_i = \frac{1}{u}\left(-\frac{F_{xsum}}{m} - \frac{RT_{bi}}{I_\omega} - \frac{R^2 F_{xi}}{I_\omega} - \frac{F_{xsum}}{m}\kappa_i \right) \tag{4.41}$$

By inserting for $\dot{\kappa}_i$ its update law, the braking moment for each tire can be computed as

$$T_{bi} = -\frac{I_\omega}{R}(\kappa_i + 1)\frac{F_{xsum}}{m} - RF_{xi} - \frac{I_\omega}{R}uM\,\mathrm{sgn}\left[\sin\left(\frac{\pi s_i}{\gamma}\right)\right] \tag{4.42}$$

For calculation of the braking moment from **(4.42)**, one should measure u, ω_i, and F_{xi}. It is assumed that u and ω_i are measured. The velocity of the car u can be measured via the accelerometer and GPS units or by using the tire velocities of the idle tires. Tire angular velocity can be measured by using the Hall Effect wheel speed sensors in the ABS system. Since tire forces cannot be measured directly, they should be estimated. Estimation of the tire longitudinal forces are based on tire angular velocity measurements as introduced in [3]. The simplified tire dynamics is written as

$$I_\omega \dot{\omega}_i = -T_{bi} - RF_{xi} \tag{4.43}$$

Estimation of the tire angular velocity $\hat{\omega}_i$ is defined as

$$I_\omega \dot{\hat{\omega}}_i = -T_{bi} + W\,\mathrm{sgn}(\overline{\omega}_i)R \tag{4.44}$$

where $\overline{\omega}_i = \omega_i - \hat{\omega}_i$ and W is a positive constant. Subtracting **(4.44)** from **(4.43)**, one can get

$$I_{\omega}\dot{\overline{\omega}}_i = -W\,\mathrm{sgn}(\overline{\omega}_i)R - F_{xi}R \tag{4.45}$$

By choosing W>max|F_{xi}|, the estimated state $\hat{\omega}_i$ tracks the real state ω_i, due to the discontinuous feedback in the observer equation. In the sliding mode, the equivalent value of $K\,\mathrm{sgn}(\overline{\omega}_i)$ is equal to the longitudinal tire force,

$$\hat{F}_{xi} = -(W\,\mathrm{sgn}(\overline{\omega}_i))_{eq} \tag{4.46}$$

To obtain the equivalent value of $W\,\mathrm{sgn}(\overline{\omega}_i)$ during sliding mode, a low pass filter is used. Using the estimated tire force $\hat{F}_{xi}$, the braking moment T_{bi} is calculated as

$$T_{bi} = -\frac{I_{\omega}}{R}(\kappa_i + 1)\frac{\hat{F}_{xsum}}{m} - R\hat{F}_{xi} - \frac{I_{\omega}}{R}uM\,\mathrm{sgn}\left[\sin\left(\frac{\pi s_i}{\gamma}\right)\right] \tag{4.47}$$

Note that s_i is defined previously in **(4.1)**. Since the estimated value of the tire force is used, s_i is calculated from

$$s_i = \hat{F}_{xi} + \rho t \tag{4.48}$$

4.3 Simulations

4.3.1 Simulation model

A validated nonlinear double track vehicle model is considered in the simulation study. The vehicle axis system is shown in Figure 4.2. Here, x is roll axis, y is pitch axis and z is yaw axis.

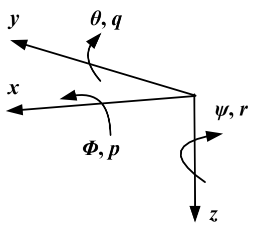

Figure 4.2 : Vehicle axis system.

The vehicle parameter values are given in Table 4.1. Top view of the vehicle model is shown in Figure 4.3.

Table 4.1 : Vehicle parameter values.

Parameter	Value	Parameter	Value
m (kg)	1590	K_f (kg/s^2)	30000
m_s (kg)	1410	K_r (kg/s^2)	20000
m_u (kg)	180	C_f (kg/s)	2206
l_f (m)	1.01	C_r (kg/s)	2206
l_r (m)	1.45	C_d	0.4
T_s (m)	0.8	A_f (m^2)	1.8
R (m)	0.3	ρ_a (kg/m^3)	1.2257
d (m)	0.0045	l_ω (m)	1.54
I_ω (kgm^2)	0.9	K_{rbf} (kgm^2/s^2)	10000
e (m)	0.26	K_{rbr} (kgm^2/s^2)	10000
I_Z (kgm^2)	2910	p_f (m)	0.277
I_{ZS} (kgm^2)	2810	p_r (m)	0.286
I_X (kgm^2)	700	h_f (m)	0.277
I_{XS} (kgm^2)	606	h_r (m)	0.286
I_Y (kgm^2)	2800	k_t (kg/s^2)	220000
I_{YS} (kgm^2)	2741		

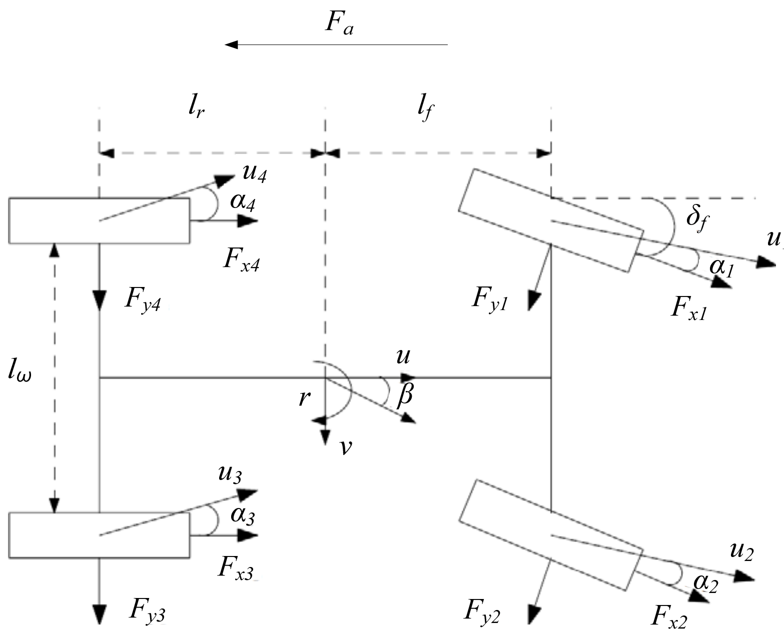

Figure 4.3 : Top view of the vehicle.

$$m_s a_{xs} + m_u a_{xu} = F_x - F_a \tag{4.49}$$

$$m_s a_{ys} + m_u a_{yu} = F_y \tag{4.50}$$

The longitudinal and lateral dynamic equations are written as in **(4.49)** and **(4.50)** where m_s, a_{xs}, m_u, a_{xu}, F_x, F_a, a_{ys}, a_{yu}, F_y are sprung mass, sprung mass longitudinal acceleration, unsprung mass, unsprung mass longitudinal acceleration, total longitudinal tire forces, aerodynamic drag force, lateral acceleration of the sprung mass, lateral acceleration of the unsprung mass and the total lateral tire forces, respectively. Unsprung mass and sprung mass longitudinal accelerations are given in **(4.51)** and **(4.52)**. Unsprung mass and sprung mass lateral accelerations are given in **(4.53)** and **(4.54)**. Detailed derivation of these acceleration terms are given in Appendix A.

$$a_{xu} = \dot{u} - vr \tag{4.51}$$

$$a_{xs} = \dot{u} - vr + \dot{q}z_s - \dot{q}e - rpz_s + rpe + 2q\dot{z}_s \tag{4.52}$$

$$a_{yu} = \dot{v} + ur \tag{4.53}$$

$$a_{ys} = \dot{v} + ur + \dot{p}z_s - \dot{p}e + rqz_s - rqe + 2p\dot{z}_s \tag{4.54}$$

where v, r, q, z_s, e, p denote lateral velocity, yaw rate of the vehicle, pitch rate, vertical motion of the sprung mass center of gravity (c.g.), distance from the roll center to the sprung mass c.g. and the roll rate, respectively. Total longitudinal and lateral tire forces are calculated by referring to Figure 4.3 as follows

$$F_x = (F_{x1} + F_{x2})\cos\delta_f - (F_{y1} + F_{y2})\sin\delta_f + F_{x3} + F_{x4} \tag{4.55}$$

$$F_y = (F_{x1} + F_{x2})\sin\delta_f + (F_{y1} + F_{y2})\cos\delta_f + F_{y3} + F_{y4} \tag{4.56}$$

The aerodynamic drag force F_a is calculated as follows

$$F_a = \frac{1}{2} C_d A_f \rho_a u^2 \tag{4.57}$$

Here C_d, A_f, ρ_a, are the aerodynamic drag coefficient, the vehicle frontal area, the air density, respectively.

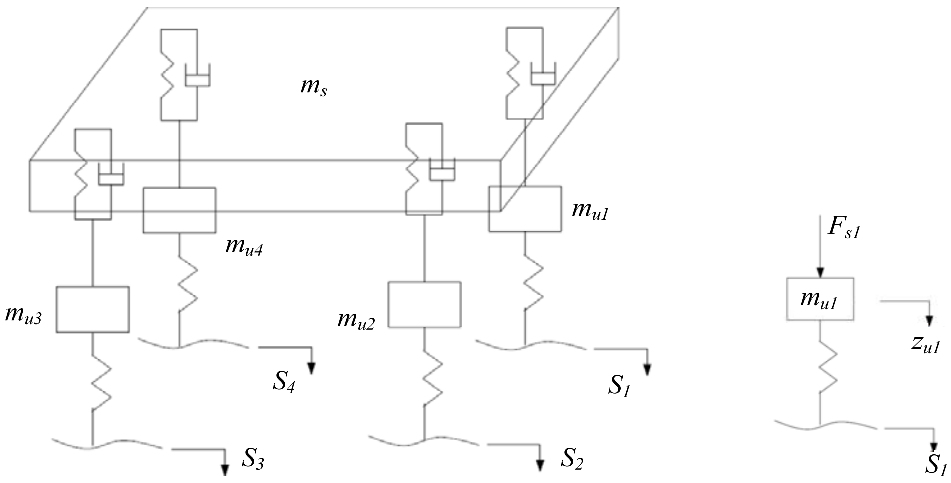

Figure 4.4 : Vehicle suspension model.

The vehicle suspension model is shown in Figure 4.4. The vertical equation of motion of the sprung mass and unsprung mass are written as

$$m_s a_{zs} = -(F_{s1} + F_{s2} + F_{s3} + F_{s4}) \tag{4.58}$$

$$m_{ui}\ddot{z}_{ui} + k_t(z_{ui} - S_i) - F_{si} = 0 \tag{4.59}$$

Here a_{zs} is the vertical acceleration of the sprung mass. F_{si} are the suspension forces acting on the sprung mass, k_t is the tire stiffness and S_i are the road inputs for each tire. The vertical acceleration of the sprung mass is calculated as

$$a_{zs} = \ddot{z}_u - p^2 z_s + p^2 e - q^2 z_s + q^2 e + \ddot{z}_s \tag{4.60}$$

Detailed derivation of this term is given in Appendix A. Here z_u is the vertical motion of the unsprung mass c.g. The suspension forces are given as

$$F_{s1} = K_f\left(z_s - l_f \sin\theta + \frac{T_s}{2}\sin\phi - z_{u1}\right) + C_f\left(\dot{z}_s - l_f \cos\theta\dot{\theta} + \frac{T_s}{2}\cos\phi\dot{\phi} - \dot{z}_{u1}\right) \tag{4.61}$$

$$F_{s2} = K_f\left(z_s - l_f \sin\theta - \frac{T_s}{2}\sin\phi - z_{u2}\right) + C_f\left(\dot{z}_s - l_f \cos\theta\dot{\theta} - \frac{T_s}{2}\cos\phi\dot{\phi} - \dot{z}_{u2}\right) \tag{4.62}$$

$$F_{s3} = K_r\left(z_s + l_r \sin\theta - \frac{T_s}{2}\sin\phi - z_{u3}\right) + C_r\left(\dot{z}_s + l_r \cos\theta\dot{\theta} - \frac{T_s}{2}\cos\phi\dot{\phi} - \dot{z}_{u3}\right) \tag{4.63}$$

$$F_{s4} = K_r\left(z_s + l_r \sin\theta + \frac{T_s}{2}\sin\phi - z_{u4}\right) + C_r\left(\dot{z}_s + l_r \cos\theta\dot{\theta} + \frac{T_s}{2}\cos\phi\dot{\phi} - \dot{z}_{u4}\right) \tag{4.64}$$

where K_f and K_r are front and rear suspension spring stiffness, C_f and C_r are front and rear suspension damping ratios, z_{ui} is the unsprung mass vertical motions. l_f and l_r are distances from the center of gravity to the front and rear axles, θ is the pitch angle, Φ is the roll angle, T_s is the distance between the left and right suspensions.

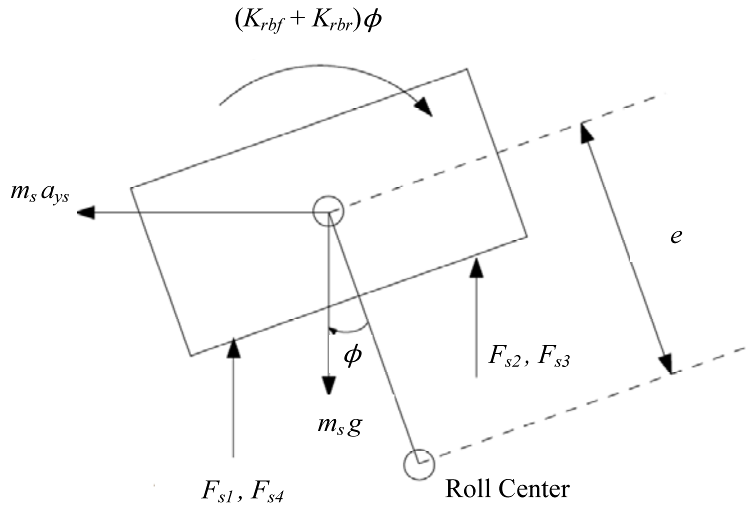

Figure 4.5 : Roll motion of the sprung mass.

In Figure 4.5, roll motion of the sprung mass is shown. The rotational equations of motions are written as follows which are known as Euler equations of motion [88]

$$I_{XS}(-\dot{p}) - (I_{YS} - I_{ZS})(q)(r) = \\ (F_{s1} + F_{s4})\frac{T_s}{2} - (F_{s2} + F_{s3})\frac{T_s}{2} - m_s ge\sin\phi - m_s a_{ys} e\cos\phi + (K_{rbf} + K_{rbr})\phi \tag{4.65}$$

$$I_{YS}(\dot{q}) - (I_{ZS} - I_{XS})(r)(-p) = \\ (F_{s1} + F_{s2})l_f - (F_{s3} + F_{s4})l_r + m_s ge\sin\theta + m_s a_{xs} e\cos\theta \tag{4.66}$$

$$I_Z(\dot{r}) - (I_X - I_Y)(-p)(q) = \left((F_{x1} - F_{x2})\cos\delta_f - (F_{y1} - F_{y2})\sin\delta_f\right)\frac{l_\omega}{2} \\ + \left((F_{x1} + F_{x2})\sin\delta_f + (F_{y1} + F_{y2})\cos\delta_f\right)l_f + (F_{x4} - F_{x3})\frac{l_\omega}{2} - (F_{y3} + F_{y4})l_r \tag{4.67}$$

where I_{XS}, I_{YS}, I_{ZS} , I_Z, I_X, I_Y are sprung mass moment of inertias on the roll axis, pitch axis, yaw axis, total moment of inertias on the yaw axis, roll axis and pitch axis, respectively. l_ω is the front and rear track widths, g is the acceleration due to the gravity, K_{rbf} and K_{rbr} are front and rear antiroll bar stiffness's.

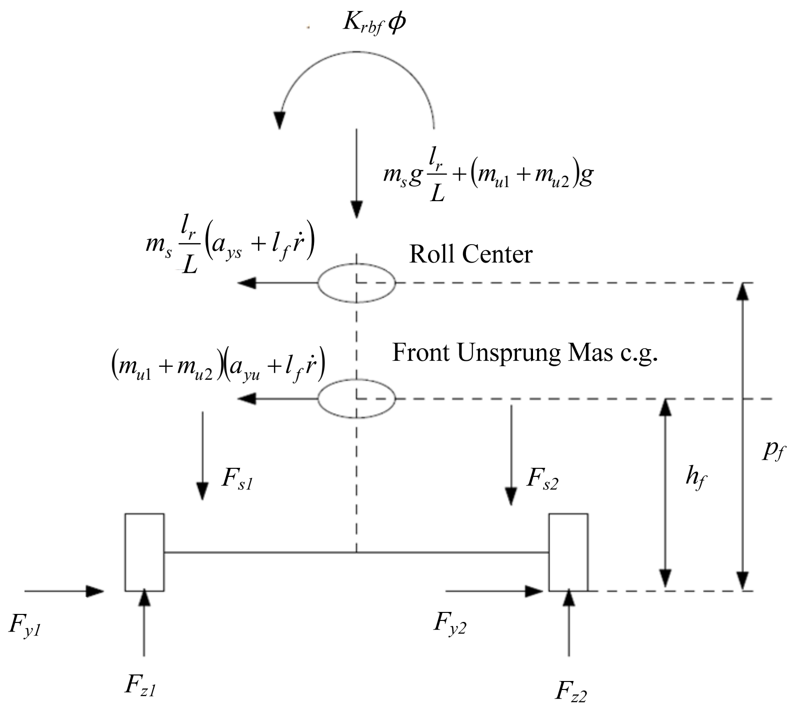

Figure 4.6 : Forces and moments acting on the front axle.

In Figure 4.6, forces and moment acting on the front axle are shown. Vertical forces for each tire are calculated as follows

$$F_{z1} = \begin{bmatrix} F_{s2}(l_\omega/2 - T_s/2) + F_{s1}(l_\omega/2 + T_s/2) + (m_s g l_r/L + (m_{u1} + m_{u2})g)l_\omega/2 \\ + K_{rbf}\phi + m_s l_r/L(a_{ys} + l_f\dot{r})p_f + (m_{u1} + m_{u2})(a_{yu} + l_f\dot{r})h_f \end{bmatrix} / l_\omega \quad \textbf{(4.68)}$$

$$F_{z2} = \begin{bmatrix} F_{s2}(l_\omega/2 + T_s/2) + F_{s1}(l_\omega/2 - T_s/2) + (m_s g l_r/L + (m_{u1} + m_{u2})g)l_\omega/2 \\ - K_{rbf}\phi - m_s l_r/L(a_{ys} + l_f\dot{r})p_f - (m_{u1} + m_{u2})(a_{yu} + l_f\dot{r})h_f \end{bmatrix} / l_\omega \quad \textbf{(4.69)}$$

$$F_{z3} = \begin{bmatrix} F_{s3}(l_\omega/2 + T_s/2) + F_{s4}(l_\omega/2 - T_s/2) + (m_s g l_f/L + (m_{u3} + m_{u4})g)l_\omega/2 \\ - K_{rbr}\phi - m_s l_f/L(a_{ys} - l_r\dot{r})p_r - (m_{u3} + m_{u4})(a_{yu} - l_r\dot{r})h_r \end{bmatrix} / l_\omega \quad \textbf{(4.70)}$$

$$F_{z4} = \begin{bmatrix} F_{s3}(l_\omega/2 - T_s/2) + F_{s4}(l_\omega/2 + T_s/2) + (m_s g l_f/L + (m_{u3} + m_{u4})g)l_\omega/2 \\ + K_{rbr}\phi + m_s l_f/L(a_{ys} - l_r\dot{r})p_r + (m_{u3} + m_{u4})(a_{yu} - l_r\dot{r})h_r \end{bmatrix} / l_\omega \quad \textbf{(4.71)}$$

where L is the distance between the front and rear axles, p_f and p_r are height of the front and rear roll center, h_f and h_r are height of the front and rear unsprung mass c.g.

By referring to Figure 4.3, it is shown that, while the vehicle is turning, a difference occurs between the direction of the tire velocity and the direction of the tire itself. This angle is called as the tire side slip angle or simply ”the slip angle” denoted as α_i. Tire slip angles are calculated as follows

$$\alpha_1 = \delta_f - \tan^{-1}\left(\frac{v + rl_f}{u + rl_\omega / 2}\right) \tag{4.72}$$

$$\alpha_2 = \delta_f - \tan^{-1}\left(\frac{v + rl_f}{u - rl_\omega / 2}\right) \tag{4.73}$$

$$\alpha_3 = -\tan^{-1}\left(\frac{v - rl_r}{u - rl_\omega / 2}\right) \tag{4.74}$$

$$\alpha_4 = -\tan^{-1}\left(\frac{v - rl_r}{u + rl_\omega / 2}\right) \tag{4.75}$$

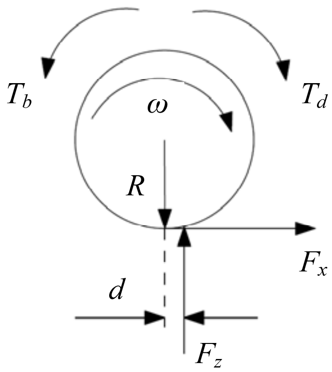

Figure 4.7 : Forces and moments acting on the wheel.

In Figure 4.7, forces and moments acting on a single wheel are shown. Rotational motion dynamics for each individual tire are given as

$$\dot{\omega}_i = \frac{T_{di} - T_{bi} - RF_{xi} - dF_{zi}}{I_w} \tag{4.76}$$

where ω_i denotes the *i*-th tire angular velocity, T_{di} is the traction moment, T_{bi} is the individual wheel braking moment, F_{zi} is the tire vertical force, I_ω is the wheel inertia and d is the pneumatic trail as shown in Figure 4.7.

When the vehicle accelerates or brakes, a difference between the tire longitudinal velocity u_{ti} and its corresponding rotational velocity $\omega_i R$ occurs. The tire longitudinal slip ratio or simply ”slip ratio” is defined based on this difference and calculated as

$$\kappa_i = -\frac{u_{ti} - \omega_i R}{u_{ti}} \tag{4.77}$$

where R is the tire effective radius, u_{ti} is the velocity on the rolling direction for the i'th individual tire. For example in a hard braking situation, if the tires are blocked (ω_i=0) but the vehicle is still moving ($u_{ti} \neq 0$), then κ_i=-1. On the contrary, in acceleration from standstill, if the tires start to spin, then $\kappa_i > 0$. In **(4.77)**, u_{ti} is calculated as follows

$$u_{t1} = (u + rl_\omega / 2)\cos\delta_f + (v + rl_f)\sin\delta_f \qquad \textbf{(4.78)}$$

$$u_{t2} = (u - rl_\omega / 2)\cos\delta_f + (v + rl_f)\sin\delta_f \qquad \textbf{(4.79)}$$

$$u_{t3} = (u - rl_\omega / 2) \qquad \textbf{(4.80)}$$

$$u_{t4} = (u + rl_\omega / 2) \qquad \textbf{(4.81)}$$

The longitudinal and lateral tire forces are changing with respect to the magnitudes of the tire slip ratio and the tire slip angle. Various analytic and empirical tire models have been developed in the literature for simulating tire forces. Some of them are the Magic Formula, Dugoff, LuGre, Burckhardt tire models. Here, for calculation of the tire forces, the Magic Formula (Also known as the Pacejka model) is used in the simulations. The general form of the formula is given as

$$y = D\sin[C\arctan\{Bx - E(Bx - \arctan Bx)\}] \qquad \textbf{(4.82)}$$

where x is the input variable such as the tire slip angle α or the tire slip ratio κ, y is the output variable representing the forces between the tire patches and the road in the longitudinal and lateral directions such as F_x and F_y. B, C, D and E are the tire stiffness, shape, peak and curvature factors, respectively. The tire model parameters are taken from [86], where the considered tire is 205/60R15. Detailed formulation of the tire model is given in Appendix B and the Matlab M-file for calculation of the tire forces is given in Appendix C. Figure 4.8, Figure 4.9, Figure 4.10 and Figure 4.11 show the tire forces calculated by using the Magic Formula Tire Model. For different road conditions, the change of the longitudinal tire force with respect to the tire longitudinal slip ratio κ is plotted in Figure 4.8. The change of the lateral tire force with respect to the tire side slip angle α is plotted in Figure 4.9. Note that the tire characteristics plotted in Figure 4.8 and Figure 4.9 are for pure slip cases.

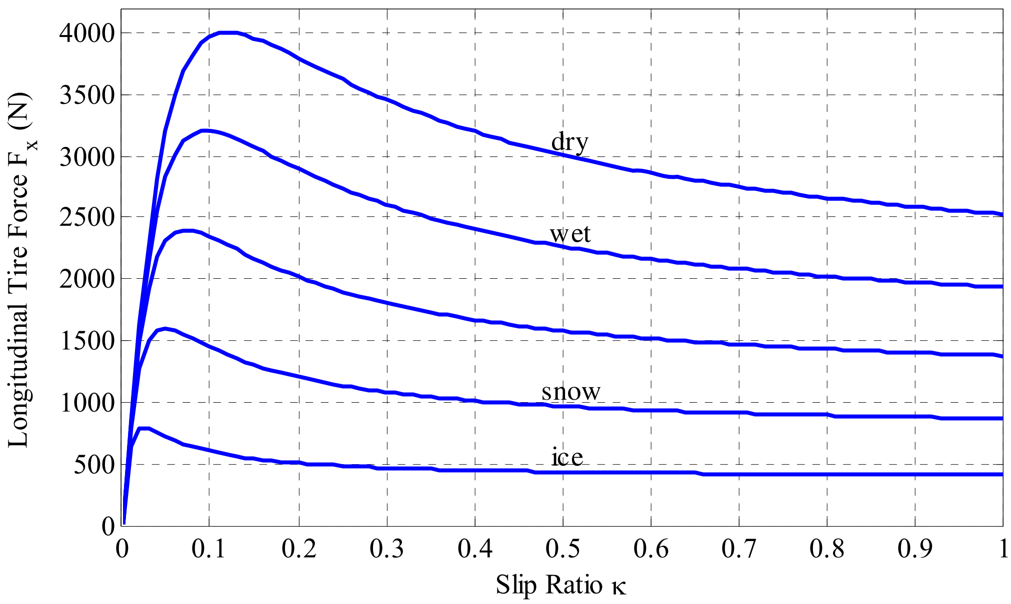

Figure 4.8 : Change of the longitudinal tire forces with respect to the tire slip ratio under pure longitudinal slip condition.

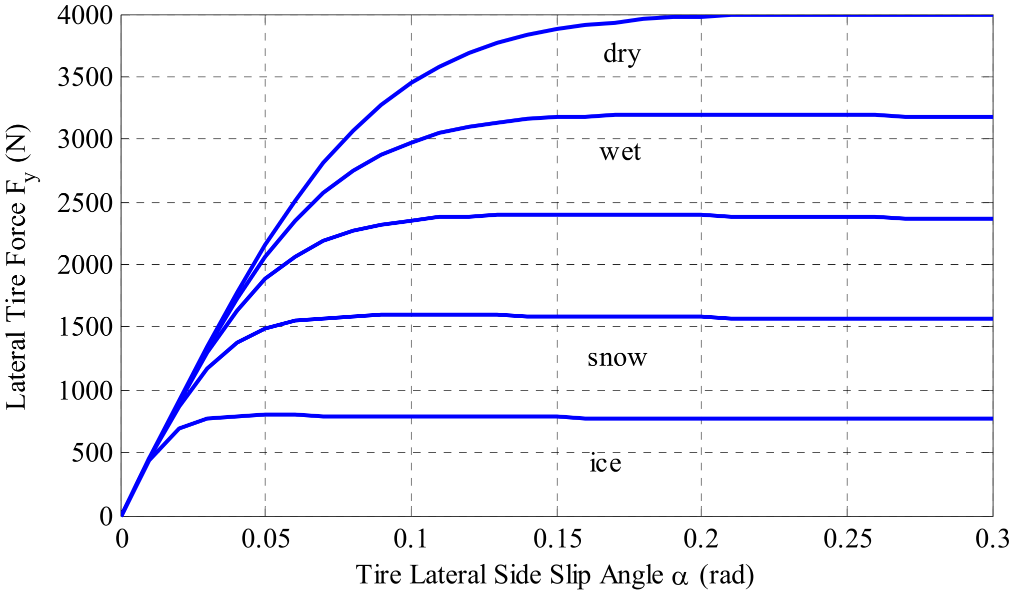

Figure 4.9 : Change of the lateral tire forces with respect to the tire side slip angle under pure lateral slip condition.

In other words Figure 4.8 shows the longitudinal tire force characteristics with respect to the tire slip ratio where the tire does not have a lateral slip value (α=0). Similarly, Figure 4.9 shows lateral tire force characteristics where the tire does not have a longitudinal slip value (κ=0). On the contrary, in combined slip cases where the tire has both longitudinal and lateral slip $(\alpha \neq 0, \kappa \neq 0)$, change of the longitudinal and lateral tire forces are plotted in Figure 4.10 and Figure 4.11. Figure 4.10 shows that if there is a lateral slip, the tire can generate less longitudinal tire force than the α=0 case. The longitudinal tire force decreases with the increasing side slip angle value as shown in Figure 4.10. Figure 4.11 shows that with the increasing longitudinal slip ratio value, the lateral force generation capability of the tire decreases. This is the reason that the steer ability of the vehicle decays during braking.

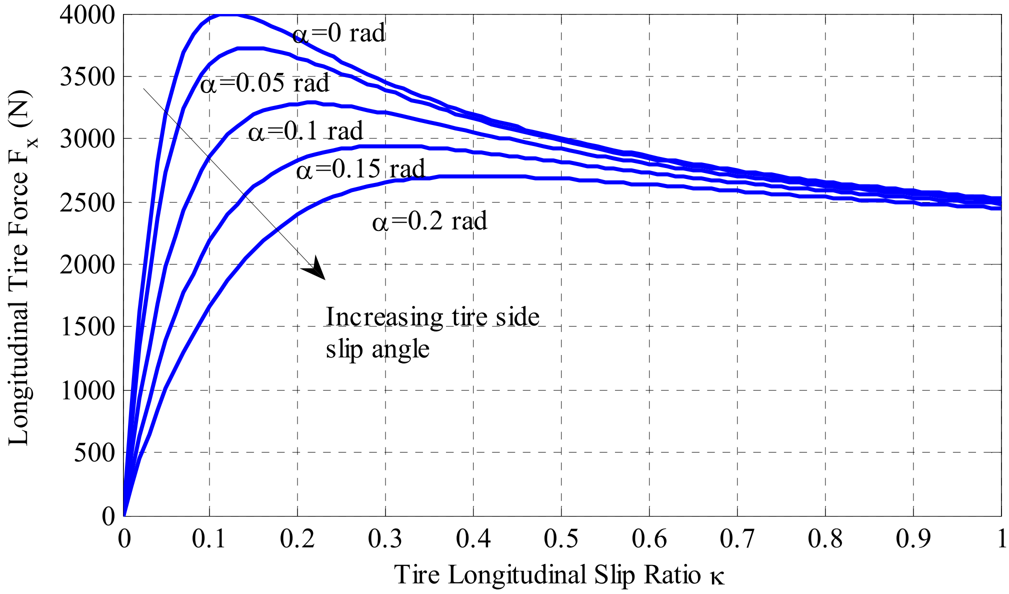

Figure 4.10 : Change of the longitudinal tire forces in combined slip case.

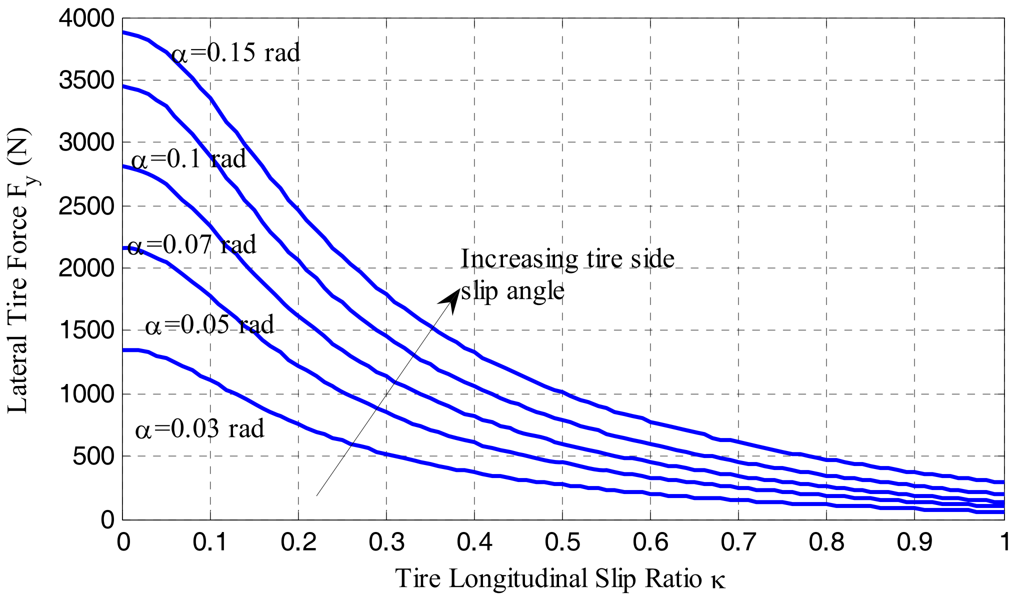

Figure 4.11 : Change of the lateral tire forces in combined slip case.

To be able to generate braking moments on each wheel, a hydraulic brake actuator model is taken into account. The schematic drawing of the hydraulic system is shown in Figure 4.12.

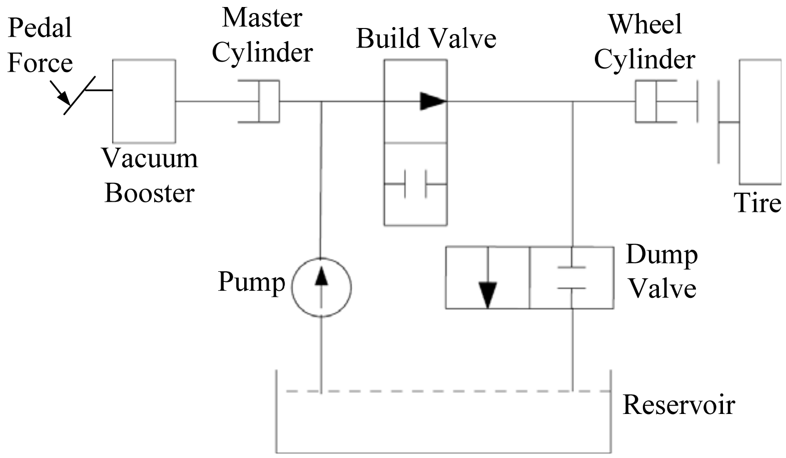

Figure 4.12 : Hydraulic brake actuator system.

For each individually actuated brake system, in order to increase the brake pressure and consequently the individual brake force between the tire patch and the road, the build valve opens and the dump valve closes. Thus, the brake pad presses on the brake disc. To decrease the brake pressure and consequently the brake force, the build valve closes and the dump valve opens, so that the fluid flows from the individual wheel cylinder to the reservoir. This operation is controlled by two inputs and the following governing differential equation,

$$\dot{P}_i = \frac{\beta_f}{V_\omega} C_{dv} A c_{d1i} \sqrt{\frac{2}{\rho_f}(P_p - P_i)} - \frac{\beta_f}{V_\omega} C_{dv} A c_{d2i} \sqrt{\frac{2}{\rho_f}(P_i - P_{low})} \quad \textbf{(4.83)}$$

where β_f, V_ω, C_{dv}, A, ρ_f, P_p, P_i, P_{low} are the brake fluid bulk modulus, wheel cylinder volume, orifice discharge coefficient, orifice area, brake fluid density, pump pressure, *i*-th wheel cylinder pressure and the reservoir pressure, respectively. c_{d1i} and c_{d2i} are the valve control inputs, which can be only 1 for an open valve or 0 for a closed valve and they are not allowed to be “1” at the same time, i.e., $c_{d1i}c_{d2i} \neq 1$, for the individually brake actuated *i*’th wheel. For each individual hydraulic brake actuator, the relationship between the wheel cylinder pressure and braking moment is given as follows

$$T_{bi} = (P_i - P_{out}) A_{\omega c} \eta B_F r_r \quad \textbf{(4.84)}$$

where P_{out}, $A_{\omega c}$, η, B_F and r_r are push out pressure, wheel cylinder area, mechanical efficiency, brake factor and effective brake disc radius, respectively.

4.3.2 Validation of the vehicle model with actual vehicle measurements

Measurements from a real vehicle are used for validation of the developed vehicle model. The actual vehicle's longitudinal, lateral and vertical accelerations, roll rate, pitch rate and yaw rates are measured from an inertial measurement unit shown in Figure 4.13. The instrumented vehicle is shown in Figure 4.14. The driver's steering input is measured from the steering wheel angle sensor. In order to compare the actual vehicle and the mathematical vehicle model, the same driver steering input measured from the real vehicle shown in Figure 4.15 is applied to the vehicle model. A cruise control unit is added to the vehicle model in order to follow the real vehicle's speed profile. The time responses of the mathematical model and the real vehicle sensor outputs are plotted in Figure 4.16, Figure 4.17, and Figure 4.18.

Figure 4.13 : Inertial measurement unit installed in the vehicle.

Figure 4.14 : Instrumented vehicle.

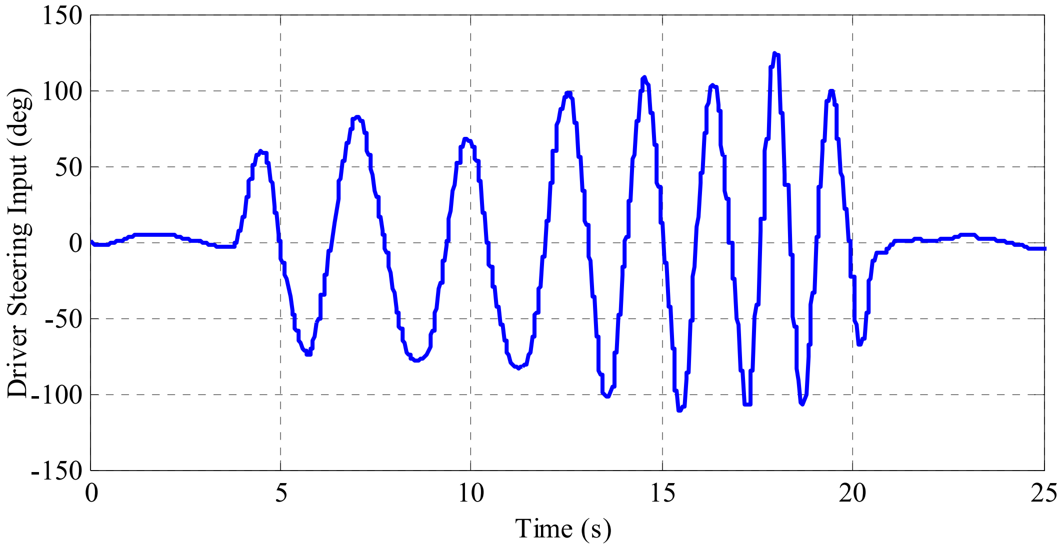

Figure 4.15 : Driver steering input.

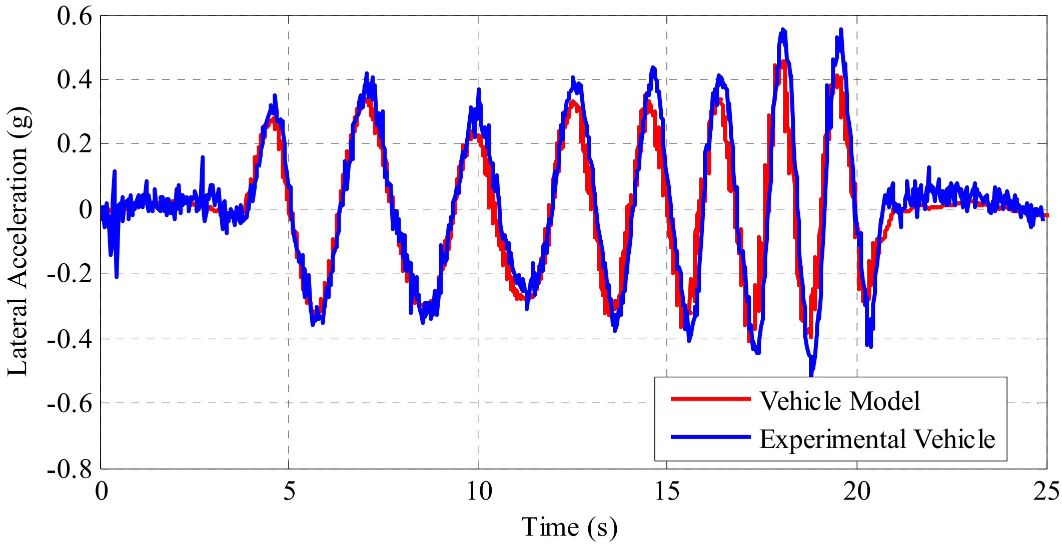

Figure 4.16 : Validation results: Lateral acceleration.

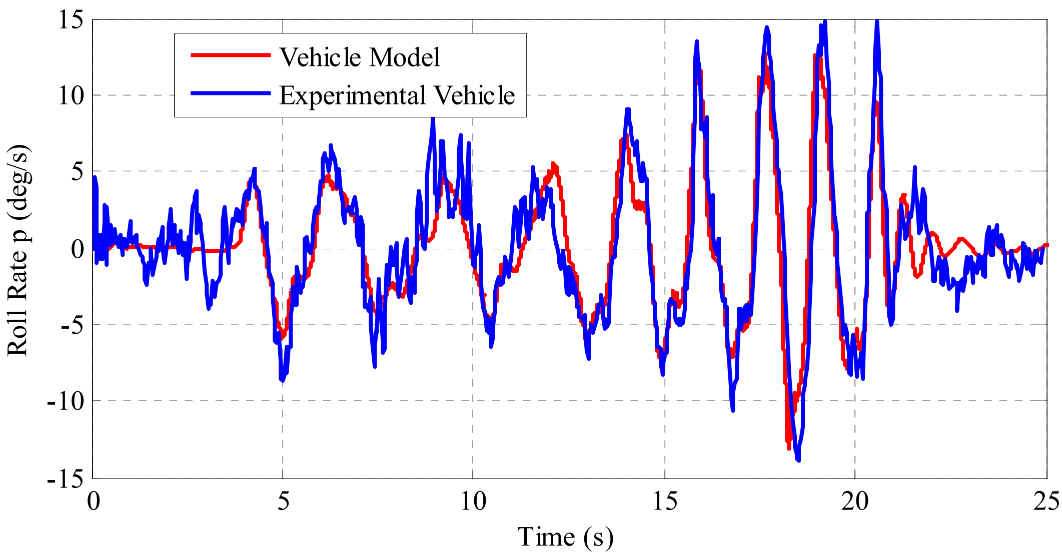

Figure 4.17 : Validation results: Roll rate.

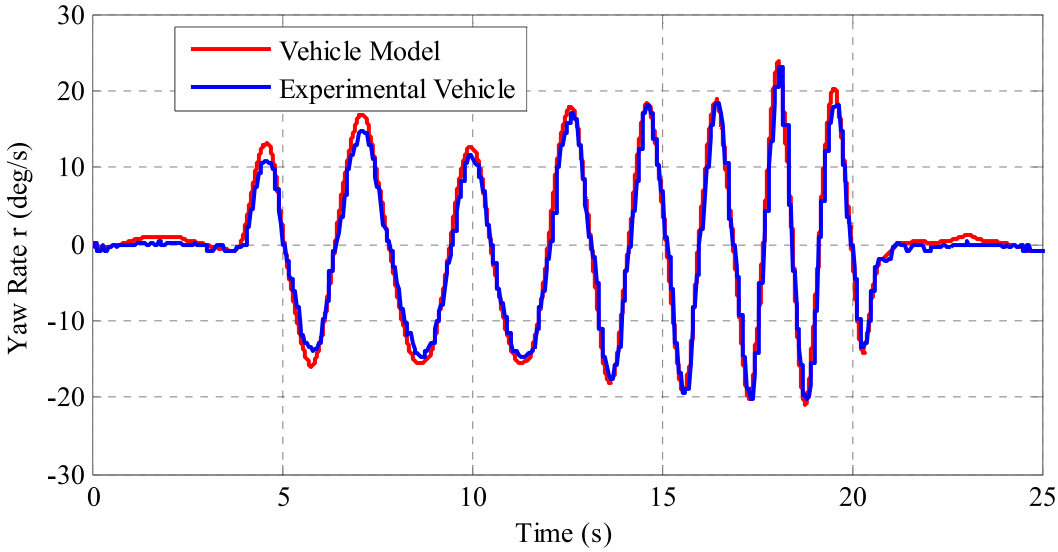

Figure 4.18 : Validation results: Yaw rate.

4.3.3 Simulation scenario 1

In the simulation scenario 1, straight line braking case is studied. The initial vehicle speed is 30 m/s. Simulations are conducted on different road conditions to show the effectiveness of the control algorithm. First, the road is selected as dry asphalt. Simulation results for normalized tire forces F_{xi}/F_{zi} are plotted in Figure 4.19.

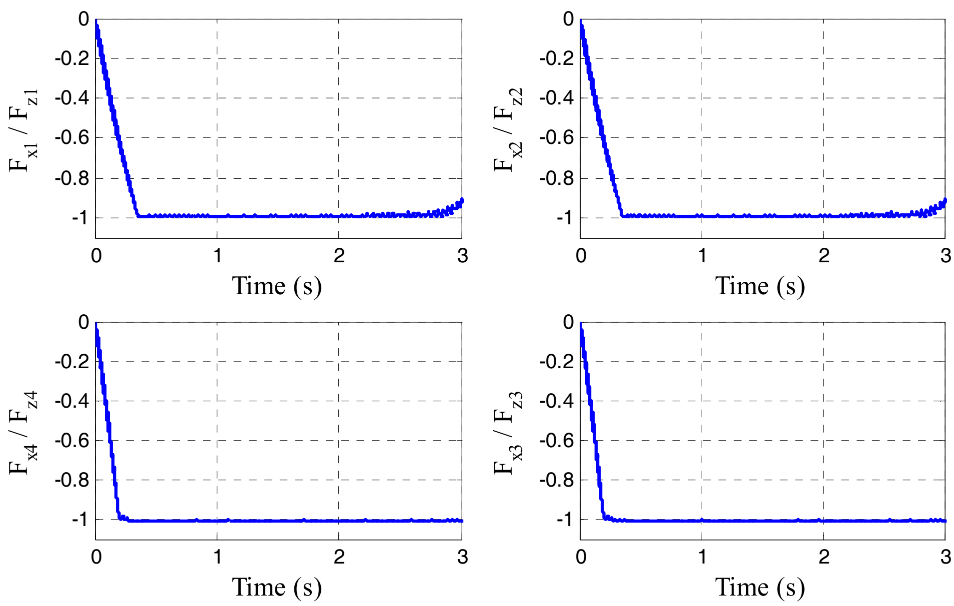

Figure 4.19 : Change of the normalized longitudinal tire forces in dry road.

Since the maximum braking force that a tire can produce can be calculated from the equation: $F_{xmax} = -\mu_{max}F_z$, where $\mu_{max} = 1$ for the dry asphalt road, it is shown that after approximately 0.2 sec., normalized tire forces are equal to $F_{xi}/F_{zi} = -1$, which means that tire forces are maximized. The controller does not use road condition information. Change of the slip ratios are plotted in Figure 4.20. Optimum slip ratios are found on-line via the search algorithm. Braking moment inputs are plotted in Figure 4.21.

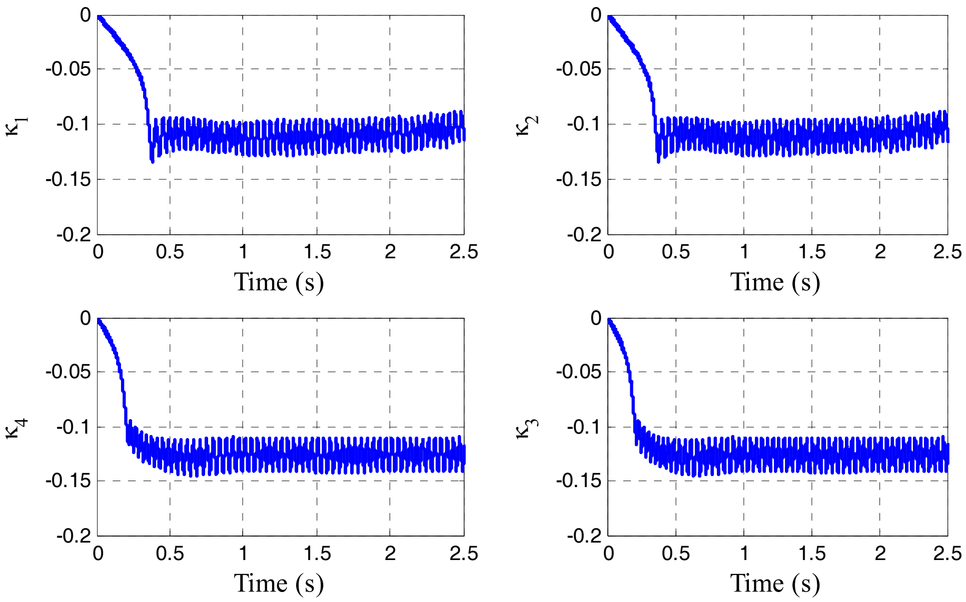

Figure 4.20 : Change of the tire slip ratios in dry road.

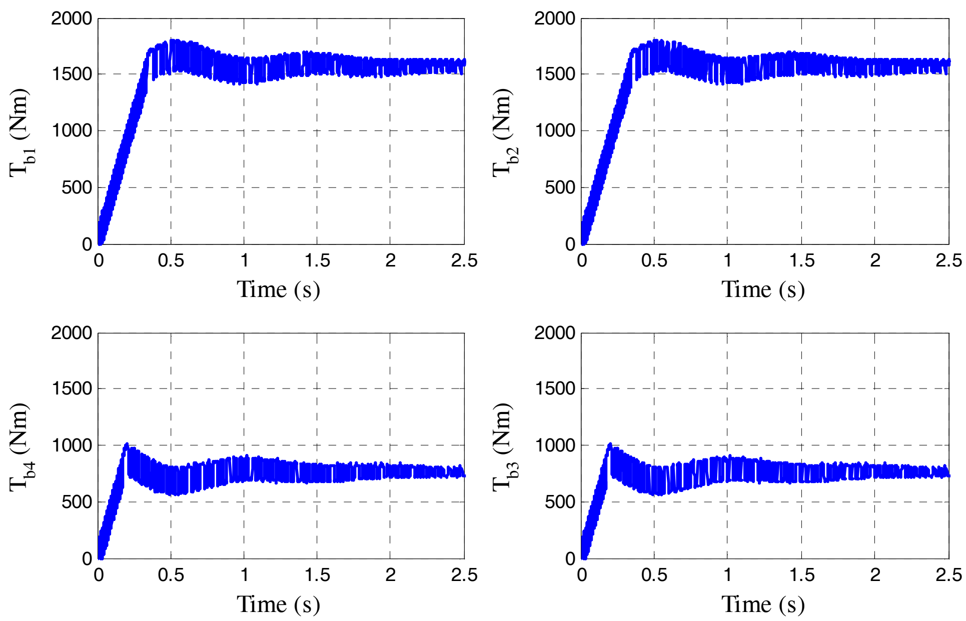

Figure 4.21 : Change of the braking moments in dry road.

Next, simulations are conducted on a μ_{max} = 0.4 road, which simulates a snowy road. Results for normalized tire forces are shown in Figure 4.22. Maximum friction potential is utilized by the search algorithm because it is shown that normalized longitudinal tire forces are reaching the value of $F_{xi}/F_{zi} = -0.4$. It is noticed that whatever the road condition is, the algorithm is robust, i.e. it finds optimum slip ratios for maximum braking forces. Change of the slip ratios and braking moment inputs are plotted for braking in snowy road in Figure 4.23 and Figure 4.24, respectively.

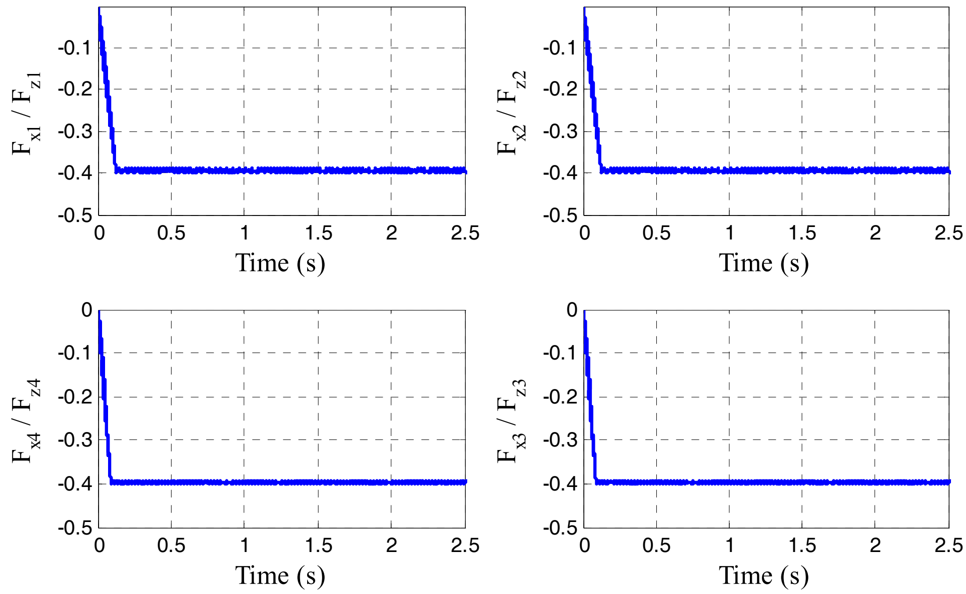

Figure 4.22 : Change of the normalized longitudinal tire forces in snowy road.

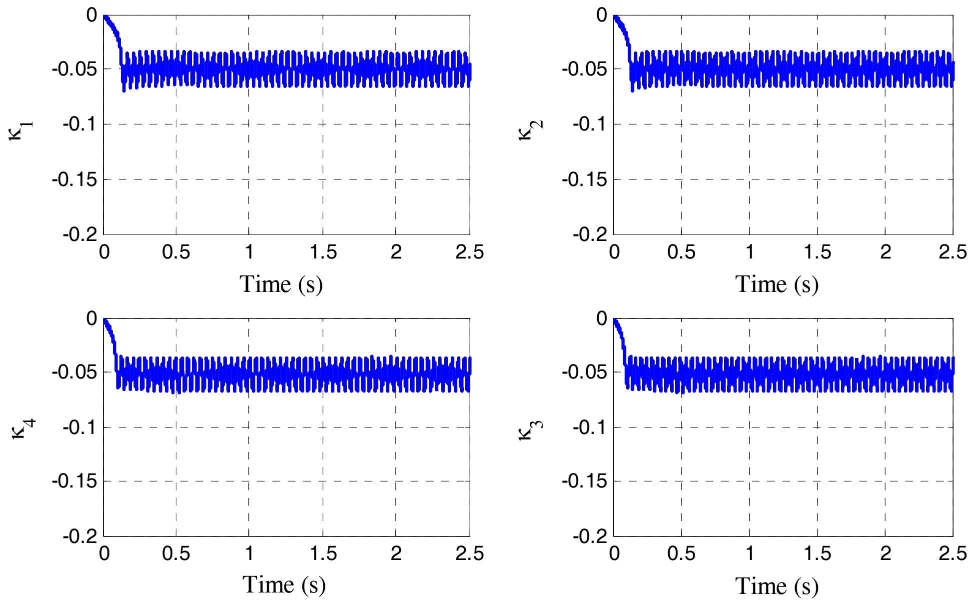

Figure 4.23 : Change of the tire slip ratios in snowy road.

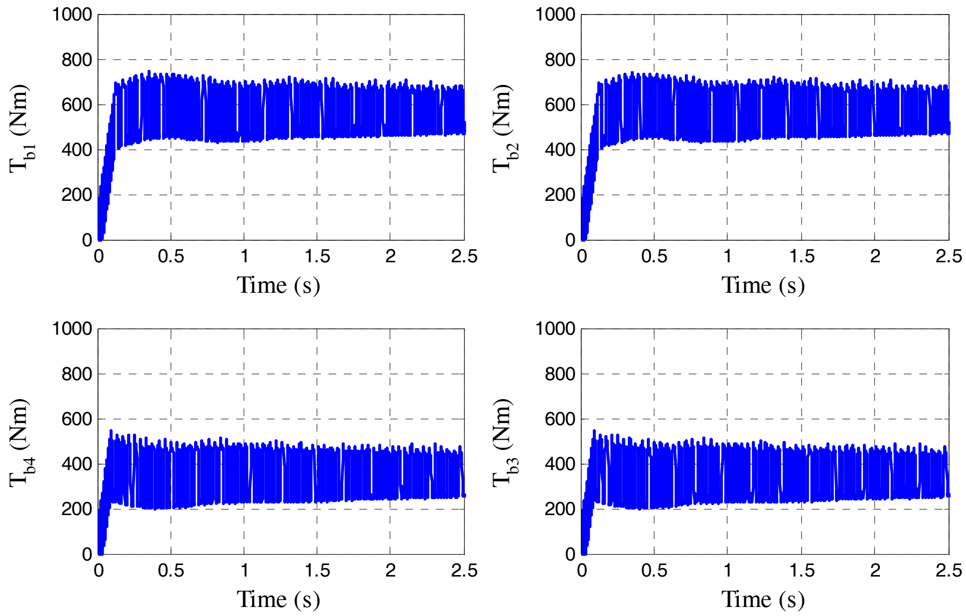

Figure 4.24 : Change of the braking moments in snowy road.

4.3.4 Simulation scenario 2

In the simulation scenario 2, combined steering and braking is studied. The driver steering input given in Figure 4.25 is applied to the vehicle model. In Figure 4.26, change of the tire slip ratios are shown. It is noticed that when steering is applied, the magnitude of front axle slip ratios start to increase. This phenomenon can be explained from Figure 4.10, where longitudinal tire force characteristics for the combined slip case are plotted. From Figure 4.10, it is shown that when there is a lateral motion in addition to the longitudinal motion, i.e. when tire side slip angles are not zero ($\alpha_i \neq 0$), the location of the optimum slip ratio for maximum longitudinal force moves forward. Since the extremum seeking algorithm searches the optimum slip ratio, it increases the slip ratio as it is shown in Figure 4.26 to track the peak point. Rear axle slip ratios did not increase because during hard braking, the weight of the rear axle decreases considerably, resulting in small lateral tire forces. These small lateral forces do not have big deforming effect on rear axle longitudinal tire forces and hence location of the optimum slip ratios on the rear axle does not change considerably. From Figure 4.11 it is seen that when slip ratio increases, the magnitude of the lateral tire force F_{yi} decreases considerably. If extremum-seeking controller keeps maximizing the braking forces by increasing the slip ratio, lateral tire forces may be insufficient. This may cause the vehicle not to swerve safely from danger. For lateral stability enhancement, extremum seeking algorithm should be modified as introduced in the next section.

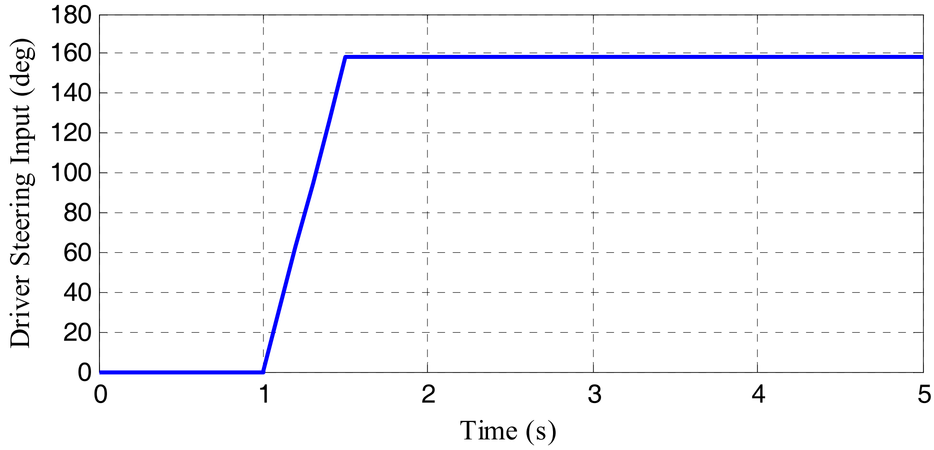

Figure 4.25 : Driver steering input for the simulation scenario 2.

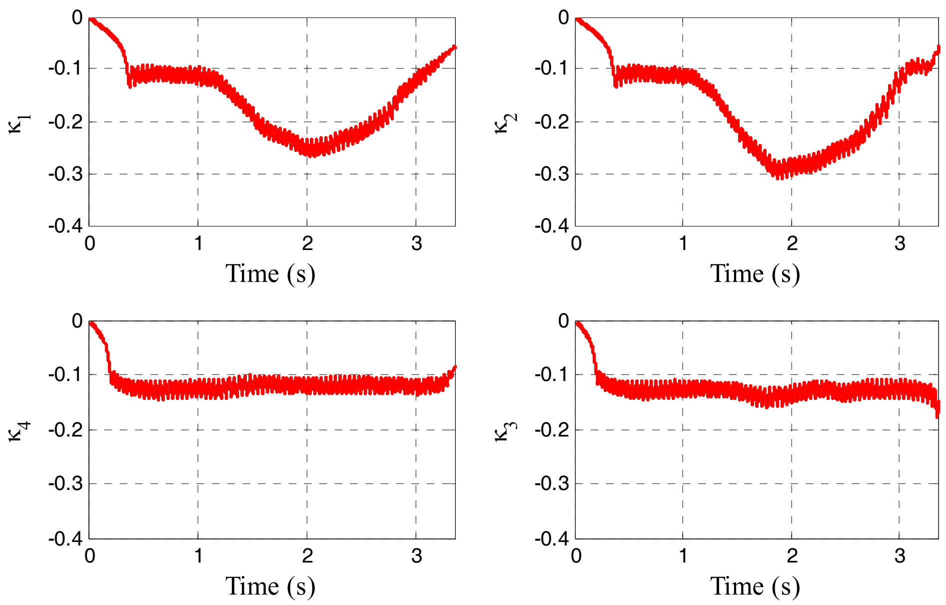

Figure 4.26 : Change of the tire slip ratios in simulation scenario 2.

4.4 Modified ESA with Lateral Force Improvement

In the previous section, extremum seeking algorithm has been introduced for the ABS problem, where the algorithm seeks optimum tire slip ratios for maximum braking forces. Via the simulations, it has been shown that the algorithm finds optimum slip ratios for maximum tire forces with respect to the different road conditions.

It has also been shown that when there is a lateral motion, i.e. $\alpha_i \neq 0$, the algorithm increases the value of the slip ratio to track the peak point of the longitudinal tire force since optimum slip ratio κ moves forward with the increasing side slip angle α as shown in Figure 4.10.

However, from Figure 4.11 it is shown that when slip ratio κ increases, the lateral tire force F_{yi} decreases dramatically. This is an undesired situation since it is also desirable to have large enough lateral tire forces in order to maneuver safely. For example, when the driver suddenly confronts an obstacle (for example another car in front of his/her path), he/she jeopardizes the control inputs such as applying at the same time hard braking and steering. In that case, if the ABS braking controller only cares to maximize the braking forces, and does not take into consideration the lateral tire forces, then although braking forces may be maximized, lateral tire forces may be insufficient. This may cause the vehicle not to swerve safely from danger and a collision with the obstacle may occur. Hence, the extremum seeking algorithm should be modified to take into account the lateral tire forces also, when the driver demands lateral motion from the vehicle.

In the previous section, it has been shown that, when there is a lateral motion in addition to braking, due to the additional contribution of $\dfrac{\partial F_{xi}(\kappa_i, \alpha_i)}{\partial \alpha_i}\dot{\alpha}_i$ in the condition **(4.32)**, the increment of F_{xi} lasts shorter and hence, slip ratio will be smaller with resulting larger lateral tire forces. This effect inspires to incorporate driver steering input information to the extremum seeking algorithm to define operating region of the tires during braking. This modification is based on the following idea: By choosing ρ and M in **(4.32)**, one defines the location of the operating region. Choosing a bigger value for the right hand side of **(4.32)**, the condition holds shorter, i.e. the increment of F_{xi} lasts shorter. In other words, the tire will operate further than its maximum force value. On the contrary, choosing a smaller right hand side of **(4.32)**, the condition will hold longer, eventually, the tire will operate closer to its maximum value. When steering input is zero, i.e. straight line braking, the operating region should be as close as possible to the maximum tire force value; hence, the right hand side should be small. On the other hand, if there is a steering wheel input, the search algorithm should not keep tracking the varying optimum slip ratio value as shown in Figure 4.10, in order to prevent any loss in lateral tire forces. Hence, the operating region should be farther from the extremum point, i.e. right hand side of **(4.32)** should be large. The adaptation law for the slip ratio is modified as

$$\dot{\kappa}_i = M \exp\left(-\varepsilon\left|\delta_f\right|\right)\operatorname{sgn}\left[\sin\left(\frac{\pi s_i}{\gamma}\right)\right] \tag{4.85}$$

where δ_f is the steering angle, ε is a constant. By combining **(4.85)** and **(4.2)**, one gets

$$\dot{s}_i = \frac{\partial F_{xi}(\kappa_i,\alpha_i)}{\partial \kappa_i} M \exp\left(-\varepsilon\left|\delta_f\right|\right)\operatorname{sgn}\left[\sin\left(\frac{\pi s_i}{\gamma}\right)\right] + \frac{\partial F_{xi}(\kappa_i,\alpha_i)}{\partial \alpha_i}\dot{\alpha}_i + \rho \tag{4.86}$$

As introduced in the analysis in section 2, assuming that at the start of optimization the value of s_i in **(4.86)** is between the values of γ and 2γ such as $\gamma < s_i(0) < 2\gamma$, then, on that interval, the following inequalities can be written from **(4.86)**

$$\lambda_1\dot{\lambda}_1 \le -\left|\lambda_1\right|\left[\frac{\partial F_{xi}(\kappa_i,\alpha_i)}{\partial \kappa_i} M \exp\left(-\varepsilon\left|\delta_f\right|\right) - \left|\frac{\partial F_{xi}(\kappa_i,\alpha_i)}{\partial \alpha_i}\dot{\alpha}_i\right| - \rho\right] \tag{4.87}$$

$$\lambda_2\dot{\lambda}_2 \le \left|\lambda_2\right|\left[\frac{\partial F_{xi}(\kappa_i,\alpha_i)}{\partial \kappa_i} M \exp\left(-\varepsilon\left|\delta_f\right|\right) + \left|\frac{\partial F_{xi}(\kappa_i,\alpha_i)}{\partial \alpha_i}\dot{\alpha}_i\right| + \rho\right] \tag{4.88}$$

where $\lambda_1 = s_i - \gamma$ and $\lambda_2 = s_i - 2\gamma$. Then as long as the condition

$$\left|\frac{\partial F_{xi}(\kappa_i,\alpha_i)}{\partial \kappa_i}\right| > \frac{\left|\dfrac{\partial F_{xi}(\kappa_i,\alpha_i)}{\partial \alpha_i}\dot{\alpha}_i\right|}{M \exp\left(-\varepsilon\left|\delta_f\right|\right)} + \frac{\rho}{M \exp\left(-\varepsilon\left|\delta_f\right|\right)} \tag{4.89}$$

holds, s_i converges to either γ or 2γ. The analysis can be generalized not for only the interval of $\gamma < s_i(0) < 2\gamma$ but for any starting point of $s_i(0)$. Then, as long as **(4.89)** holds, s_i will converge to a constant value $w=\gamma k$ depending on its initial value $s_i(0)$ where k is an integer number with $k = (0,\pm1,\pm2, ...)$. Then, from **(4.1)**

$$s_i = w = F_{xi}(\kappa_i,\alpha_i) + \rho t \tag{4.90}$$

$$F_{xi}(\kappa_i,\alpha_i) = -\rho t + w \tag{4.91}$$

$$\dot{F}_{xi} = -\rho \tag{4.92}$$

Hence, braking force $F_{xi}(\kappa_i, \alpha_i)$, which is negative, will increase in magnitude with the slope of ρ, i.e. the tire operating point will approach the peak point of the force-slip curve as long as condition **(4.89)** holds. It is noticed that by increasing the steering wheel angle, the right hand side of **(4.89)** increases, meaning that the condition **(4.89)** holds for shorter time, i.e. the increment of F_{xi} lasts shorter, resulting in the tires operating further than their maximum longitudinal force values. This approach provides larger lateral forces.

4.5 Simulations

4.5.1 Simulations with scenario 2

In the previous chapter, during the simulations of combined braking and steering maneuver, it was shown in Figure 4.26 that the control algorithm increases the slip ratio value to track the maximum braking force value. In Figure 4.27, it is shown that with the modified algorithm, the increment in slip ratio is prevented where blue figures show the results of the modified algorithm and red figures show the results of the first version.

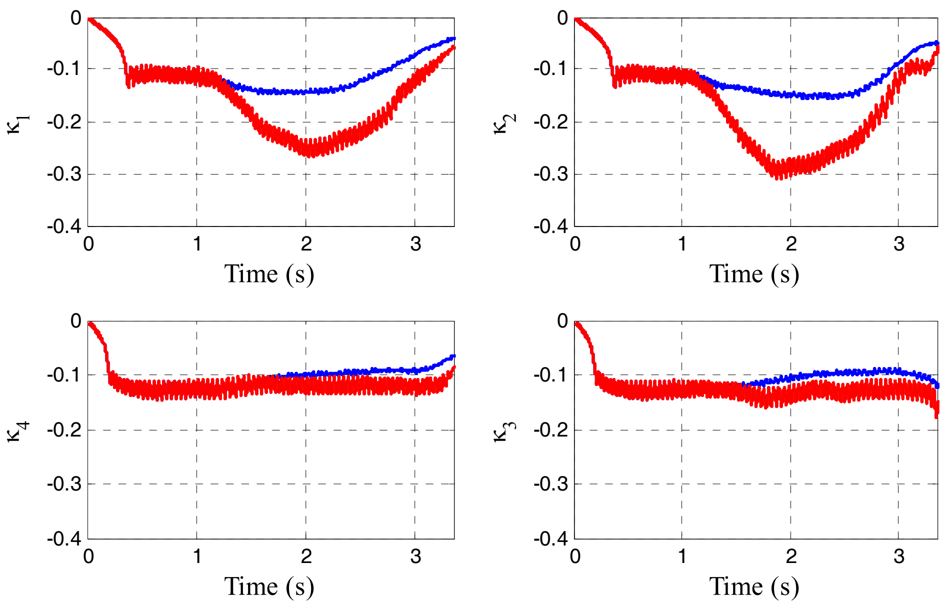

Figure 4.27 : Change of the slip ratios in simulation scenario 2, dry road. (red: first version, blue: modified version).

This color notation will be used in the figures of the remaining of the chapter. Figure 4.28 shows the improvement in lateral tire forces. Since in the modified algorithm tires operate further than their maximum operating region, a decrement is noticed in the longitudinal tire forces as shown in Figure 4.29.

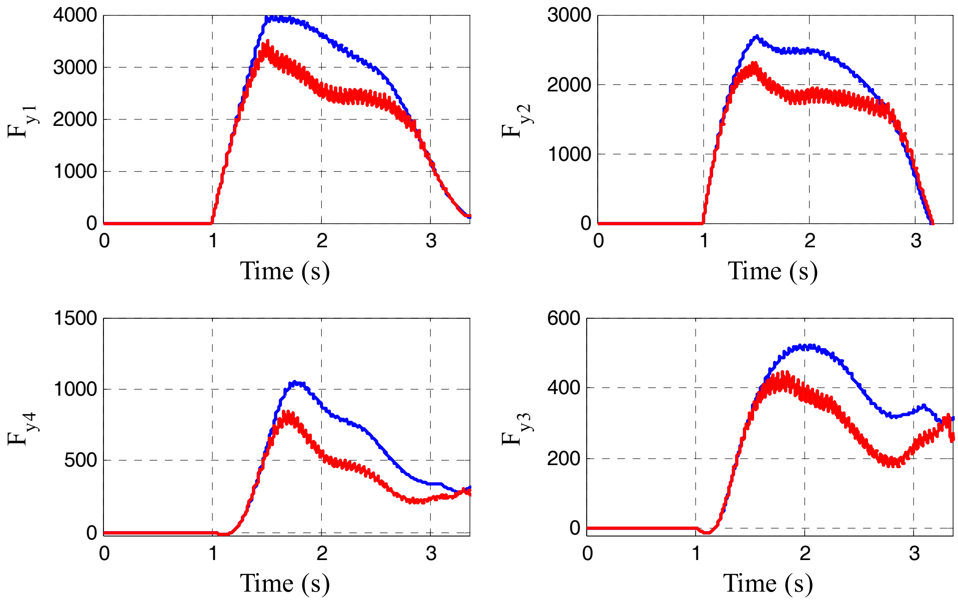

Figure 4.28 : Change of lateral tire forces in simulation scenario 2, dry road.

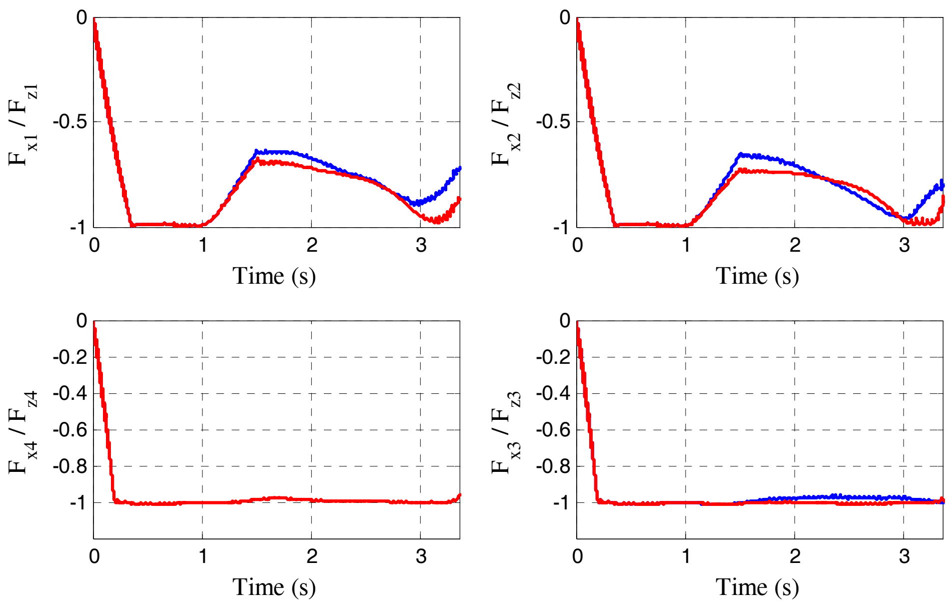

Figure 4.29 : Change of longitudinal tire forces in simulation scenario 2, dry road.

However, this decrement results in only a small difference of the stopping time as shown in Figure 4.30. It is noticed that the difference on the stopping time is minor but the improvement in lateral tire forces is considerable. The improvement in lateral acceleration value of the vehicle is shown in Figure 4.31.

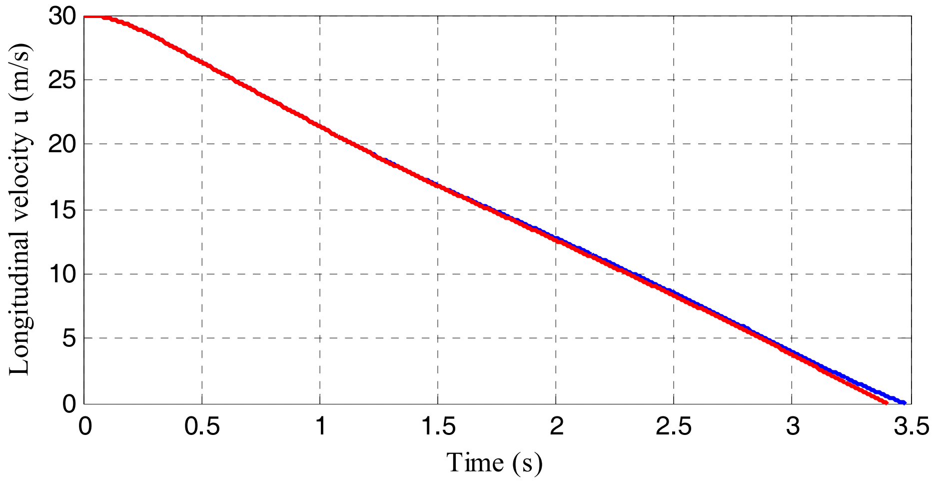

Figure 4.30 : Change of longitudinal speed in simulation scenario 2, dry road.

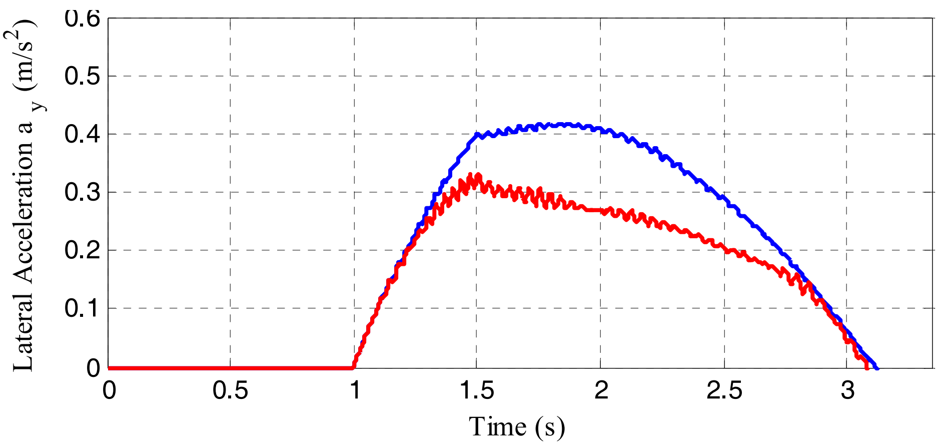

Figure 4.31 : Change of lateral accelerations in simulation scenario 2, dry road.

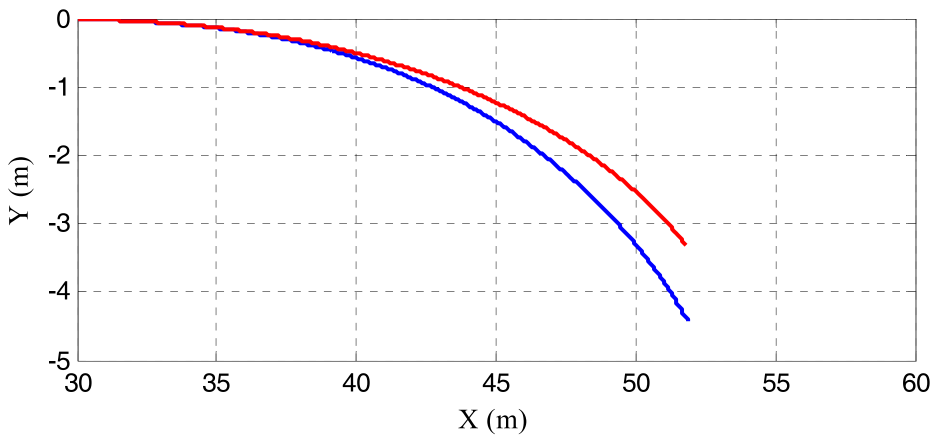

Figure 4.32 : Vehicle trajectories in simulation scenario 2, dry road.

The increment in lateral acceleration means that the vehicle can maneuver sharply than the conventional algorithm. While still getting large braking forces, the lateral stability of the vehicle is improved considerably with the proposed algorithm when it is observed that the driver demands lateral motion in addition to emergency braking. The vehicle trajectories are shown in Figure 4.32 where it is shown that the cornering capability of the vehicle is improved considerably.

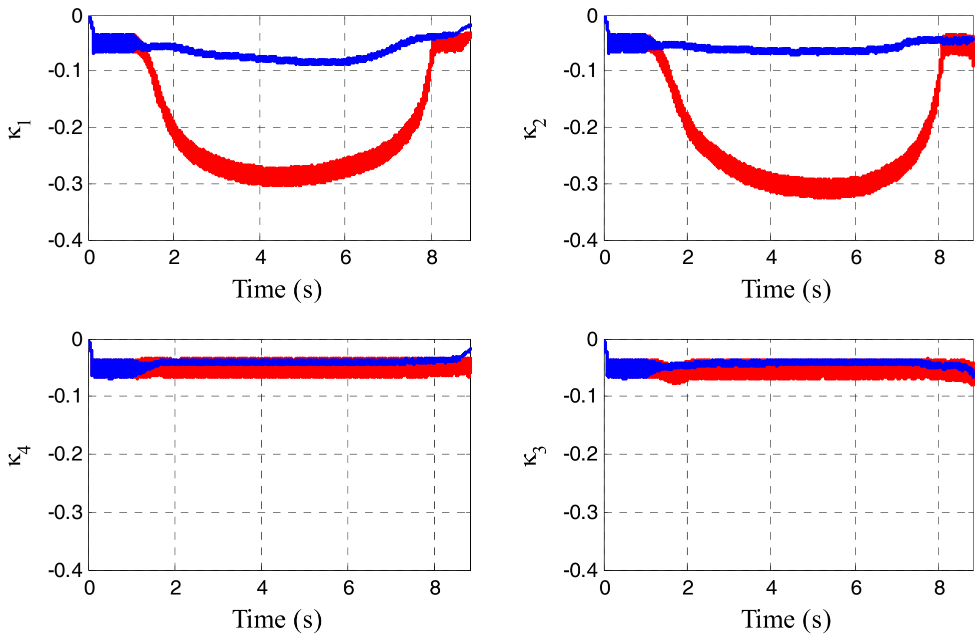

Figure 4.33 : Change of the slip ratios in simulation scenario 2, snowy road.

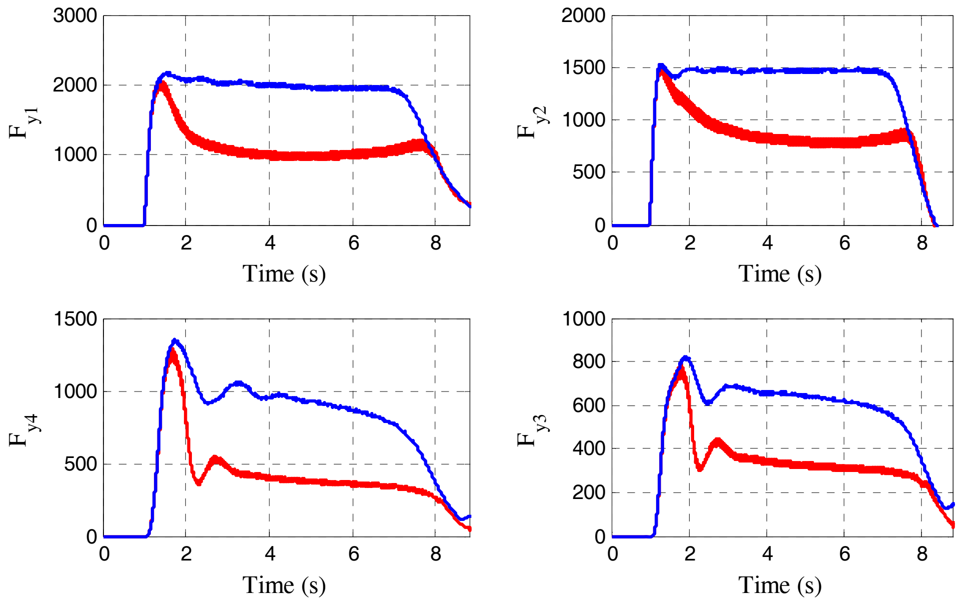

Figure 4.34 : Change of lateral tire forces in simulation scenario 2, snowy road.

Next, the responses of the vehicle model are shown for braking and maneuvering on a snowy road. In Figure 4.33, it is shown that with the modified algorithm, the increment in slip ratio is prevented.

Figure 4.34 shows the improvement in lateral tire forces. Longitudinal tire forces and stopping times are shown in Figure 4.35 and Figure 4.36. Again, it is noticed that the difference of the stopping time is minor but improvement in lateral tire forces is considerable. The improvement in lateral acceleration value and the vehicle trajectories are shown in Figure 4.37, Figure 4.38.

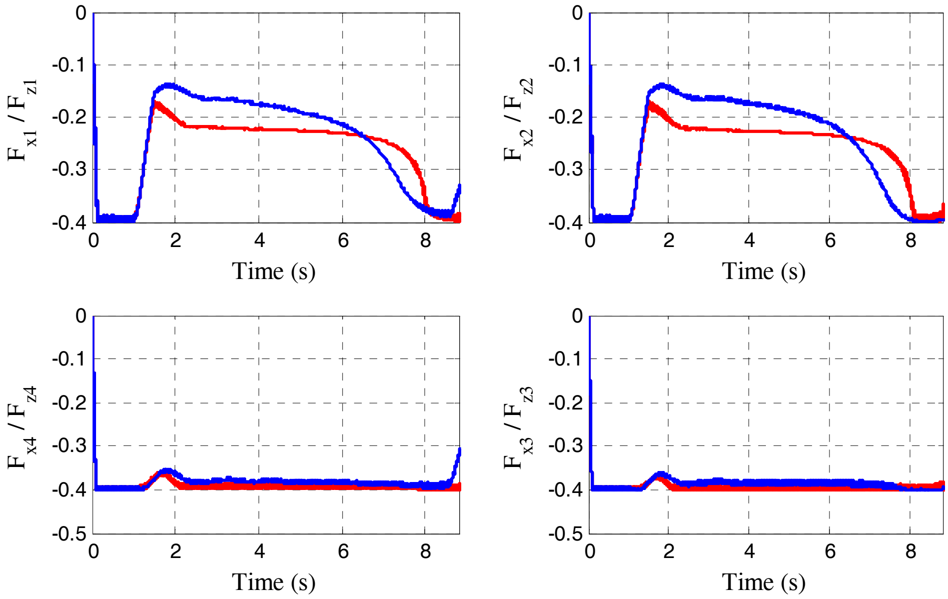

Figure 4.35 : Longitudinal tire forces in simulation scenario 2, snowy road.

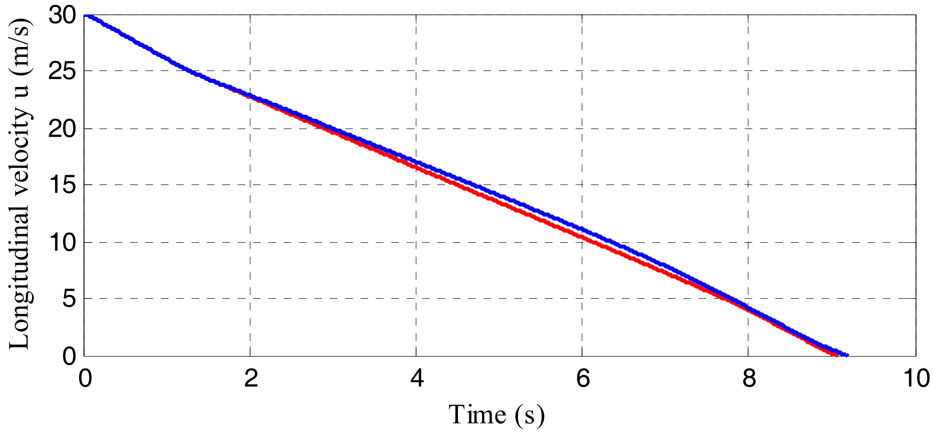

Figure 4.36 : Longitudinal speed in simulation scenario 2, snowy road.

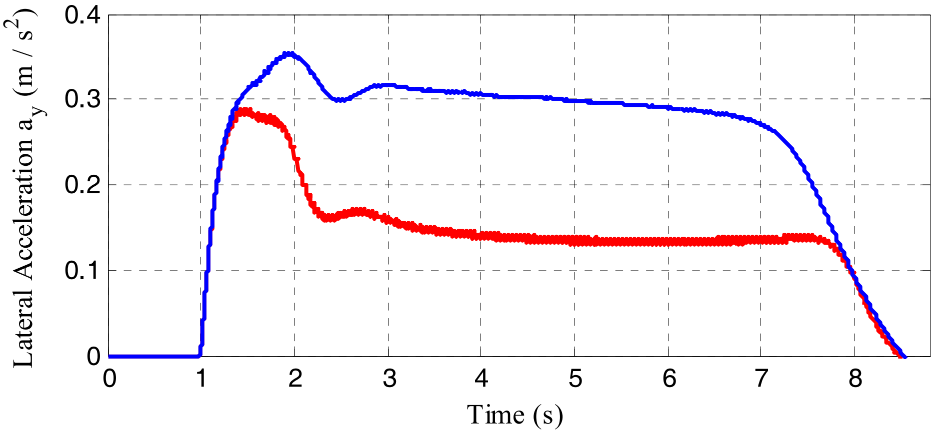

Figure 4.37 : Lateral accelerations in simulation scenario 2, snowy road.

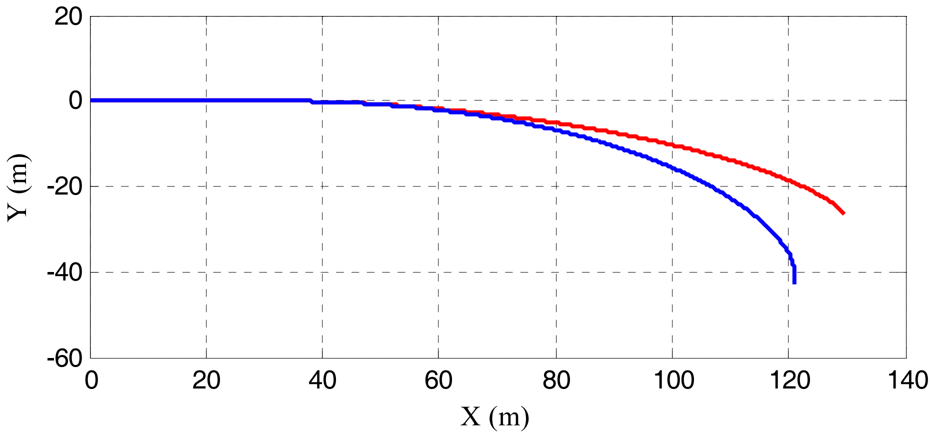

Figure 4.38 : Vehicle trajectories in simulation scenario 2, snowy road.

4.5.2 Simulation scenario 3

In Figure 4.8, longitudinal tire force characteristics are plotted for different road conditions. During braking, when the road condition changes suddenly from dry road to the snowy road, the tire's operating point may drop to the right side of the maximum force value. When steering is applied in addition to braking, since the modified braking algorithm adapts the tire slip ratio update rule, which increases the operating region of the search algorithm, this may result in the tires operating further than the peak point with an increase in the slip ratio value. This will even worsen the lateral tire forces since lateral tire forces degrade with increasing tire slip ratio value as shown in Figure 4.11. In order to show whether the controller results in such an undesired situation, simulations are performed with changing road conditions. In simulation scenario 3, straight line braking starts on a dry road and after 1 s, the road condition changes to a snowy road. After 2 s, driver steering input given in Figure 4.25 is applied on this snowy road. InFigure 4.39, normalized longitudinal tire forces are shown. Braking algorithm finds maximum braking force for the dry road. After 1 s the road condition changes suddenly to a snowy road. Braking algorithm finds again optimum slip ratio of the snowy road for maximum braking force. After 2 s, driver steering input is initialized. It is shown that the differences on the longitudinal tire forces are small but the improvement in lateral tire forces is considerable with the modified algorithm as shown in Figure 4.40.

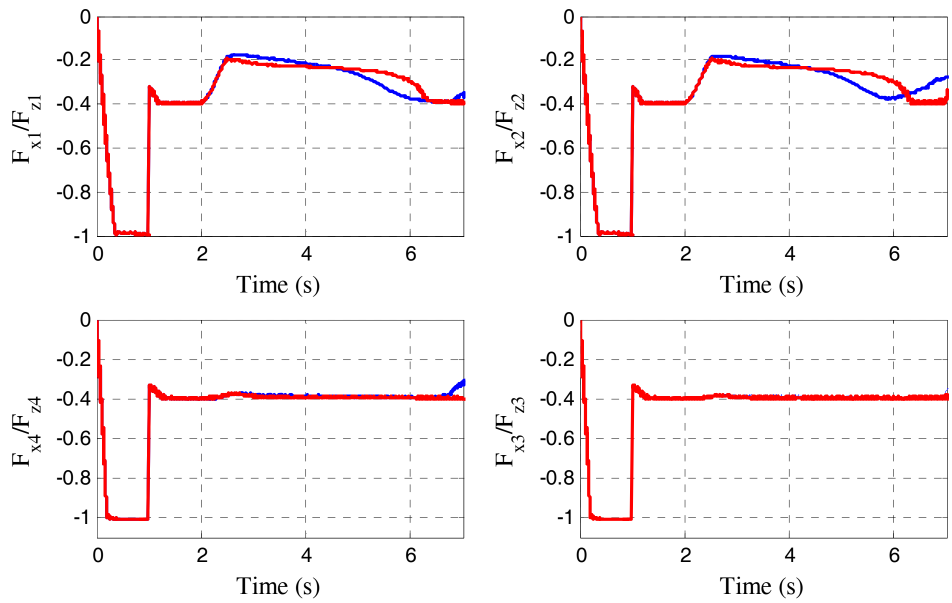

Figure 4.39 : Normalized longitudinal tire forces in simulation scenario 3.

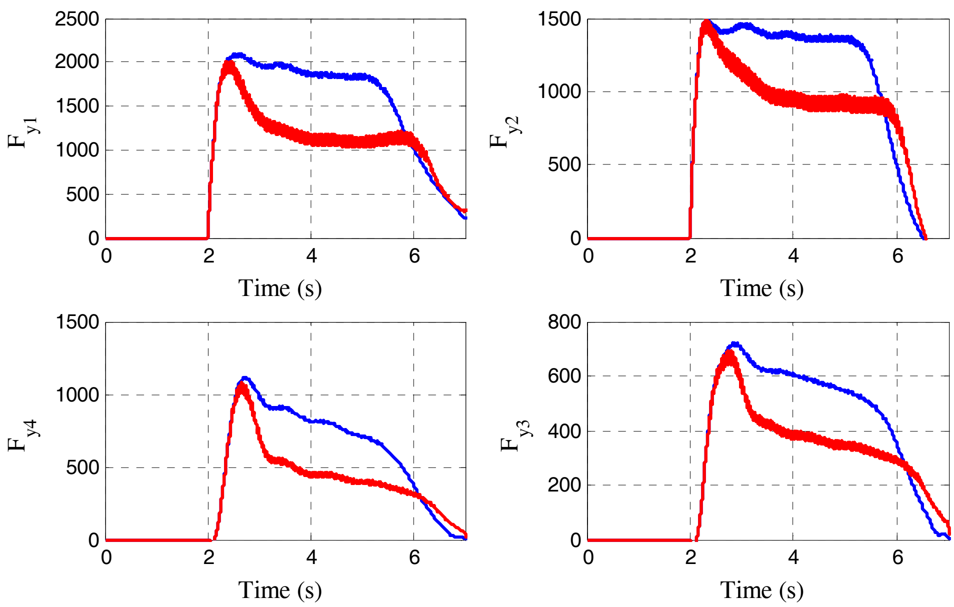

Figure 4.40 : Lateral tire forces in simulation scenario 3.

Change of the tire slip ratios are plotted in Figure 4.41 where it is shown that increase on the slip ratio is prevented. Vehicle speeds are plotted in Figure 4.42 where it is realized that while improving lateral tire forces considerably with the modified algorithm, the loss in longitudinal tire forces are so small that the stopping time is almost equal. In Figure 4.43 and Figure 4.44 change of the lateral accelerations and vehicle trajectories are plotted respectively.

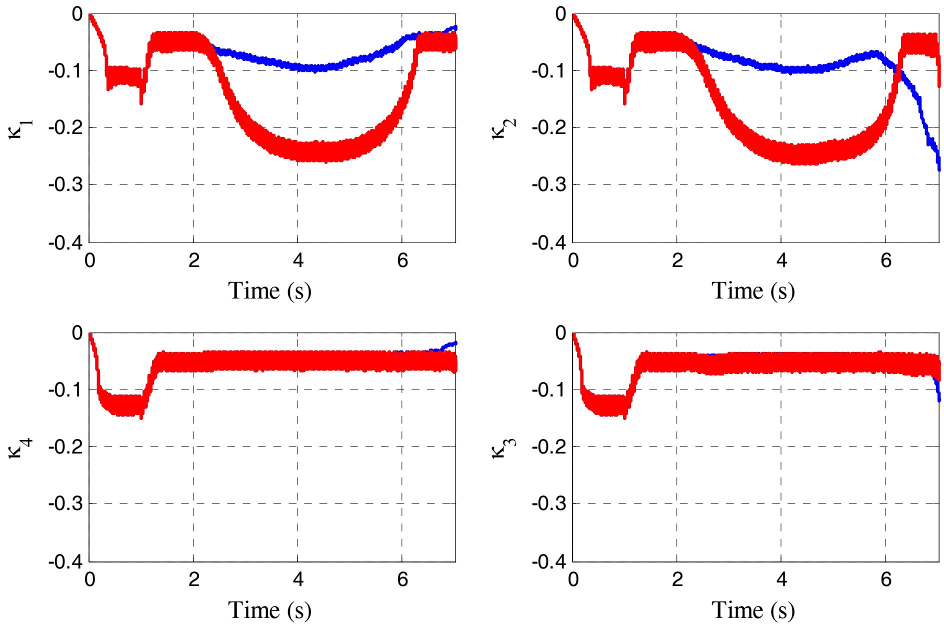

Figure 4.41 : Longitudinal tire slip ratios in simulation scenario 3.

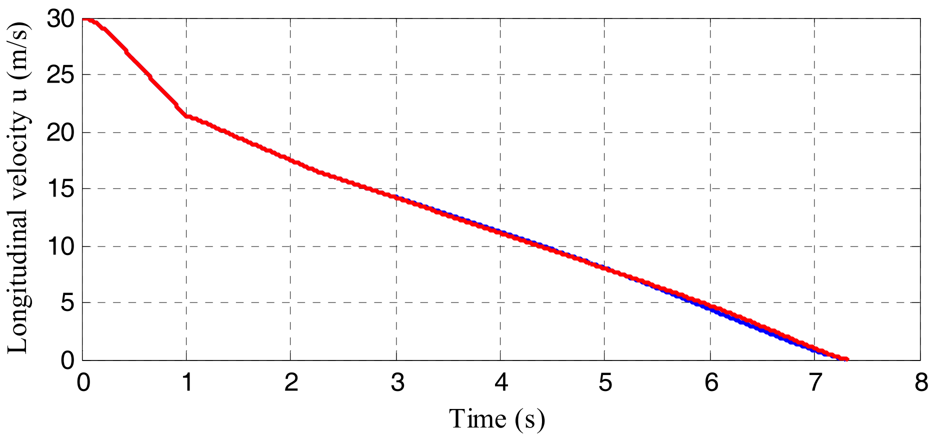

Figure 4.42 : Longitudinal speeds in simulation scenario 3.

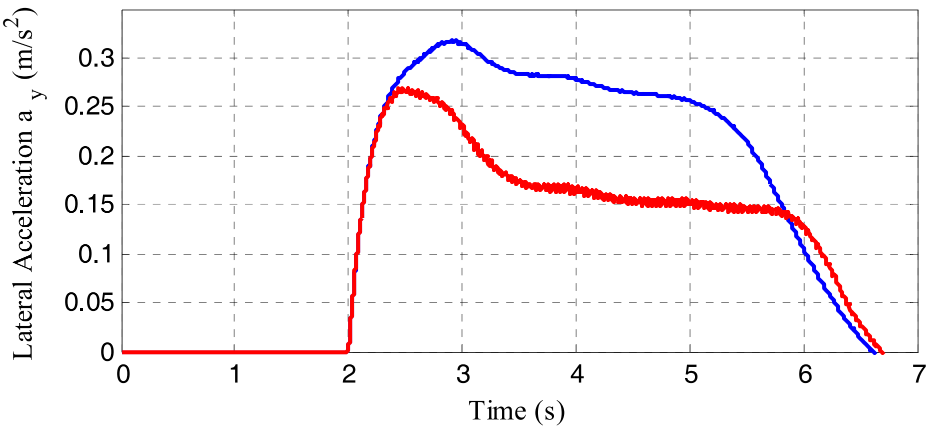

Figure 4.43 : Lateral accelerations in simulation scenario 3.

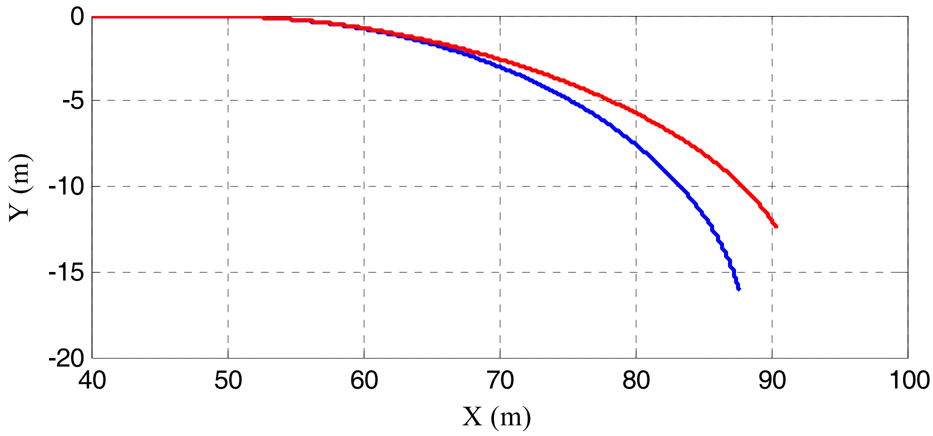

Figure 4.44 : Vehicle trajectories in simulation scenario 3.

4.5.3 Simulation scenario 4

In simulation scenario 4, steering is applied at the same time with the change of the road condition. After 1 s, the driver steering input given in Figure 4.25 is applied to the vehicle and at the same time the road condition changes from dry road to snowy road. Change of the tire slip ratios are plotted in Figure 4.45. It is shown that increase on the slip ratio is prevented. Improvements in lateral tire forces are shown in Figure 4.46. In Figure 4.47, changes of the lateral accelerations are plotted.

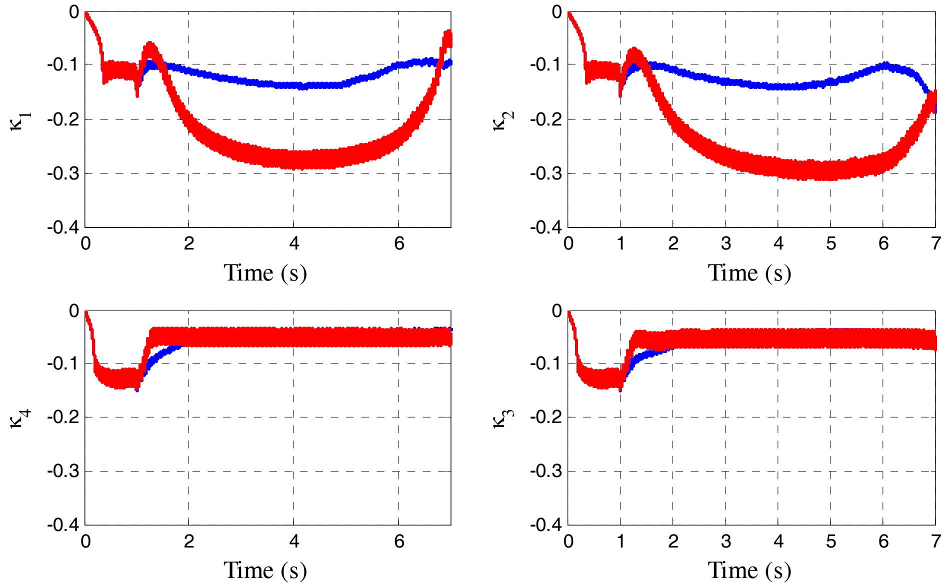

Figure 4.45 : Longitudinal tire slip ratios in simulation scenario 4.

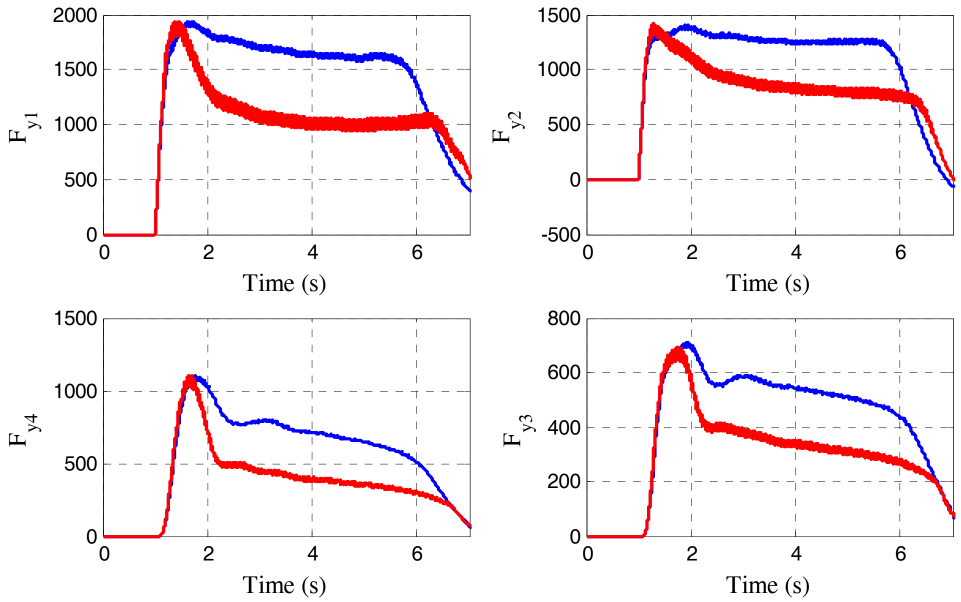

Figure 4.46 : Lateral tire forces in simulation scenario 4.

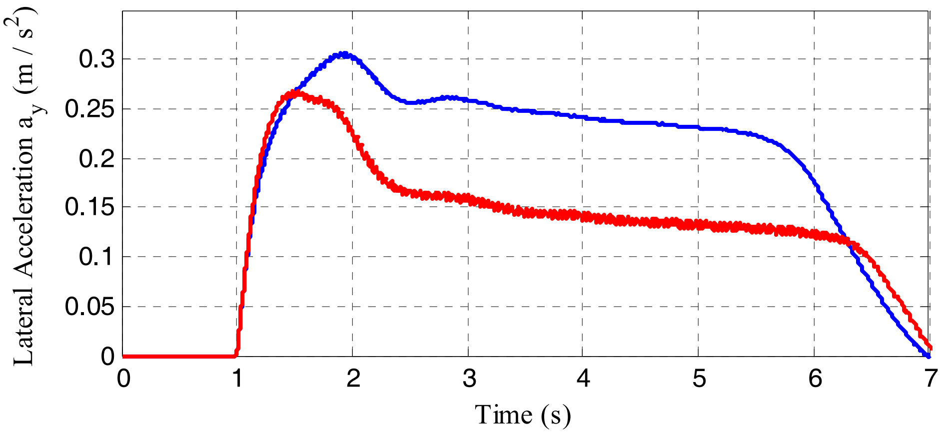

Figure 4.47 : Lateral accelerations in simulation scenario 4.

4.6 Chapter Summary

In this chapter, the sliding mode based extremum seeking algorithm is adapted as the self-optimization routine that seeks the peak point of the force-slip curve without needing knowledge of the optimum slip information. The proposed algorithm incorporates driver steering input information into the optimization procedure to determine the operating region of the tires on the tire force-slip ratio characteristics curve. This is a novel approach in ABS control area and constitutes the main contribution of the study to the existing literature on ABS control. The algorithm operates the tires near the peak point of the force-slip curve during emergency straight line braking. When the driver demands lateral motion in addition to emergency braking, the operating regions of the tires are modified for improving lateral stability of the vehicle also. It is shown using a detailed simulation study with a validated vehicle model that, during cornering, while getting large braking forces, lateral tire forces can be improved considerably and hence the cornering capability of the vehicle can be enhanced significantly.

5. EXTREMUM SEEKING BASED ENERGY MANAGEMENT STRATEGY FOR HYBRID ELECTRIC VEHICLES

5.1 Introduction

An energy management control strategy for a parallel hybrid electric vehicle based on the extremum seeking algorithm (ESA) for splitting torque between the internal combustion engine and electric motor is proposed in this chapter.

Rule based solutions as given in [63-70] are simple and easy to implement. However, this kind of energy management strategy requires correct tuning of all the controller parameters in order to assure the correct behavior of the algorithm. The approach is not easily exportable to other vehicle configurations. Instantaneous optimization methods based on equivalent consumption minimization strategy (ECMS) as given in [74-78] provide a real time, near optimal solution. Since the electrical energy and the fuel energy are not directly comparable, an equivalence factor is needed to calculate equivalent fuel consumption value. The performance of the control algorithm depends heavily on the calculation of the equivalence factor. An error in calculating the equivalence factor will affect the performance of the controller considerably

In this chapter, an instantaneous optimization procedure based on the extremum seeking method is proposed where the algorithm searches optimum torque distribution between the available power sources for maximum powertrain efficiency. Different than rule based controllers as in [63-70], the algorithm possesses optimality criterion as it searches for the maximum powertrain efficiency. It is different from the algorithms given in [74-78], since it does not use ECMS there is no need to calculate an equivalence factor

The ESA strategy presented here aims at maximizing overall powertrain efficiency of a parallel HEV during various driving cycles. An upper level controller decides first the operation mode such as regenerative braking, EM only, ICE only, or ICE plus EM-charge modes. In this study, engine downsizing is not considered in the modeling of the hybrid powertrain. The selected internal combustion engine is sufficient to drive the vehicle alone in high power demands; hence, the control algorithm does not include the EM power assist mode. In the ICE plus EM-charge mode, optimum torque distribution between the internal combustion engine and the electric motor is determined via the extremum seeking algorithm that searches for maximum powertrain efficiency. Various constraints are considered during the control process, e.g. in order to prevent full depletion or overcharge of the battery, the battery state of charge value (*SOC*) is limited. In order to evaluate performance of the proposed algorithm, its results are compared with the dynamic programming (DP) solution, which is used as a benchmark of the minimum attainable fuel consumption values. The comparison of the DP results with the proposed algorithm shows that the ESA with its two level online control structure with powertrain efficiency maximization manages to get substantial fuel consumption improvement. The main goal of the ESA algorithm given in this chapter is to maximize powertrain efficiency and hence to improve fuel consumption. Emission reduction will be studied in a future study and takes place indirectly here. In the EM only mode of operation, there are no emissions from the ICE. In the ICE+EM-charge mode, the ICE operates at a higher torque level where the emission levels are usually lower.

The rest of the chapter is organized as follows. In Section 5.2, models of the ICE, EM, battery and vehicle dynamics are introduced. In Section 5.3, the upper level controller and the extremum seeking algorithm, which is part of the lower level controller, are introduced. The dynamic programming solution applied to HEV is presented in Section 5.4. The detailed simulation study in Section 5.5 shows the effectiveness of the proposed algorithm. The chapter ends with conclusions.

5.2 Hybrid Electric Vehicle Model

A parallel HEV model is developed for the study. In Figure 5.1, the schematic representation of the powertrain is shown. For calculation of ICE efficiency and fuel consumption, the efficiency map shown in Figure 5.2 is used.

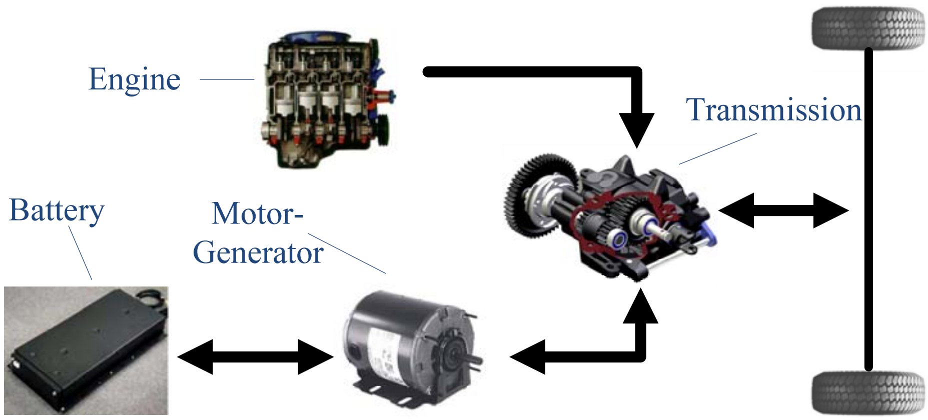

Figure 5.1 : Parallel hybrid electric vehicle powertrain model.

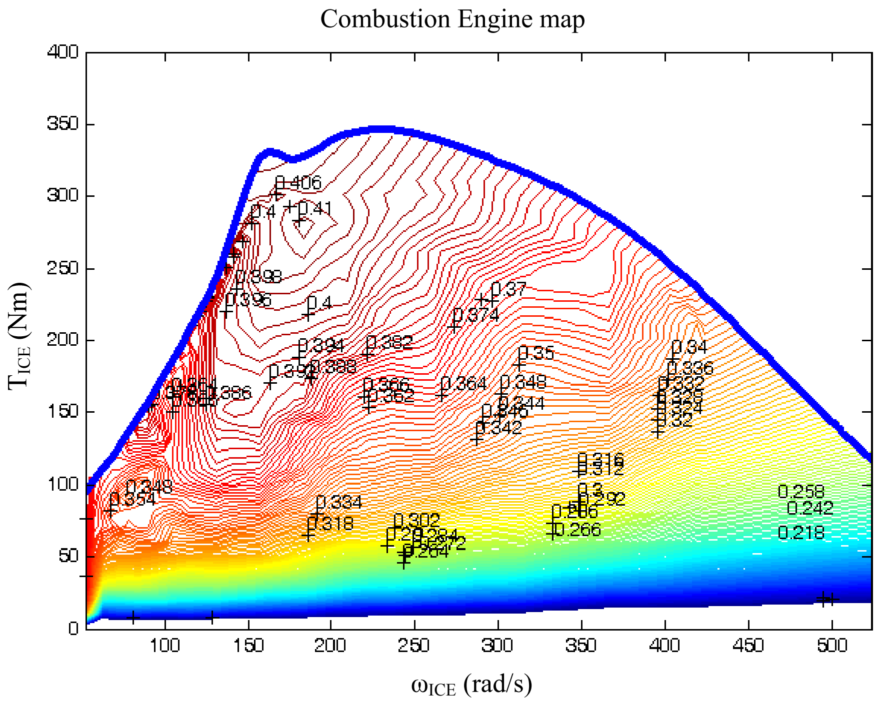

Figure 5.2 : Representative ICE efficiency map.

The controller demands from the ICE the torque command $T_{ice,cmd}$. The dynamics of the ICE is simply modeled as a first order system between the torque command input and the actual ICE torque T_{ice} given as

$$\dot{T}_{ice} = \frac{T_{ice,cmd} - T_{ice}}{\tau_{ice}} \tag{5.1}$$

where τ_{ice} is the time constant of the ICE. For calculation of the fuel consumption, fuel power P_{fuel} is calculated as

$$P_{fuel} = \frac{T_{ice}\omega_{ice}}{\eta_{ice}} \tag{5.2}$$

where ω_{ice} is the engine angular speed, $T_{ice}\omega_{ice}$ is the ICE power, and η_{ice} is the engine efficiency calculated from the efficiency map shown in Figure 5.2. The rate of the fuel usage $\dot{m}_f$ is calculated as given in **(5.3)**.

$$\dot{m}_f = \frac{P_{fuel}}{H_u} \tag{5.3}$$

where H_u is the lower heating value for the gasoline. Fuel consumption m_f is calculated by integrating $\dot{m}_f$.

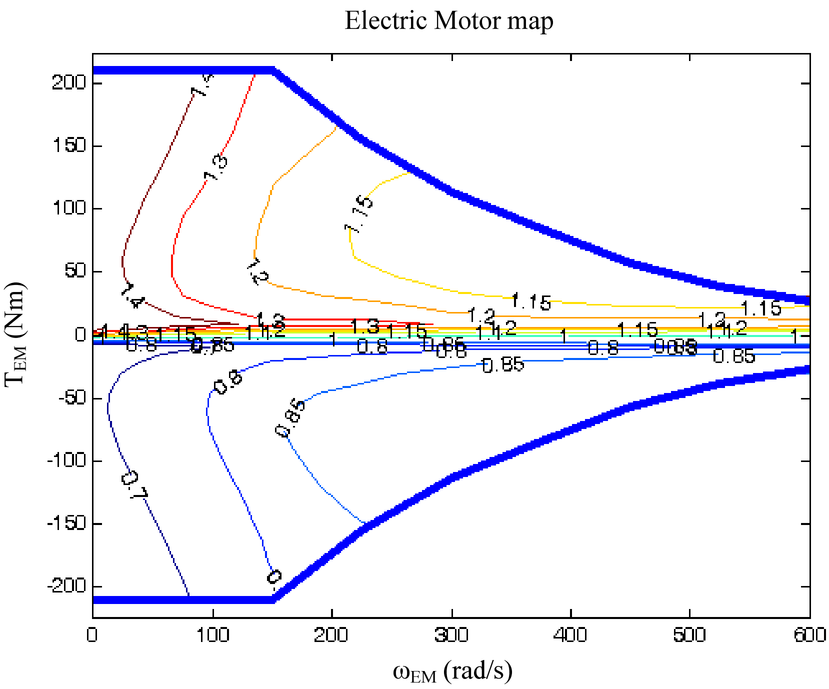

Figure 5.3 : Representative EM efficiency map in [85].

For calculation of the EM efficiency, the efficiency map shown in Figure 5.3 is used. The controller demands from EM $T_{em,cmd}$, which is the commanded torque value. The electric motor dynamics is assumed to be a first order model here. The actual EM torque T_{em} is then calculated from **(5.4)** where τ_{em} is the time constant.

$$\dot{T}_{em} = \frac{T_{em,cmd} - T_{em}}{\tau_{em}} \tag{5.4}$$

The power value, which is taken from the battery while discharging or placed into the battery while charging is calculated as

$$P_t = T_{em}\omega_{em}\eta_{em} \tag{5.5}$$

where ω_{em} is the EM angular speed, $T_{em}\omega_{em}$ is the power generated by the EM and η_{em} is the electric motor efficiency calculated from efficiency map shown in Figure 5.3. In **(5.5)** electric motor efficiency is multiplied both for discharging and charging cases since as shown in Figure 5.3, the efficiency values are less than 1 during the charging case.

Before using the electric motor to drive the vehicle or to charge the batteries in its generator mode, the charge level of the batteries called state of charge (*SOC*) should be taken into consideration. The *SOC* value is recommended to be kept between specified upper and lower limits by battery manufacturers. As long as the *SOC* level is inside the recommended permissible range, the electric motor can be used to drive the vehicle or to charge the batteries. Use of the battery at an improper *SOC* level outside the recommended permissible range will either decrease the battery life or cause permanent damage to the battery. Charge level of the battery *SOC* is calculated as

$$SOC = \frac{Q}{Q_0} \tag{5.6}$$

where Q is the electric charge and Q_0 is the constant battery nominal capacity. Battery electric charge is the integral of the battery current I

$$\dot{Q} = I \tag{5.7}$$

Basic physical model of the battery can be derived by considering an equivalent circuit of the system given in Figure 5.4, where the battery is represented by an ideal open-circuit voltage source in series with an internal resistance. In Figure 5.4, U_{oc}, R_i, and U are the open-circuit voltage, internal resistance, and terminal voltage, respectively.

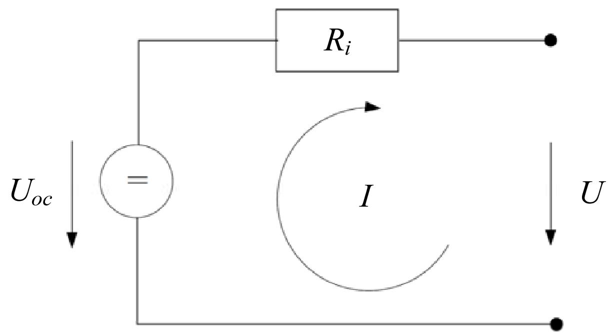

Figure 5.4 : Equivalent circuit of the battery [60].

Kirchhoff's voltage law for the equivalent circuit in Figure 5.4 results in

$$U_{oc} - R_i I = U \tag{5.8}$$

By using $I=I_{dis}$ as the current during discharging and multiplying both side of **(5.8)** with the discharge current I_{dis}, battery terminal power while discharging is calculated as

$$UI_{dis} = P_t = U_{oc} I_{dis} - R_{dis} I_{dis}^{\ 2} \tag{5.9}$$

where R_{dis} is the internal resistance while discharging, $U_{oc} I_{dis}$ is the battery internal power and $R_{dis} I_{dis}^{\ 2}$ is the power loss due to the internal resistance. The discharge current I_{dis} is calculated by solving the following second order equation

$$R_{dis} I_{dis}^{\ 2} - U_{oc} I_{dis} + P_t = 0 \tag{5.10}$$

$$I_{dis} = \frac{U_{oc} - \sqrt{U_{oc}^{\ 2} - 4R_{dis} P_t}}{2R_{dis}} \tag{5.11}$$

While charging, the battery terminal power is written as

$$UI_{chg} = -P_t = U_{oc} I_{chg} + R_{chg} I_{chg}^{\ 2} \tag{5.12}$$

where R_{chg} is the internal resistance while charging and I_{chg} is the current during charging. The negative sign in **(5.12)** is for making the left hand side of the equation positive since the sign of P_t in **(5.5)** is negative during charging. The charge current I_{chg} is calculated by solving the following second order equation

$$R_{chg} I_{chg}{}^{2} + U_{oc} I_{chg} + P_t = 0 \tag{5.13}$$

$$I_{chg} = \frac{-U_{oc} + \sqrt{U_{oc}{}^{2} - 4R_{chg}P_t}}{2R_{chg}} \tag{5.14}$$

For calculation of the discharge current I_{dis} from **(5.11)** or calculation of the charge current I_{chg} from **(5.14)** one should know the values of U_{oc}, R_{dis}, R_{chg}. These are calculated as functions of *SOC* shown in Figure 5.5, Figure 5.6, and Figure 5.7, which are plotted for a constant battery temperature of $T_{bat} = 35^{\circ} C$ for a typical battery.

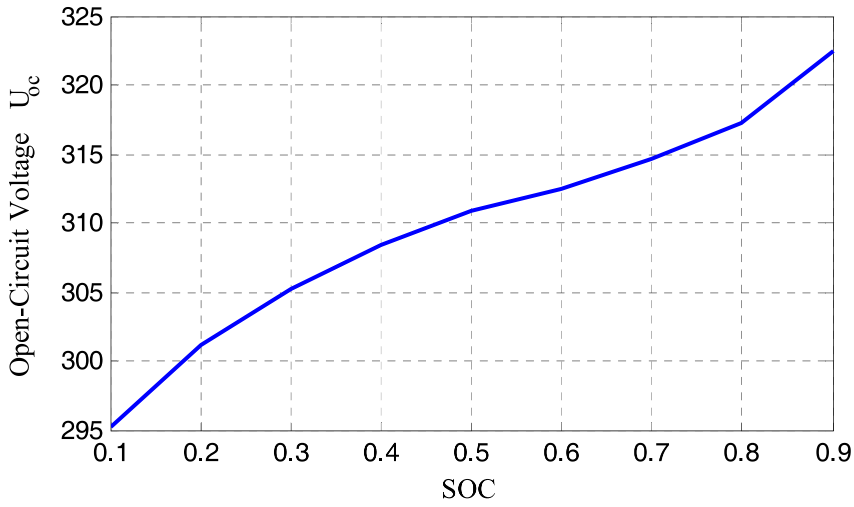

Figure 5.5 : Function of open circuit voltage U_{oc}.

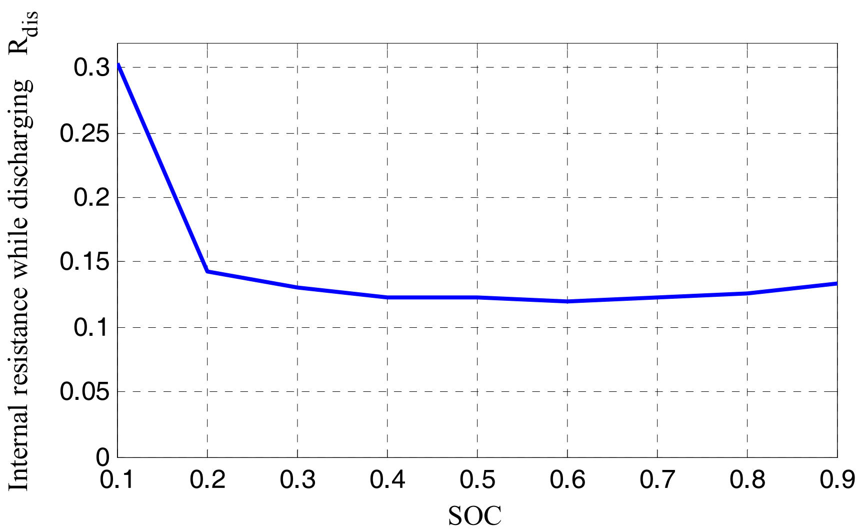

Figure 5.6 : Function of battery discharge resistance R_{dis}.

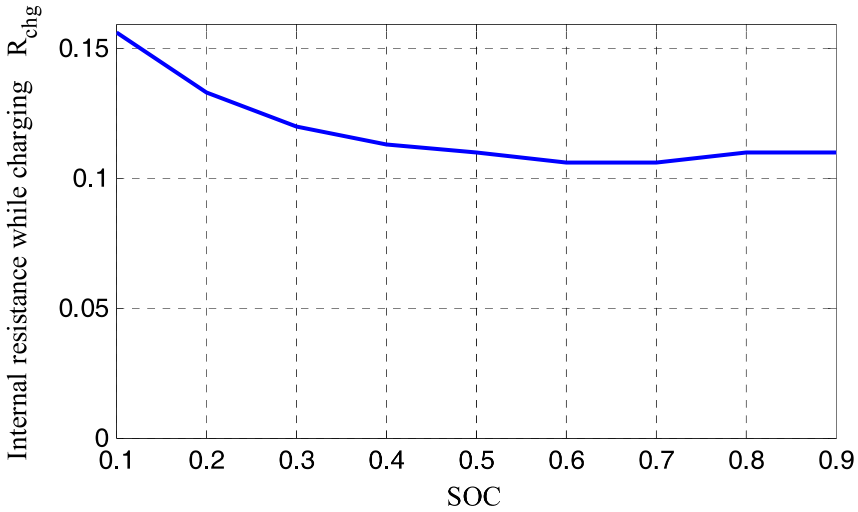

Figure 5.7 : Function of battery charge resistance R_{chg} .

After calculating the current I from **(5.11)** or **(5.14)**, battery SOC value can be calculated from **(5.6)** and **(5.7)**.

Longitudinal vehicle and tire dynamic models are shown in Figure 5.8. The longitudinal vehicle dynamics equation is written as

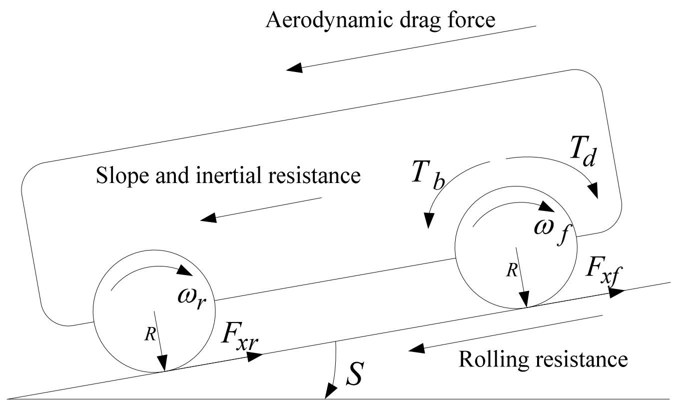

Figure 5.8 : Longitudinal vehicle and tire dynamic models.

$$m\dot{u} = 2F_{xf} + 2F_{xr} - \underbrace{\frac{1}{2}C_d A_f \rho_a u^2}_{\text{aerodynamic drag}} - \underbrace{mgC_{roll}\cos(S)}_{\text{rolling resistance}} - \underbrace{mg\sin(S)}_{\text{slope resistance}} \tag{5.15}$$

where m, u, F_{xf} and F_{xr} are vehicle mass, longitudinal speed, front and rear tire longitudinal forces, respectively. C_d , A_f , ρ_a , C_{roll} and S are the aerodynamic drag coefficient, vehicle frontal area, air density, rolling resistance coefficient and road slope, respectively. Tire rotational equations of motions are

$$I_\omega \dot{\omega}_f = T_d - T_b - RF_{xf} \tag{5.16}$$

$$I_\omega \dot{\omega}_r = -RF_{xr} \tag{5.17}$$

where I_ω, ω_f, ω_r, T_d, T_b, and R are the tire moment of inertia, front tire's angular velocity, rear tire's angular velocity, traction moment, braking moment, and effective tire radius, respectively. The vehicle is assumed to be driving straight, hence no need for lateral dynamics and lateral tire forces. It is assumed that traction and braking moments (regenerative braking) are applied to the front axle only.

Longitudinal tire forces F_{xf} and F_{xr} are calculated by using the Magic Formula Tire Model [86]. This tire model enables realistic simulation of tire forces that occur between the tire and the road during driving. Its input is the longitudinal tire slip ratio, which is a measure of the difference between the tire rotational velocity and translational velocity. When traction or braking moment is applied to the wheels, slip occurs between the tires and the road. Tire longitudinal slip ratio is calculated as

$$\kappa = \frac{\omega R - u}{u} \tag{5.18}$$

where ω is front or rear tire angular velocity. The general form of the tire model is

$$F_x = D\sin[C\arctan\{B\kappa - E(B\kappa - \arctan B\kappa)\}] \tag{5.19}$$

where B is the tire stiffness factor, C the shape factor, D peak value, E the curvature factor.

5.3 Control Algorithm

5.3.1 Upper level controller

During driving, an upper level controller chooses operation mode of the HEV. The modes are as follows: Regenerative braking, EM only, ICE only, and ICE+EM in battery charge modes. The mode decision is accomplished according to the required powertrain power P_{req} and battery charge level *SOC*. The flowchart of the algorithm is shown in Figure 5.9. The flowchart is realized via Matlab/Simulink/Stateflow shown in Figure 5.10. Stateflow is a graphical design and development tool for simulating complex reactive systems based on finite state machine theory.

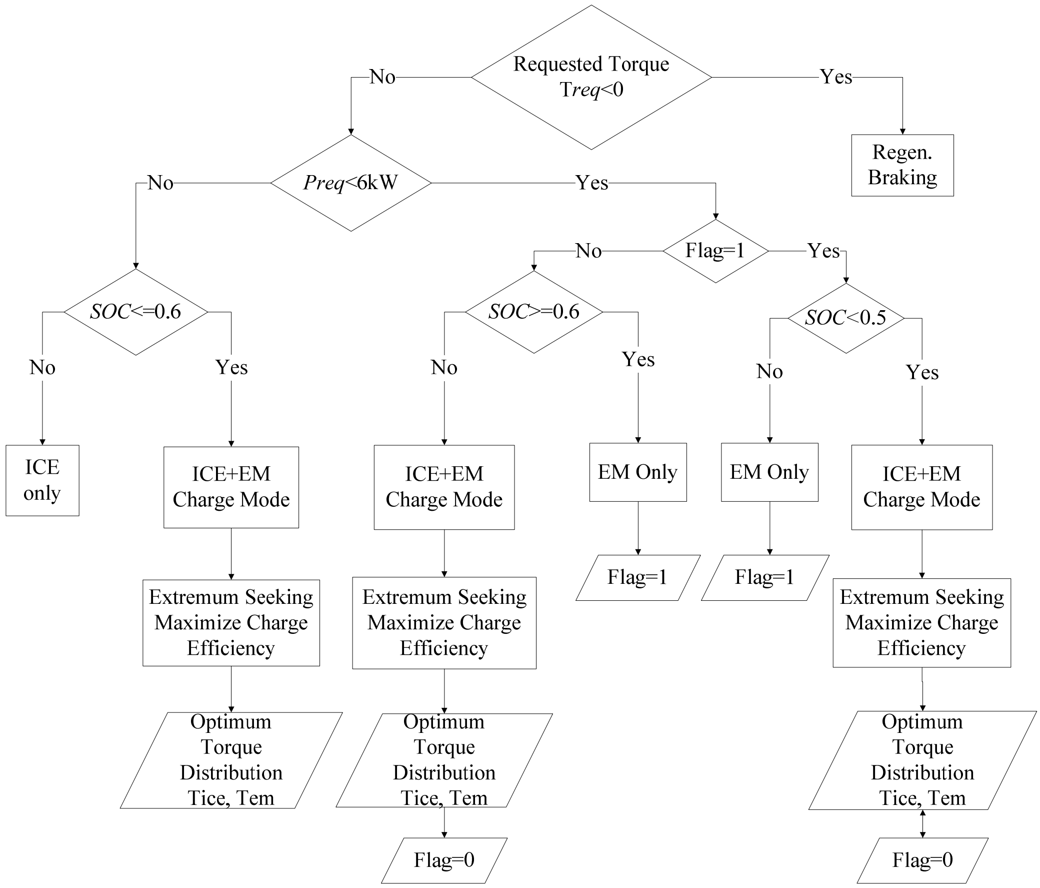

Figure 5.9 : Flowchart of the control algorithm.

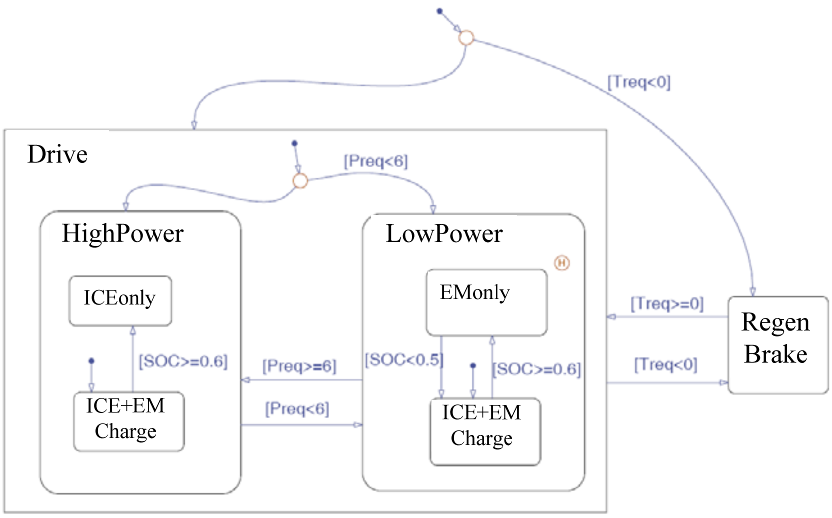

Figure 5.10 : Matlab/Stateflow diagram of the upper level controller.

The logic of the upper level controller is established as follows: When required power is negative, regenerative braking mode will be activated where the EM produces necessary braking power, which charges the battery. The hydraulic brake unit will assist if the torque capacity of the EM is not enough to produce necessary braking torque. When the required power is positive and less than 6 kW, the ICE should not be operated alone in this low power value since it operates inefficiently. EM will provide the required torque alone if there is enough battery charge. If there is not enough battery charge, the electric motor is not operated to drive the vehicle since it will cause over depletion of the battery. For a long battery lifetime, use of battery in improper charge level should be avoided. The EM will be operated in the charge mode in this case. This will increase the battery charge and enable ICE to operate more efficiently due to the additional load from the EM. The torque distribution between ICE and EM-charging will be determined via the Extremum Seeking Algorithm (ESA).

When the power request is above 6 kW and the battery charge is below the nominal value, again EM will be operated in the charge mode to increase *SOC* level and ICE efficiency. When *SOC* is greater than the nominal value, only ICE will provide the necessary torque to drive the vehicle.

In the flowchart given in Figure 5.9, initial value of the Flag variable is Flag=0. The role of the Flag variable is as follows: When Low Power Mode is activated and if $SOC < 0.6$, then the battery will be charged until the charge level reaches to $SOC \geq 0.6$. After that, electric motor will drive the vehicle only, which will decrease again the battery charge level. If charging the battery is initialized as soon as the *SOC* level drops below to 0.6, it will result in the electric motor operating in an oscillating way with charging and discharging the battery repeatedly. To prevent this, the Flag variable is used which provides that the vehicle will be driven by only EM until the battery *SOC* level drops to 0.5 value. In other words, via the Flag variable, EM operates in the charge mode until $SOC \geq 0.6$ and in the discharge mode until $SOC < 0.5$.

By referring to Figure 5.10, where the stateflow diagram of the upper level controller is shown, it is realized that, once “High Power” or “Low Power” Mode is selected, the internal mode decisions (ICE Only, EM only, ICE+EM Charge) are accomplished only according to the battery state of charge value (*SOC*). These internal decisions do not depend on driving conditions or vehicle configurations. They are done to prevent over depletion or over charging the battery. The main concern here is operating the battery in proper charge level for a long life battery operation. As long as the *SOC* level is within the recommended permissible range, the electric motor can be used to drive the vehicle or to charge the batteries. These internal decisions are valid for any driving conditions and vehicle configurations.

The main design problem here is decision between the two main modes ("High Power" or "Low Power"). The decision variable is P_{req} (Driver's demanded power from the powertrain). When $0<P_{req}<6$ kW the Low Power Mode is selected, when $P_{req}>=6$ kW High Power Mode is selected. This threshold (6 kW here) should be determined by considering the chosen vehicle engine in the hybrid powertrain. It should be determined such that when in High Power Mode, ICE Only case is selected, the ICE should operate efficiently for $P_{ice}>6$ kW.

In the upper level controller, the only vehicle dependent decision variable is the threshold value of 6 kW. In fact, the proposed logic can be used without making any significant modification in other mid size (sedan) hybrid electric vehicle applications since this threshold value represents an approximate value separating mid size vehicle engines low power and high power operation areas.

5.3.2 Extremum seeking algorithm

When ICE+EM-charge mode is activated, the torque distribution between the power sources is determined via the Extremum Seeking Algorithm (ESA) for maximizing overall powertrain efficiency. ESA is a derivative free search algorithm that finds the optimum operating point of the chosen performance function. In the HEV problem discussed here, the performance function is chosen as $J=\eta_T$, which is the overall powertrain efficiency. Optimum operating point is the optimum torque distribution between ICE torque and EM-charging load torque.

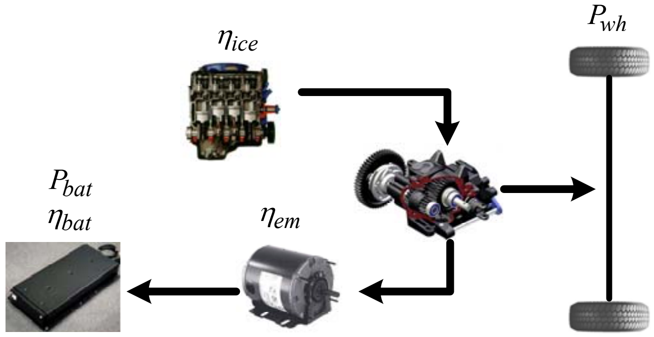

Figure 5.11 : Power flow during battery charging.

The power flow during ICE+EM-charge mode is shown in Figure 5.11 where P_{wh} and P_{bat} are power at the wheel level and battery internal power, respectively. Powertrain efficiency η_T is formulated as

$$\eta_T = \frac{P_{bat} + P_{wh}}{\dfrac{P_{bat}}{\eta_{bat}\eta_{em}\eta_{ice}} + \dfrac{P_{wh}}{\eta_{ice}}} \quad \textbf{(5.20)}$$

where η_{bat} is the battery efficiency calculated as

$$\eta_{bat} = \frac{U_{oc} I}{UI} = \frac{U_{oc}}{U_{oc} + IR_i} \quad \textbf{(5.21)}$$

In **(5.20)**, transmission, coupling and differential efficiencies are neglected due to their relatively constant and high values. Hence, it is considered that η_T depends only on ICE and EM operating points. Then, performance function J can be formulated as

$$J = \eta_T\left(T_{ice}, \omega_{ice}, T_{em}, \omega_{em}\right) \quad \textbf{(5.22)}$$

Since there is a relation between ICE and EM torques as

$$T_{ice} + T_{em} = T_{req} \quad \textbf{(5.23)}$$

and considering that $\omega_{ice} = \omega_{em}$ in the parallel HEV powertrain model, **(5.22)** can be written as

$$J = \eta_T\left(T_{req}, T_{em}, \omega_{em}\right) \quad \textbf{(5.24)}$$

In the sliding mode based extremum seeking algorithm formulation given in [4] a sliding surface is selected, which forces the objective function to follow a time increasing function. For the optimization parameter, a discontinuous switching function is selected. This methodology is adapted here for the powertrain efficiency function maximization. Optimum value of the EM torque T_{em} in **(5.24)** is searched via ESA. The sliding surface variable s is selected as

$$s = \eta_T \left(T_{req}, T_{em}, \omega_{em}\right) - o(t) \tag{5.25}$$

where $o(t)$ is taken as a positive time increasing function. The aim of selecting the sliding surface as in **(5.25)** is to force η_T to follow the time increasing positive function $o(t)$, in the direction of its maximum value. Taking the time derivative of s in **(5.25)**, one obtains

$$\dot{s} = \frac{\partial \eta_T}{\partial T_{req}} \dot{T}_{req} + \frac{\partial \eta_T}{\partial T_{em}} \dot{T}_{em} + \frac{\partial \eta_T}{\partial \omega_{em}} \dot{\omega}_{em} - \dot{o} \tag{5.26}$$

When the convergence rate of the extremum seeking algorithm is much faster than the change of the driver torque request, it can be considered that the contribution of $\frac{\partial \eta_T}{\partial T_{req}} \dot{T}_{req}$ in **(5.26)** is relatively small with respect to the other terms. The convergence rate of the extremum seeking is shown in Figure 5.18 where it is shown that the algorithm converges in approx. 0.2 sec. Filtering the driver's sudden torque request fluctuations and considering that torque request changes much slower than the convergence rate shown in Figure 5.18, **(5.26)** can be written as

$$\dot{s} = \frac{\partial \eta_T}{\partial T_{em}} \dot{T}_{em} + \frac{\partial \eta_T}{\partial \omega_{em}} \dot{\omega}_{em} - \dot{o} \tag{5.27}$$

Theorem: Assuming that an upper bound can be assigned for the gradient value $\partial \eta_T / \partial \omega_{em}$ as follows

$$\left| \frac{\partial \eta_T}{\partial \omega_{em}} \right| < \overline{U} \tag{5.28}$$

By selecting $\dot{o}$ as

$$\dot{o} = -\overline{U} \left| \dot{\omega}_{em} \right| + \rho_0 \tag{5.29}$$

and the update law for T_{em} as

$$\dot{T}_{em} = M\mathrm{sgn}\left[\sin\left(\frac{\pi s}{\gamma}\right)\right] \tag{5.30}$$

then it is guaranteed to keep η_T increase and converge to the maximum efficiency value. In **(5.29)** and **(5.30)** ρ_0, M and γ are positive constants and the function sgn(x) is defined as

$$\mathrm{sgn}(x) = \begin{cases} 1 & \text{if } \; x > 0; \\ 0 & \text{if } \; x = 0; \\ -1 & \text{if } \; x < 0. \end{cases} \tag{5.31}$$

Proof: By combining **(5.26)** and **(5.30)** one gets

$$\dot{s} = \frac{\partial \eta_T}{\partial T_{em}} M\mathrm{sgn}\left[\sin\left(\frac{\pi s}{\gamma}\right)\right] + \frac{\partial \eta_T}{\partial \omega_{em}}\dot{\omega}_{em} - \dot{o} \tag{5.32}$$

Assuming that at the start of optimization the value of s in **(5.25)** is between the values of γ and 2γ

$$\gamma < s(0) < 2\gamma \tag{5.33}$$

Then, on that interval, the following mathematical expression is true

$$\mathrm{sgn}\left[\sin\left(\frac{\pi s}{\gamma}\right)\right] = -\mathrm{sgn}(s-\gamma) = \mathrm{sgn}(s-2\gamma) \tag{5.34}$$

By combining **(5.32)** and **(5.34)** one gets

$$\dot{s} = -\frac{\partial \eta_T}{\partial T_{em}} M\,\mathrm{sgn}(s-\gamma) + \frac{\partial \eta_T}{\partial \omega_{em}}\dot{\omega}_{em} - \dot{o} \tag{5.35}$$

Defining a variable λ_1 as

$$\lambda_1 = s - \gamma \tag{5.36}$$

$$\dot{\lambda}_1 = \dot{s} \tag{5.37}$$

Then from **(5.35)**

$$\dot{\lambda}_1 = -\frac{\partial \eta_T}{\partial T_{em}} M \,\mathrm{sgn}(\lambda_1) + \frac{\partial \eta_T}{\partial \omega_{em}} \dot{\omega}_{em} - \dot{o} \tag{5.38}$$

$$\lambda_1 \dot{\lambda}_1 = -\frac{\partial \eta_T}{\partial T_{em}} M |\lambda_1| + \frac{\partial \eta_T}{\partial \omega_{em}} \dot{\omega}_{em} \lambda_1 - \dot{o} \lambda_1 \tag{5.39}$$

Following inequality can be written from **(5.39)**

$$\lambda_1 \dot{\lambda}_1 \le -\frac{\partial \eta_T}{\partial T_{em}} M |\lambda_1| + \left|\frac{\partial \eta_T}{\partial \omega_{em}}\right| |\dot{\omega}_{em}| |\lambda_1| + \dot{o} |\lambda_1| \tag{5.40}$$

By using **(5.28)** it can be written that

$$\lambda_1 \dot{\lambda}_1 \le -\frac{\partial \eta_T}{\partial T_{em}} M |\lambda_1| + \overline{U} |\dot{\omega}_{em}| |\lambda_1| + \dot{o} |\lambda_1| \tag{5.41}$$

By combining **(5.29)** and **(5.41)**

$$\lambda_1 \dot{\lambda}_1 \le -\frac{\partial \eta_T}{\partial T_{em}} M |\lambda_1| + \rho_0 |\lambda_1| \tag{5.42}$$

$$\lambda_1 \dot{\lambda}_1 \le -|\lambda_1| \left[\frac{\partial \eta_T}{\partial T_{em}} M - \rho_0 \right] \tag{5.43}$$

As long as

$$\frac{\partial \eta_T}{\partial T_{em}} > \frac{\rho_0}{M} \tag{5.44}$$

is true, from **(5.43)** it can be written that

$$\lambda_1 \dot{\lambda}_1 < 0 \,;\, \lambda_1 \to 0 \,;\, s \to \gamma \tag{5.45}$$

Hence, after a finite time interval $s = \gamma$ is obtained. From **(5.25)**

$$\eta_T \left(T_{req}, T_{em}, \omega_{em} \right) = o(t) + \gamma \tag{5.46}$$

$$\dot{\eta}_T \left(T_{req}, T_{em}, \omega_{em} \right) = \dot{o} > 0 \tag{5.47}$$

Hence, efficiency η_T will increase with the slope of $\dot{o}$, specified to be positive, converging to the maximum value. The condition **(5.44)** can be interpreted as the gradient value being larger than a constant value ρ_0/M. As long as the gradient is larger than ρ_0/M, extremum seeking algorithm will force the objective function increase. When the condition **(5.44)** is not true but

$$\frac{\partial \eta_T}{\partial T_{em}} < -\frac{\rho_0}{M} \tag{5.48}$$

then by combining **(5.32)** and **(5.34)**

$$\dot{s} = \frac{\partial \eta_T}{\partial T_{em}} M \operatorname{sgn}(s - 2\gamma) + \frac{\partial \eta_T}{\partial \omega_{em}} \dot{\omega}_{em} - \dot{o} \tag{5.49}$$

and continuing the analysis as before, it can be shown that after a finite time interval, $s = 2\gamma$ will be obtained. Then,

$$\eta_T\left(T_{req}, T_{em}, \omega_{em}\right) = o(t) + 2\gamma \tag{5.50}$$

Again, efficiency η_T will increase with the slope of $\dot{o}$ converging to the maximum value. The analysis can be continued not for only **(5.33)** but for any initial value of $s(0)$. Hence, it is concluded that whether **(5.44)** or **(5.48)** holds, η_T is increased to the maximum value with the proposed algorithm. When both **(5.44)** and **(5.48)** do not hold, the increasing of the performance function is not guaranteed. By selecting the values of control parameters ρ_0 and M, one defines the operating region of the ESA. By decreasing the size of the region where **(5.44)** and **(5.48)** do not hold, the success of the optimization algorithm is increased. **(End of proof)**

In this manner, extremum seeking algorithm determines electric motor torque value T_{em} by searching for the maximum value of the powertrain efficiency η_T. In **(5.29)**, $\dot{\omega}_{em}$ can be calculated by using differential and transmission ratios and by estimation of front tire angular acceleration $\dot{\hat{\omega}}_f$. In order to estimate $\dot{\hat{\omega}}_f$, **(5.16)** can be used. For the estimation of the tire force $\hat{F}_{xf}$, the tire force observer given in [3] can be used. After T_{em} is calculated by the controller, ICE torque can be calculated from **(5.51)**, since the total powertrain torque should be equal to the desired powertrain torque value. The ESA optimization scheme is shown in Figure 5.12.

$$T_{ice} = T_{req} - T_{em} \tag{5.51}$$

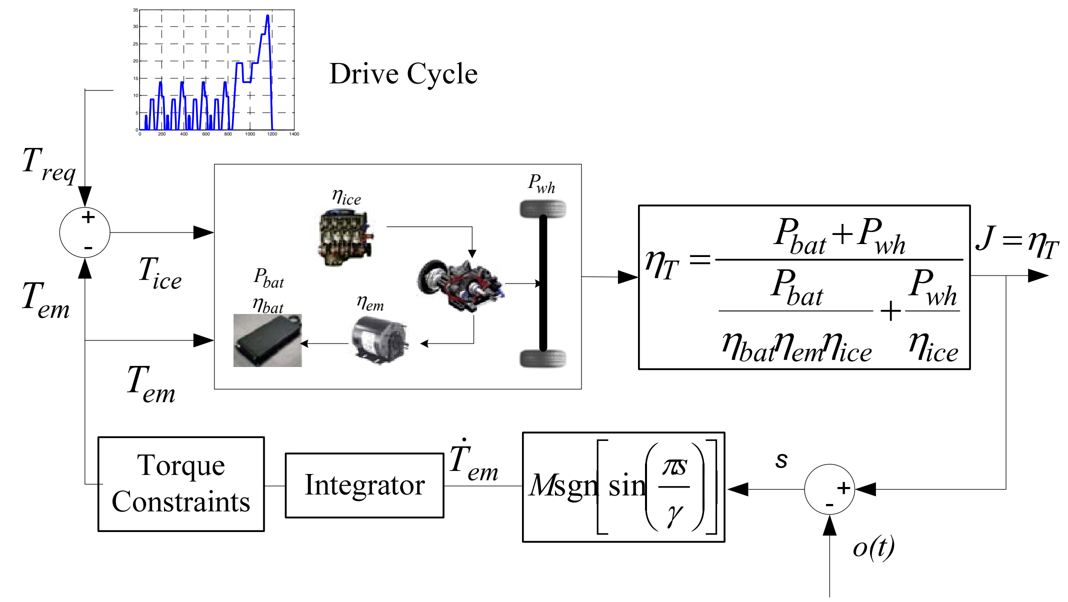

Figure 5.12 : The ESA scheme for efficiency maximization.

5.4 Dynamic Programming

5.4.1 Introduction

In order to show the effectiveness of the proposed extremum seeking algorithm given in the previous section, its results should be compared with the optimal results. An optimal solution calculation is not feasible in a practical implementation as the future driver torque request or the future velocity profile needs to be known. This, of course, is not possible and an optimal solution cannot be used in practice. That is the motivation for and the major advantage of using the proposed extremum seeking algorithm as it provides a fast solution that only uses the current information and does not require the knowledge of future information. For benchmarking and performance evaluation purposes however, an optimal solution based on chosen driving cycle inputs can be calculated and used. The optimal and ideal solution that is calculated can then be compared with the result of the extremum seeking algorithm to see how close the ESA solution is to the ideal, optimal one.

One method for calculating the optimal solution might be evaluating all possible power distributions at each time instant of the drive cycle starting from the beginning to the end. Since a driving cycle lasts hundreds of seconds and at each instant, there are many possibilities that need to be calculated, this method is not effective and conceivable. A more effective choice would be to use Dynamic Programming (DP), which is introduced as follows.

The principle of optimality is given in [87] page 54 as follows:

An optimal policy has the property that whatever the initial state and initial decision are, the remaining decisions must constitute an optimal policy with regard to the state resulting from the first decision.

The following example illustrates the procedure for making a single optimal decision with the aid of the principle of optimality. Considering that the optimum path (e.g. lowest cost) is searched for the route from *b* to *f* as shown in Figure 5.13.

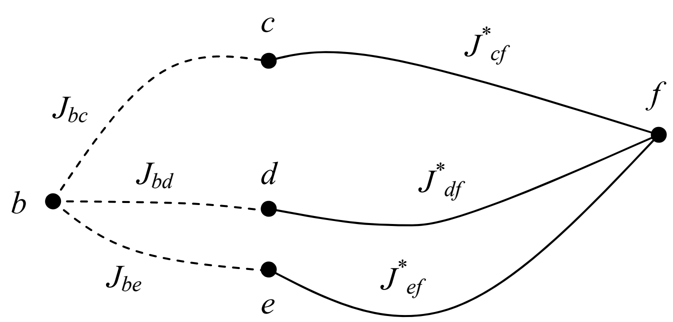

Figure 5.13 : Paths resulting from all allowable decisions at *b* [88].

It is considered that the costs of the routes *c-f, d-f, e-f* are known, in other words the values of J^*_{cf}, J^*_{df}, J^*_{ef} are at hand. Then, the decision must be made among the interval points of *c*, *d*, *e*, when the route starts from *b*. The optimal trajectory that starts at *b* and ends in *f* is found by comparing the following costs

$$\begin{aligned} C^*_{bcf} &= J_{bc} + J^*_{cf} \\ C^*_{bdf} &= J_{bd} + J^*_{df} \\ C^*_{bef} &= J_{be} + J^*_{ef} \end{aligned} \quad \textbf{(5.52)}$$

Optimal path and minimum cost can be calculated as $J^*_{bf} = \min\{C^*_{bcf}, C^*_{bdf}, C^*_{bef}\}$, which determines the next point after starting from *b*. Dynamic programming is a computational technique which extends the above decision making concept to sequences of decisions which together define an optimal policy and trajectory. In the given example above, the costs to the terminal point *f* from the last stages (*c-f, d-f, e-f*) are known, and decision of the route from *b* to one of the points *c*, *d*, *e* is made. The backwards calculation procedure is noticed. This policy is applied for calculation of minimum fuel consumption of the hybrid electric vehicle model. DP calculates optimum power distributions at each time instant by proceeding backwards from the final to the initial stage. It solves one-stage sub problems involving the last stage, last two stages, last three stages ... etc., until the whole driving cycle is covered. This backward procedure decreases the amount of calculations considerably but application of the DP procedure requires that the whole driving cycle should be known in advance.

5.4.2 Application of DP for calculation of minimum fuel consumption

The procedure starts with creating a state space as shown in Figure 5.14 where the states are taken as representing the energy levels stored in the battery. Via the simulations with various driving cycles, it is noticed that the proposed controller resulted in *SOC* deviations that stayed between 0.58 and 0.62 (see Figure 5.24 for example). The state space is created by uniformly discretizing the battery energy level E_{bat} into *n* number of states between $0.58\,E_{cap} < E_{bat} < 0.62\,E_{cap}$ where E_{cap} is the total energy capacity of the battery (equivalent to *SOC*=1 or 100% *SOC*). The initial energy level is selected as $E_0 = 0.6\,E_{cap}$ (equivalent to *SOC*=0.6). In the literature, the final energy level at the end of the drive cycle is selected as constant such as $E_{end} = 0.6\,E_{cap}$, such that the quantity of energy in the rechargeable source will be the same before and after the trip. This is called charge-sustaining strategy. The proposed controller given in the previous section does not force an end point constraint but it keeps *SOC* level in a permissible range. Henceforth, an end point energy level constraint is also not included in DP. If in DP calculations a final battery energy level constraint was used, which is equal to the final *SOC* value of the hybrid electric vehicle with the proposed controller, then the fuel consumption results of the DP would be closer to the hybrid vehicle results. But here, DP calculations are done to get the answer to the following question: “What would be the minimum obtainable fuel consumption, if the battery energy levels remained between $0.58E_{cap}<E_{bat}<0.62E_{cap}$ (Equivalent to $0.58<SOC<0.62$)".

Since states used in DP here are constrained to be between $0.58\,E_{cap} < E_{bat} < 0.62\,E_{cap}$, E_{end} will be very close to $0.6E_{cap}$ here as is desired and it can be assumed that the charge-sustaining strategy is automatically fulfilled. An additional final constraint is therefore not required. The state space of the DP algorithm is shown in Figure 5.14 where T_{end} is the duration of the driving cycle.

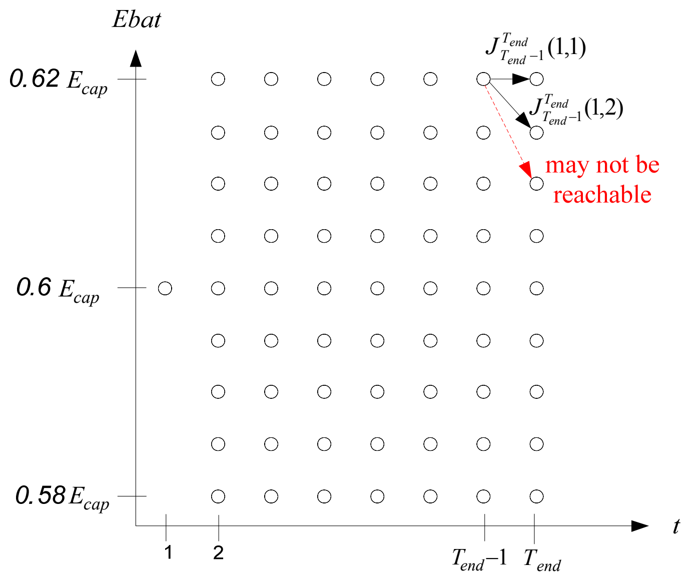

Figure 5.14 : State space of the DP algorithm.

The dynamic programming solution procedure starts with the last stage before the final point, i.e. $t = T_{end} - 1$. Fuel consumption values are calculated for state transitions between the energy levels of stages from $t = T_{end} - 1$ into $t = T_{end}$. The state transition function is given as

$$E_{bat}(t+1) - E_{bat}(t) = -P_{bat}(t)\Delta t \tag{5.53}$$

where $E_{bat}(t)$ and $E_{bat}(t+1)$ are current and next energy levels, respectively. The negative sign is because during charging, the power P_{bat} being applied as a load on the ICE is negative in the formulation and hence the battery energy level increases. Since time is discretized into one second intervals, i.e. Δt =1 s, battery power is calculated from **(5.53)** as follows

$$P_{bat}(t) = -\left(E_{bat}(t+1) - E_{bat}(t)\right) \tag{5.54}$$

EM power P_{em} can be calculated from **(5.54)** by considering EM and battery efficiencies. Since the requested powertrain power P_{req} can be calculated by using the speed profile and vehicle dynamic equations, the ICE power is calculated as

$$P_{ice} = P_{req} - P_{em} \tag{5.55}$$

By using **(5.53)**, **(5.54)**, **(5.55)** and ICE efficiency map, the performance function J, which is fuel consumption here, for the state transitions between $t = T_{end} - 1$ and $t = T_{end}$ can be calculated. Among the state transitions between the first state of $t = T_{end} - 1$ into other states of $t = T_{end}$, the transition with minimum performance function value $J^*_{T_{end}-1}$ is given as

$$J^*_{Tend-1}(1) = \min\left\{J^{T_{end}}_{T_{end}-1}(1,1),\ J^{T_{end}}_{T_{end}-1}(1,2),\ \ldots,\ J^{T_{end}}_{T_{end}-1}(1,n)\right\} \tag{5.56}$$

In **(5.56)**, $J^{T_{end}}_{T_{end}-1}(1,2)$ is the performance function value during the state transition from the first state at $t = T_{end} - 1$ into the second state at $t = T_{end}$ as shown in Figure 5.14.

As shown in Figure 5.14, not all state transitions between t=T_{end}-1 and t=T_{end} are possible due to EM and ICE power limits. Hence, in calculating **(5.56)**, only possible state transitions are considered. The calculation is repeated for state transitions from the other states of $t = T_{end} - 1$ into the states of $t = T_{end}$ as given in **(5.57)**.

$$\begin{aligned}&\text{for } 1 \le k \le n \\ &J^*_{Tend-1}(k) = \min\left\{J^{T_{end}}_{T_{end}-1}(k,1),\ J^{T_{end}}_{T_{end}-1}(k,2),\ \ldots,\ J^{T_{end}}_{T_{end}-1}(k,n)\right\}\end{aligned} \tag{5.57}$$

After calculations in **(5.57)** are completed, the algorithm has determined optimum transitions for each state at $t = T_{end} - 1$ into $t = T_{end}$. Next, calculations are accomplished for the stage of $t = T_{end} - 2$. Among the state transitions between the first state of $t = T_{end} - 2$ into other states of $t = T_{end} - 1$, the transition with minimum fuel consumption is calculated as follows

$$J^*_{Tend-2}(1) = \min \left\{ \begin{array}{l} \left(J^{T_{end}-1}_{T_{end}-2}(1,1) + J^*_{Tend-1}(1)\right), \left(J^{T_{end}-1}_{T_{end}-2}(1,2) + J^*_{Tend-1}(2)\right), \\ \ldots,\ \left(J^{T_{end}-1}_{T_{end}-2}(1,n) + J^*_{Tend-1}(n)\right) \end{array} \right\} \qquad \textbf{(5.58)}$$

Calculation is repeated for the other states of $t = T_{end} - 2$ as given in **(5.59)**.

$$\text{for } 1 \le k \le n$$

$$J^*_{Tend-2}(k) = \min \left\{ \begin{array}{l} \left(J^{T_{end}-1}_{T_{end}-2}(k,1) + J^*_{Tend-1}(1)\right), \left(J^{T_{end}-1}_{T_{end}-2}(k,2) + J^*_{Tend-1}(2)\right), \\ \ldots,\ \left(J^{T_{end}-1}_{T_{end}-2}(k,n) + J^*_{Tend-1}(n)\right) \end{array} \right\} \qquad \textbf{(5.59)}$$

The procedure is repeated for the last three stages, last four stages… etc. Finally, for t=1, the optimum path into t=2 is calculated. When the DP procedure solution is completed, optimum paths for each state value are stored in memory. Next, by proceeding forward from the start, the optimum path can be followed and the optimum solution giving the minimum fuel consumption is determined.

In Appendix C, Matlab M-file is given for calculation of minimum fuel consumption of the HEV model via DP algorithm as introduced above.

5.5 Simulation Study

A detailed simulation study is presented in this section to illustrate the strength of the proposed extremum seeking algorithm based HEV control strategy. In the simulations, a vehicle model with a mass of 1000 kg is chosen. Maximum ICE and EM torques are 350 Nm and 210 Nm as shown in Figure 5.2 and Figure 5.3. Battery energy capacity is 2.4 kWh.

5.5.1 Simulation study 1

The first simulation study will show that extremum seeking algorithm finds maximum powertrain efficiency. In this simulation scenario, vehicle speed and required torque level T_{req} is considered as constant. First, powertrain efficiency values (η_T) are calculated for different torque distributions between the EM and ICE.

Considered torque distribution space for calculation of η_T's is shown in Figure 5.15 where ω_{ICE}=ω_{EM}≈152 rad/s and T_{req}=50 Nm.

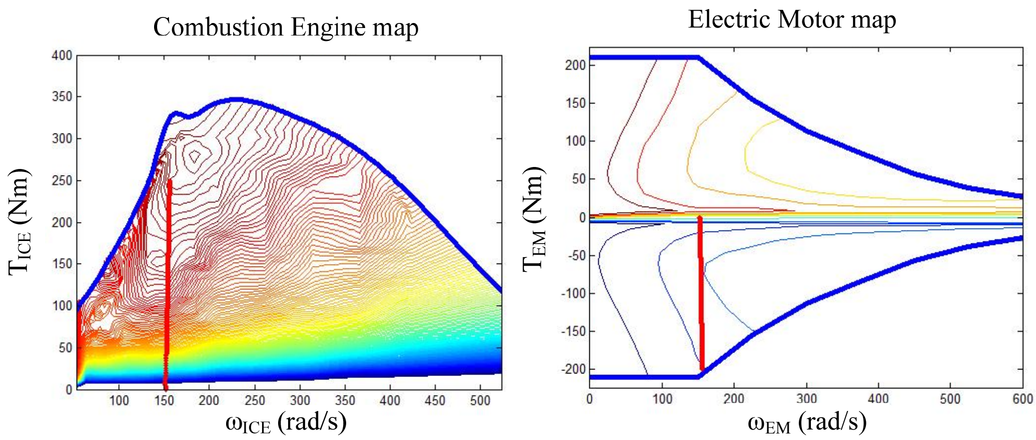

Figure 5.15 : Torque distribution area between ICE and EM.

As shown in Figure 5.15, while EM torque is increased in charging region with negative sign, ICE torque is increased equally to provide overall required torque level of T_{req}=50 Nm. Change of the powertrain efficiency on this torque distribution space is shown in Figure 5.16 where *x* axis is the EM torque values.

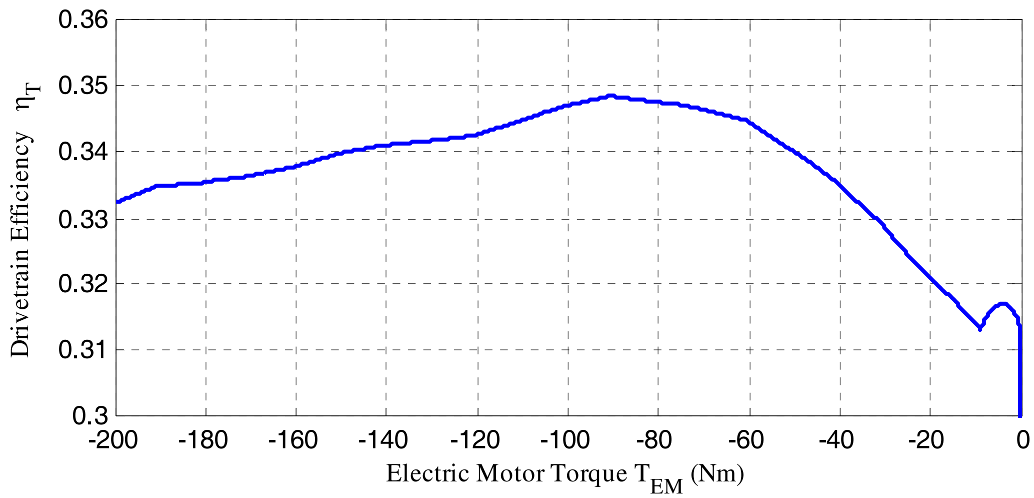

Figure 5.16 : Powertrain efficiency η_T with change of EM torque.

From Figure 5.16 it is shown that the global maximum value of the powertrain efficiency value is η_T=0.3486 which occurs at T_{EM}=-90 Nm.

Next, the extremum seeking control algorithm is applied to the vehicle model to find optimum torque distribution. The torque distribution result of the ESA is shown in Figure 5.17. Change of the powertrain efficiency is plotted in Figure 5.18. Powertrain efficiency value of η_T=0.348 is found in approx 0.2 s. The control algorithm finds optimum torque distribution fast enough, which shows its real-time applicability in a real vehicle.

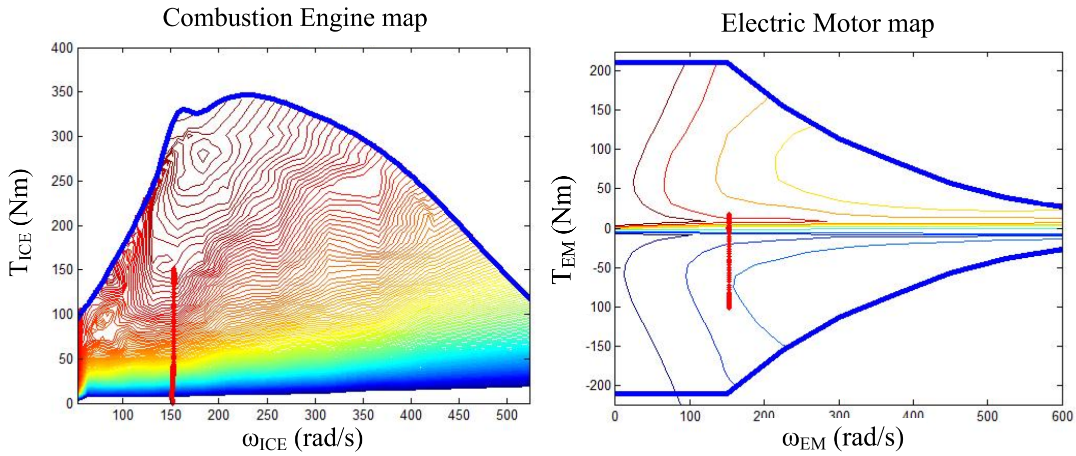

Figure 5.17 : Torque distribution result of the ESA.

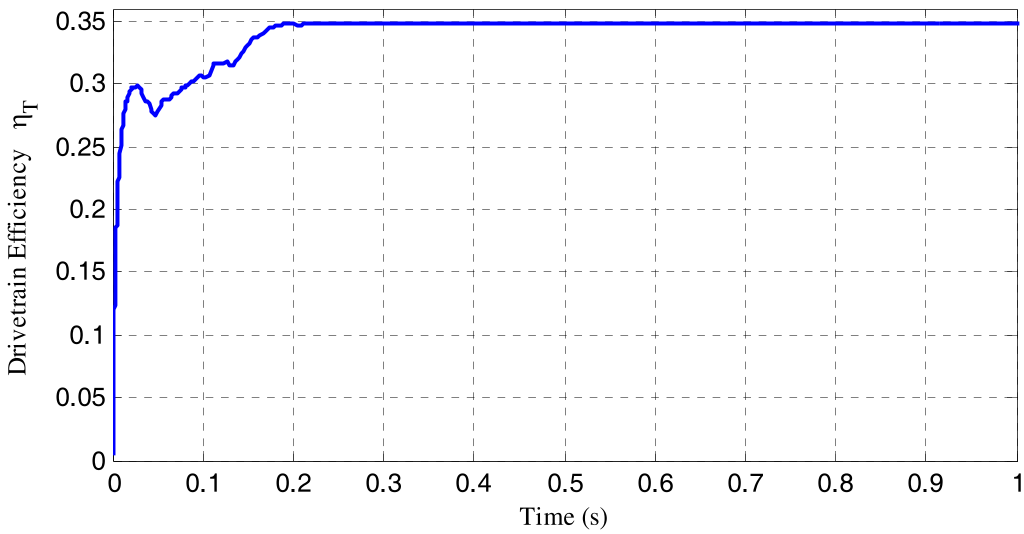

Figure 5.18 : Powertrain efficiency result of the ESA.

5.5.2 Simulation study 2

Simulation results of the hybrid electric vehicle with the proposed control algorithm are compared with those of the conventional vehicle and with those of the dynamic programming solution using standard driving cycles. For an example driving cycle, the New European Driving Cycle (NEDC) speed and gear profiles are shown in Figure 5.19 and Figure 5.20, respectively.

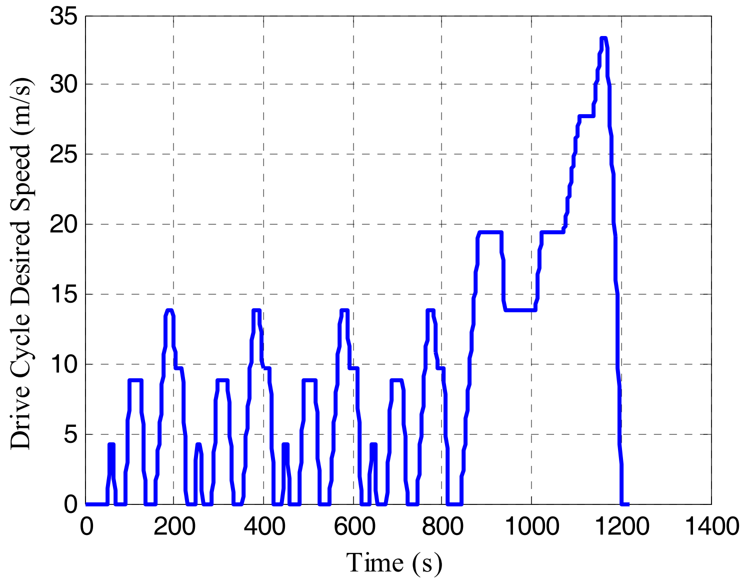

Figure 5.19 : Speed profile for the NEDC in [85].

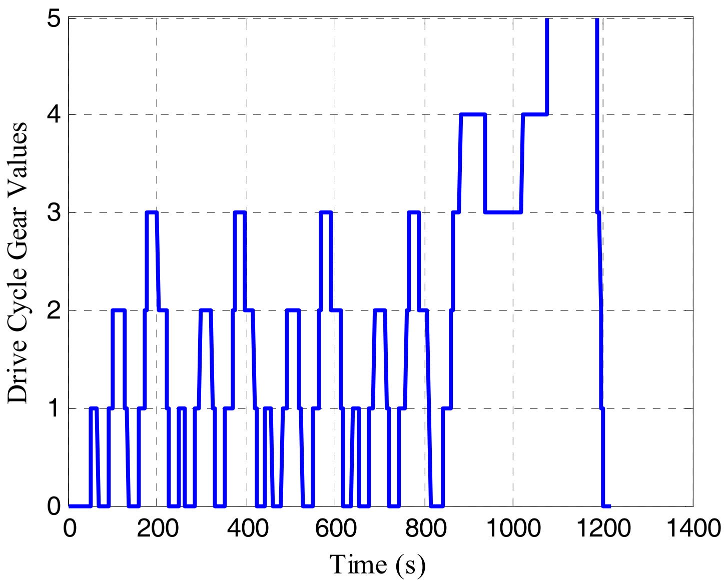

Figure 5.20 : Gear profile for the NEDC in [85].

When the conventional vehicle is driven with the speed and gear profiles shown in Figure 5.19 and Figure 5.20, the ICE operating points are located as shown in Figure 5.21. Only a small fraction of the torque capacity is used in the conventional vehicle and operating points are located in inefficient regions. For the hybrid electric vehicle with the proposed extremum seeking algorithm-based controller, operating points of the ICE and EM for the NEDC are located as shown in Figure 5.22 and Figure 5.23. It is shown that the ICE is operated in points that are more efficient. Change of the corresponding battery charge level *SOC* is shown in Figure 5.24.

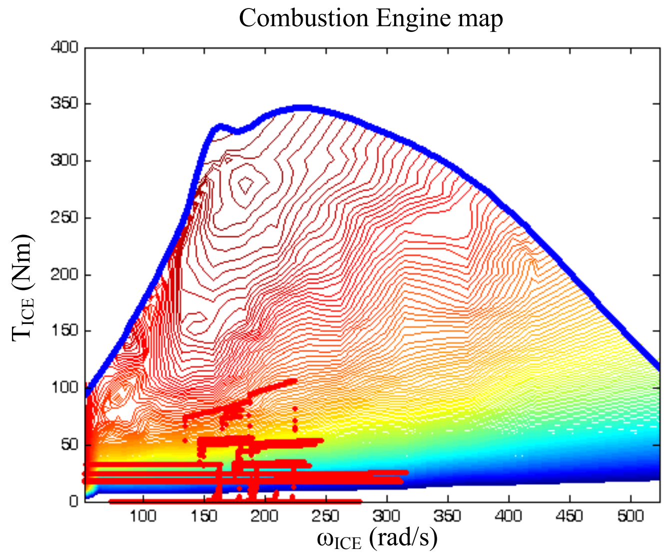

Figure 5.21 : ICE operating points in the conventional vehicle for NEDC.

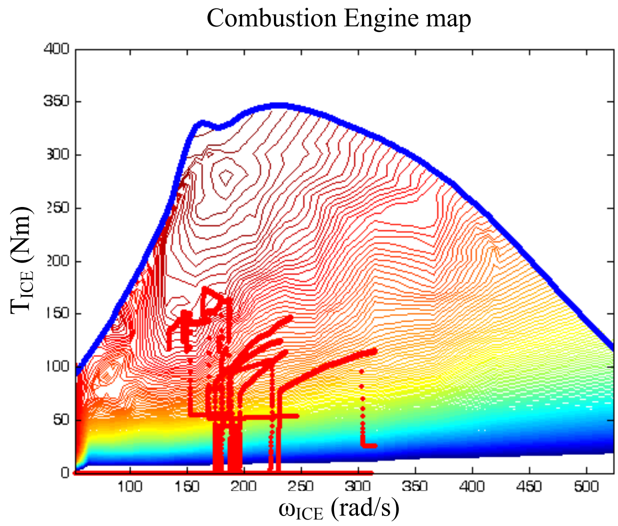

Figure 5.22 : ICE operating points in HEV for NEDC.

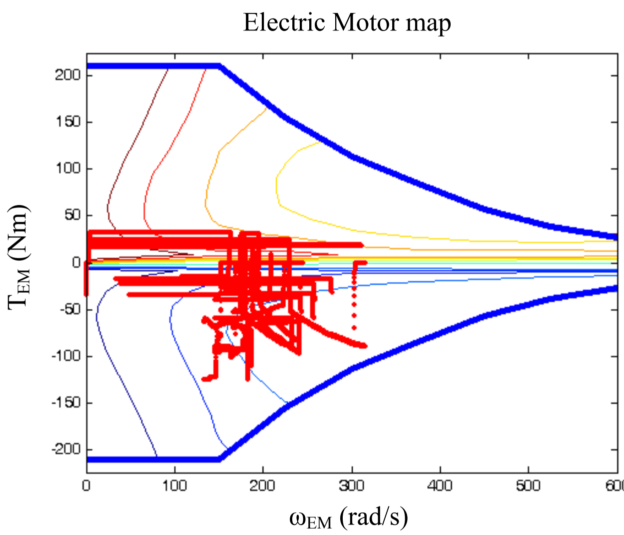

Figure 5.23 : EM operating points in HEV for NEDC.

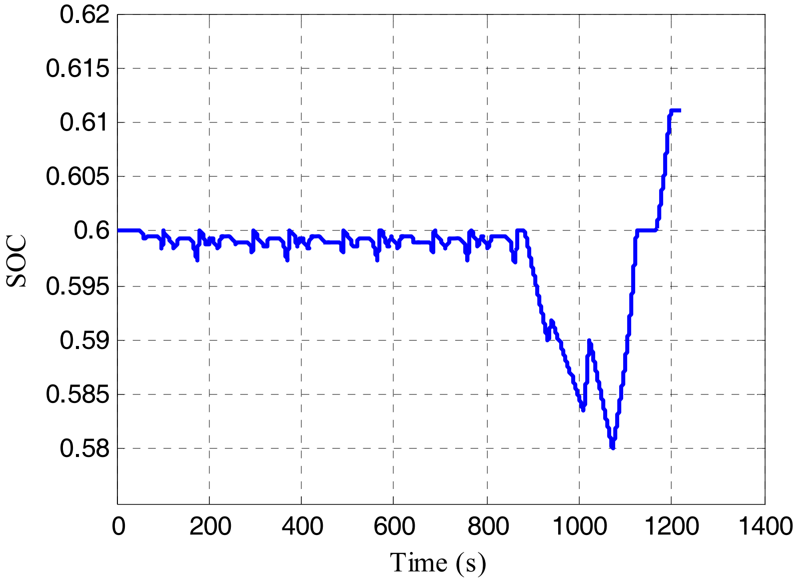

Figure 5.24 : Change of SOC for NEDC.

Dynamic programming results are shown in Figure 5.25, Figure 5.26 and Figure 5.27, where ICE, EM operating regions and change of the normalized battery energy level are shown, respectively. Fuel consumption results of the conventional vehicle, hybrid electric vehicle with the proposed controller and dynamic programming solution are shown graphically in Figure 5.28 and are tabulated in Table 5.1. These results show that the proposed extremum seeking algorithm based controller has superior performance in comparison to the conventional vehicle, with a fuel consumption performance that is close to the ideal DP solution for the NEDC cycle.

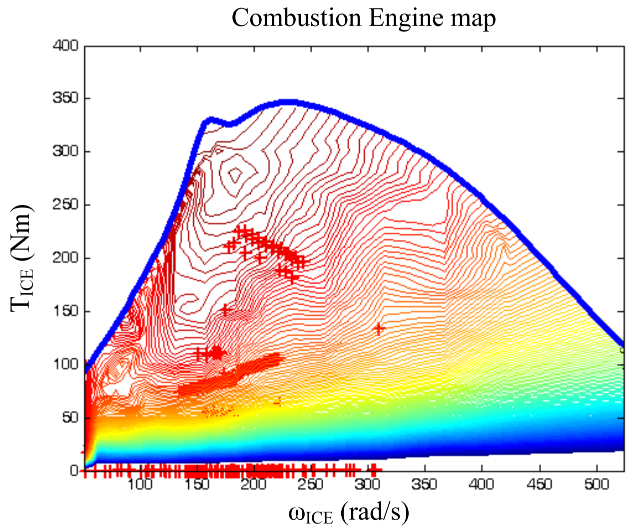

Figure 5.25 : DP solution of ICE operating points for NEDC.

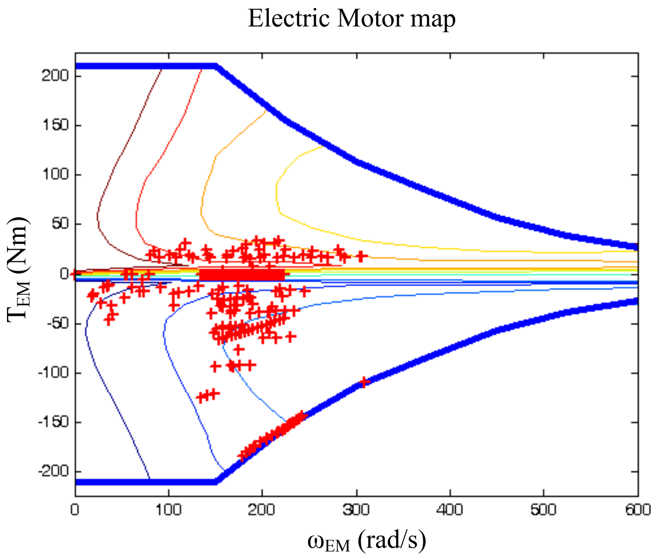

Figure 5.26 : DP solution of EM operating points for NEDC.

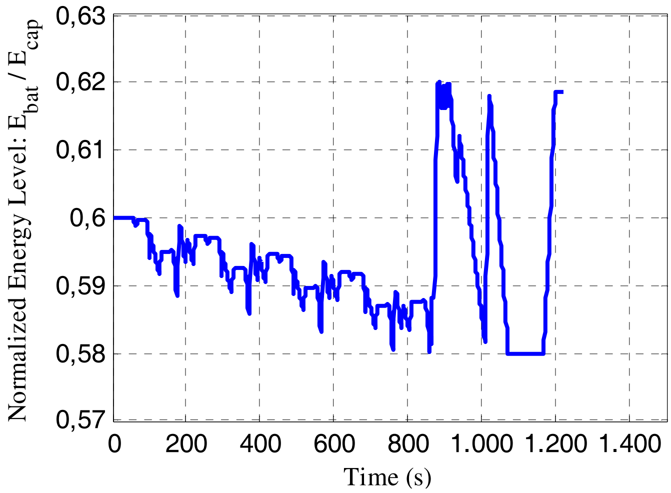

Figure 5.27 : DP solution of normalized battery energy level for NEDC.

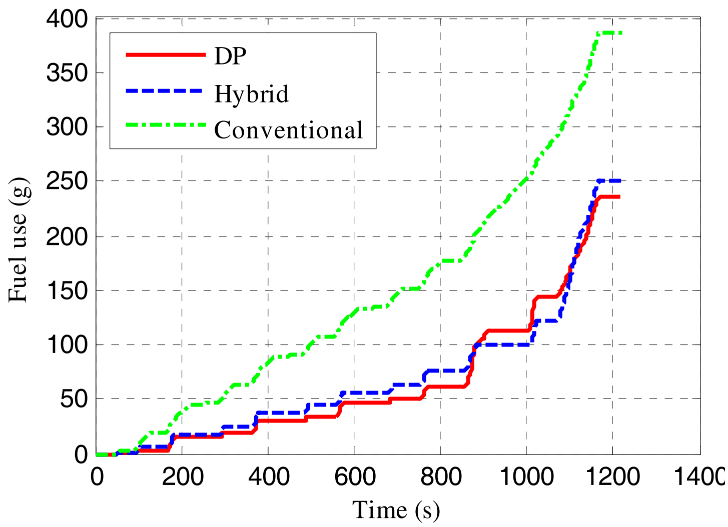

Figure 5.28 : Fuel consumption results for NEDC.

Table 5.1: NEDC fuel consumption results.

Mode	Fuel Consumption (g)	Improvement
Conventional	385.8919	
Hybrid	251.0844	% 34.9
DP	235.5011	% 38.9

Similar results are obtained for other common driving cycles used in practice. In Figure 5.30, Figure 5.31, Figure 5.32 and Table 5.2, simulation results for the ECE_R15 driving cycle shown in Figure 5.29 are given.

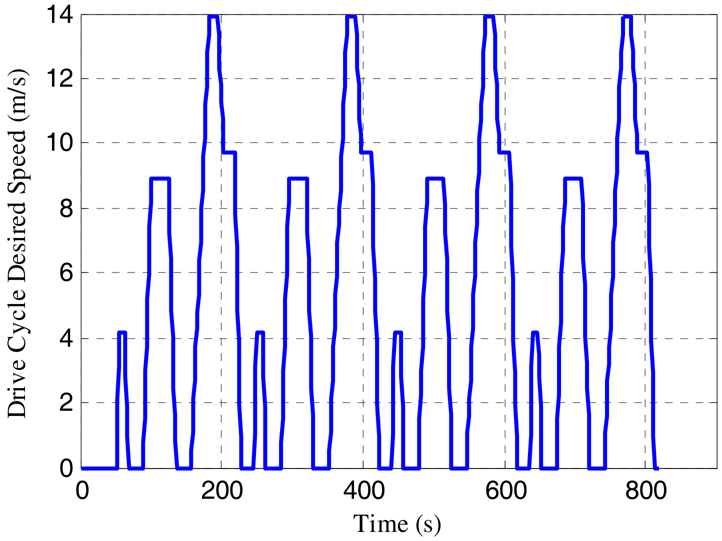

Figure 5.29 : ECE_R15 speed profile [85].

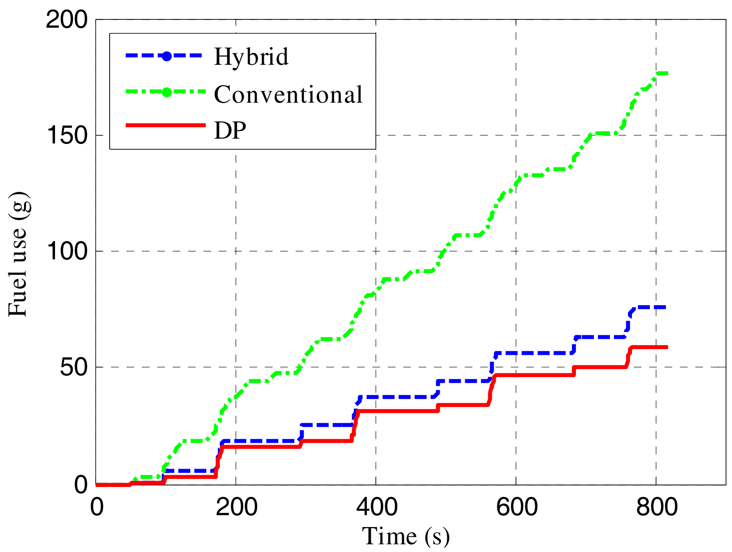

Figure 5.30 : ECE_R15 fuel consumption results

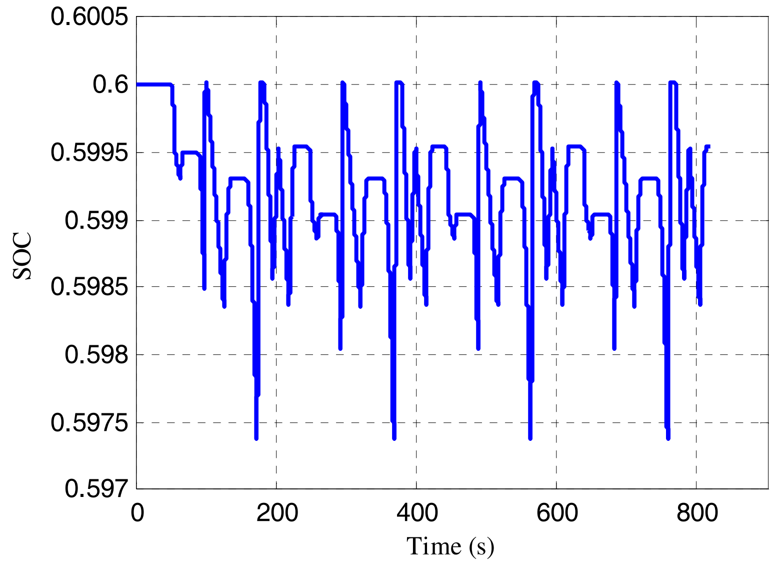

Figure 5.31 : Change of *SOC* for ECE_R15.

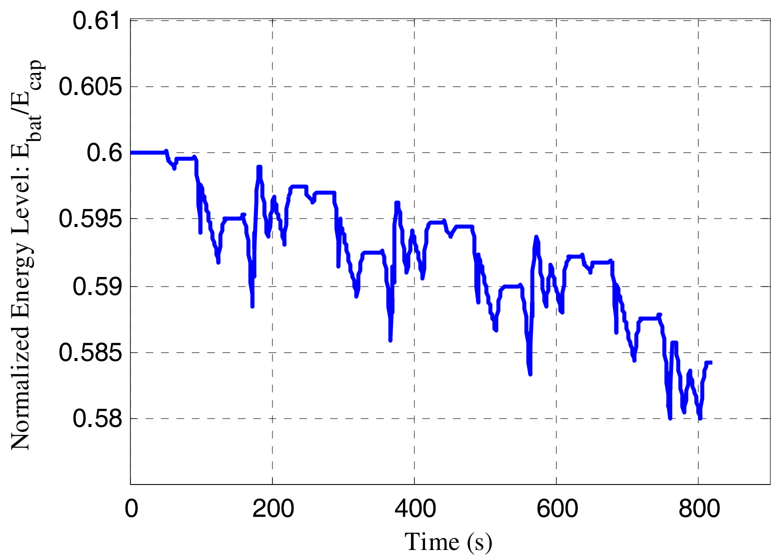

Figure 5.32 : DP solution of normalized battery energy level for ECE_R15.

Table 5.2: ECE_R15 fuel consumption results.

Mode	Fuel Consumption (g)	Improvement
Conventional	176.3690	
Hybrid	75.7823	% 57
DP	59.0676	% 66.5

In Figure 5.34, Figure 5.35, Figure 5.36 and Table 5.3, simulation results for the USA CITY_I driving cycle shown in Figure 5.33 are given.

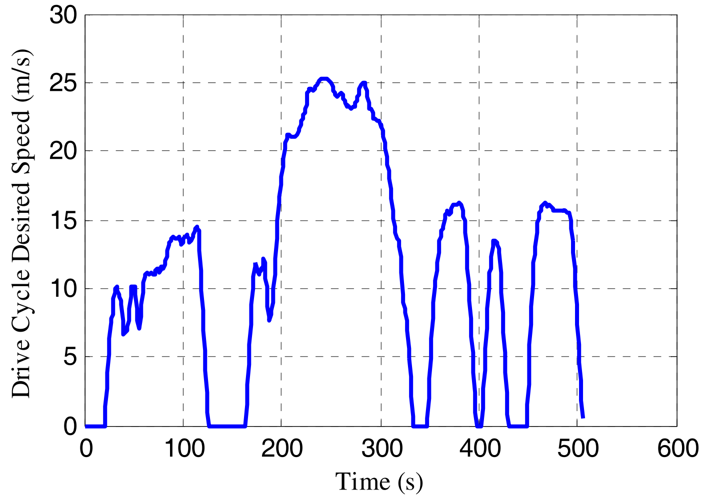

Figure 5.33 : USA CITY_I speed profile [85].

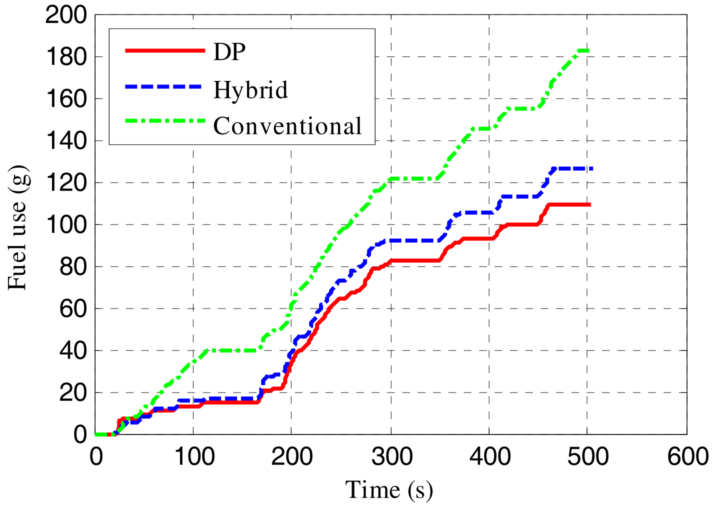

Figure 5.34 : USA CITY_I fuel consumption results.

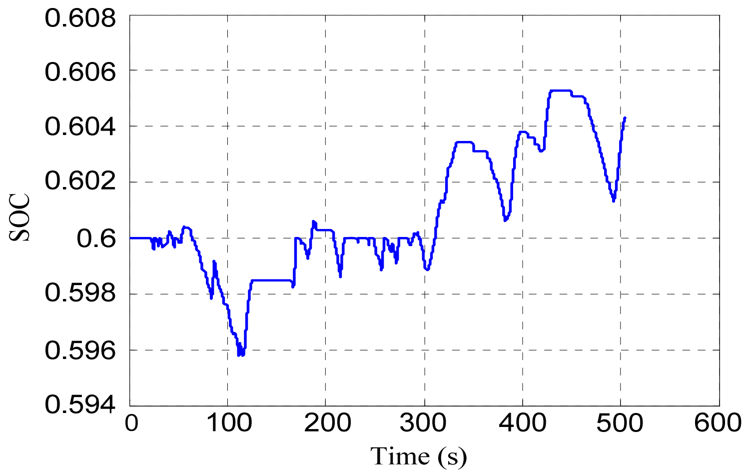

Figure 5.35 : Change of *SOC* for USA CITY_I.

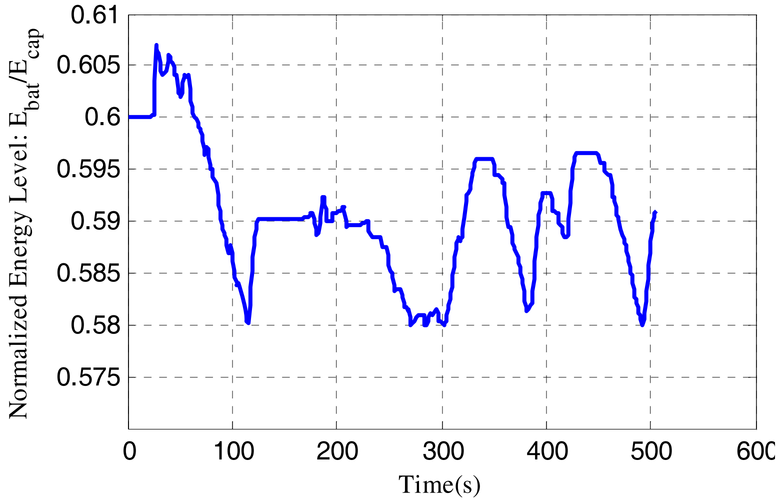

Figure 5.36 : DP solution of normalized battery energy level for USA CITY_I.

Table 5.3:USA CITY_I fuel consumption results.

Mode	Fuel Consumption (g)	Improvement
Conventional	182.3061	
Hybrid	125.9186	% 30.9
DP	109.5202	% 39.9

In all cases, the proposed extremum seeking algorithm based HEV controller achieves better fuel economy as compared to the conventional vehicle. USA CITY_I is a driving cycle with high speeds. For this driving cycle, fuel consumption improvement of the hybrid electric vehicle with the considered control algorithm is % 30.9. On the other hand, ECE_R15 cycle characterizes low speed urban driving scenario where fuel consumption improvement of the HEV is % 57. The results show that in low speed i.e. low power driving situations, the hybrid electric vehicle shows better fuel consumption than high speed driving cycles due to the fact that ICE operates inefficiently in low power but efficiently in high power demands. NEDC driving cycle contains both low speed and high-speed scenarios where fuel consumption improvement is % 34.9 which is between the results of low speed and high speed driving cycles. The extremum seeking algorithm based HEV controller fuel economy results are close to the ideal fuel economy results obtained with the DP solution.

For each driving cycles, the change of the *SOC* variables of the hybrid electric vehicle with the proposed controller and change of the battery energy levels of the

DP calculations are shown. If in DP calculations a final battery energy level constraint was used, which is equal to the final *SOC* value of the hybrid electric vehicle with the proposed controller, then the fuel consumption result of the DP would be closer to the hybrid vehicle results. However, in the paper, a final energy level constraint is not used in DP calculations. DP calculations are done to get the answer to the question of: “What would be the minimum obtainable fuel consumption, if the battery energy levels remained between $0.58E_{cap}<E_{bat}<0.62E_{cap}$”.

5.5.3 Real Time Simulations

Next, simulations are conducted with CarMaker software and dSPACE DS1005 real time hardware. CarMaker is vehicle simulation software with including validated vehicle models. Via CarMaker, these vehicle models can be simulated in different road and driving conditions. Developed control algorithms can be tested on these models. A screen shot of the CarMaker simulation is shown in Figure 5.37.

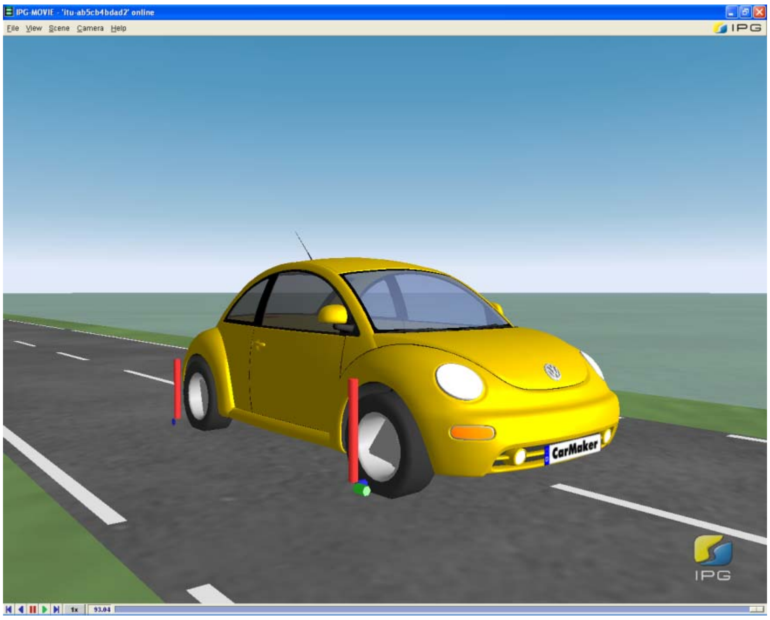

Figure 5.37 : CarMaker simulation screen shot.

The interface of the CarMaker is shown in Figure 5.38. One can choose a vehicle model from different sets of models. Once the model is selected, one can further change parameters of the selected model such as masses, inertias, characteristics of suspension, brake, steering, powertrain systems, etc. Different maneuvers and roads can be defined with this interface.

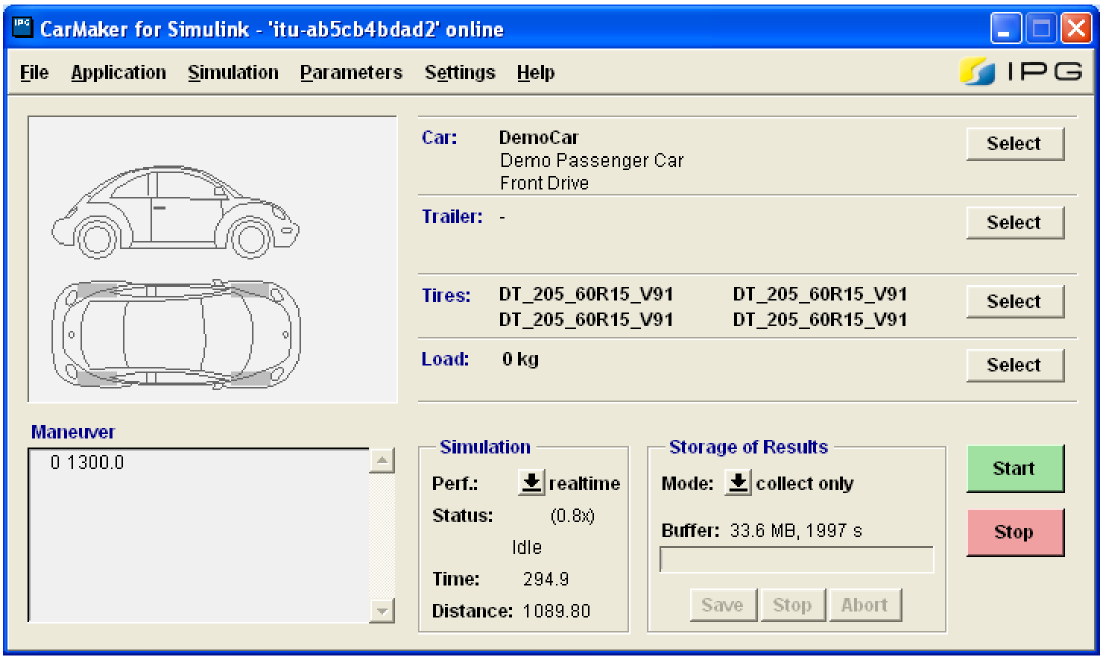

Figure 5.38 : CarMaker interface.

One can integrate his/her control algorithm to a CarMaker vehicle model by using Matlab/Simulink toolbox. A CarMaker vehicle model is represented in Matlab/Simulink environment via S-function blocks as shown in Figure 5.39.

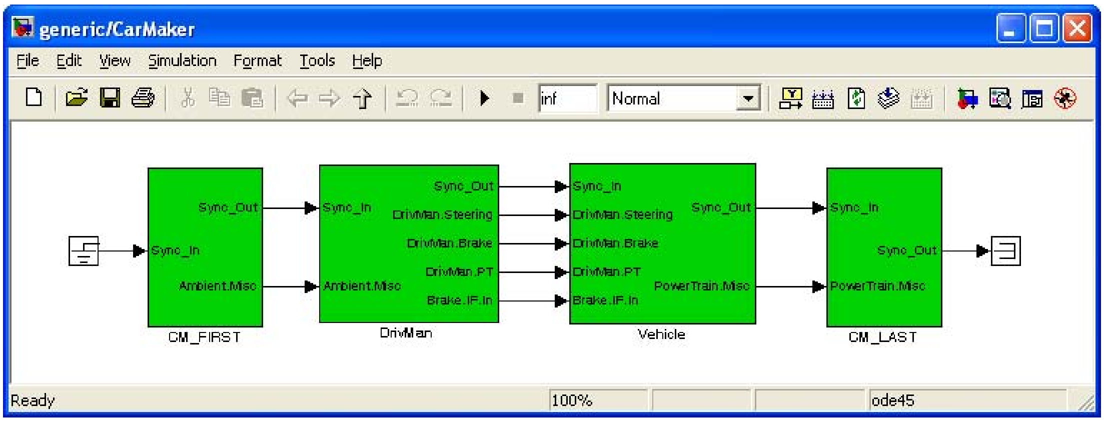

Figure 5.39 : CarMaker model represented as Simulink S-function blocks.

By integrating the control algorithm to the CarMaker S-function blocks and making neccessary connections between blocks, the CarMaker vehicle model can be controlled via the developed control algorithm.

This methodology is applied here by integrating the developed control algorithm introduced in this chapter into the CarMaker model. The CarMaker vehicle model is hybridized by including electric motor and battery models. In order to conduct real time simulations, a real time hardware unit DS1005 by dSPACE is used. The real time simulation setup is shown in Figure 5.40. The control algorithm and CarMaker vehicle model is uploaded into the DS1005 to operate the system in real time. Real time simulation result of the vehicle speed value compared with the drive cycle speed profile for NEDC is shown in Figure 5.41. Change of the fuel consumption results for the conventional and hybridized CarMaker models are shown in Figure 5.42. Change of the *SOC* variable is shown in Figure 5.43. In Figure 5.44, Figure 5.45 and Figure 5.46, real time simulation results for the USA CITY_I are plotted.

Figure 5.40 : DS1005 hardware and CarMaker screenshot.

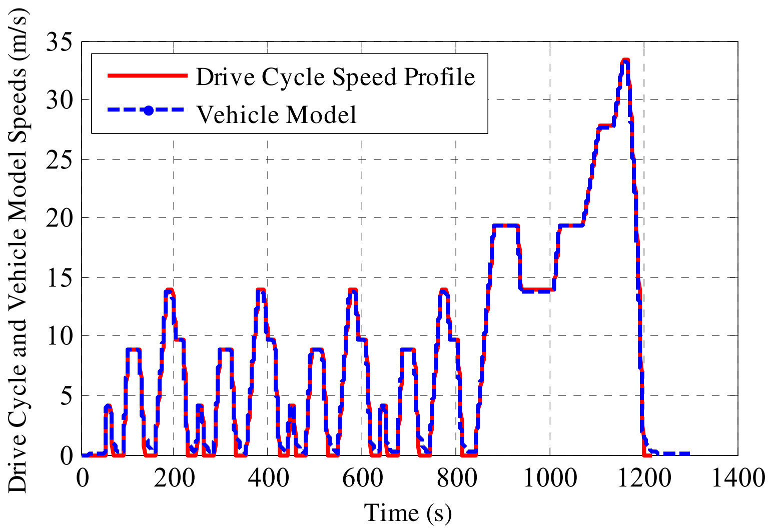

Figure 5.41 : Real time simulation result of the vehicle speed for NEDC.

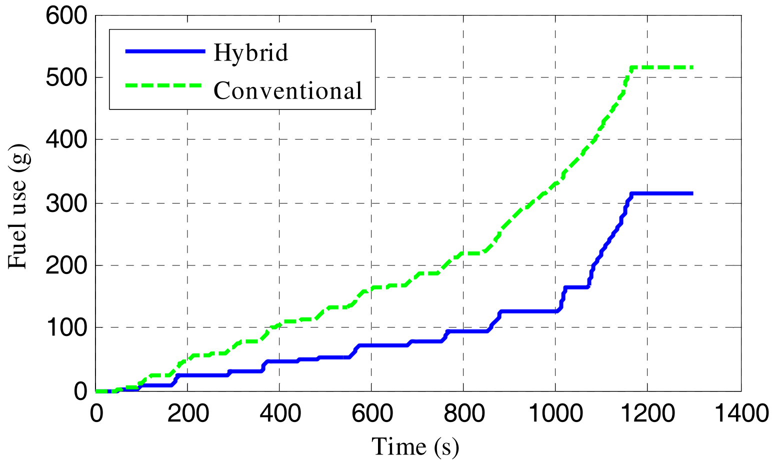

Figure 5.42 : Real time simulation results of fuel consumptions for NEDC.

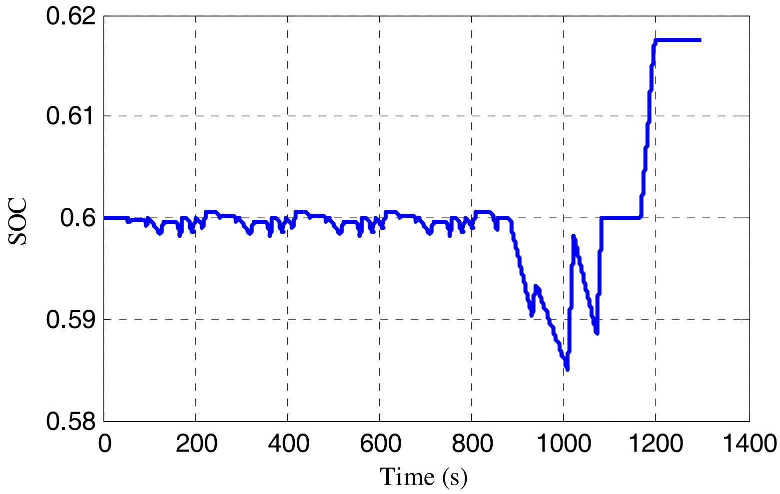

Figure 5.43 : Real time simulation result of *SOC* for NEDC.

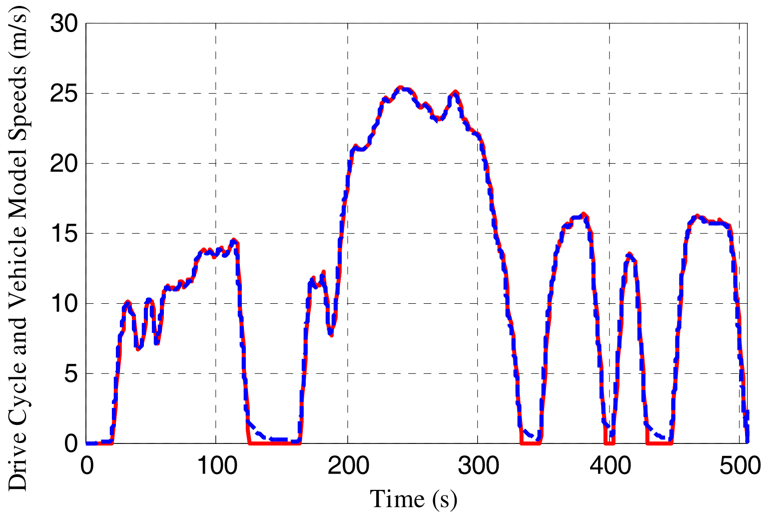

Figure 5.44 : Real time simulation result of the vehicle speed for USA CITY_I.

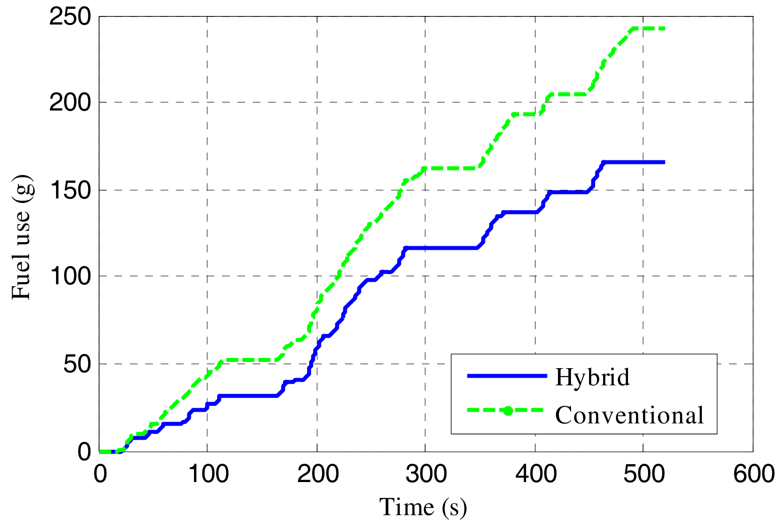

Figure 5.45 : Real time simulation results of fuel consumption for USA CITY_I.

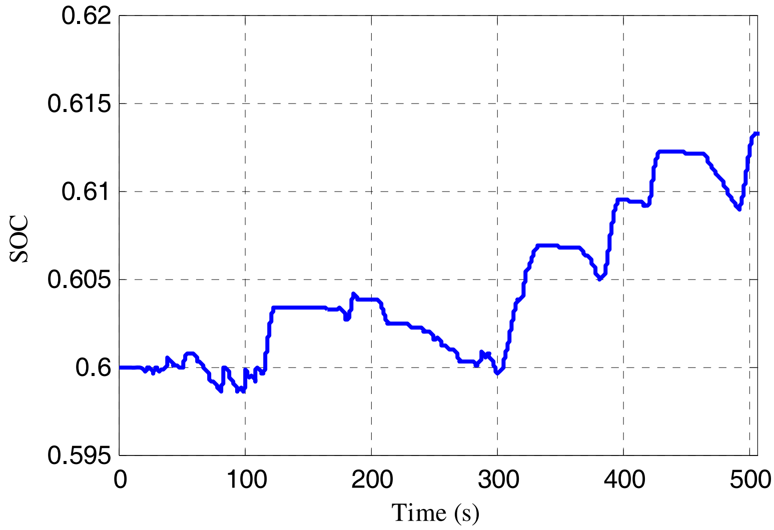

Figure 5.46 : Real time simulation result of *SOC* for USA CITY_I.

For the USA CITY_I drive cycle, the fuel consumption improvement of the hybrid vehicle with respect to the conventional vehicle is % 31 which is equal to the value given in Table 5.3. For the NEDC, the fuel consumption improvement of the hybrid vehicle with respect to the conventional vehicle is % 38. This improvement is bigger than the result shown in Table 5.1, which was % 35. This is because the selected CarMaker vehicle model (1300 kg) is bigger than the vehicle model given in Section 5.2. Hybridized CarMaker model resulted more fuel consumption improvement for the characteristics of NEDC. Real time simulations with CarMaker model show that the developed HEV energy management strategy results substantial fuel consumption improvement.

5.6 Chapter Summary

This chapter has proposed a control algorithm for a parallel hybrid electric vehicle model. An upper level controller chooses vehicle operation mode such as regenerative braking, EM only, ICE only, or ICE plus EM-charge modes. In the ICE plus EM-charge mode, optimum torque distribution between the internal combustion engine and the electric motor is determined via the extremum seeking algorithm that searches for maximum powertrain efficiency. In the literature, this is the first time an extremum seeking algorithm is applied to the hybrid electric vehicle control problem. In order to evaluate performance of the proposed algorithm, its results are compared with those of the dynamic programming solution, which is used as a benchmark of the minimum attainable fuel consumption values. Comparison of the DP results with the proposed algorithm shows that the two levels online control structure with powertrain efficiency maximization based ESA manages to get substantial fuel consumption improvement, comparable to the DP solution.

In order to show the real-time applicability of the algorithm in HEV control problem, simulations are repeated with CarMaker software and dSPACE DS1005 real time hardware

In hybrid electric vehicle applications, a downsized internal combustion engine can be used since there is an additional power source, which is the electric motor. When, in a specific moment of the drive cycle, the required power is beyond the ICE limits, EM may assist to produce the required power. When engine is downsized, it operates more efficiently than the bigger engine, since internal combustion engines operate efficiently in high loading conditions. In this study, engine downsizing is not considered in the modeling of the hybrid powertrain. The ICE is considered same as the one used in the conventional vehicle model. Since the selected internal combustion engine is sufficient to drive the vehicle alone in high power demands, motor assisting mode is not included for keeping the control structure as simple as possible. If downsized engine had been used in this study, the fuel consumption improvement would have been even better due to the small and hence more efficient engine.

The main goal of the ESA algorithm given in this study is to maximize powertrain efficiency and hence to improve fuel consumption. Emission reduction takes place indirectly here. In the EM only mode of operation, there are no emissions from the ICE. In the ICE+EM-charge mode, the ICE operates at a higher torque level where the emission levels are usually lower.

6. CONCLUSIONS

Applications of the extremum seeking algorithm into the ABS and hybrid electric vehicle control problem were covered in the thesis. The thesis developed novel methodologies that are not present in the current literature. In order to show the performance of the developed methodologies, a realistic and detailed vehicle model was generated.

The second chapter introduced literature study for the extremum seeking algorithm, ABS and hybrid electric vehicle control problems. Literature study for the extremum seeking algorithm was divided into four section including sliding mode based, perturbation based, numerical optimization based and gradient-based extremum seeking algorithms. In the literature study of the ABS and hybrid electric vehicle control problems, firstly, theoretical basics were introduced and then the various solutions given in the literature were reviewed.

In the third chapter, a control algorithm was introduced for maximizing braking force by combining sliding mode based extremum seeking algorithm with the adaptation of the tire model parameters. Unlike the common extremum seeking algorithms available in the literature, where the black box approach is conducted by considering completely unknown objective function, an analytic approach was performed by utilizing adaptation of the tire model parameters integrated with the self-optimization routine and hence the necessity of the online objective function measurement was removed. Simulation studies showed that the proposed controller managed to maximize friction potential of the road without estimating the road conditions. The robustness of the proposed control algorithm was illustrated using simulations under different road conditions. Real time simulations were conducted with the microautobox hardware to show real time applicability of the proposed control algorithm.

In the fourth chapter, sliding mode based extremum seeking algorithm was further developed for emergency braking cases including lateral motion such as obstacle avoidance maneuvers. The proposed algorithm incorporated driver steering input information into the optimization procedure to determine the operating region of the tires on the tire force-slip ratio characteristics curve. This is a novel approach in ABS control area and constitutes the main contribution of the study to the existing literature. The algorithm operates the tires near the peak point of the force-slip curve during emergency straight line braking. When the driver demands lateral motion in addition to emergency braking, the operating regions of the tires are modified for improving lateral stability of the vehicle also.

A 15 degree of freedom (6 dof from longitudinal, lateral, vertical, yaw, roll, pitch motions, 4 dof from suspension units, 4 dof from tire rotations and 1 dof from front wheel steering) vehicle model was developed. Measurements from a real vehicle were used for validation of the developed vehicle model. Magic Formula Tire Model was integrated into the vehicle model for calculating the forces that occur between the road and the tires. A hydraulic brake actuator model was used to generate required brake pressure on the wheel cylinders.

It was shown using a detailed simulation study with the validated full vehicle model that, during cornering, while achieving large braking forces, lateral tire forces can be improved considerably and hence the cornering capability of the vehicle can be enhanced significantly.

The fifth chapter proposed a control algorithm for a parallel type hybrid electric vehicle model. An upper level controller chooses the vehicle operation mode such as regenerative braking, EM only, ICE only, or ICE plus EM-charge modes. In the ICE plus EM-charge mode, optimum torque distribution between the internal combustion engine and the electric motor is determined via the extremum seeking algorithm that searches for maximum powertrain efficiency. In the literature this is the first time an extremum seeking algorithm is applied to the hybrid electric vehicle control problem.

A parallel type hybrid electric vehicle model including internal combustion engine (ICE), electric motor (EM), battery model and vehicle dynamics was developed for the study. ICE and EM efficiency maps were used to calculate powertrain efficiency and fuel consumption values.

A dynamic programming (DP) solution was obtained and used to form a benchmark for performance evaluation of the proposed method based on extremum seeking. DP solution gives the minimum obtainable fuel consumption in a considered driving cycle and driving conditions. In order to apply DP procedure, the whole driving cycle and driving conditions should be known in advance. Since future driving conditions are unknown in a real vehicle, DP cannot be utilized in a real time controller. The dynamic programming solution was used offline for performance evaluation of the real time control algorithm.

The comparison of the DP results with the proposed algorithm showed that the two level online control structure with powertrain efficiency maximization based ESA manages to get substantial fuel consumption improvement, the results being comparable to the DP solution.

REFERENCES

[1] **Korovin, S. K. and Utkin, V. I.**, 1974. Using Sliding Modes in Static Optimization and Nonlinear Programming, *Automatica*, **10** (5), pp. 525-532.

[2] **Drakunov, S.**, 1993. Sliding Mode Control of the Systems with Uncertain Direction of Control Vector, *Proceedings of the IEEE Conference on Decision and Control*, **3**, pp. 2477-2478.

[3] **Drakunov, S., Özgüner, Ü., Dix, P., and Ashrafi, B.**, 1995. ABS control using optimum search via sliding modes, *IEEE Trans. Contr. Syst. Technol.*, **3** (1), pp. 79–85.

[4] **Haskara, I., Ozguner, U., Winkelman, J.**, 2000. Extremum Control for Optimal Operating Point Determination and Set Point Optimization via Sliding Modes, *Journal of Dynamic Systems, Measurement, and Control*, **122** (4), pp. 719-724.

[5] **Haskara, I., Ozguner, U., Winkelman, J.**, 2000. Wheel Slip Control for Antispin Acceleration via Dynamic Spark Advance, *Control Engineering Practice*, **8** (10), pp. 1135-1148.

[6] **Pan, Y., Ozguner, U., Acarman, T.**, 2003. Stability and Performance Improvement of Extremum Seeking Control with Sliding Mode, *International Journal of Control*, **76** (9-10), pp. 968-985.

[7] **Yu, H., Ozguner, U.,** 2002. Extremum-Seeking Control Strategy for ABS System with Time Delay, *Proceedings of the American Control Conference*, pp. 3753-3758.

[8] **Yu, H., Ozguner, U.,** 2003. Smooth Extremum-Seeking Control via Second Order Sliding Mode, *Proceedings of the American Control Conference*, pp. 3248-3253.

[9] **Pan, Y., Ozguner, U.,** 2004. Sliding Mode Extremum Seeking Control for Linear Quadratic Dynamic Game, *Proceedings of the American Control Conference*, pp. 614-619.

[10] **Pan, Y., Acarman, T., Ozguner, U.,** 2002. Nash Solution by Extremum Seeking Control Approach, *Proceedings of the 41st IEEE Conference on Decision and Control*, pp. 329-334.

[11] **Haskara, I., Zhu, G. G, Winkelman, J.**, 2006. Multivariable EGR/Spark Timing Control for IC Engines via Extremum Seeking, *Proceedings of the 2006 American Control Conference*, pp. 1173-1178.

[12] **Krstic, M., Wang, H.-H.**, 1997. Design and Stability Analysis of Extremum Seeking Feedback for General Nonlinear Systems, *Proceedings of the 36th Conference on Decision and Control*, pp. 1743-1748.

[13] **Krstic, M., Wang, H.-H.**, 2000. Stability of Extremum Seeking Feedback For General Nonlinear Dynamic Systems, *Automatica*, **36** (4), pp. 595-601.

[14] **Krstic, M.**, 2000. Performance Improvement and Limitations in Extremum Seeking Control, *Systems & Control Letters*, **39** (5), pp. 313-326.

[15] **Tan, Y., Nešic, D., Mareels, I.**, 2006. On non-local stability properties of extremum seeking control, *Automatica*, **42**, pp. 889-903.

[16] **Takata, H., Hachino, T., Tamura, R., and Komatsu, K.**, 2005. Design of Extremum Seeking Control with Accelerator, *IEICE Trans. Fundamentals*, **E88–A** (10), pp. 2535-2540.

[17] **Wang, H.-H. and Krstic, M.**, 2000. Extremum Seeking for Limit Cycle Minimization, *IEEE Transactions On Automatic Control*, **45**, (12), pp. 2432-2437.

[18] **Choi, J.-Y., Krstic, M., Ariyur, K. B., and Lee, J. S.**, 2002. Extremum Seeking Control for Discrete-Time Systems, *IEEE Transactions On Automatic Control*, **47**, (2), pp. 318-323.

[19] **Ariyur, K. B., Krstic, M.**, 2002. Analysis and Design of Multivariable Extremum Seeking, *Proceedings of the American Control Conference*, Anchorage, AK May 8-10, pp. 2903-2908.

[20] **Tanelli, M., Astolfi, A., and Savaresi, S. M.**, 2006. Non-local Extremum Seeking Control for Active Braking Control Systems, *Proceedings of the 2006 IEEE International Conference on Control Applications*, Munich, Germany, October 4-6, pp. 891-896.

[21] **Zhi-dan, Z., Hai-bo, H., Xin-jian, Z., Guang-yi, C., Yuan, R.**, 2008. Adaptive Maximum Power Point Tracking Control of Fuel Cell Power Plants, *Journal of Power Sources*, **176**, pp. 259–269.

[22] **Ariyur, K. B., Krstic, M.**, 2004. Slope Seeking: A Generalization of Extremum Seeking, *International Journal of Adaptive Control and Signal Processing*, **18** (1), pp. 1-22.

[23] **Schustera, E., Xua, C., Torresa, N., Morinagad, E., Allen, C., Krstic, M.**, 2007. Beam Matching Adaptive Control via Extremum Seeking, *Nuclear Instruments and Methods in Physics Research A*, **581,** pp. 799–815.

[24] **Zhang, C., Siranosian, A., Krstic, M.**, 2007. Extremum Seeking for Moderately Unstable Systems and for Autonomous Vehicle Target Tracking Without Position Measurements, *Automatica*, **43** (10), pp. 1832-1839.

[25] **Zhang, C., Arnold, D., Ghods, N., Siranosian, A., Miroslav Krstic, M.**, 2007. Source Seeking with Non-Holonomic Unicycle Without Position Measurement and with Tuning of Forward Velocity, *Systems & Control Letters*, **56,** pp. 245 – 252.

[26] **Cochran, J., Antranik Siranosian, A., Ghods, N., and Krstic, M.**, 2009. 3-D Source Seeking for Underactuated Vehicles Without Position Measurement, *IEEE Transactions On Robotics*, **25** (1), pp. 117-129.

[27] **Peterson, K. S., Stefanopoulou, A. G.**, 2004. Extremum Seeking Control for Soft Landing of an Electromechanical Valve Actuator, *Automatica*, **40** (6), pp. 1063-1069.

[28] **Tan, Y., Nešic, D., Mareels, I. M. Y., Astolfi, A.**, 2009. On Global Extremum Seeking in the Presence of Local Extrema, *Automatica*, **45**, pp. 245-251.

[29] **Li, P., Li, Y., Seem, J. E.**, 2010. Efficient Operation of Air-Side Economizer Using Extremum Seeking Control, *Journal of Dynamic Systems, Measurement, and Control*, **132**, pp. 1-10.

[30] **Killingsworth, N. J., Aceves, S. M., Flowers, D. L., Loza, F. E. and Krstic, M.**, 2009. HCCI Engine Combustion-Timing Control: Optimizing Gains and Fuel Consumption via Extremum Seeking, *IEEE Transactions on Control Systems Technology*, **17** (6), pp. 1350-1361.

[31] **Popovic, D., Jankovic, M., Magner, S., and Teel, A. R.**, 2006. Extremum Seeking Methods for Optimization of Variable Cam Timing Engine Operation, *IEEE Transactions on Control Systems Technology*, **14** (3), pp. 398-407.

[32] **Zhang, C., Ordonez, R.**, 2007. Numerical Optimization-Based Extremum Seeking Control with Application to ABS Design, *IEEE Transactions on Automatic Control*, **52** (3), pp. 454-467.

[33] **Zhang, C., Ordonez, R.**, 2006. Extremum Seeking Control based on Numerical Optimization and State Regulation – Part I: Theory and Framework, *Proceedings of the 45th IEEE Conference on Decision & Control*, pp. 4466-4471.

[34] **Zhang, C., Ordonez, R.**, 2006. Extremum Seeking Control based on Numerical Optimization and State Regulation – Part II: Robust and Adaptive Control Design, *Proceedings of the 45th IEEE Conference on Decision & Control*, pp. 4460-4465.

[35] **Zhang, C., Ordonez, R.**, 2009. Robust and Adaptive Design of Numerical Optimization-Based Extremum Seeking Control, *Automatica*, **45** , pp. 634-646.

[36] **Teel, A. R. and Popovic, D.**, 2001. Solving Smooth and Nonsmoooth Multivariable Extremum Seeking Problems by the Methods of Nonlinear Programming, *Proceedings of the American Control Conference*, pp. 2394-2399.

[37] **Zhang, C., Ordonez, R.**, 2006. Non-gradient Extremum Seeking Control of Feedback Linearizable Systems with Application to ABS Design, *Proceedings of the 45th IEEE Conference on Decision & Control*, pp. 6666-6671.

[38] **Guay, M., Zhang, T.**, 2003. Adaptive Extremum Seeking Control of Nonlinear Dynamic Systems with Parametric Uncertainties, *Automatica*, **39** (7), pp. 1283-1293.

[39] **DeHaan, D., Guay, M.**, 2005. Extremum Seeking Control of State Constrained Nonlinear Systems, *Automatica*, **41** (9), pp. 1567-1574.

[40] **Adetola, V., Guay, M.**, 2006. Adaptive Output Feedback Extremum Seeking Receding Horizon Control of Linear Systems, *Journal of Process Control*, **16**, pp. 521–533.

[41] **Guay, M., Peters, N.**, 2006. Real-time dynamic optimization of nonlinear systems: A flatness-based approach, *Computers and Chemical Engineering*, **30**, pp. 709–721.

[42] **Guay, Dochain, D., Perrier, M., and Hudon, N.**, 2007. Flatness-Based Extremum-Seeking Control Over Periodic Orbits, *IEEE Transactions on Automatic Control*, **52** (10), pp. 2005-2012.

[43] **Adetola, V., Guay, M.**, 2007. Parameter Convergence in Adaptive Extremum-Seeking Control, *Automatica*, **43**, pp. 105 – 110.

[44] **Peters, N., Guay, M., DeHaan, D.**, 2007. Real-Time Dynamic Optimization of Batch Systems, *Journal of Process Control*, **17**, pp. 261–271

[45] **Rajamani, R.**, 2006. *Vehicle Dynamics and Control*, Springer.

[46] **Mi, C., Lin, H., and Zhang, Y.**, 2005. Iterative Learning Control of Antilock Braking of Electric and Hybrid Vehicles", *IEEE Transactions On Vehicular Technology*, **54** (2), pp. 486-494.

[47] **Mirzaei A., Moallem, M., Dehkordi, B. M., and Fahimi, B.**, 2006. Design of an Optimal Fuzzy Controller for Antilock Braking Systems, in *Proc. 2006 IEEE Transactions On Vehicular Technology*, **55** (6), pp. 1725-1730.

[48] **Harifi, A., Aghagolzadeh, A., Alizadeh, G., Sadeghi, M.**, 2008. Designing a Sliding Mode Controller for Slip Control of Antilock Brake Systems, *Transportation Research Part C,* **16** (6), pp. 731-741.

[49] **Oniz, Y., Kayacan, E., and Kaynak, O.**, 2009. A Dynamic Method to Forecast the Wheel Slip for Antilock Braking System and Its Experimental Evaluation, *IEEE Transactions On Systems, Man, And Cybernetics—Part B: Cybernetics,* **39**, (2), pp. 551-560.

[50] **Mirzaeinejad, H., Mirzaei, M.**, 2010. A Novel Method for Non-Linear Control of Wheel Slip in Anti-Lock Braking Systems, *Control Engineering Practice*, **18** (8), pp. 918-926.

[51] **Layne, J. R., Passino, K. M., and Yurkovich, S.**, 1993. Fuzzy Learning Control for Antiskid Braking Systems, *IEEE Trans. Contr. Syst. Technol*., **1**, pp. 122–129.

[52] **Lin, C. M. and Hsu, C. F.**, 2003. Self-Learning Fuzzy Sliding-Mode Control for Antilock Braking Systems, *IEEE Trans. Control Syst. Technol*., **11** (2), pp. 273–278.

[53] **Mauer, G. F.**, 1995. A Fuzzy Logic Controller for an ABS Braking System, *IEEE Trans. Fuzzy Syst*., **3** (4), pp. 381–388.

[54] **Patel, N., Edwards, C., and Spurgeon, S.**, 2007. Optimal Braking and Estimation of Tyre Friction in Automotive Vehicles Using Sliding Modes, *International Journal of Systems Science*, **38** (11), pp. 901–912.

[55] **Lee, Y., and Zak, S. H.**, 2002. Designing a Genetic Neural Fuzzy Antilock-Brake-System Controller, *IEEE Transactions on Evolutionary Computation,* **6** (2), pp. 198-211.

[56] **Zhao, Z., Yu, Z., Sun, Z.**, 2006. Research on Fuzzy Road Surface Identification and Logic Control for Anti-lock Braking System, *IEEE International Conference on Vehicular Electronics and Safety, ICVES 2006*, pp. 380–387.

[57] **Rattasiri, W., Wickramarachchi, N., and Halgamuge, S. K.**, 2007. An Optimized Anti-Lock Braking System in the Presence of Multiple Road Surface Types, *International Journal of Adaptive Control and Signal Processing,* **21**, (6), pp. 477–498.

[58] **Drakunov, S., Özgüner, Ü., Dix, P., and Ashrafi, B.**, 1994. ABS Control Using Optimum Search via Sliding Modes, *Proceedings of the 33rd Conference on Decision and Control*, pp. 466–471.

[59] **Tanelli, M., Astolfi, A., and Savaresi, S.**, 2008. Robust Nonlinear Output Feedback Control for Brake by Wire Control Systems, *Automatica.*, **44** (4), pp. 1078-1087.

[60] **Guzzella, L., Sciarretta, A.**, 2002. *Vehicle Propolsion Systems*, Springer-Verlag, Berlin Heidelberg.

[61] **Salmasi, F. R.**, 2007. Control Strategies for Hybrid Electric Vehicles: Evolution, Classification, Comparison, and Future Trends, *IEEE Transactions on Vehicular Technology*, **56** (5), pp. 2393-2404.

[62] **Chan, C. C.**, 2007. The State of the Art of Electric, Hybrid, and Fuel Cell Vehicles, *Proceedings of the IEEE. Technol.*, **95** (4), pp. 704-718.

[63] **Baumann, B. M., Washington, G., Glenn, B. C., and Rizzoni, G.**, 2000. Mechatronic Design and Control of Hybrid Electric Vehicles, *IEEE/ASME Transactions on Mechatronics*, **5** (1), pp. 58-71.

[64] **Amiri, M., Esfahanian, V., Yazdi, M. R. H., Esfahanian, M., Fazeli, A. M., Nabi, A.**, 2009. Feed-Forward Modelling and Fuzzy Logic Based Control Strategy for Powertrain Efficiency Improvement in a Parallel Hybrid Electric Vehicle, *Mathematical and Computer Modelling of Dynamical Systems*, **15**, (1), pp. 191-207.

[65] **Schouten, N. J., Salman, M. A., and Kheir N. A.**,2002. Fuzzy Logic Control for Parallel Hybrid Vehicles, *IEEE Transactions On Control Systems Technology*, **10**, (3), pp. 460-468.

[66] **Zhong, H., Wang, F., Ao, G.-Q., Qiang, J.-X., Yang, L., Zhuo, B., Mao, X.-J.**, 2008. An Optimal Torque Distribution Strategy for an Integrated Starter–Generator Parallel Hybrid Electric Vehicle Based on Fuzzy Logic Control, *Proceedings of the Institution of Mechanical Engineers, Part D: Journal of Automobile Engineering*, **222** (1), pp. 79-92.

[67] **Boyalı, A, Demirci, M., Acarman, T., Güvenç, L, Tür, O., Uçarol, H., Kiray, B., Özatay, E.**, 2006. Modeling and Control of a Four Wheel Drive Parallel Hybrid Electric Vehicle, *Proccedings of the 2006 IEEE*

International Conference on Control Applications, Munich, pp. 155-162.

[68] **Lin, C. C., Peng, H., Grizzle, J. W., and Kang, J. M.**, 2003. Power Management Strategy for a Parallel Hybrid Electric Truck, *IEEE Transactions on Control Systems Technology*, **11** (6), pp. 839-849.

[69] **Poursamad, A., Montazeri, M.**, 2008. Design of Genetic-Fuzzy Control Strategy for Parallel Hybrid Electric Vehicles, *Control Engineering Practice*, **16**, pp. 861-873.

[70] **Wang, F., Mao, X. J., Zhuo, B., Zhong, H., and Ma, Z. L**., 2009. Parallel Hybrid Electric System Energy Optimization Control with Automated Mechanical Transmission, *Proceedings of the Institution of Mechanical Engineers Part D: Journal of Automobile Engineering*, **223**, pp. 151-166.

[71] **Adhikari, S., Halgamuge, S. K., and Watson, H. C.**, 2010. An Online Power-Balancing Strategy for a Parallel Hybrid Electric Vehicle Assisted by an Integrated Starter Generator, *IEEE Transactions On Vehicular Technology*, **59** (6), pp. 2689-2699.

[72] **Park, J-Y, Park, Y-K, and Park, J-H**, 2008. Optimal Power Distribution Strategy for Series–Parallel Hybrid Electric Vehicles, *Proceedings of the Institution of Mechanical Engineers Part D: Journal of Automobile Engineering*, **222**, pp. 989-1000.

[73] **Rousseau, G., Sinoquet, D., and Rouchon**, **P.**, 2007. Constrained Optimization of Energy Management for a Mild-Hybrid Vehicle, *Oil & Gas Science and Technology*, **62**, pp. 623-634.

[74] **Paganelli, G., Tateno, M., Brahma, A., Rizzoni, G., and Guezennec, Y.**, 2001. Control Development for a Hybrid Electric Sport Utility Vehicle: Strategy, Implementation and Field Test Results, *Proceedings of the American Control Conference*, Arlington, pp. 5064-5069.

[75] **Delprat, S., Guerra, T. M., Paganelli, G., Lauber, J., and Delhom, M.**, 2001. Control Strategy Optimization for a Hybrid Parallel Powertrain, *Proceedings of the American Control Conference, Arlington, VA, United States,* pp. 1315-1320.

[76] **Paganelli, G., Delprat S., Guerra T.M., Rimaux J., and Santin J.J.**, 2002. Equivalent Consumption Minimization Strategy for Parallel Hybrid Powertrains, *Proceedings of Conference sponsored by Vehicular Transportation Systems (VTS) and IEEE*, *Atlantic City, NJ, USA*, pp. 2076-2081.

[77] **Sciarretta, A., Back, M., and Guzzella, L.**, 2004. Optimal Control of Parallel Hybrid Electric Vehicles, *IEEE Transactions on Control Systems Technology*, **12** (3), pp. 352-363.

[78] **Musardo, C., Rizzoni, G., and Staccia, B.**, 2005. A-ECMS: An Adaptive Algorithm for Hybrid Electric Vehicle Energy Management, *Proceedings of the 44th IEEE Conference on Decision and Control, and the European Control Conference*, Seville, Spain, pp. 1816-1823.

[79] **Hofman, T., Steinbuch, M., Van Druten, R., Serrarens, A.**, 2007. Rule-Based Energy Management Strategies for Hybrid Vehicles, *International Journal of Electric and Hybrid Vehicles*, **1** (1), pp. 71-94.

[80] **Pisu, P. and Rizzoni, G**, 2007. A Comparative Study of Supervisory Control Strategies for Hybrid Electric Vehicles, *IEEE Transactions on Control Systems Technology*, **15** (3), pp. 506-518.

[81] **Rousseau, G., Sinoquet, D., Sciarretta, A., Milhau, Y.**, 2008. Design Optimisation and Optimal Control for Hybrid Vehicles, *International Conference on Engineering Optimization*, pp. 1-10.

[82] **Lin, X., Banvait, H., Anwar, S., and Chen, Y.**, 2010. Optimal Energy Management for a Plug-in Hybrid Electric Vehicle: Real-time controller, *American Control Conference*, pp. 5037-5042.

[83] **Huang, Y.-J., Yin, C.-L., and Zhang, J.-W.**, 2009. Design of an Energy Management Strategy for Parallel Hybrid Electric Vehicles Using a Logic Threshold and Instantaneous Optimization Method, *International Journal of Automotive Technology*, **10** (4), pp. 513-521.

[84] **Kiencke, U., Nielsen, L.**, 2005. *Automotive Control Systems for Engine, Driveline, and Vehicle*, Springer-Verlag Berlin-Heidelberg.

[85] **Guzzella, L., Amstutz, A.**, 2005. The QSS Toolbox Manual [Online], Available: http://www.idsc.ethz.ch/Downloads/qss, accessed at 19.10. 2009.

[86] **Pacejka, H. B.**, 2002. *Tyre and Vehicle Dynamics*, Oxford: Butterworth-Heinemann.

[87] **Kirk, D. E.**, 1970. *Optimal control theory: an introduction*, Prentice-Hall.

[88] **Greenwood, D. T.**, 1988. *Principles of Dynamics*, Prentice-Hall.

[89] **Musardo, C., Staccia, B.**, 2004. Energy Management Strategies for Hybrid Electric Vehicles, *M.S. Thesis*, Politecnico di Milano.

[90] **Aytekin, B., Dinçmen, E., Aksun Güvenç, B., Altuğ, E., Güvenç, L., Daniş, S., Acarman, T., Sezer, V., Ararat, Ö., Öncü, S.**, 2010. Framework for Development of Driver Adaptive Warning and Assistance Systems that will be Triggered by a Driver Inattention Monitor, *International Journal of Vehicle Design*, **52** (1/2/3/4), pp. 20-37.

[91] **Aksun Güvenç, B., Güvenç, L., Karaman, S.**, 2010. Robust MIMO Disturbance Observer Analysis and Design with Application to Active Car Steering, *International Journal of Robust and Nonlinear Control*, **20**, pp.873-891.

[92] **Aksun Güvenç, B., Güvenç, L., Karaman, S.**, 2009. Robust Yaw Stability Controller Design and Hardware in the Loop Testing for a Road Vehicle, *IEEE Transactions on Vehicular Technology*, **58** (2), pp.555-571.

[93] **Aksun Güvenç, B.**, 2010. Lecture Notes: MAK450-Vehicle System Dynamics and Control, Istanbul Technical University.

[94] **Güvenç, L.**, 2010. Lecture Notes: MAK654E-Vehicle Control Systems, Istanbul Technical University.

APPENDICES

APPENDIX A : Obtaining the Vehicle Model Absolute Acceleration Vector.
APPENDIX B : Magic Formula Tire Model Formulation.
APPENDIX C : Computer Programmes (in cd).

APPENDIX A

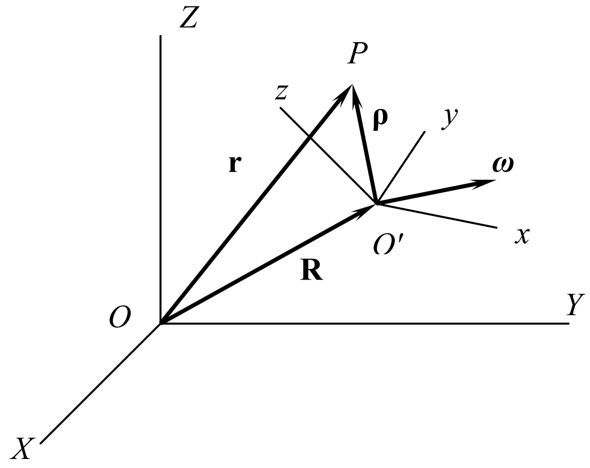

Figure A.1 : Position vectors of a point P relative to a fixed system and a moving system.

Referring to Figure A.1 the equations for the absolute velocity and acceleration of a particle P that is in motion relative to a moving coordinate system will be obtained. The XYZ system is fixed in an inertial frame and the xyz system translates and rotates relative to it. In Figure A.1, $\mathbf{r}$ is the position vector of P and $\mathbf{R}$ is the position vector of O', both relative to point O in the fixed XYZ system. Then

$$\mathbf{r} = \mathbf{R} + \boldsymbol{\rho} \tag{A.1}$$

where $\boldsymbol{\rho}$ is the position vector of P relative to O'. Differentiating with respect to time, the absolute velocity is obtained

$$\mathbf{v} = \dot{\mathbf{r}} = \dot{\mathbf{R}} + \dot{\boldsymbol{\rho}} \tag{A.2}$$

where both derivatives are calculated from the viewpoint of a fixed observer. It can be written that

$$\dot{\boldsymbol{\rho}} = \left(\dot{\boldsymbol{\rho}}\right)_{\mathrm{r}} + \boldsymbol{\omega} \times \boldsymbol{\rho} \tag{A.3}$$

Here $\boldsymbol{\omega}$ is the absolute rotation rate of the xyz system. $\left(\dot{\boldsymbol{\rho}}\right)_{\mathrm{r}}$ is the velocity of P relative to O', as viewed by an observer rotating with the xyz system. Then

$$\mathbf{v} = \dot{\mathbf{R}} + (\dot{\boldsymbol{\rho}})_{\mathrm{r}} + \boldsymbol{\omega} \times \boldsymbol{\rho} \tag{A.4}$$

Next, the absolute acceleration of P will be obtained. Taking the derivatives

$$\frac{d}{dt}\left(\dot{\mathbf{R}}\right) = \ddot{\mathbf{R}} \tag{A.5}$$

$$\frac{d}{dt}[(\dot{\boldsymbol{\rho}})_r] = (\ddot{\boldsymbol{\rho}})_r + \boldsymbol{\omega} \times (\dot{\boldsymbol{\rho}})_r \tag{A.6}$$

$$\frac{d}{dt}(\boldsymbol{\omega} \times \boldsymbol{\rho}) = \dot{\boldsymbol{\omega}} \times \boldsymbol{\rho} + \boldsymbol{\omega} \times \dot{\boldsymbol{\rho}} = \dot{\boldsymbol{\omega}} \times \boldsymbol{\rho} + \boldsymbol{\omega} \times (\dot{\boldsymbol{\rho}})_{\mathbf{r}} + \boldsymbol{\omega} \times (\boldsymbol{\omega} \times \boldsymbol{\rho}) \tag{A.7}$$

Combining the equations **(A.4)**, **(A.5)**, **(A.6)**, and **(A.7)** one can get the absolute acceleration of *P* as follows as given in [88]

$$\mathbf{a} = \ddot{\mathbf{R}} + \dot{\boldsymbol{\omega}} \times \boldsymbol{\rho} + \boldsymbol{\omega} \times (\boldsymbol{\omega} \times \boldsymbol{\rho}) + (\ddot{\boldsymbol{\rho}})_{\mathbf{r}} + 2\boldsymbol{\omega} \times (\dot{\boldsymbol{\rho}})_{\mathbf{r}} \tag{A.8}$$

In the above equation $\dot{\boldsymbol{\omega}} \times \boldsymbol{\rho}$ is tangential acceleration, $\boldsymbol{\omega} \times (\boldsymbol{\omega} \times \boldsymbol{\rho})$ is centripetal acceleration, $(\ddot{\boldsymbol{\rho}})_{\mathbf{r}}$ is acceleration of the point *P* relative to the *xyz* system, that is, as viewed by an observer moving with the *xyz* system. The last term $2\boldsymbol{\omega} \times (\dot{\boldsymbol{\rho}})_{\mathbf{r}}$ is the Coriolis acceleration.

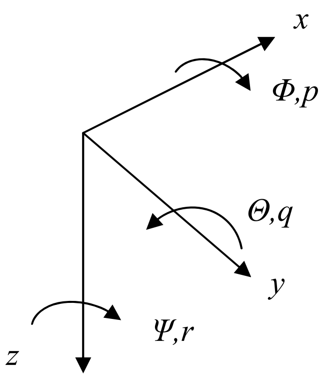

Figure A.2 : Vehicle axis system.

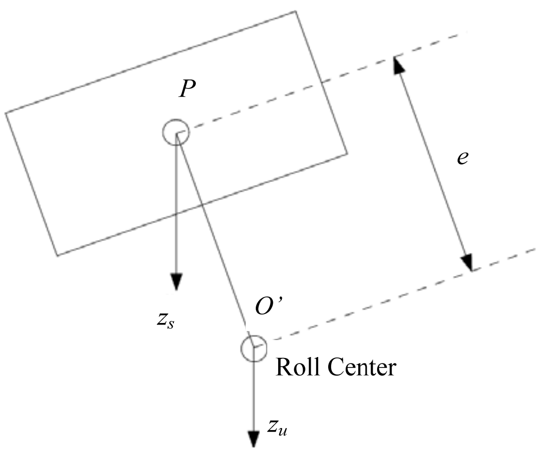

Figure A.3 : Roll motion of the sprung mass.

Comparing with the vehicle system, *O′* is the roll center and *P* is sprung mass c.g. (Figure A.3). In **(A.8)**, $\ddot{\mathbf{R}}$ is the absolute acceleration of the roll center. The velocity vector of the roll center is

$$\mathbf{V}_{rc} = u\mathbf{i} + v\mathbf{j} + \dot{z}_u\mathbf{k} \tag{A.9}$$

Absolute angular velocity of roll center with respect to inertial frame is

$$\boldsymbol{\omega}_{\mathbf{rc}} = r\mathbf{k} \tag{A.10}$$

Absolute acceleration vector of roll center with respect to inertial frame is found by using **(A.9)** and **(A.10)** as follows

$$\ddot{\mathbf{R}} = \dot{u}\mathbf{i} + \dot{v}\mathbf{j} + \ddot{z}_1\mathbf{k} + r\mathbf{k} \times \left(u\mathbf{i} + v\mathbf{j} + \dot{z}_u\mathbf{k}\right) \tag{A.11}$$

$$\ddot{\mathbf{R}} = (\dot{u} - vr)\mathbf{i} + (\dot{v} + ur)\mathbf{j} + \ddot{z}_u\mathbf{k} \tag{A.12}$$

From **(A.12)**, unsprung mass accelerations are defined as

$$\begin{aligned} a_{xu} &= \dot{u} - vr \\ a_{yu} &= \dot{v} + ur \\ a_{zu} &= \ddot{z}_u \end{aligned} \tag{A.13}$$

In **(A.8)**, $\boldsymbol{\rho}$ is the position vector of sprung mass c.g. relative to roll center, which is

$$\boldsymbol{\rho} = -(e - z_s)\mathbf{k} \tag{A.14}$$

In **(A.8)** $\left(\dot{\boldsymbol{\rho}}\right)_{\mathbf{r}}$ is the velocity of sprung mass c.g. relative to roll center, as viewed by an observer rotating with the body fixed axes in the roll center.

$$\left(\dot{\boldsymbol{\rho}}\right)_{\mathbf{r}} = \dot{z}_s\mathbf{k} \tag{A.15}$$

In **(A.8)** $\boldsymbol{\omega}$ is the absolute rotation rate of the body fixed axis system. To obtain this, the rotation matrices will be defined. The rotation of the vehicle sprung mass is given with the Euler angles (*ψ, θ, -Φ*). Here the roll motion is taken as negative. The rotation matrices are found as follows

$$RM(\psi) = \begin{bmatrix} \cos\psi & \sin\psi & 0 \\ -\sin\psi & \cos\psi & 0 \\ 0 & 0 & 1 \end{bmatrix} \tag{A.16}$$

$$RM(\theta) = \begin{bmatrix} \cos\theta & 0 & -\sin\theta \\ 0 & 1 & 0 \\ \sin\theta & 0 & \cos\theta \end{bmatrix} \tag{A.17}$$

$$RM(\phi)=\begin{bmatrix}1 & 0 & 0\\ 0 & \cos\phi & -\sin\phi\\ 0 & \sin\phi & \cos\phi\end{bmatrix} \quad \textbf{(A.18)}$$

The absolute angular velocity vector of the sprung mass body with respect to inertial coordinate system is found as follows.

$$\begin{bmatrix}\omega_x\\ \omega_y\\ \omega_z\end{bmatrix}=RM(\phi)\times\begin{bmatrix}-p\\ 0\\ 0\end{bmatrix}+RM(\phi)\times RM(\theta)\times\begin{bmatrix}0\\ q\\ 0\end{bmatrix}+RM(\phi)\times RM(\theta)\times RM(\psi)\times\begin{bmatrix}0\\ 0\\ r\end{bmatrix} \quad \textbf{(A.19)}$$

$$\begin{aligned}\begin{bmatrix}\omega_x\\ \omega_y\\ \omega_z\end{bmatrix}&=\begin{bmatrix}1 & 0 & 0\\ 0 & \cos\phi & -\sin\phi\\ 0 & \sin\phi & \cos\phi\end{bmatrix}\times\begin{bmatrix}-p\\ 0\\ 0\end{bmatrix}+\begin{bmatrix}1 & 0 & 0\\ 0 & \cos\phi & -\sin\phi\\ 0 & \sin\phi & \cos\phi\end{bmatrix}\times\begin{bmatrix}\cos\theta & 0 & -\sin\theta\\ 0 & 1 & 0\\ \sin\theta & 0 & \cos\theta\end{bmatrix}\times\begin{bmatrix}0\\ q\\ 0\end{bmatrix}\\ &+\begin{bmatrix}1 & 0 & 0\\ 0 & \cos\phi & -\sin\phi\\ 0 & \sin\phi & \cos\phi\end{bmatrix}\times\begin{bmatrix}\cos\theta & 0 & -\sin\theta\\ 0 & 1 & 0\\ \sin\theta & 0 & \cos\theta\end{bmatrix}\times\begin{bmatrix}\cos\psi & \sin\psi & 0\\ -\sin\psi & \cos\psi & 0\\ 0 & 0 & 1\end{bmatrix}\times\begin{bmatrix}0\\ 0\\ r\end{bmatrix}\end{aligned} \quad \textbf{(A.20)}$$

$$\begin{bmatrix}\omega_x\\ \omega_y\\ \omega_z\end{bmatrix}=\begin{bmatrix}-p-r\sin\theta\\ q\cos\phi-r\cos\theta\sin\phi\\ r\cos\theta\cos\phi+q\sin\phi\end{bmatrix} \quad \textbf{(A.21)}$$

Angular velocity vector is given from **(A.21)** as follows

$$\boldsymbol{\omega}=(-p-r\sin\theta)\mathbf{i}+(q\cos\phi-r\cos\theta\sin\phi)\mathbf{j}+(r\cos\theta\cos\phi+q\sin\phi)\mathbf{k} \quad \textbf{(A.22)}$$

Angular velocity vector given in **(A.22)** is simplified as

$$\boldsymbol{\omega}=-p\mathbf{i}+q\mathbf{j}+r\mathbf{k} \quad \textbf{(A.23)}$$

Combining equations **(A.8)**, **(A.12)**, **(A.14)**, **(A.15)** and **(A.23)**, the absolute acceleration vector of the sprung mass is obtained as follows:

$$\begin{aligned}\mathbf{a}&=(\dot{u}-vr+\dot{q}z_s-\dot{q}e-rpz_s+rpe+2q\dot{z}_s)\mathbf{i}+\\ &(\dot{v}+ur+\dot{p}z_s-\dot{p}e+rqz_s-rqe+2p\dot{z}_s)\mathbf{j}+\\ &(\ddot{z}_u-p^2z_s+p^2e-q^2z_s+q^2e+\ddot{z}_s)\mathbf{k}\end{aligned} \quad \textbf{(A.24)}$$

From the sprung mass absolute acceleration vector of **(A.24)**, acceleration components for the sprung mass are defined as

$$\begin{aligned}a_{xs}&=\dot{u}-vr+\dot{q}z_s-\dot{q}e-rpz_s+rpe+2q\dot{z}_s\\ a_{ys}&=\dot{v}+ur+\dot{p}z_s-\dot{p}e+rqz_s-rqe+2p\dot{z}_s\\ a_{zs}&=\ddot{z}_u-p^2z_s+p^2e-q^2z_s+q^2e+\ddot{z}_s\end{aligned} \quad \textbf{(A.25)}$$

APPENDIX B

Calculation of the tire forces according to the Magic Formula Tire Model as given in [86]. In all of the formulas given below, the coefficients p_x, q_x, r_x and s_x are non-dimensional model parameters.

Longitudinal Force (Pure Longitudinal Slip)

$$F_{x0} = D_x \sin\left[C_x \arctan\left\{B_x\kappa_x - E_x\left(B_x\kappa_x - \arctan\left(B_x\kappa_x\right)\right)\right\}\right] + S_{Vx} \quad \textbf{(B.1)}$$

$$\kappa_x = \kappa + S_{Hx} \quad \textbf{(B.2)}$$

$$C_x = p_{Cx1} \quad \textbf{(B.3)}$$

$$D_x = \mu_{x\max} F_z \quad \textbf{(B.4)}$$

$$\mu_{x\max} = (p_{Dx1} + p_{Dx2} df_z) \cdot \lambda_{\mu x} \quad \textbf{(B.5)}$$

$$df_z = \frac{F_z - F_{z0}}{F_{z0}} \quad \textbf{(B.6)}$$

$$E_x = (p_{Ex1} + p_{Ex2} \cdot df_z + p_{Ex3} df_z^{\,2})(1 - p_{Ex4} sign(\kappa_x)) \quad \textbf{(B.7)}$$

$$K_{x\kappa} = F_z (p_{Kx1} + p_{Kx2} \cdot df_z) \exp(p_{Kx3} \cdot df_z) \quad \textbf{(B.8)}$$

$$B_x = K_{x\kappa} / (C_x D_x + \varepsilon_x) \quad \textbf{(B.9)}$$

$$S_{Hx} = (p_{Hx1} + p_{Hx2} df_z) \quad \textbf{(B.10)}$$

$$S_{Vx} = F_z (p_{Vx1} + p_{Vx2} df_z) \cdot \lambda'_{\mu x} \quad \textbf{(B.11)}$$

$$\lambda'_{\mu x} = A_\mu \lambda_{\mu x} / \left\{(1 + (A_\mu - 1)\lambda_{\mu x}\right\} \quad \textbf{(B.12)}$$

In the above equations $\lambda_{\mu x}$ is the longitudinal friction coefficient scaling factor. With that tool the effect of changing friction coefficient can be quickly investigated without having the need to implement a completely new tire data set. S_{Vx} and S_{Hx} are horizontal and vertical shifts with respect to origin. F_{z0} is the nominal load.

Longitudinal Force (Combined Slip)

$$F_x = G_{x\alpha} F_{x0} \quad \textbf{(B.13)}$$

$$G_{x\alpha} = \cos\left[C_{x\alpha} \arctan\left\{B_{x\alpha}\alpha_s - E_{x\alpha}\left(B_{x\alpha}\alpha_s - \arctan\left(B_{x\alpha}\alpha_s\right)\right)\right\}\right] / G_{x\alpha 0} \quad \textbf{(B.14)}$$

$$G_{x\alpha 0} = \cos\left[C_{x\alpha} \arctan\left\{B_{x\alpha}S_{Hx\alpha} - E_{x\alpha}\left(B_{x\alpha}S_{Hx\alpha} - \arctan\left(B_{x\alpha}S_{Hx\alpha}\right)\right)\right\}\right] \quad \textbf{(B.15)}$$

$$\alpha_S = \alpha^* + S_{Hx\alpha} \quad \textbf{(B.16)}$$

$$B_{x\alpha} = r_{Bx1} \cos\left[\arctan(r_{Bx2}\kappa)\right] \quad \textbf{(B.17)}$$

$$C_{x\alpha} = r_{Cx1} \quad \textbf{(B.18)}$$

$$E_{x\alpha} = r_{Ex1} + r_{Ex2} df_z \quad \textbf{(B.19)}$$

$$S_{Hx\alpha} = r_{Hx1} \quad \textbf{(B.20)}$$

Lateral Force (Pure Side Slip)

$$F_{y0} = D_y \sin\left[C_y \arctan\left\{B_y\alpha_y - E_y\left(B_y\alpha_y - \arctan\left(B_y\alpha_y\right)\right)\right\}\right] + S_{Vy} \quad \textbf{(B.21)}$$

$$\alpha_y = \alpha^* + S_{Hy} \quad \textbf{(B.22)}$$

$$\alpha^* = \tan(\alpha) \quad \textbf{(B.23)}$$

$$C_y = p_{Cy1} \quad \textbf{(B.24)}$$

$$D_y = \mu_{y\max} F_z \quad \textbf{(B.25)}$$

$$\mu_{y\max} = (p_{Dy1} + p_{Dy2} df_z)\lambda_{\mu y} \quad \textbf{(B.26)}$$

$$E_y = (p_{Ey1} + p_{Ey2} df_z)(1 - p_{Ey3} sign(\alpha_y) \quad \textbf{(B.27)}$$

$$K_{y\alpha 0} = p_{Ky1} F_{z0} \sin(2\arctan(F_z / (p_{Ky2} \cdot F_{z0}))) \quad \textbf{(B.28)}$$

$$K_{y\alpha} = K_{y\alpha 0} \quad \textbf{(B.29)}$$

$$B_y = K_{y\alpha} / (C_y D_y + \varepsilon_y) \qquad \textbf{(B.30)}$$

$$S_{Vy} = F_z \{p_{Vy1} + p_{Vy2} df_z\} \lambda'_{\mu y} \qquad \textbf{(B.31)}$$

$$S_{Hy} = (p_{Hy1} + p_{Hy2} df_z) \qquad \textbf{(B.32)}$$

Lateral Force (combined slip)

$$F_y = G_{y\kappa} F_{y0} + S_{Vy\kappa} \qquad \textbf{(B.33)}$$

$$G_{y\kappa} = \cos[C_{y\kappa} \arctan\{B_{y\kappa}\kappa_s - E_{y\kappa}(B_{y\kappa}\kappa_s - \arctan(B_{y\kappa}\kappa_s))\}] / G_{y\kappa 0} \qquad \textbf{(B.34)}$$

$$G_{y\kappa 0} = \cos[C_{y\kappa} \arctan\{B_{y\kappa} S_{Hy\kappa} - E_{y\kappa}(B_{y\kappa} S_{Hy\kappa} - \arctan(B_{y\kappa} S_{Hy\kappa}))\}] \qquad \textbf{(B.35)}$$

$$\kappa_S = \kappa + S_{Hy\kappa} \qquad \textbf{(B.36)}$$

$$B_{y\kappa} = r_{By1} \cos[\arctan\{r_{By2}(\alpha^* - r_{By3}\}] \qquad \textbf{(B.37)}$$

$$C_{y\kappa} = r_{Cy1} \qquad \textbf{(B.38)}$$

$$E_{y\kappa} = r_{Ey1} + r_{Ey2} df_z \qquad \textbf{(B.39)}$$

$$S_{Hy\kappa} = r_{Hy1} + r_{Hy2} df_z \qquad \textbf{(B.40)}$$

$$S_{Vy\kappa} = D_{Vy\kappa} \sin[r_{Vy5} \arctan(r_{Vy6}\kappa)] \qquad \textbf{(B.41)}$$

$$D_{Vy\kappa} = \mu_y F_z (r_{Vy1} + r_{Vy2} df_z) \cos[\arctan(r_{Vy4}\alpha^*)] \qquad \textbf{(B.42)}$$

CURRICULUM VITAE

Candidate's full name: Erkin DİNÇMEN

Place and date of birth: Trabzon, 21.06.1978

Permanent Address: İdealtepe mah., Küçüktur yolu., 26/13, Maltepe, 34841, İstanbul-Turkey.

Universities and Colleges attended: Istanbul Technical University, Department of Mechanical Engineering, Ph.D., 2005-2011

Istanbul Technical University, Department of Mechanical Engineering, M.Sc., 2000-2003

Istanbul Technical University, Department of Mechanical Engineering, B.Sc., 1996-2000

Publications:

- **Dincmen, E.,** Uygan, İ. M. C., Guvenc, B. A., Acarman, T, 2010. Powertrain Control of Parallel Hybrid Electric Vehicles via Extremum Seeking Algorithm, *Proceedings of the ASME 2010 10th Biennial Conference on Engineering Systems Design and Analysis ESDA2010, July 12-14, Istanbul, Turkey*, pp. 147-156.
- **Dincmen, E.,** Acarman, T., Guvenc, B. A., 2010. ABS Control Algorithm via Extremum Seeking Method with Enhanced Lateral Stability, *Proceedings of the 6th IFAC Symposium Advances in Automotive Control, July 12-14, Munich, Germany*.
- Aytekin, B., **Dincmen, E.,** Guvenc, B. A., Altug, E., Guvenc, L., Danis, S., Acarman, T., Sezer, V., Ararat, O., Oncu, S., 2010. Framework for Development of Driver Adaptive Warning and Assistance Systems That Will Be Triggered by a Driver Inattention Monitor, *International Journal of Vehicle Design*, **52**, no: 1/2/3/4, pp. 20-37.
- **Dincmen, E.,** Acarman, T., 2009. ABS Control via Extremum Seeking with Parameter Tuning", , *Proceedings of the* 2009 *European Control Conference, August 23-26, Budapest, Hungary,* pp. 2664-2669.
- **Dincmen, E.,** Acarman, T., 2008. Active Coordination of the Individually Actuated Wheel Braking and Steering to Enhance Vehicle Lateral Stability and Handling, *Proceedings of the 17th IFAC World Congress, July 6-11, Seoul*, *Korea*, pp. 10738-10743.

- **Dincmen, E.,** Acarman, T., 2007. Application of Vehicle Dynamics Active Control to a Realistic Vehicle Model, *Proceedings of the 2007 American Control Conference, July 11-13, New York City, USA*, pp. 200-205.
- **Dincmen, E.,** Acarman, T., 2007. Enhancement of Handling and Cornering Capability for Individual Wheel Braking Actuated Vehicle Dynamics, *Proceedings of the* 2007 *Intelligent Vehicles Symposium, June 13-15, Istanbul, Turkey,* pp. 888-893.